

University of London

Development of Metal-based Catalysts for Phosphate Ester Hydrolysis

Mariya Chernobryva

Supervisors:

Prof. Michael Watkinson

Prof. Marina Resmini

Submitted in partial fulfilment of the requirements of the Degree of Doctor of
Philosophy

Statement of Originality

I, Mariya Chernobryva, confirm that the research included within this thesis is my own work or that where it has been carried out in collaboration with, or supported by others, that this is duly acknowledged below and my contribution indicated. Previously published material is also acknowledged below.

I attest that I have exercised reasonable care to ensure that the work is original, and does not to the best of my knowledge break any UK law, infringe any third party's copyright or other Intellectual Property Right, or contain any confidential material.

I accept that the College has the right to use plagiarism detection software to check the electronic version of the thesis.

I confirm that this thesis has not been previously submitted for the award of a degree by this or any other university.

The copyright of this thesis rests with the author and no quotation from it or information derived from it may be published without the prior written consent of the author.

Signature:

Date: 15 November 2016

Details of publications:

- A. Jorge, M. Chernobryva, S. E. J. Rigby, M. Watkinson and M. Resmini, *Chem. Eur. J.*, 2016, **22**, 3764-3774.

Abstract

The development of artificial metal-based catalytic systems for phosphate ester hydrolysis is the central focus of this work. Currently, significant efforts are concentrated in this field of research as phosphate esters are remarkably stable linkages and are found in the molecules of life DNA and RNA, as well as in toxic compounds, such as nerve agents, pesticides and herbicides.

The thesis describes the design and synthesis of a series of *N*-functionalised azamacrocyclic ligands suitable for metal chelation. An efficient strategy is described, where an aminated precursor is used for the selective *N*-alkylation of a cyclen moiety, in order to obtain non-bridged and ethylene-bridged cyclen-based ligands. Thereafter, the synthesis of the tetraamine Co(III) and Zn(II) aqua-hydroxo complexes is detailed, followed by a study of the coordination chemistry of Co(III)-based cyclen complexes. Moreover, the redox behaviour of such complexes is investigated by means of cyclic voltammetry.

The hydrolytic activity of these complexes towards phosphate ester substrates is then presented. The hydrolytic activity of the cyclen-based Co(III) complexes is shown to be extremely sensitive to modest changes in the ligand structures, even though they do not affect the coordination geometry. Cyclen-based Zn(II) complexes appear to have no appreciable activity towards hydrolysis of phosphate mono- and di-esters under the same experimental conditions. The effect of incorporating polymerisable tetraamine Co(III) complexes into the nanogels on their hydrolytic efficiency is also investigated using molecular imprinting technique.

The design and synthesis of structurally similar tripodal 'click' ligands, suitable for the preparation of a range of d-block metal complexes is then presented. The coordination chemistry of the complexes of these structurally similar ligands is explored using a range of techniques including single crystal X-ray crystallography, EPR and UV-Vis spectroscopies and cyclic voltammetry. Due to their poor aqueous solubility various ways to improve this are also examined.

Future developments of the metal-based catalysts are then discussed including key issues to be addressed to achieve their potential applications in biological systems.

Table of Contents

<i>Statement of Originality</i>	2
<i>Abstract</i>	3
<i>List of Abbreviations</i>	10
<i>Acknowledgements</i>	12
Chapter 1: Introduction	15
1.1. Overall Aims of the Project	15
1.2. The Role of Phosphate Esters in the Chemistry of Life	15
1.2.1. Structure and Reactivity of Phosphate Esters.....	16
1.2.2. Hazardous Phosphate Esters and Their Role in Chemical Weaponry	18
1.2.3. Advances in the Decontamination of Toxic Phosphate Esters.....	20
1.3. Cleavage of Phosphate Esters	23
1.3.1. Uncatalysed Hydrolysis of Phosphate Esters	23
1.3.2. Catalysis of Phosphate Ester Hydrolysis by Natural Enzymes.....	24
1.3.3. Biomimetic Catalysts for Phosphate Ester Hydrolysis: From Small-Molecule Hydrolytic Agents to Large Enzyme-like Systems	27
1.3.3.1. Non-metallic Hydrolytic Agents	28
1.3.3.2. Metal-based Promoters of Phosphate Ester Hydrolysis	30
1.3.3.2.1. Lanthanide-based Systems	31
1.3.3.2.2. Co(III)-Tetraamine Small-Molecule Complexes	32
1.3.3.2.3. Zn(II)-Azamacrocyclic Hydrolytic Agents.....	35
1.3.3.2.4. Multimetallic Systems.....	37
1.3.3.2.5. The Role of the Chemical Environment in the Activity of Synthetic Hydrolytic Agents	42
1.4. Molecular Imprinting	45
1.4.1. Overview and Main Concepts	45
1.4.2. Approaches in MIP	46
1.4.3. Origins and Applications	48
1.4.4. Catalytically Active MIPs	49

1.4.4.1. Overview and Approaches	49
1.4.4.2. The Role of Metals in Molecular Imprinting and Their Merits	51
1.4.4.2.1. Catalytically Active Metal-based MIPs.....	53
1.4.5. Materials in Molecular Imprinting	56
1.4.5.1. Microgels and Nanogels.....	56
1.5. Bibliography	60
Chapter 2: Design and Synthesis of Macrocyclic Ligands with the View to Generate Small-Molecule Co(III) and Zn(II)-based Catalysts for Phosphate Ester Hydrolysis	65
2.1. Project Strategy: Introduction and Aims.....	65
2.1.1. Part One: Co(III)-based MIP Nanogels as Catalysts for Phosphate Ester Hydrolysis	65
2.1.1.1. Choice of the Basic Catalytic Unit	65
2.1.1.2. Use of the Molecular Imprinting Methodology	68
2.1.2. Part Two: Development of the Small-Molecule Metal Complexes for the Phosphate Ester Hydrolysis.....	70
2.1.2.1. Cyclen-based Metal Complexes	71
2.2. Introduction to the Synthesis of the Functionalised Tetraamine Ligands	72
2.2.1 Methods for Generation of <i>N</i> -functionalised Macrocyclic Ligands	73
2.3. Results and Discussion	74
2.3.1. Synthesis of the Non-bridged Mono- and Di-alkylated Cyclen-based Derivatives	74
2.3.2. Introduction to Ethylene-bridged Azamacrocycles: Special Characteristics.....	81
2.3.2.1. Synthesis of the Ethylene-bridged Ligands	84
2.3.3. Small-Molecule Biomimetic Systems: Synthesis, Structure and Characterisation of the Cyclen-based Co(III) and Zn(II) Complexes	88
2.3.3.1. Small-Molecule Hydrolytic Agents: Synthesis and Characterisation of the Tetraamine Co(III) Complexes.....	90
2.3.3.2. Other Methods for the Synthesis of Cyclen-based Co(III) Complexes.....	99
2.3.3.3. Generation of the Hydrolytically Active $[\text{Co}(\text{L})(\text{OH}_2)\text{OH}]^{2+}$ Species.....	100

2.3.3.4. Electrochemical Studies on the $[\text{Co}(\text{L})\text{Cl}_2]\text{Cl}$ and $[\text{Co}(\text{L})(\text{OH}_2)\text{OH}]^{2+}$ Complexes	103
2.3.3.5. Generation of Zn(II) Complexes Using Cyclen-based Ligand Derivatives ...	107
2.4. Conclusions	109
2.5. Bibliography	110
Chapter 3: Phosphatase-like Activity of Small-Molecule Metal Complexes and Imprinted Polymers	114
3.1. Introduction	114
3.1.1. The Choice of Reaction: Selection of the pH and the Target Substrate <i>p</i> -Nitrophenyl Phosphate (NPP) and Bis(<i>p</i> -Nitrophenyl) Phosphate (BNPP)	115
3.2. Phosphate Ester Hydrolysis: Uncatalysed and Promoted by Small- Molecule <i>N</i> -Functionalised Tetraamine Co(III) and Zn(II) Complexes	119
3.2.1. Studies of the Uncatalysed NPP Hydrolysis	119
3.2.2. Phosphate Ester Hydrolysis Promoted by Cyclen-based Co(III) Complexes	120
3.2.3. Phosphate Ester Hydrolysis Promoted by Cyclen-based Zn(II) Complexes	125
3.2.3.1. Hydrolytic Studies With 7	126
3.2.3.2. Hydrolytic Studies With 8	126
3.2.4. Molecular Imprinted Polymers as an Alternative to Small-Molecule Metal Complexes.....	127
3.2.4.1. Why Molecular Imprinted Nanogels?	127
3.2.4.2. MIP Nanogel Synthesis and Characterisation ⁷	128
3.2.5. Hydrolytic Studies Using Imprinted <i>Versus</i> Non-Imprinted Co(III) Complex Polymers	131
3.2.5.1. Hydrolytic Studies Using Catalytic Amounts of the Non-Imprinted Co(III) Complexes 16 and 50	131
3.2.6. Evaluation of the Catalytic Activity of the Co(III)-Imprinted Nanogels.....	132
3.2.6.1. Catalytic Activity at Different Substrate Concentrations.....	133
3.2.6.2. Catalytic Activity Over Time	134

3.2.6.3. Factors that Influence the Catalytic Activity of P1 and P2 : The Effect of Template Structure	135
3.3. Conclusions	137
3.4. Bibliography	139
Chapter 4: Synthesis and Characterisation of Complexes of Tripodal ‘Click’-based Ligands as Potential Small-Molecule Catalysts for Phosphate Ester Hydrolysis	141
4.1. Introduction	141
4.1.1. The Choice of Triazole-based Tripodal Ligands and Their Corresponding Metal Complexes as Potential Promoters of Phosphate Ester Hydrolysis	142
4.1.2. The Cu(I)-Catalysed Azide-Alkyne Cycloaddition (CuAAC) or ‘Click’ Reaction ...	147
4.1.2.1. ‘Click’-based Methods for the Generation of the Triazole-based Ligands .	149
4.2. Synthesis of Tripodal ‘Click’-based Ligands.....	150
4.2.1. TBTA and Derivatives	150
4.2.2. Synthesis and Characterisation of Triazole-based d-Block Metal Complexes ...	156
4.2.2.1. Preparation of the Chloride and Perchlorate Metal Complexes	156
4.2.2.2. Characterisation of the Complexes.....	158
4.2.2.2.1. Characterisation of Co(II) Complexes	158
4.2.2.2.2. Characterisation of Cu(II) Complexes	162
4.2.2.2.3. Characterisation of Ni(II) Complexes	168
4.2.2.2.4. Characterisation of Mn(II) Complexes	173
4.2.2.2.5. Characterisation of Zn(II) Complexes.....	177
4.3. Conclusions and Final Remarks.....	180
4.4. Bibliography	182
Chapter 5: Conclusions and Future Work	184
5.1. An Overview	184
5.2. Small-Molecule Tetraamine Co(III) and Zn(II) Complexes	185
5.3. Molecular Imprinted Polymers as an Alternative to Small-Molecule Metal Complexes.....	189
5.4. Metal Complexes of Tripodal ‘Click’-based Ligands as Potential Small-Molecule Catalysts for Phosphate Ester Hydrolysis.....	191

5.5. Bibliography	194
Chapter 6: Experimental Section	196
6.1. General Information	196
6.2. Synthesis of the Cyclen-based Compounds	199
6.2.1. Synthesis of the Amino Salts	200
6.2.1.1. Mono-alkylation: General Procedure ⁶ as Demonstrated by the Synthesis of 64	200
6.2.1.2. Di-alkylation: General Procedure ⁶ as Demonstrated by the Synthesis of 70	204
6.2.2. Synthesis of the Cyclen-based Ligands <i>via</i> Amino Precursors	206
6.2.3. Synthesis of Inorganic Salts and Coordination Compounds	214
6.2.3.1. Synthesis of the Co(III) Carbonate Complexes: General Procedure ^{11,14} as Demonstrated by the Synthesis of cis-[Co(44)CO ₃]HCO ₃ 84 ¹⁵	214
6.2.3.2. Synthesis of the Di-chloride Co(III) Complexes: General Procedure ^{11,14} as Demonstrated by the Synthesis of cis-[Co(44)Cl ₂]Cl 85 ^{11,16,19}	221
6.2.3.3. Synthesis of the Zn(II) Complexes: General Procedure ¹⁰ as Demonstrated by the Synthesis of [Zn(44)OH ₂](ClO ₄) ₂ 21 ²³	227
6.3. Kinetics	233
6.3.1. Determination of the Amount of Product Formed in the Uncatalysed Reaction	233
6.3.2. Determination of the Amount of Product Formed in the Presence of the Small-Molecule Metal Complexes Used in Excess.	233
6.3.2.1. Small-Molecule Aqua-Hydroxo Co(III) Complexes	233
6.3.2.2. Small-Molecule Zn(II) Complexes.....	234
6.3.3. Kinetic Studies with Nanogels P1 and P2 and Small-Molecule Co(III) Complexes 16 and 50	234
6.3.3.1. Small-Molecule Co(III) Complexes 16 and 50	235
6.3.3.2. Nanogels P1 and P2	235
6.4. Synthesis of the 'Click'-based Compounds	236

6.4.1. Synthesis of the 'Click'-based Tripodal Ligands	236
6.4.2. Synthesis of the 'Click'-based Coordination Complexes	240
6.4.2.1. Synthesis of the Chloride Complexes of Ligands 110 and 111 : General Procedure ⁹ as Demonstrated by the Synthesis of [Co(110)Cl]Cl 109 ³⁰	240
6.4.2.2. Synthesis of the Perchlorate Metal Complexes of Ligands 110 and 111 : General Procedure ³² as Demonstrated by the Synthesis of [Cu(110)](ClO ₄) ₂ 133	245
6.5. Single X-Ray Crystallography.....	249
6.5.1. Data for [Co(68)CO ₃]MeCO ₃ 86	249
6.5.2. Data for [Co(78)Cl]Cl 89 ¹⁸	249
6.5.3. Data for [78 H ₃][CoCl ₄]Cl	250
6.5.4. Data for [Cu(111)Cl ₂] 138	250
6.5.5. Data for [Ni(110)(OH ₂)Cl]Cl 130	250
6.5.6. Data for [Mn(111) ₂](ClO ₄) ₂ 144	251
6.5.7. Data for [Zn(111)Cl] ₂ [ZnCl ₄] 141	251
6.6. Bibliography	252

List of Abbreviations

δ	Chemical shift
AIBN	2,2'-Azodiisobutyronitrile
BNPP	Bis(<i>p</i> -nitrophenyl) phosphate
Boc	<i>t</i> -Butyloxycarbonyl
BSA	Bovine Serum Albumin
CAPS	3-(Cyclohexylamino)-1-propanesulfonic acid
CAPSO	3-(Cyclohexylamino)-2-hydroxy-1-propanesulfonic acid
CD	Cyclodextrin
CHES	2-(Cyclohexylamino) ethanesulfonic acid
CuAAC	Cu(I) Azide-Alkyne Cycloaddition
DCM	Di-chloro methane
DIPEA	<i>N,N</i> -Diisopropylethylamine
DLS	Dynamic Light Scattering
DMF	<i>N, N'</i> - Dimethylformamide
DMSO	Dimethylsulfoxide
EDTA	Ethylenediamine tetraacetic acid
EGDMA	Ethyleneglycol dimethacrylate
EI	Electron Ionisation
EPR	Electron Paramagnetic Resonance
equiv.	Equivalent
Et ₂ O	Diethyl Ether
EtOAc	Ethyl acetate
EtOH	Ethanol
FAAS	Flame Atomic Absorption Spectroscopy
h	Hours
HEPES	4-(2-Hydroxyethyl) piperazine-1-ethanesulfonic acid
HPLC	High Performamnce Liquid Chromatography
HRMS	High Resolution Mass Spectrometry
IR	Infrared radiation
<i>J</i>	Coupling constant
M	Molar

MBA	<i>N, N'</i> -Methylene Bisacrylamide
MeCN	Acetonitrile
MeOH	Methanol
MES	2-(<i>N</i> -morpholino) ethanesulfonic acid
min	Minutes
MIP	Molecular Imprinted Nanogels
mmol	Millimoles
MOF	Molecular Organic Framework
m.p.	Melting point
NMR	Nuclear Magnetic Resonance
NPP	<i>p</i> -Nitrophenyl phosphate
NPPA	<i>p</i> -Nitrophenyl phosphonate
PEG	Polyethylene glycol
POP	Porous Organic Polymer
PIPES	piperazine- <i>N,N'</i> -bis(2-ethanesulfonic acid)
ppm	parts per million
RT	Room Temperature
SCE	Saturated Calomel Electrode
SHE	Standard Hydrogen Electrode
TACN	1,4,7-Triazacyclononane
<i>t</i> -BuOH	Tert-Butyl alcohol
<i>t</i> -BuONO	Tert-Butyl nitrite
TLC	Thin Layer Chromatography
TMS	Tetramethylsilyl
TMSN ₃	Trimethylsilyl azide
Tris	2-Amino-2-hydroxymethyl-propane-1,3-diol
TSA	Transition State Analogue
UV-Vis	Ultraviolet/visible radiation

Acknowledgements

Firstly and most importantly I would like to express my deep gratitude and appreciation to my PhD supervisors Prof. Mike Watkinson and Prof. Marina Resmini for fulfilling my dream - for providing me with an exciting opportunity to carry out this PhD project and learn the insights of chemistry. Thank you for your tremendous help, support, priceless wise advice and patience; for guiding me through these years, sharing your valuable knowledge, for believing in me and teaching me to trust myself. This list can be much-much longer, and it is almost impossible to put in words how thankful and delighted I am for this great adventure with such talented supervisors, who have big hearts.

I am thankful to my academic panel members- Dr. Isaac Abrahams and Dr. Steve Dunn- for greatly contributing to my research project with inspiring useful ideas. Thank you very much for your comments and encouraging suggestions.

Another big thank you goes to the all SBCS staff for your help and support when I needed it through the four years. In particular- to Majid Motevalli for helping me with X-ray crystallography, Dr. Harold Toms for his great support with NMR issues and Dr. Enrico Salvadori for the EPR measurements and useful discussions.

And of course I would like to express my deep appreciation to the Watkinson and Resmini group members: Aneta, Jess, KJ, Gennadiy, Vikki, Phil, Giorgio, Gabri, Dolca, Fosca, and Sofia - you have been very helpful and supportive through all these years. Thank you for going through my reports and presentations with me and for being like sunny rays to me in the lab. Anetochka, I was very lucky to have you in our group in my last year of PhD- it would have been much harder to go through this by myself without you. Thank you for giving me guidance and sharing your experience with me- I learnt a lot from it. You made my last days in the lab lively, fun and easy. Especially, I want give my big love to the 'girls corner'- Svetulia, Yolochka and Kashunia. You are simply my best friends that I could only wish for- thank you for making my life eventful and full of colours in QM and beyond it. Lazaros Mavridis, thank you for your supportive advice and IT help and for being a good friend to all of us.

Also, I particularly want to thank Edward for helping me with the thesis writing, for the template and for his great help with the formatting. Additionally, I am very grateful to

Maxie's group members- John, Nolwenn and Martina for guiding me on the electrochemical experiments and for their prompt response for every problem I had with the instruments as well as helping me to solve some of my bizarre voltammograms.

In particular, I would like to acknowledge past member of the Watkinson and Resmini group Dr. Rita Jorge for providing me with insightful discussions and very useful advice for this PhD project. Thank you for all your efforts and of course for starting this interesting PhD project that I could take forward.

My 'native' London friends- Vickulia, Yulechka, Svetulia – the sunniest people I've ever met- and a lot of other numerous people from the Inspiration2Dance group- you've been an incredible source of inspirations to live, to dance and to study for all these years since I met you. Super big thank you for your laughter, cheerful stories, amazing fun parties and celebrations, that really helped me to go through some of the dark and tedious 'chemistry' days. Vickulia and Yulechka, thank you for your friendship and the unforgettable experience. You've beautifully proven that it is possible to develop something truly wonderful when it seems impossible at the first sight. And by the way, thank you Yulia for helping me to put my things into the 'right corners' in the room for a good luck! Especially I want to thank Yarik for continuously reminding me that I have a 'big thing' to do, for his wise words of advice, admiration, strong belief in me and for always showing me the bright side in the dark days. You will be always in my heart.

And now I would like express my kind appreciation to my lovely family. Thank you to my mum for believing in me, for your prayers, for giving me courage and warm support to go through this big and difficult endeavour. I would have never had such an opportunity to go that far without your great efforts! And thank you my dad, who was supporting me from another continent- thank you for all your skype conversations and wise advice. Especially, I am deeply grateful for the encouragement and warm love that I received from my granny! Thank you for immensely believing in me! Another big thank you goes to Kate, who provided me with a lovely home and place to write my PhD thesis- I am very grateful for your generosity. My uncle Yuri and his wife Katia (and my best childhood friend)- I love you very much and truly grateful for the fun times with you and your warm love to me. Musia, my little cat, I am so glad that to have you in the house! You make me smile everyday.

Especially I want to express my love and appreciation to Misha- you've been very caring and supportive during writing. I was very lucky to have you by my side during these final difficult times of my PhD project. Thank you for solving my problems and dealing with my requests and of course for providing a nice beautiful home for writing my PhD thesis; and also big regards to your supportive family. I was very happy and delighted to write half of my PhD thesis in a very unusual and beautiful city St. Petersburg with its little magic- white nights, which kept me awake until 3 am and helped to gain more inspiration for the thesis writing.

And finally, I would like to dedicate this thesis to my lovely and witty cousin Olga, who I only met in my second year of PhD and who is turning 5 years old next month. I really hope that this endeavour will give you great inspiration and courage to fulfil your future dreams and aspirations. Best of luck to you, my dear.

Chapter 1: Introduction

1.1. Overall Aims of the Project

The central aim of this research project was the development of a number of artificial biomimetic metal-based catalysts for phosphate ester hydrolysis. This thesis presents efforts to explore the effects of the structural modifications of the tetraazamacrocyclic Co(III) and Zn(II) small-molecule metal complexes on their ability to facilitate hydrolysis of *p*-nitrophenyl phosphate as a surrogate substrate.

Within the broad field of biomimetic chemistry, the design and synthesis of hydrolytically active mimics of a range of natural enzymes has been ongoing for many years and remains a fascinating area of research. It is known that reproducing the substrate selectivity and rate enhancements achieved by enzymes through the development of synthetic models that do not suffer from their inherent instability (at high/low temperatures and extreme pHs) and substrate limitations, is extremely challenging and thus stimulates research in the field.¹ Several approaches have been utilised to achieve this goal not only involving the careful design of the biomimetic hydrolytic agents, but also the use of lower polarity materials that mimic the hydrophobic environment of the enzyme's active site.² Molecular imprinted (MIP) nanogel materials are used in part of this work to investigate whether imbedding small-molecule coordination complexes in them using molecular imprinting technique results in an enhancement of their hydrolytic activity.

This introductory chapter highlights the importance of the phosphate ester bond and its hydrolysis and also presents an overview of the main achievements in the field of man-made hydrolytic enzyme mimics.

1.2. The Role of Phosphate Esters in the Chemistry of Life

Phosphorus is ubiquitous in Nature and is fundamental to a number of key biological processes. It is known to be involved in a multitude of biochemical transformations, such as energy transduction, the synthesis of biological molecules and the regulation of secondary messengers balance, as well as in the storage of genetic information and the regulation of protein function.³ In the majority of such biological processes, phosphorus is normally

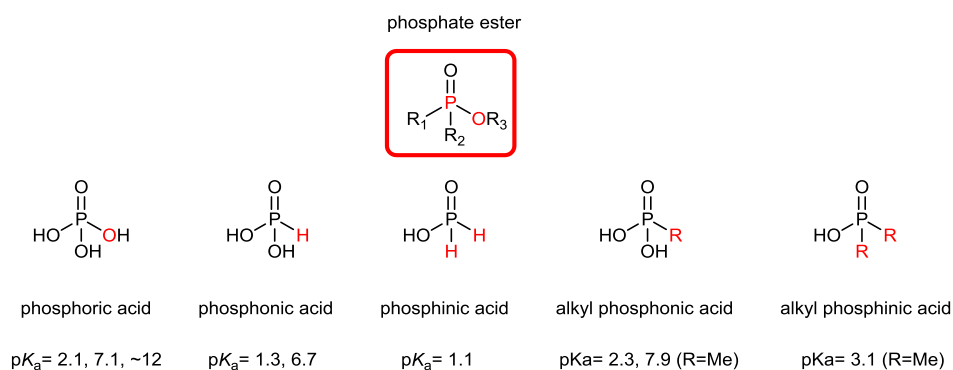
present in the form of phosphate esters, although a few naturally occurring forms with phosphorus-nitrogen and phosphorus-carbon bonds are also known.⁴

Phosphorus in its inorganic form, PO_4^{3-} , is normally absorbed by plants and marine components, such as algae and seaweed, which initiates the phosphorus cycle and allows its passage up the food chain. It is then converted *via* a number of biochemical transformations into more complex polymeric phosphate esters that are the major components of the genetic materials DNA and RNA, as well as of biological energy reservoirs in the form of ATP.

The ability of organophosphates to reliably store genetic information and chemical energy in living cells is attributed to their incredible stability in aqueous environments at physiological pH (section 1.3.1). Cleavage of phosphate ester bonds can be facilitated by particular enzymes, which advantageously results in the release of exothermic energy that can be then used in essential biological processes. Thus, such unique properties of phosphate esters and their abundance in Nature signify their vital role in the chemistry of life. It is generally known that the reactivity of organophosphates is dependent on the particular structure of the system, therefore substitution around the phosphorus atom can either result in phosphates that are harmless to humans and the environment or make them life-threatening (nerve agents) or environmentally toxic biocides.⁵

1.2.1. Structure and Reactivity of Phosphate Esters

Organophosphates are derived from phosphorus oxy-acids and thus contain phosphoryl $\text{P}=\text{O}$ or the related thiophosphoryl $\text{P}=\text{S}$ groups.³ A range of such phosphorus oxy-acids, including a generic structure of the phosphate ester are shown in Scheme 1.1.



Scheme 1.1- Generic structure of the phosphate ester group (where R_1 , R_2 and R_3 are any alkyl or other lipophilic groups) and types of phosphorus oxy acids and their pK_a values.^{3,6}

Phosphate esters mainly take part in two types of reactions: alkylation and phosphorylation. Alkylation is known to occur with most derivatives of strong phosphoric ($P=O(OH)_3$) and pyrophosphoric ($(P=O)(OH)_2O(P=O)(OH)_2$) acid, as their corresponding anions are good leaving groups.⁵ Phosphorylation reaction involves nucleophilic substitution at the electrophilic phosphorus atom, which results in the transfer of the phosphorus group from a donor to a suitable acceptor. The presence of certain structural motifs within the organophosphate (section 1.2.2) can result in detrimental biological effects.

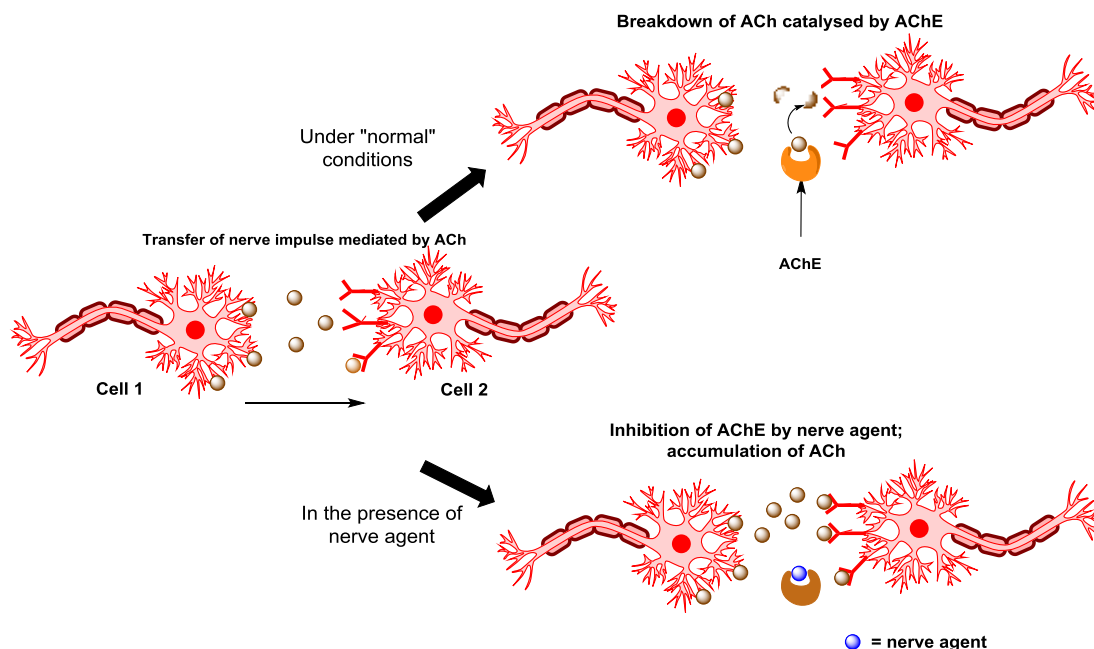


Figure 1.1- Schematic representation of AChE inhibition by a nerve agent.⁶

For example, potent biocides, such as nerve agents, covalently bind to the hydroxyl group of the catalytically active serine amino acid residue in the active site of the Acetylcholinesterase (AChE) enzyme, whose main biological function is to catalyse the breakdown of the neurotransmitter acetylcholine (ACh) (Figure 1.1).⁷ Phosphorylation with the nerve agent results in irreversible inhibition of AChE preventing the hydrolysis of ACh, which plays a key role in the stimulation of the nerve fibre and muscle activation. Thus, this results in accumulation of the neurotransmitter, which in turn causes overstimulation of the nervous system, excessive muscular contraction and ultimately death.⁷ A number of research groups continue to study the phosphorylation of the AChE enzyme with an aim to further improve understanding of nerve agent mode of action to develop an appropriate treatment.⁷ Unfortunately as our cells have not yet developed a mechanism of distinguishing and destroying these hazardous organophosphates, and as they undergo rapid biological uptake, this chemistry has been utilised by mankind in the development of some of the most inhumane agents ever made: chemical weapons.³

1.2.2. Hazardous Phosphate Esters and Their Role in Chemical Weaponry

A typical chemical structure of neurotoxic organophosphorus compounds is shown in Figure 1.2 and is characterised by the pentavalent phosphorus centre bonded to four substituents: an oxygen or sulfur atom *via* a double bond, a good leaving group and two other substituents (e.g. alkoxy groups), with the structures showing considerable variation according to the type of neurotoxin.⁸

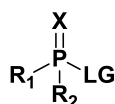


Figure 1.2- General chemical structure representing deadly organophosphate species, where X=O or S, LG= leaving group, R₁ and R₂= alkyl, O-alkyl or OH.⁸

It is generally known that organophosphorus compounds exhibit greater toxicity due to the highly polarised nature of the P=O bond compared to the less polarised P=S bond in organosulfur compounds, making them less reactive in phosphorylating AChE.⁸ In addition to the electronegative phosphorus atom, larger leaving groups lead to higher reactivity which results in higher acute toxicity. Cheap and easily accessible starting materials, together with a relatively simple manufacturing process, make phosphate-based nerve agents particularly dangerous.

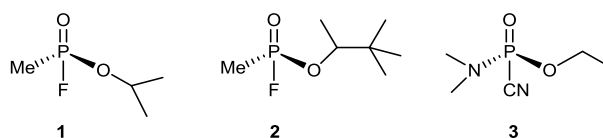


Figure 1.3- Chemical structures of three nerve agents Sarin **1**, Soman **2** and Tabun **3**.⁹

The first use of nerve agents as chemical warfare tools dates back to their discovery in 1937, when Dr. Gerhard Schrader synthesised the nerve agent Tabun **3** (Figure 1.3) during his effort to prepare more potent insecticides. Tabun showed a rapid, lethal effect in animal tests and its remarkable acute toxicity (reflected in the ability to kill 100% of the biological samples in concentrations as dilute as 1:200,000) drew the attention of the War Ministry in Germany.¹⁰ This resulted in further development of the structurally similar nerve agents Sarin **1** and Soman **2** (Figure 1.3) in the 1940's, which were stockpiled but fortunately never used as chemical weapons in the second World War. The production of these chemical weapons did however result in a large number of industrial accidents, with several workers being killed.¹⁰ This significant discovery prompted an extensive research effort during and after World War II principally in the US, UK and former Soviet Union in the quest for ever more potent chemical weapons. However, only less potent structural variants were produced on a large scale and never used. However, more powerful organophosphates were developed and stockpiled during the Cold War by both the British (VX) and the Russians (VR55). According to statistics, there were approximately 65 production facilities and 71,000 metric tonnes of these chemical agents stockpiled around the world. Eventually, the use of such weapons of mass destruction was prohibited by the Geneva Convention and resulted in the formation of the Chemical Weapon Convention (CWC) organisation in 1997, a program which was directed towards eliminating the development, production, stockpiling and use of these chemical weapons. Nevertheless, there are countries, such as Israel, Libya, Iraq and North Korea, who are not signatories to this agreement and whose stockpiles remain unknown.¹⁰

There have been several military nerve agent attacks during the 1980's and 1990's, with the most well-known occurring in the Iran-Iraq war by the Iraqi forces. It was estimated that 2,000 villages were destroyed and approximately 5,000 people were killed in the Halabja massacre of Kurds in 1988.¹¹ Also, terrorist organisations carried out Sarin attacks in Japan in Tokyo in 1994 and in Matsumoto in 1995 with thousands of people affected and killed. The possibility of further attacks and the large stockpiles of weapons that exist have

resulted in scientists carrying out extensive research towards the development of effective detection and decontamination methods for nerve agents.¹⁰

1.2.3. Advances in the Decontamination of Toxic Phosphate Esters

The detection and decontamination of chemical warfare agents is an important challenge and involves the rapid removal of hazardous chemical agents from the environment, which can be achieved by both physical and chemical methods. Initially, the decontamination of potent biocides was carried out by physical methods, such as land burial, open burning, controlled explosion and dumping at sea, which were eventually prohibited by the CWC due to their harmful environmental impact and public health concerns. Chemical methods were then developed and oxidative agents such as bleach and KMnO_4 were amongst the first decontaminants used; solutions of alkaline salts (Na_2CO_3 , NaOH and KOH) were also found to rapidly detoxify lethal agents. However, the ineffectiveness of these systems at low temperatures as well as the highly corrosive by-products caused health concerns and prompted research towards novel more efficient and environmentally benign decontaminants. For example, acid digestion, biological detergents, neutralisation, some requiring the use of organic solvents are amongst the most common methods utilised previously and were commonly described as simple and efficient. However, they still are undesirable due to their hazardous nature causing additional health and safety concerns. Thus, the search for an optimal method that should display low cost, be safe, whilst not generating any (or low) toxic by-products and be technically simple, remains an active area of research.¹²

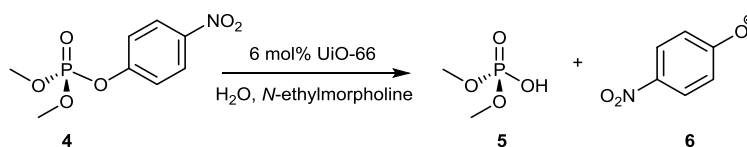
The majority of systems developed to date are based on the hydrolysis of the nerve agent to give non-toxic products. Given that uncatalysed hydrolytic cleavage of phosphate esters in water is too slow for real world applications, the search for catalysts specific for the hydrolysis of organophosphates attracted considerable attention and, despite some interesting advances, is still an important challenge.¹²

In the search for catalysts for the rapid detoxification of nerve agent stimulants, much work has been done in studying the catalytic activity of natural and synthetic enzymes towards P-O bond cleavage in nerve agents. Most of the enzymes that simultaneously exhibited high specificity and efficacy towards the detection and catalytic hydrolysis of nerve agents

had a bacterial origin or were genetically engineered.^{13,14} Some interesting examples of such dual function systems include enzymes that have been attached to diverse materials, such as hollow fibre reactors,¹⁵ cotton,¹⁶ glass beads,¹⁷ nylon,¹⁸ single walled nanotubes¹⁹ and gold nanoparticles²⁰. Enzymes that were expressed on the cell surface of bacteria and immobilised onto the various material supports with the help of a binding domain, represent some of the most successful examples of decontamination systems reported.^{21,22} Despite representing the majority of useful and effective decontamination methods, biologically derived enzymes have important disadvantages. For example, the isolation and synthesis of the enzyme is costly and time-consuming. Also, the fragile nature of their protein units, which are easily degraded e.g. in the presence of organic solvents, high temperatures and other denaturing conditions, such as extreme pHs, which normally cause denaturation of enzymes and causes them to lose their activity.²³ With an aim to overcome this issue, there is a considerable interest in developing synthetic enzyme-like agents that are capable of hydrolytic cleavage of P-O bonds with considerable rate accelerations. It is known that natural enzymes that are capable of catalytic P-O bond cleavage contain one to three metal cations in their active sites (section 1.3.2). Thus, taking inspiration from Nature, Lewis acid catalysis has been extensively explored for the catalytic destruction of toxic chemicals and this approach is central to many decontamination systems that are currently under investigation. For example, a number of groups studied the role of homogeneous Ln(III),^{24,25} Ce(IV)²⁶ and Al(III)^{27,28} Lewis acidic centres in the degradation of the less toxic nerve agent simulants, such as methyl paraoxon **4**.

Solid-supported catalysts were also explored by Hupp *et al.* for the efficient hydrolysis of P-O bonds, which included metal functionalised porous organic polymers (POPs).²⁹ Specifically Al(III)-porphyrin-containing and Ln(III)-catechol-containing POPs were shown to carry out catalytic methanolysis of **4**. The activity of metal-oxides has also been studied and they exhibited reactivity towards phosphate ester-based nerve agent hydrolysis. In particular, Peterson and co-workers demonstrated that utilization of zirconium hydroxide lead to the effective decomposition of the nerve agent Soman.^{29,30} Inspired by this observation another class of heterogeneous materials, metal-organic frameworks (MOFs), have been developed as nerve agent decontaminants. MOFs are porous materials that can be tuned according to their composition and were considered as attractive and appealing catalysts for a wide range of chemical reactions.³¹ Advantageously, given their resolved X-

ray structure, MOFs allow mechanistic studies, which are more difficult at the surface of the metal oxides functionalised POPs.³² In 2014 Hupp *et al.* reported the use of zirconium-based MOF UiO-66, where UiO-66 is a $[\text{Zr}_6\text{O}_4(\text{OH})_4]$ -based node within the MOF comprised of several Zr(IV)-OH-Zr(IV) species, which reflect the Zn(II)-OH-Zn(II) active site of the bimetallic phosphotriesterase enzyme.²⁹ MOF UiO-66 is among the most efficient catalysts reported for the methanolysis of the methyl paraoxon ($5 \times 10^{-6} \text{ M s}^{-1}$ rate factor), which reduced the half-life of this reaction by 2-3 times compared to the analogous reaction using Al(III)-based POPs and ten times compared to the homogenous supramolecular Al(III)-porphyrin-based catalysts.²⁹ Additionally, MOF UiO-66 proved to be an appealing catalyst for the hydrolysis of the organophosphate nerve agent simulants and is particularly attractive due to its high chemical, hydrothermal and mechanical stability. For example, the hydrolysis of **4** (Scheme 1.2) by Zr(IV)-based MOF afforded a 50 minute reaction half-life, which was 40 times shorter than that exhibited by the previously reported MOF Cr-MIL-101.³¹



Scheme 1.2- Hydrolysis of methyl paraoxon **4 catalysed by MOF UiO-66.**²⁹

Hydrolytic activity of the functionalised UiO-66 derivatives towards methyl paraoxon cleavage was also explored by Hupp and co-workers. For example, amine functionalised MOF-based UiO-66-NH₂ showed a 20-fold increase in the hydrolysis rate of the parent MOF-UiO-66 providing a half-life of 1 minute.³² Currently, factors, such as increasing the number Zr(IV)-OH-Zr(IV) species in the node are also being investigated. For example, 6-connected Zr(IV)-based nodes display the highest hydrolysis rate among all Zr(IV)-based MOFs reported to date and show reusability. Thus, UiO-66 system is known to be among the most effective MOF-based catalyst for phosphate ester hydrolysis to date.³²

The remarkable intrinsic stability of phosphate esters, allied to the inherent toxicity of nerve agents, complicates the search for an ideal method for their catalytic cleavage. As phosphate ester hydrolysis reaction is central to this project, the key mechanisms and systems that are utilised by Nature and adopted by scientists to accelerate this reaction are extensively discussed in the next section.

1.3. Cleavage of Phosphate Esters

1.3.1. Uncatalysed Hydrolysis of Phosphate Esters

As mentioned above, the high stability of phosphate esters at ambient pH is responsible for their ability to preserve and maintain the integrity of genetic material. This is reflected in the half-lives for spontaneous hydrolysis of DNA and RNA backbones under physiological conditions, which have been experimentally estimated to be 200 million years and 1000 years respectively.³³ In comparison, other man-made organophosphates, such as NPP **7** and BNPP **8** (Figure 1.4) are less stable and have significantly higher reactivity given their half-lives of approximately 2000 years.⁶ They are therefore called ‘activated phosphates’ and are widely used by researchers as model substrates to study the progress of spontaneous and catalysed phosphate ester hydrolysis. The advantage of using **7** and **8** is particularly attributed to the release of the chromophoric hydrolysis product **6**, which absorbs in the visible region and allows simple monitoring of the reaction by UV-Vis spectroscopy (Chapter 3, section 3.1.1).

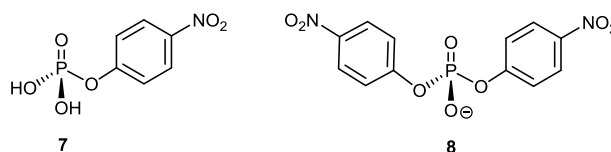
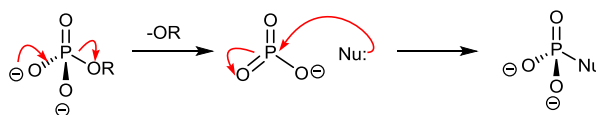


Figure 1.4- Chemical structures of the ‘activated’ phosphate esters *p*-nitrophenyl phosphate NPP **7** and bis(*p*-nitrophenyl) phosphate BNPP **8**.

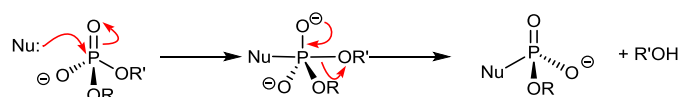
The mechanism of the uncatalysed P-O bond cleavage reaction has been extensively studied by a number of research groups and the data revealed that it can proceed following either associative (A_N+D_N) (*via* pentavalent phosphorus intermediate) or dissociative (D_N+A_N) (*via* trivalent Intermediate) pathways.¹



Scheme 1.3- Dissociative mechanism for the uncatalysed phosphate ester hydrolysis.

It was initially suggested that the dissociative two step mechanism shown in Scheme 1.3 is responsible for the hydrolysis of phosphate esters.³⁴ It occurs *via* the unstable planar metaphosphate anion, which is formed in a rate-determining step after the departure of the leaving group. This is followed by nucleophile addition to deliver the desired product.

However, the inability to detect the presence of the metaphosphate intermediate resulted in the proposal of an alternative associative mechanism, presented in Scheme 1.4.^{34,35} This involves nucleophile attack at the phosphorus atom, which results in the formation of the pentavalent trigonal bipyramidal phosphorene intermediate. Leaving group departure then occurs with inversion of stereochemistry and produces the desired product. This mechanism is analogous to the hydrolysis of carboxylic acid esters. Computational calculations suggest that the activation barriers for each of the aforementioned pathways are very similar and thus are difficult to differentiate.^{35, 37}



Scheme 1.4- Associative mechanism for the uncatalysed phosphate ester hydrolysis.

Although it was found that hydrolysis of phosphate esters occurs predominantly *via* P-O bond cleavage, there is also the possibility of alkyl C-O bond cleavage occurring for alkyl esters with a slightly different mechanistic pathway compared to phosphates.³⁸

According to a number of relevant studies, phosphate diesters are considered to be more stable than monoesters and triesters in neutral water. It has generally been accepted, that phosphomonoesters undergo uncatalysed cleavage mainly following dissociative pathway, whereas nucleophilic substitution for di and triesters occurs *via* associative pathways.³⁹

1.3.2. Catalysis of Phosphate Ester Hydrolysis by Natural Enzymes

The crucial role of phosphate ester hydrolysis reactions in biological systems has resulted in the evolution of natural enzyme catalysts that promote P-O bond cleavage with very high rate accelerations. This family of enzymes is known as phosphatases and it comprises more than 140 different types of proteins, displaying large structural diversity. These enzymes are known to work in a wide range of pHs and utilise different mechanisms of action, such as indirect water attack or enzyme-derived nucleophilic displacement reactions.⁴⁰ According to crystallographic studies, the majority are metalloenzymes and contain one to three divalent metal ions in their active sites, which play a key role in their high catalytic activity. Mg(II), Fe(II)/(III), Zn(II) and Ca(II), are the most common metal ions employed in phosphatases.^{1,40,41} Whilst there are only a few monometallic phosphoesterases present in Nature, metal ions in multimetallic enzymes are normally bridged in the enzymes active

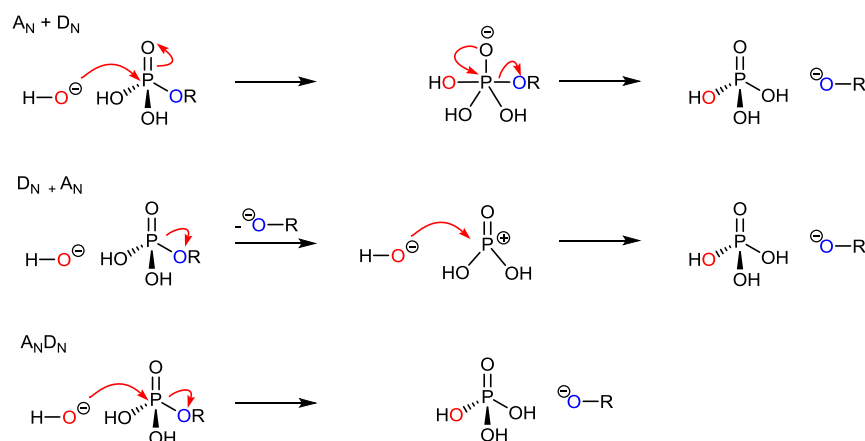
sites by either the hydroxyl groups from amino acid residues, by water molecules or by hydroxide nucleophiles. Amino acid residues also assist the metal ions by providing additional electrostatic stabilisation and hydrogen bonds to activate and orient the substrates.^{1,40}

Natural enzymes show the largest rate enhancement reported to date and remain the most efficient catalysts for phosphate ester hydrolysis.¹ Certain enzymes, such as serine and threonine phosphatases can accelerate otherwise slow hydrolytic cleavage of the P-O bond by an impressive 10^{21} -fold, while the *staphylococcal* nuclease promotes hydrolysis of DNA by 10^{17} times over the background reaction.¹

Another well-studied example of phosphoesterases is binuclear purple acid phosphatase (PAP) that normally contains Fe(II) and Fe(III) ions in its active site and can catalyse the hydrolysis of phosphate ester under acidic conditions (pH 4.9-6.0).⁴⁰ Binuclear Zn(II)-based alkaline phosphatases, on the other hand, display their optimal activity at pHs higher than 7.5.⁴⁰

There is a special class of phosphoesterases called nucleases, which efficiently catalyse DNA cleavage and are necessary to repair damaged DNA and to eliminate foreign DNA.^{1,40} One of the most studied example is DNA polymerase I which activity requires the presence of Zn(II) or Mg(II) ions in its active site. Nucleases also play a role in DNA expression and duplication processes, such as binuclear Zn(II) P1 nuclease. Another type of nuclease enzyme that only cleaves DNA at specific nucleotide sequences is termed the restriction enzymes, e.g. binuclear Mg(II) deoxyribonuclease enzyme.⁴⁰

Mechanistic studies by Kamerlin and Wilkie revealed that there are three possible pathways for the metal catalysed hydrolysis of phosphates: associative (A_N+D_N) and dissociative (D_N+A_N) mechanisms already discussed in the previous section; alternatively, a concerted mechanism (A_ND_N) is also known for such substitution reaction. The latter pathway is characterised by the simultaneous attack of the nucleophile and departure of the leaving group in a single reaction step, which results in a high energy transition state without any observed intermediates (Scheme 1.5).^{1,4}



Scheme 1.5- Three types of mechanism of phosphate ester hydrolysis by metal ions: associative (A_N+D_N), dissociative (D_N+A_N) and concerted (A_ND_N).⁴

The review by Mancin and Scrimin in 2012 reported a general consensus that metal-catalysed phosphate ester hydrolysis most likely occurs *via* this last concerted mechanism.¹ However, whilst the mechanism of the uncatalysed hydrolysis of phosphate ester depends on the structure of the substrate, the enzyme's mechanism is determined by the presence and quantity of the metal ions in its active site. Computational studies have revealed that metal-containing enzymes are prone to show a more associative-like mechanism, whereas non-metal enzymes are more likely to catalyse P-O bond cleavage *via* a stepwise dissociative pathway.¹ It has been suggested, that enzymes without metal ions have larger active sites which are able to accommodate the various intermediates associated with the dissociative mechanism. Tyrosine phosphatase is an example of such class of enzymes. Non-metallic enzymes are thought to exist because some substrates, including RNA and phosphatidylinositols, are more 'activated' due to the presence of β -hydroxyl group and do not require the presence of metal cations for their hydrolysis.⁴⁰

Given the biological significance of phosphate ester cleavage, it stimulated a great interest in the mechanism of enzyme action. A large number of studies have been carried out to understand the crucial differences between the uncatalysed and enzyme-catalysed P-O cleavage reactions with the help of synthetic phosphoesterases which provide high efficiency and selectivity.¹

In order to elucidate such mechanistic details, it is first necessary to gain insight into the structure of the enzyme's active sites. A number of physical and spectroscopic methods

(e.g. X-ray crystallography, EPR, NMR spectroscopies) were used to thoroughly study the key features of the enzyme's active site with the view to generate suitable models. A great deal of useful information was extracted by these studies, including the coordination behaviour of metal ions and their interaction with amino acid residues (ligands), metal separation distance (for multimetallic enzymes) and electronic interactions between metals. For example, it was found that ligands at the metal ion sites may well contribute to the enzymatic reaction by holding the metal ions in certain positions inside the catalytic cavity. More importantly, functional groups of amino acids may play more direct roles in catalytic mechanisms by interacting with substrates, intermediates or products. In other words, these well-organised functional groups of amino acids create a secondary coordination sphere around the metal ions in the catalytic sites- a feature that has a vital importance for the catalytic activity of metalloenzymes.⁴⁰

The field of biomimetic catalysis remains an active area of research with large efforts have been made to reproduce the activity of the natural enzymes with particular attention devoted to the factors that regulate the catalytic mechanism of such systems.

1.3.3. Biomimetic Catalysts for Phosphate Ester Hydrolysis: From Small-Molecule Hydrolytic Agents to Large Enzyme-like Systems

One of the current areas of interest in the field of enzyme mimicry is the identification of the structural requirements for an 'ideal' catalyst for phosphate ester hydrolysis. Over the last three decades there have been a large number of small-molecule examples reported, that are able to reproduce the behaviour of natural enzymes providing high rate accelerations by up to 10^{12} -fold over the uncatalysed reaction. Most models indeed contributed to the mechanistic knowledge and elucidated some kinetic aspects of enzymatic catalysis. Some systems, however, were reported to be significantly different from their natural counterparts (e.g. the substrate remains linked to the active sites resulting in no catalytic turnover). Unfortunately, non-biological catalysts often showed lack of substrate specificity and low/no turnover. Thus, the development of an artificial catalyst that can hydrolytically cleave P-O bond with high efficiency, selectivity and catalytic turnover is still a fascinating challenge. A feature that is especially difficult to reproduce in the enzyme mimicry is the secondary coordination sphere around the metal ion inside the catalytic pocket of the enzyme, which comprises the interactions between the metal,

amino acid residues and the substrate. Over the last 30 years, scientists put a large effort towards the realisation of synthetic phosphoesterases with a particular attention to the approaches required to reproduce and even improve the efficiency of their natural counterparts.^{1,2} The most notable and successful examples are highlighted and discussed in the rest of this chapter.

1.3.3.1. Non-metallic Hydrolytic Agents

Although the majority of the artificial hydrolytic agents for phosphate ester cleavage are metal-based, there are some examples of non-metallic organic systems that are able to promote the hydrolysis of phosphate esters.

Breslow *et al.* studied the hydrolysis of RNA using imidazole, which was amongst the first organic ribonuclease models. It was found that the general mode of hydrolysis action involves cooperation with the imidazole **9**/imidazolium **10** species shown in Figure 1.5.⁴¹ Extensive kinetic studies revealed that both functional groups participate in phosphate ester hydrolysis, with one component promoting the formation of the phosphorene intermediate (Scheme 1.4), and another catalysing its breakdown. Thus, it was postulated, that compounds that contain both acid-base functionalities have a tendency to catalyse the reaction in the same cooperative manner.^{33,41}

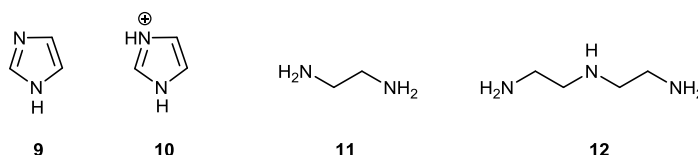
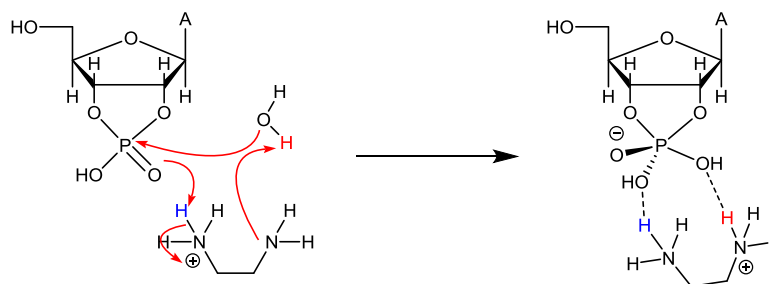


Figure 1.5- Examples of organic hydrolytic agents for RNA hydrolysis, imidazole and polyamines.³³

Researchers postulated that RNA hydrolysis involves two parallel reaction pathways: a concerted base-catalysed reaction and an acid-catalysed breakdown of the pentavalent phosphorene intermediate, with comparable rates at pH 7.0.³³

The same cooperative acid-base mode of action was successfully demonstrated in oligoamines, such as ethylenediamine **11** and diethylenetriamine **12**, where the aliphatic amine and ammonium ion cooperate to promote P-O bond cleavage as shown in Scheme 1.6. The proximity of the amino residues and the basicity of the neutral amino residues have been identified as the main factors that affect reactivity. Compounds where three

carbons separate the amino groups showed maximum activity among such polyamine systems.³³



Scheme 1.6- Polyamine catalysis of RNA hydrolysis.^{6,42}

The identification of amine-based compounds as some of the most active non-metallic hydrolytic agents prompted further development of more complex amine-based systems by a number of research groups. Some of the most successful examples of these were naphthalimide-based amino-alkyl derivative that showed specific cleavage of RNA, as shown in Figure 1.6.

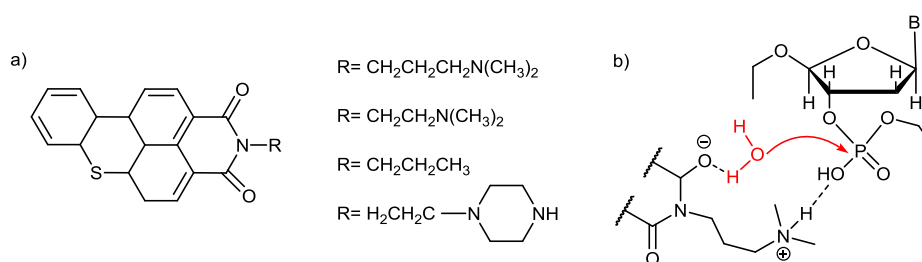


Figure 1.6- a) Chemical structure of naphthalimide-based derivatives; b) mechanism of RNA hydrolysis catalysed by naphthalimide derivatives.⁴²

Alternatively the highly functionalised oligosaccharide antibiotic Neomycin B **13** was presented as a hydrolytic catalyst (Figure 1.7).⁴³ It is characterised by the presence of both amino and hydroxyl groups that also show cooperative action and interaction with the backbones of DNA and RNA. Hydrolytic experiments resulted in a first order rate constant of $1.6 \times 10^{-5} \text{ s}^{-1}$ for Neomycin B in the hydrolysis of RNA, which represents an approximately three times faster rate compared to those observed with simple unstructured diamines.

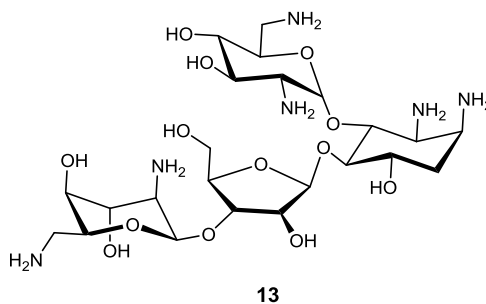


Figure 1.7- Functionalised oligosaccharide antibiotic Neomycin B.⁴³

However, the rate accelerations provided by non-metallic systems are far from those observed in enzyme catalysed reactions. Moreover, organic hydrolytic agents are normally used in approximately ten-fold excess over the phosphate substrate, which means they do not act as ‘real’ catalysts and are really used as reagents.³³ Therefore, the research in enzyme mimics was extended to metal-based hydrolysis of phosphate esters.

1.3.3.2. Metal-based Promoters of Phosphate Ester Hydrolysis

Given the crucial role metals play in catalysing phosphate ester hydrolysis in the active sites of natural phosphatases and nucleases,⁴⁰ the design and development of biomimetic metal-ligand complexes is one of the most interesting and useful approaches in the field of artificial phosphatases.¹

Transition and lanthanide metal ions in biologically relevant oxidation states are generally strong Lewis acids and can activate phosphate esters, nucleophiles, stabilise transition states and leaving groups. There are known to be three main modes of action that metals use to assist hydrolytic P-O bond cleavage, which are depicted in Figure 1.8; **(a)** involves Lewis acid activation of the phosphate group including stabilisation of the transition state; in **(b)** there is activation of the leaving group (decreasing the pK_a of the leaving group); **(c)** presents an intermolecular nucleophile activation by water coordination to the metal making it more acidic and thus ensuring a higher concentration of hydroxide ions at neutral pH; furthermore, in **(d)** and **(e)** it is shown, that metal-bound hydroxide or water molecules can participate in ‘indirect’ acid/base catalysis.⁴⁴ Interestingly, in 1999 Chin *et al.* analysed each mode of activation quantitatively and proposed that intramolecular nucleophile activation provides the most important contribution to the catalysis giving 10^8 -fold rate acceleration, followed by leaving group activation (10^6 -fold) and Lewis acid activation (10^2 -fold).¹ Combination of these modes can result in more complex and effective catalytic

processes that are normally observed in multimetallic systems, which will be discussed in the next section.

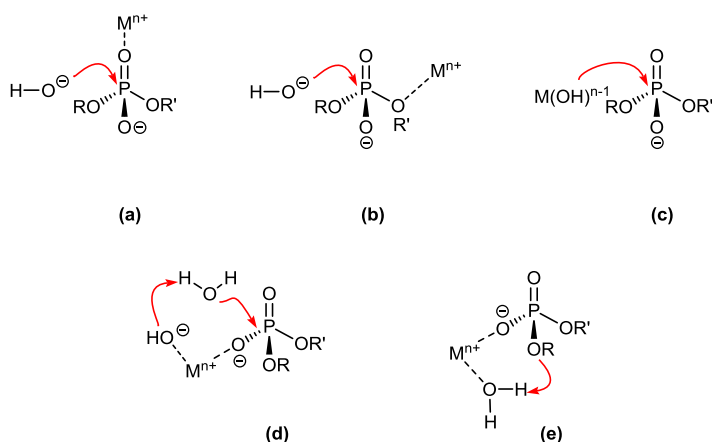


Figure 1.8- Mechanisms of metal catalysed phosphate ester hydrolysis.⁴⁴

There is a wide range of reports covering the catalysis of phosphate ester hydrolysis using an array of metal ions, both on their own and assisted by ligands, including lanthanides and transition metal ions, such as Ni(II), Fe(III), Cu(II), Co(III), and Ir(III) together with other metal cations, such as Mg(II) and Zn(II).^{1,45} Some of the most interesting examples are highlighted and discussed in the next five sections.

1.3.3.2.1. Lanthanide-based Systems

Lanthanide-based systems, such as Ce(IV), are known to be amongst the most active inorganic biomimetic catalysts reported to date.¹ They show remarkable hydrolytic activity in cleaving robust DNA bonds, which is attributed to their hard Lewis acidity, fast ligand exchange rates and a lack of accessible redox chemistry precluding radical-based cleavage mechanisms observed with some redox active metals, such as Cu(II).^{1,33,45,46} Komiyama and co-workers were the first to report lanthanide-mediated phosphate ester hydrolysis in 1993. They showed, that high hydrolytic activity of the ‘free’ Ce(IV)-based systems seems to be related to the formation of the dimeric species in solution. The experimental studies showed that there was a linear relationship between the rate enhancement and an increase in hydroxo-cluster dimer concentration, $[\text{Ce}_2(\text{OH})_4]^{4+}$, for RNA hydrolysis. Other prominent examples of the ligand-based lanthanide complexes effective for DNA cleavage include Ln(III)-based systems.³³

High valent Ce(IV), U(IV)O₂ and Th(IV) lanthanides and actinides were also used to promote hydrolysis of aryl phosphate models, often used to mimic nerve agents and DNA.^{1,33,45,46} Without any ligand assistance, lanthanide cations showed rate accelerations of 10⁶-fold in the hydrolysis of BNPP, while the presence of simple ligands (such as bis-tris propane buffers) resulted in 10⁸-fold acceleration factors.⁴⁶ However, most of the work with lanthanide-based systems has focused on developing restriction enzyme models whereby DNA and RNA have been mainly used as substrates. DNA-based hydrolysis facilitated by lanthanides involves coordination of the metal ion acting as a DNA scissor to the specific site of oligomeric DNA moieties to form a metal-complex DNA hybrid followed by the hydrolytic cleavage of the P-O bond.⁴⁶

Despite the truly remarkable achievements made using lanthanide-based systems, they are not deemed to be appealing hydrolytic agents for phosphate ester hydrolysis. Firstly, aqueous lanthanides are highly toxic and can cause damage to cell components, which makes them unsuitable for *in vivo* applications. Secondly, they are rare earth metals and therefore their low bioavailability and big demand often results in lanthanides being expensive. Moreover, their activity and scope of application are greatly reduced due to their tendency to form gels in solutions at neutral pH.^{1,46} In order to prevent such gel formation, researchers have used surfactants, sugars (ribose, maltose) and other coordination moieties, although this further increases the environmental impact of any putative lanthanide-based catalytic system. For these reasons, the quest for an 'ideal' catalyst for phosphate ester hydrolysis continued.

1.3.3.2.2. Co(III)-Tetraamine Small-Molecule Complexes

The class of Co(III)- tetraamine complexes particularly stands out in the area of artificial hydrolases. These small molecule complexes, of the type *cis*-[Co(N₄)(X)(Y)]ⁿ⁺, where N₄ is a tetraamine ligand have been extensively studied as phosphatase and ATPase models by a number of research groups over the last 20 years and have been identified as some of the most active small-molecule hydrolytic agents to date, providing up to 10⁷-fold rate acceleration (for monometallic complexes) compared to the uncatalysed reaction.^{1,47} Chin *et al.* made a remarkable contribution to this discovery and some of the first examples of the tetraamine Co(III) complexes that were reported to be capable of phosphate ester hydrolysis are presented in Figure 1.9.^{48,49,50,51}

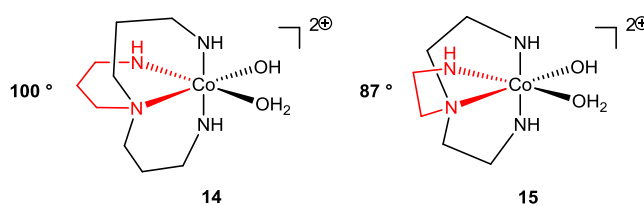


Figure 1.9- Chemical structures of the trpn[tris(aminopropyl)amine] Co(III) complex **14** (N_{eq} -Co- N_{eq} angle highlighted in red is 100°) and tren[tris(aminoethyl)amine] Co(III) complex **15** (N_{eq} -Co- N_{eq} angle highlighted in red is 87°).⁴⁹

Compared to the highly reactive lanthanides, Co(III) complexes (together with Ir(III) cations) are known to be suitable for mechanistic investigations with ^1H and ^{31}P NMR spectroscopy and are largely used by researchers to shed light on the mechanistic details of P-O bond cleavage (which will be discussed in detail in Chapter 3, section 3.1.2.1). This is attributed to the kinetic inertness of the Co(III) cation, which results in ligand exchange being slow enough to obtain meaningful kinetic data.^{1,51,52,53}

Especially interesting candidate amongst tetraamine macrocyclic Co(III) complexes is the cyclen-based Co(III) complex **16** (Figure 1.10), which was established by Chin *et al.* as one of the most active mimetic systems for phosphate ester hydrolysis, showing a rate enhancement of up to 10^7 in the hydrolysis of BNPP.⁵²

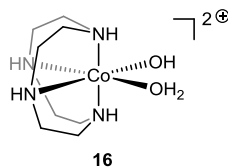


Figure 1.10- Chemical structure of the hydrolytically active cyclen-based aqua-hydroxo Co(III) complex.⁵²

Interestingly, it was found by Chin *et al.* that even small variations in the tetraamine ligand structure led to significant alterations in the hydrolytic activity of the complex.⁵⁰ This prompted extensive investigations in the structure-activity relationship of the tetraamine Co(III) complexes with an aim to identify the key structural factors that influence the hydrolytic efficiency of these complexes. In particular, Chin *et al.* demonstrated that the ease of formation of the four-membered chelate between metal complex and substrate in the rate-determining step of the hydrolytic reaction is the most important factor (Chapter 3, section 3.2.2).⁴⁹ Additionally, it was found that the formation of this four-membered chelate ring intermediate is greatly affected by the size of the N_{eq} -Co- N_{eq} angle opposite to it as well as *N*-alkylation of the axial nitrogen atoms of the ligand (Figure 1.11). For example, the finding by Chin *et al.* that the trpn[tris(aminopropyl)amine] cobalt complex

14, with an $N_{eq}\text{-Co-}N_{eq}$ angle size of 100° , hydrolysed BNPP 300 times faster than its structural analogue tren[tris(aminoethyl)amine] cobalt complex **15**, which possesses a $N_{eq}\text{-Co-}N_{eq}$ angle of 87° , indicating that larger $N_{eq}\text{-Co-}N_{eq}$ angles tend to result in an apparent enhancement of hydrolytic activity of the complexes and this may be a feature to replicate in putative catalytic systems.⁴⁹

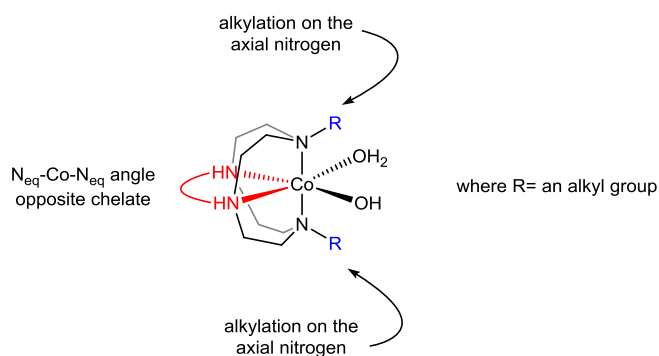


Figure 1.11- Structural features that influence the ease of the four-membered ring formation on Co(III) cyclen-based complexes.

Kim *et al.* built on this work by testing and comparing the hydrolytic activity of the complexes **16**, **17** and **18** shown in Figure 1.12. Their findings revealed that alkylation of the cyclen ligand by introducing one methyl group on an axial nitrogen resulted in a decrease in the hydrolytic activity of the complex in NPP and BNPP hydrolysis.⁵⁴

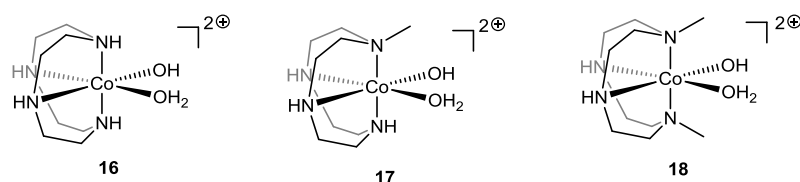
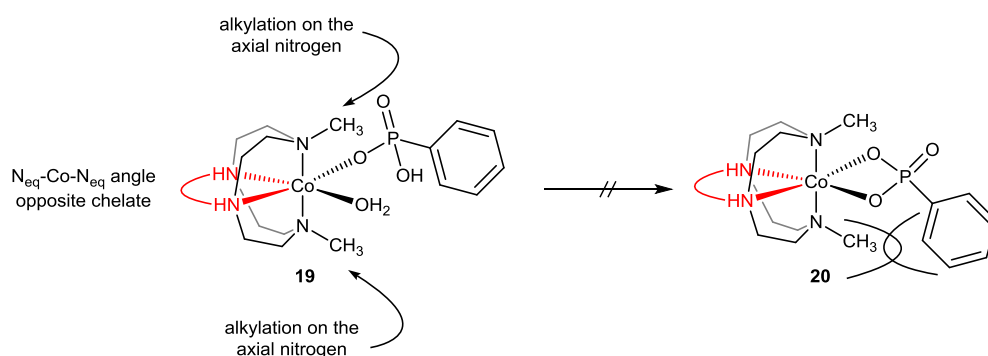


Figure 1.12- Structures of the cyclen-based Co(III) complexes, whose hydrolytic activity towards the NPP and BNPP substrates was studied by Kim *et al.*⁵⁴

Additionally, the introduction of a second methyl group in **18**, resulted in a dramatic decrease in the activity compared to other complexes. ^1H NMR studies showed that the formation of the phosphonate chelate ring was inhibited in **19**, due to steric interactions between the phosphonate ring and the second methyl group, as illustrated in Scheme 1.7.



Scheme 1.7- Binding of phenyl phosphonate to 18: Inhibition of the four-membered ring chelate formation due to steric interactions between the methyl group on the cobalt complex and phenyl ring on the phosphonate, proposed by J.Kim *et al.*⁵⁴

Furthermore, it was also reported by Knight *et al.* in 2004 that alkylation at a single nitrogen atom of Co(III) cyclen complexes with *p*-bromomethyl benzoic acid resulted in a 25% reduction in its activity to facilitate DNA hydrolysis.⁵⁵

Despite the high rate accelerations reported for the tetraamine Co(III) complexes, the central disadvantage encountered with these complexes is their hydrolytic inertness, which gives rise to the tight binding of the hydrolytic product to the Co(III) complex. This resulted in the complexes displaying no catalytic turnover (Chapter 3, section 3.1.2.1) and that was normally tackled by using them in large excess over the phosphate ester substrate in the reaction.⁵¹

1.3.3.2.3. Zn(II)-Azamacrocyclic Hydrolytic Agents

Zn(II) azamacrocycles are also deemed appealing candidates for mediating the cleavage of the P-O bond and have been widely studied as phosphatase models by a number of research groups.⁵⁶ Some of them are used as synthetic model catalysts for the hydrolysis of RNA dinucleotide analogues. Zn(II)-based complexes are known to show many advantageous characteristics, such as lack of kinetic inertness of the cation, which allows the exchange of hydrolytic ligands to occur more rapidly and hence does not lead to the inhibition of the complex, as in the case with Co(III)-based complexes. Also, the lack of redox chemistry in Zn(II) ion excludes the competitive oxidative mechanism of phosphate ester hydrolysis. Moreover, as mentioned in section 1.3.2, Zn(II) is present in the active site of many natural phosphatase enzymes, such as alkaline phosphatase, which normally comprises two Zn(II) centres surrounded by different chemical environments in the active sites.^{57,58} Thus, there is an increasing number of reports that explore the factors that

influence the reactivity of the Zn(II)-based complexes towards P-O hydrolysis to gain valuable knowledge about the behaviour of natural phosphatases. The effect of the ligand structure on the efficiency of Zn(II)-based hydrolytic agents has been widely investigated. Some of the first examples of hydrolytically active azamacrocyclic Zn(II) complexes were reported by Kimura *et al.* (Figure 1.13), who compared the hydrolytic activity of these complex based on the ligand structures. It was revealed, that Zn(II)- 1,4,7-triazacyclododecane complex **22** showed higher rate accelerations in BNPP hydrolysis compared to Zn(II)- 1,4,7,10-tetraazacyclododecane **21** (Chapter 3, section 3.1.2.2).⁵⁷

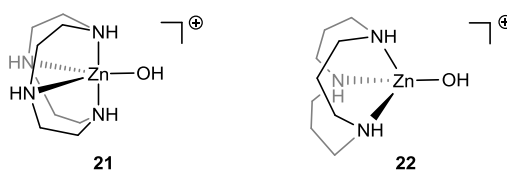


Figure 1.13- Structures of the two azamacrocyclic Zn(II) complexes **21** and **22**, whose efficiency in BNPP hydrolysis was tested and compared by Kimura *et al.*⁵⁷

Other structure-reactivity studies showed that anchoring of other functional groups (basic or nucleophilic auxiliary groups) to a chelate ligand can potentially provide additional substrate interactions and increase the hydrolytic efficiency of the complexes. In 2008 Subat *et al.* demonstrated that incorporation of a heterocyclic moiety into **21** enhanced the BNPP hydrolysis rate of the Zn(II) complex of of **23** by up to six times over the parent cyclen-Zn(II) complex, the effect attributed to the additional hydrophobic interactions between the aromatic moiety and the substrate (section 1.3.3.2.5). Complexes **24** and **25** showed slightly lower activity than complex **23** (Figure 1.14).⁵⁹

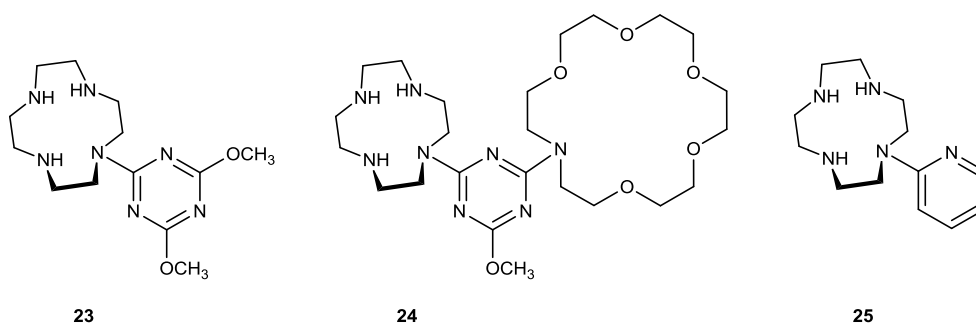


Figure 1.14- Chemical structures of the cyclen-based ligands used to prepare Zn(II) complexes.⁵⁹

The opposite effect of the *N*-alkylation of the cyclen-based Co(III) complexes may be attributed to the difference in the mechanistic action between Co(III) and Zn(II) hydrolytic agents (Chapter 3, section 3.1.2).

Furthermore, Kimura *et al.* discovered that phosphatase-like activity of azamacrocyclic Zn(II) complexes **21** and **22** increases with increased pH, with the best hydrolytic activity observed at pH 9-11 at 25°C. This effect was attributed to the higher concentration of the hydrolytically active metal-hydroxide species in the solution at higher pHs.⁵⁷

Overall, despite the remarkable rate accelerations achieved with mononuclear metal complexes, turnover has rarely been obtained. Based on the outcomes of the structure-reactivity studies, particular attention in the area of enzyme mimics was devoted to the structural design of the metallic hydrolytic agents with a view to increasing their efficiency towards phosphate ester hydrolysis.

1.3.3.2.4. Multimetallic Systems

As mentioned in section 1.3.2, the active sites of natural metallophosphoesterases normally possess two or more metal ions, such as Mg(II), Ca(II) and Zn(II), whose cooperative action results in an extraordinary hydrolytic efficiency of the enzyme. Taking inspiration from Nature, scientists developed a novel strategy to enhance catalytic rates of artificial hydrolytic agents by improving catalyst design and increasing the number of metal ions in the synthetic nucleases.¹

Multinuclear systems have different mechanisms of ester hydrolysis compared to mononuclear systems. The combination of several metal ions assists P-O bond cleavage mainly *via* associative mechanisms. Mechanistic studies have revealed that bimetallic systems utilise three main modes of action to catalyse phosphate ester hydrolysis, which are depicted in Figure 1.15. Such catalysis can occur *via* double Lewis acid activation (**a**), or *via* combination of Lewis acid activation with nucleophile activation (**b**) and with leaving group activation (**c**).¹

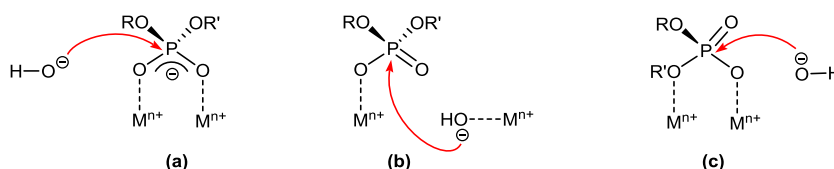


Figure 1.15- Three modes of action of mechanism of phosphate ester hydrolysis catalysed by two metal ions.¹

X-ray crystallography studies of natural nucleases elucidated that metal ions in their active sites are positioned within narrow distances in the range of 3-4 Å to achieve optimal cooperativity.⁴⁰ This special localisation is essential to ensure optimal cooperation between the metals and metal-substrate interactions. Researchers were guided by these criteria in an effort to generate multimetallic complexes with improved hydrolytic efficiency. Not surprisingly, such multimetallic systems showed significantly higher rate accelerations compared to the mononuclear systems. For example, Chin *et al.* proposed that addition of the second metal ion to the monometallic complex would result in cooperation and hence in enhanced hydrolytic activity. The authors then prepared a bimetallic Co(III) cyclen-based complex that gave a 10^{11} rate enhancement in the hydrolysis of certain phosphate esters with respect to the uncatalysed reaction, which is significant enhancement of the 10^7 factor achieved by the mononuclear analogue. Additionally, in 1998 Chin *et al.* demonstrated that another azamacrocyclic TACN-based Co(III) bimetallic complex provided an increase of 11 orders of magnitude in the hydrolysis of methyl *p*-nitrophenyl phosphate by double Lewis acid activation (Figure 1.16), whilst its monometallic analogue gave only 50-fold rate acceleration in this reaction.^{1,60}

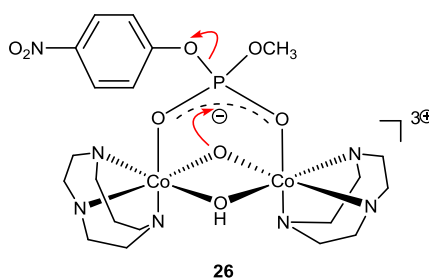


Figure 1.16- Mechanism of methyl *p*-nitrophenyl phosphate by TACN-based bimetallic Co(III) complex.^{1,60}

Amongst the most efficient bimetallic systems reported to date are the bimetallic Ce(IV) complex of the polyaminocarboxylate ligand HXTA **27** and the bimetallic Fe(III) complex based on a benzimidazolymethyl derivative of 1,3,5-diazapnetate DTPB **28** (Figure 1.17). Que and co-workers demonstrated that the Ce₂(HXTA) complex at 10 μM concentration, pH 8.0 and 37 °C cleaves plasmid DNA with a rate constant of $1.4 \times 10^{-4} \text{ s}^{-1}$, which corresponds

to a half-life of 1.4 hours. Whereas Liu and co-workers observed, that in the presence of $\text{Fe}_2(\text{DTPB})$ at 100 μM , pH 7.0 and 37 °C supercoiled DNA is degraded with a half-life of 5 minutes, which is one of the highest values obtained so far for the hydrolytic cleavage of plasmid DNA.¹

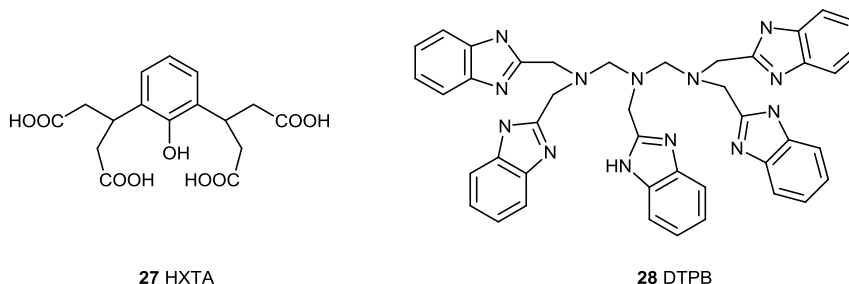


Figure 1.17- Chemical structures of HXTA **27** and DTPB **28** ligands used to prepare Ce(IV) and Fe(II) complexes for DNA hydrolysis.¹

Other bimetallic lanthanide-based complexes are also known, such as bimetallic Ln(III) complex of the 30 membered azacrown macrocycle **29** (Figure 1.18) studied by Zhu and co-workers, which showed DNA cleavage with a rate constant of $1.0 \times 10^{-3} \text{ s}^{-1}$ at 37 °C, pH 7.0. However, the rigid structure of the large azacrown macrocyclic ligand makes such complexes less appealing as enzyme mimics.⁴⁴

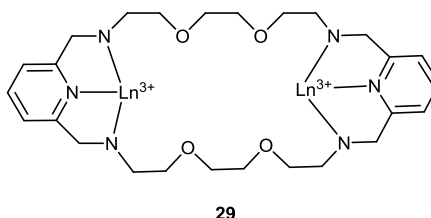
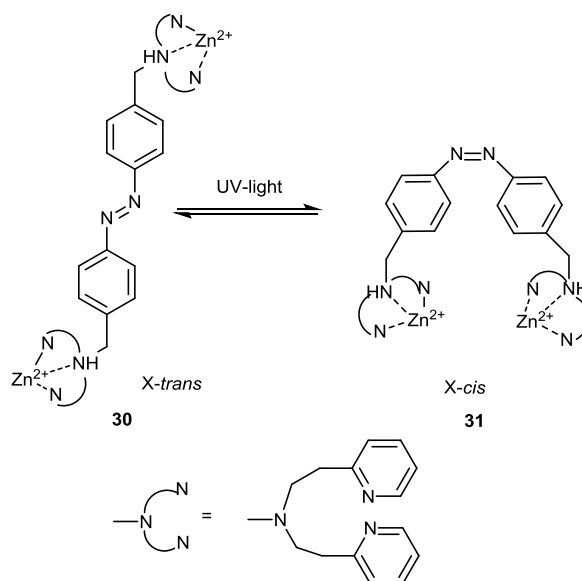


Figure 1.18- Structure of the bimetallic Ln(III) complex, which showed hydrolytic activity towards DNA.⁴⁴

It has been established that the hydrolytic activity of bimetallic and multimetallic complexes depends on the affinity of the complex for the substrate and the cooperation between the metal ions within the complex. The $\text{Fe}_2(\text{DTPB})$ complex, for example, showed a remarkable affinity to plasmid DNA ($K_a = 1 \times 10^5 \text{ M}^{-1}$), which is most likely attributed to the high positive charge on this complex.¹ It was found, that cooperativity between metal ions, which depends on the distance between metal ions in the system, is essential and can be used to control the activity of the multimetallic systems. Hirota and co-workers provided experimental proof for this phenomenon by synthesising the bimetallic complex **30** (Scheme 1.8), where the Zn(II) complex is connected through an azobenzene photoswitch, which can be photoisomerised between the *trans*- and *cis*-forms. Although both forms

showed binding ability to DNA with $K_a = 4.6$ and $4.9 \times 10^4 \text{ M}^{-1}$ respectively, only the *cis*-isomer showed DNA cleavage. This is explained by the fact, that the distance between the benzylic atoms in the *cis*-chromophore **31** is 8 Å compared to 12 Å in the *trans*-form, resulting in closer separation of the metal centres and in cooperativity between metal cations, which in turn results in the hydrolytic activity of the complex as opposed to the analogous *trans* isomer. Another photoswitchable bimetallic Cu(II) complex also reported by Hirota *et al.* in 2008, showed a similar effect.¹



Scheme 1.8- Photoswitchable bimetallic Zn(II) complex undergoing photoisomerisation.¹

The degree of cooperativity between metal ions was also demonstrated by Subat *et al.* in 2008 based on the cyclen-Zn(II) complexes. It was shown that the lengths of the spacer between the two metal units affected the hydrolytic activity of the Zn(II) complexes with ligands **32** and **33** (Figure 1.19). The Zn(II) complex of **33** which has a shorter triazine-based spacer was able to facilitate BNPP hydrolysis by 1 to 2 orders of magnitude faster than the Zn(II) complex of **32** with the longer 2,2'-bipyridine spacer.⁵⁹

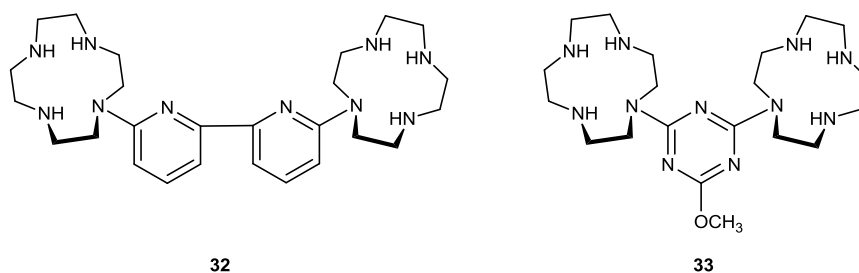


Figure 1.19- Chemical structures of the cyclen-based ligands used to prepare dinuclear Zn(II) complexes.⁵⁹

Another key factor in determining the reactivity of the systems is the formation of the μ -hydroxo bridge between the two metal ions. Kinetically labile metal ions, for example, such as Cu(II), are known to form μ -hydroxo-bridged complexes that hamper their hydrolytic activity.¹ There are also several examples of multimetallic Zn(II) complexes, which are depicted in Figure 1.20. Studies of their hydrolytic activity revealed that an increase in the number of metal ions also resulted in an increase in their activity. For example, in 1997 Komiyama *et al.* showed that the trinuclear Zn(II) complex **36** is ten-fold more active than its dinuclear analogue **35** in the hydrolysis of RNA and RNA models. The authors were the first to show the active bimetallic Zn(II) complex **34** as molecular scissors for the site selective cleavage of RNA.³³ Building on this work, similar systems were developed.⁴⁴

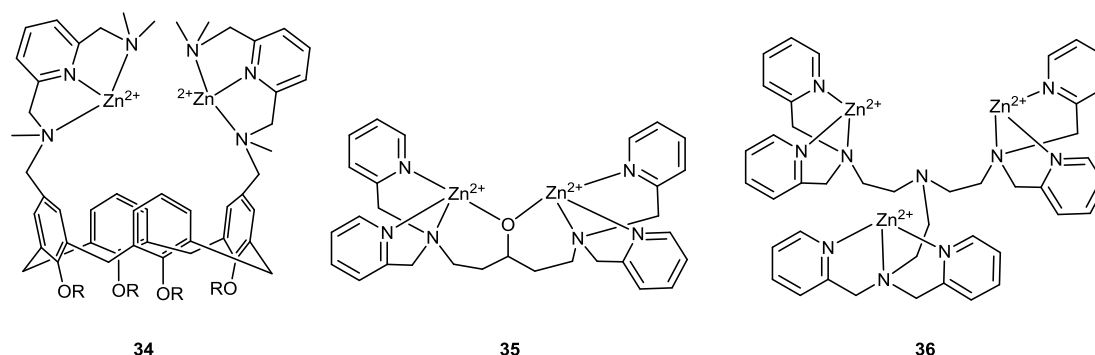


Figure 1.20- Structures of the multimetallic pyridine-based Zn(II) complexes.³³

Although multimetallic systems presented in this section are some of the most active catalytic agents reported to date of the 'activated' and 'non-activated' phosphate esters, they do not provide sufficient mechanistic insight into the P-O hydrolysis due to the kinetic lability of the Zn(II) metal centres.¹

Increasing the number of metal ions is certainly a successful strategy to enhance the hydrolytic efficiency of the synthetic hydrolytic agents. However, it is noteworthy that the catalytic pockets in natural enzymes have only a limited number of metals, and it is thus the quality of the active site environment that plays a key role in determining the activity of the enzyme, rather than the number of metal ions and the activity is enhanced through hydrophobic/hydrophilic interactions.²

Although there has been substantial progress in the field with novel approaches developed and the first applications of synthetic hydrolytic agents in the manipulation of DNA having

been demonstrated, enzyme-like accelerations have not been achieved. This suggests that a more detailed understanding of catalyst design is required together with a deeper understanding of the relevant factors that affect reaction rates.¹

1.3.3.2.5. *The Role of the Chemical Environment in the Activity of Synthetic Hydrolytic Agents*

A biomimetic catalyst is normally referred to as ‘a chemical catalyst that mimics certain key features of the enzymatic systems.’⁶¹ Although various effective synthetic agents were carefully designed that contained metal ions/and or organic groups organised in a certain fashion to achieve optimal cooperation, the behaviour and rate accelerations observed in enzymes were not exactly reproduced.

Recently, considerable attention has been given not only to the design of artificial metal-based systems, but also to the careful choice of the chemical environment around these simple metallic systems. Thus, another promising strategy utilised to enhance the activity of the hydrolytic agent involves the use of lower polarity solvents, organic macromolecules and polymers that create hydrophobic environments around the metal centre, which is similar to that present in the active site of the enzyme and is different to that of the bulk aqueous medium.^{1,2,61}

Further progress in the field of enzyme mimicry has resulted in the significant discovery that placing such small-molecule complexes in a low polarity environment, that closely mimic the dielectric environment of the active sites of enzymes, results in much higher catalytic activity and turnover with reduced catalytic load. Interestingly Brown *et al.* demonstrated that placing triazamacrocyclic bimetallic Zn(II) complex **37** (Figure 1.21) into lower polarity solvents (compared to aqueous solutions), such as MeOH, resulted in a gain in hydrolytic efficiency giving rate accelerations of up to 12 orders of magnitude in the hydrolysis of certain phosphate esters, compared to the 10⁸-fold achieved by the same complexes in an aqueous environment.^{62,63,64} More recently, Scrimin *et al.* reported that Zn(II) complexes of azamacrocyclic ligands showed remarkable increase in cleavage efficiency of certain phosphate ester models in an aqueous environment when anchored to gold nanoparticles.^{2a} According to the authors, this effect can be attributed to the decrease in the polarity of the reaction site. Additionally, the increase in the length of alkyl spacer that is located between the nanoparticle surface and metallic unit lead to significant increase in the reactivity of these Zn(II) synthetic agent.

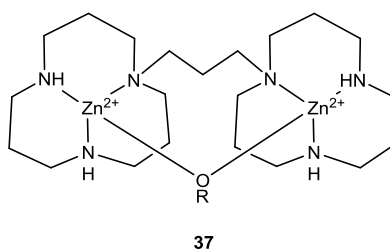


Figure 1.21- Chemical structure of the bimetallic azamacrocyclic Zn(II) complex **37**.⁶³

Metal-based complexes have also been incorporated into larger structures with a view to mimic the structure of natural enzymes that contain a metal-based active site inside the polymeric protein matrix.⁶¹ Examples of such larger systems include polymers and cyclodextrins. Cyclodextrins (CDs) are cyclic oligosaccharides composed of glucose monomers and the most commonly utilised isomers are depicted in Figure 1.22.^{61,65} Due to their commercial availability, well-established synthetic methods which allow a wide range of functional moieties to be introduced, and the presence of the hydrophobic cavity that enables flexible incorporation of smaller guest molecules, cyclodextrins have been extensively explored as biomimetic catalysts.

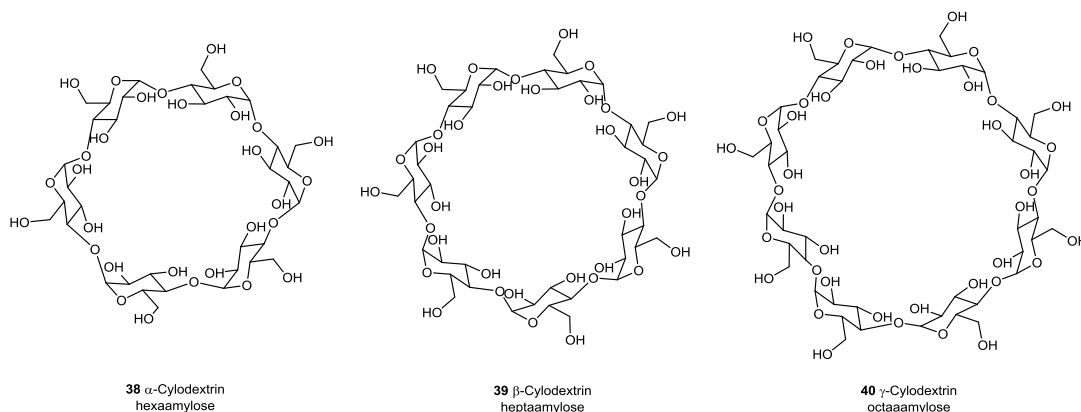


Figure 1.22- Chemical structures of the three most commonly used isomers of α , β and γ -cyclodextrins.⁶¹

The activity among Co(II)-based small-molecule metal complexes is very rarely reported due to the areal oxidation of Co(II). This issue was tackled by scientists by incorporating Co(II) complexes into more hydrophobic environments that could potentially stabilise cobalt in its 2+ oxidation state.⁶⁵

β -cyclodextrins functionalised with dinuclear Co(II)-ligand complex, as in **41** (Figure 1.23) were prepared and present an example of bimetallic hydrolases. The hydrophobic interactions delivered by the supramolecular host stabilise the ligated Co(II) species and

were reported to play a role in the rate determining step in the hydrolysis of BNPP and NPP, which in turn lead to enhanced hydrolytic activity and substrate specificity. A dinuclear Zn(II) complex was also conjugated with β -CD to form a bimetallic Zn(II)-bis- β -cyclodextrin complex, which provided 730-fold rate enhancements in the hydrolysis of NPP and accelerated the cleavage of BNPP by 10^3 -fold.⁶⁵

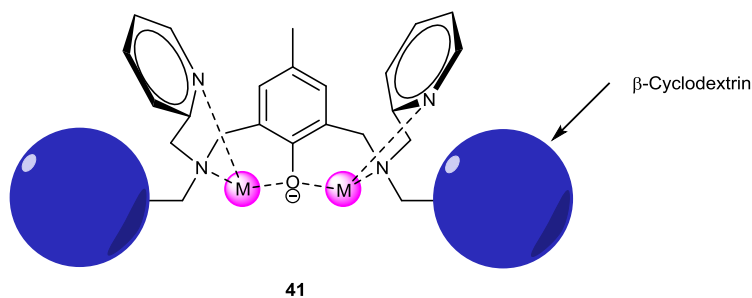


Figure 1.23- An example of dinuclear divalent metal-ligand cyclodextrin complex used to facilitate phosphate ester hydrolysis; M= Co(II), Cu(II) and Zn(II).⁶⁵

Cu(II) and Zn(II) complexes of the imidazole-based tetradentate polyamine ligand **42** (Figure 1.24) were immobilized by co-polymerisation with ethyleneglycol dimethacrylate (EGDMA) and showed efficient hydrolytic cleavage of BNPP **8**. According to Severin *et al.* these polymeric catalysts were found to be 56 times more active towards BNPP hydrolysis compared to the corresponding homogeneous metal complexes in aqueous solutions.⁶⁶

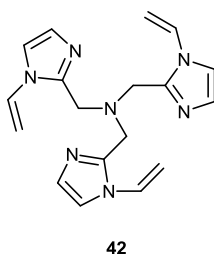


Figure 1.24- Chemical structure of the imidazole-based tripodal ligand that was used by Severin *et al.* to prepare hydrolytically active pre-polymerisation Zn(II) and Cu(II) complexes.⁶⁶

As already mentioned in section 1.2.3, Zr(IV)-cluster-containing MOFs became an appealing heterogeneous materials for catalysing phosphate ester hydrolysis. In particular, amine functionalised MOF UiO-66-NH₂ is amongst the most active MOF-based systems showing 20-fold increase in the hydrolysis rate of the parent MOF-UiO-66, which is reflected in a half-life of only 1 minute.³²

Another appealing strategy that combines careful design of the catalytic system and choice of the chemical environment is molecular imprinting, which is discussed in more details in the next section.

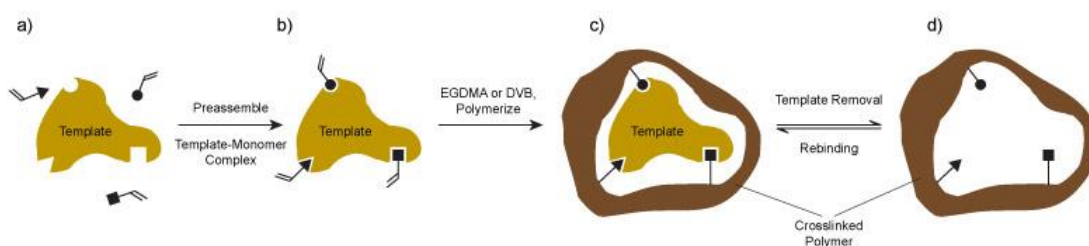
1.4. Molecular Imprinting

Enzymes can be described as three-dimensional polymers, where protein chains are folded in a complex well-defined way to form catalytic pockets called active sites, which sometimes can contain metals. A feature that is especially important for the catalytic activity of metalloenzymes (section 1.3.2.), is the secondary coordination sphere around the metal ion surrounded by well-organised functional groups of amino acids in the catalytic pocket. The interactions (covalent and non-covalent) and cooperation between the metal, amino acid residues and the substrate are essential to create and maintain this secondary coordination sphere- aspect that is particularly challenging to reproduce when designing synthetic metal-based enzyme mimics.

Among the different approaches used to mimic an enzyme's secondary structure, the use of large supramolecular systems (organic hosts), such as metal-containing molecular imprinted polymers (MIPs) has attracted considerable attention for a variety of reasons. The MIP approach offers an opportunity to generate highly specific three-dimensional metal-based catalytic sites inside the polymeric matrix. Such carefully controlled catalytic microenvironments within a macromolecule can better mimic the enzyme's active site and its secondary coordination sphere.⁶⁷

1.4.1. Overview and Main Concepts

Molecular imprinting is a *'process of generating synthetic polymers with binding sites with high recognition ability, through the assembly of functional and cross-linking monomers around a target molecule (the template), in the presence of an inert solvent.'*⁶ The polymerisation process is followed by the removal of the template to obtain the polymeric matrix that contains a three-dimensional imprint (or recognition site) complementary in size, shape and functionality to the original template (or imprint) molecule. The cavity provides the molecular recognition properties thus allowing the selective re-binding of the template. A schematic diagram for the MIP process is shown in Scheme 1.9.



Scheme 1.9- Schematic representation of the molecular imprinting process: a) mixing of the template with polymerisable functional monomers; b) template-monomer complex formation; c) polymerisation of this complex with the cross-linking monomer; d) removal of the template from the polymer and generation of the three-dimensional cavity.⁶⁸

There are three key steps in the molecular imprinting approach:^{68,69}

- 1) First step involves the formation of a stable complex between functional monomers and target template, either through reversible covalent bonds or by non-covalent interactions in a suitable solvent system;
- 2) In the second step the crosslinker is added followed by the initiator, which starts the polymerisation process and the formation of the three-dimensional structure. At this point the template molecule is complexed within the polymeric matrix.
- 3) In the final step, the template molecule is removed from the polymeric matrix by breaking the interactions between the template and the functional monomers by washing with acidic aqueous solutions or other solvents that favour particle swelling. Once the template is removed, the resulting polymeric matrix possesses a cavity with a so called 'molecular memory' provided by the functional groups that remain within the polymer. This allows either the efficient and selective rebinding of the template or catalysis of the target substrate.

Overall, the molecular imprinting approach allows the creation of specifically tailored cavities, structurally complementary to the target molecule, characterised by very good molecular recognition properties.

1.4.2. Approaches in MIP

Given the different types of interactions between the template and functional monomers, researchers distinguish two key classical approaches to the molecular imprinting strategy: covalent or 'pre-organised approach' and non-covalent or 'self-assembly approach'.

The first method requires the formation of the covalent bonds between the template and functional monomers in the MIP conjugate. Following the polymerisation process, this covalent bond is then cleaved, which allows the formation of another one upon rebinding. In the non-covalent approach, on the other hand, the imprinting adducts are generated or ‘self-assembled’ *in situ* in an appropriate solvent that induces the non-covalent bonding between the template and functional monomers, such as hydrogen and coordination interactions as well as ionic bonds.⁷⁰

Table 1.1- Key differences between the covalent and non-covalent methods used for the preparation of molecular imprinted polymers.⁷⁰

	Covalent	Non-covalent
Synthesis of monomer-template conjugate/adduct	necessary	unnecessary
Polymerisation conditions	rather free	restricted
Removal of template after polymerisation	difficult	easy
Guest bonding and guest release	slow	fast
Structure of the guest binding site	clear	less clear
Homogeneity of bonding sites	high	lower
Typical applications	chromatography (HPLC)	bio/chemo sensors

The choice of one approach over the other determines the overall experimental synthetic strategy for the polymers and depends on the type of the target molecule used for rebinding studies as well as the type of the applications of the polymers in question. For example, the separate synthesis of the template-monomer conjugate using covalent method generally results in more defined cavities, but can be time-consuming in the cases where extensive synthesis of the functional monomers is required. On the other hand, the generation of the MIP adduct that involves hydrogen or ionic bonds can be easily achieved *in situ*. However, the polymerisation conditions are restricted and the solvent choice has to be carefully considered for the non-covalent method. For example, the use of protic solvents that can disrupt such non-covalent interactions must be avoided. The major advantages and disadvantages of each method are presented in Table 1.1.

Progress in the area of materials chemistry, in particular nanotechnology has allowed the development of new approaches for the synthesis of imprinted polymers. For example, the

mixed semi-covalent method was developed by Whitcombe *et al.* that merged the differences of the other two approaches.⁶⁸ Additionally, there were cases when the imprinting adduct involved the coordination bonds between the template and functional monomers that could not be defined by either of the two classical methods and therefore other aspects have to be considered which will be mentioned later in this chapter.⁶⁹

1.4.3. Origins and Applications

The first report on molecular imprinting can be dated back to 1949, when Dickey and co-workers⁷¹ demonstrated that dye molecules could be imprinted into silica gels. Further progress in the field is attributed to the two separate landmark reports by Wulff (1972)⁷² and Mosbach (1984),⁷³ where they revealed (using covalent and non-covalent approaches respectively) the remarkable ability of the polymeric matrices not only to retain the 'molecular memory' of the template molecules, but also to distinguish between the enantiomers of the same optically active compound. This prompted academic research in the area and attracted considerable attention from industrial stakeholders.

After this, progress in molecular imprinting research has developed and expanded rapidly and was proven to be efficient and versatile in a wide variety of applications. These involve antibody and receptor mimics, generation of biosensor-like devices, solid-phase extraction, separation and drug delivery. MIPs are also increasingly used by researchers to obtain enzymatic as well as non-biological catalytic agents. The ability of imprinted polymers to recognise and re-bind the target template is a key requirement for all applications.⁷⁴

One of the major advantages of MIPs over other recognition systems (i.e. those based on biomolecules), is that polymeric materials can be used under a much larger variety of experimental conditions, such as high temperature, organic solvent, high and low pH solutions.⁶⁷

Development of imprinted polymers as catalysts with enzyme-like activities has attracted increasing attention however despite some interesting results, it remains a challenge. A number of MIPs properties, such as high inherent selectivity, stability and reusability combined with the ease of their preparation and cost-effectiveness make them appealing

candidates for the purpose of catalysis. Several strategies to obtain catalytic MIPs and their examples will be briefly discussed in the next section.

1.4.4. Catalytically Active MIPs

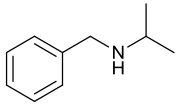
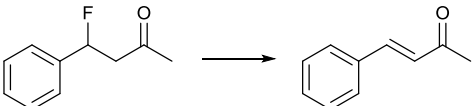
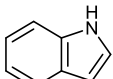
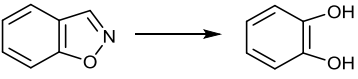
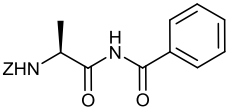
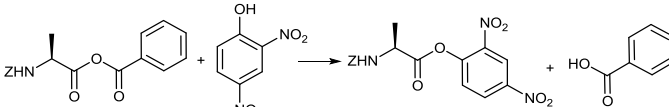
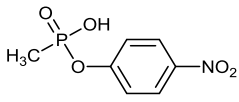
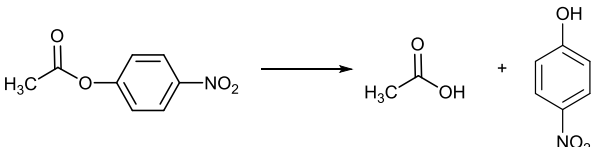
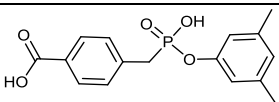
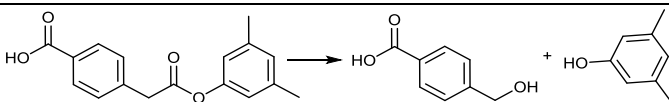
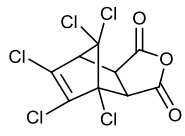
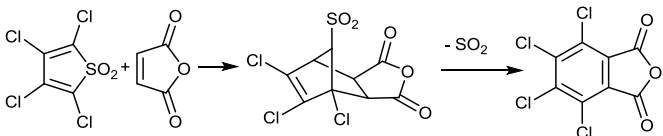
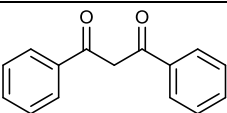
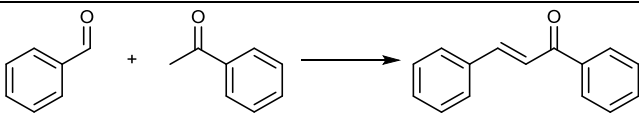
1.4.4.1. Overview and Approaches

Main approaches towards generation of catalytically active MIPs include the use Substrate and Product Analogues, Transition State Analogue (TSA) and the use of Cofactors as the print molecule with some of the key examples presented in Table 1.2.⁷⁵

A number of MIP catalysts have been prepared using the Transition State Analogue approach, which is considered to be the most common and one of the most studied methods to prepare imprinted polymers using covalent or non-covalent approaches. This strategy requires the use of the imprint molecule that bears resemblance to the transition state. This imprint is functionalised with the polymerisable unit for the incorporation of the adduct to the cross-linked polymer, which matrices are designed to stabilise the reaction transition states. It is interesting to note, that the use of this transition state analogue approach has resulted in the most active polymers to date, that showed catalytic activity in the reactions that involve C-C bond formation with promising rate accelerations and enzyme-like kinetics.⁷⁶ The MIPs performance in simple hydrolytic reactions where phosphonates were used as tetrahedral transition state mimics was also assessed.

In the Substrate Analogue approach, the imprint molecule (which is a mimic of a substrate) is normally coupled to the catalytic unit which results in the cavity that is complementary to the substrate shape. In other words, it required the use of the imprint molecule that mimics the reaction complex between the substrate and the matrix. Catalytic groups are 'biased' by the print species inside the cavity, which results in their fixed positions suitable to accommodate the target substrate. The contact between the substrate and these catalytic groups then initiates the reaction. High catalytic activities have been achieved by molecular imprinted polymers prepared by using the substrate approach. However, one of the problems encountered with this method is product inhibition, which was demonstrated in the hydrolysis of the amino acid analogues for example. This strategy has also been used for the elimination reactions, which involved dehydrohalogenation of β -fluoroketones.

Table 1.2- Key approaches for the design of catalytically active MIPs and some relevant examples. Source: Ramström *et.al.*⁷⁵

	Print Molecule	Reaction
Substrate analogue		
	 ref. 77	
	 ref. 78	
Transition State Analogue	 ref. 79	
	 ref. 80	
Product Analogue	 ref. 81	
Co-factor	 ref. 76	

The product analogue as the print molecule is also used to prepare catalytically active polymers similar to the Substrate Analogue method, product inhibition can also occur in this case. The Product Analogue strategy is particularly advantageous for the cases, when product intermediate is rearranged leading to stable final target product. The determining factor in overcoming the entropic barriers required for the formation of the product can be a product intermediate stabilisation that is followed by the spontaneous rearrangement of

the molecule. Some of the molecular imprinting polymers generated using this approach resulted in the rate enhancement of the Diels-Alder reaction 270 times with respect to the uncatalysed reaction.⁸¹

Final approach towards the synthesis of the catalytically active polymers involves the use of cofactors, i.e. any organic or inorganic auxiliary reagents that enhance catalytic activity of the polymer, similar to those used by enzymes. The cofactors employed by natural enzymes include vitamins, co-enzymes and metal ions. The majority of the cofactors in the MIP area are metals that are loosely bound to the active centre.⁷⁵ Metal assisted catalysis resulted in the generation of some of the most active MIPs to date and the central discoveries in this field are highlighted and discussed in the next section.

1.4.4.2. The Role of Metals in Molecular Imprinting and Their Merits

Given the crucial role metals play in the active sites of natural enzymes, the design and development of biomimetic metal-based molecular imprinting polymers drew considerable attention as one of the most promising and potentially useful approaches in the field of artificial enzyme mimics. Metals in MIP systems normally play a dual role: they hold a template into place during the polymerisation process and after template removal are key catalytic centres. Also, metal-ligand coordinative bonds are particularly advantageous contrary to other types of interactions (i.e. hydrogen and ionic bonds, π - π stacking etc.) normally used in molecular imprinting.⁸² For example, coordination bonds allow MIPs to bind a wider range of templates in a variety of solvents (including aqueous solutions). A number of factors influence the strength of the metal-template bond, such as the type of ligands coordinated to the metal, the temperature and the solvent of choice. The spontaneous complexation between the metal and the ligand leads to thermodynamically stable and kinetically labile compounds. Thus, template release occurs more easily compared to the MIP systems that have covalent types of binding.⁸³

When a metal-template complex is incorporated into the polymer, the three-dimensional polymeric matrix provides an additional secondary sphere as a result of the supramolecular networks, similar to what is also found in natural enzymes. This sphere defines the microenvironment around the metal ion and can control such characteristics as hydrophobicity, polarity, electrostatics, solvation and dielectric constant. Moreover, the presence of the polymeric cavity provides additional points of interactions, assists the

substrate binding and its subsequent transformation, which is advantageous for the generation of the enantioselective MIP catalysts.⁶⁷ Therefore, careful design of metal-based MIPs is important to ensure the desired properties of the system (or generate an appealing catalyst) and there are several aspects that require special attention when preparing metallic MIPs.

One of them is the synthetic procedure. For example, the assembly of the polymerisable metallomonomer prior to its incorporation into the polymer presents better advantage rather than simultaneous co-polymerisation of the metal complex, template and polymerisable functional monomers. This is because in the former case, the structure of the MIP adduct can be controlled better before its immobilisation into the polymer.

Also, it is important to evaluate the coordination chemistry of the complex (adduct) in solution prior to its polymerisation, to ensure its stability under polymerisation conditions (i.e. high temperature, such as 70°C) and to investigate effect of the polymerisable unit on the coordination mode of the complex.^{83,84}

The detailed investigation of the coordination behaviour of the metal-based MIP adducts is essential for the rational design of selective cavities. In his review in 2004 Striegler⁸² highlighted: *“Simple mixing of target templates with polymerisable monomers followed by a one-pot polymerization procedure is unlikely to create outstanding material properties, such as highly selective, and ideally homogeneously shaped and distributed binding sites. Instead, the rational design of selective cavities is a difficult, time consuming and sometimes even frustrating task, which requires a careful investigation of the coordination properties of the compounds associated prior to immobilization in a highly cross-linked matrix.”*

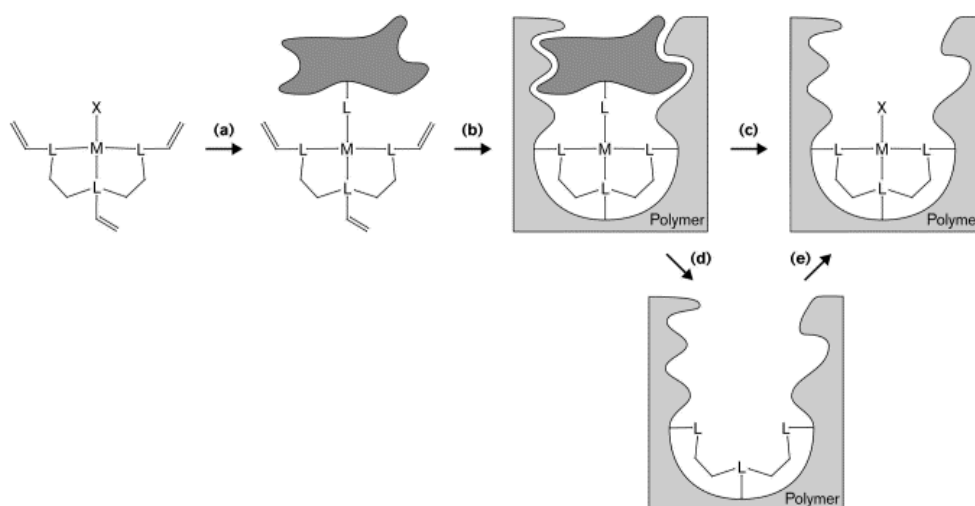
There have been a number of reviews about the use of the metal templated sites in the areas of sensing and molecular recognition.^{83,85} Examples include highly enantioselective systems that showed recognition of chiral amino acids⁸⁶ as well as helical metal complexes.⁸⁷ The use of metals also allowed the detection of large templates, such as bovine serum albumin (BSA).⁸⁸ Moreover, Er(III) doped polymers and toxic agents as

templates resulted in one of the most sensitive detectors for a number of organophosphate pesticides and nerve agents and resulted in their commercial use.⁸⁹

For the purposes of this thesis, however, special attention will be devoted to the generation of metal-based catalytic MIPs.

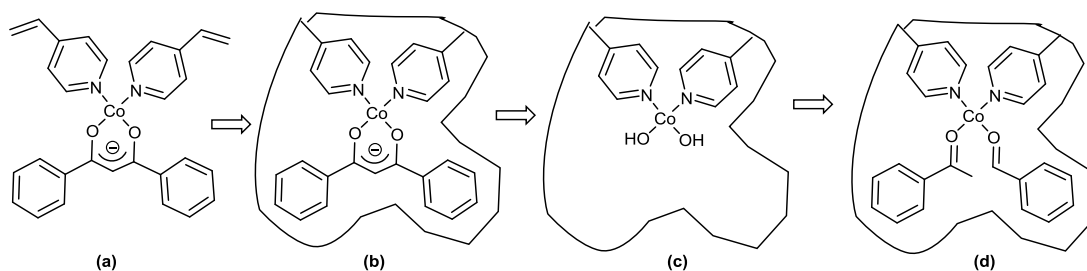
1.4.4.2.1. Catalytically Active Metal-based MIPs

As shown in Scheme 1.10, the first step towards the synthesis of the molecular imprinted catalyst with a metallomonomer is the preparation of an imprinting adduct, which requires coordination of the polymerisable ligand to a metal and its subsequent binding to the template. This adduct is then covalently incorporated into the polymeric matrix by a polymerisation process, which is followed by the removal of the template by breaking the bond between the metal and the template molecule. Metals can also be then washed out from the polymer using strong metal chelators like EDTA.⁸³



Scheme 1.10- Assembly of a metal-based molecularly imprinted catalyst (source: Severin *et.al.*)⁸³. (a) An assembly of the imprinting adduct by coordination of the template (pseudo-substrate); (b) copolymerisation in presence of large excess of cross-linker; (c) selective cleavage of the template; (d) simultaneous removal of the metal ion; (e) generation of the metal-based imprinted catalyst.

The first case of metal-based MIPs can be dated back to 1980's, when Matsui *et al.* prepared catalytic molecular imprinted polymer with the cobalt-based metallomonomer for the catalysis of the aldol condensation (Scheme 1.11), which gave an 8-fold rate acceleration compared to the homogeneous catalysis. Unfortunately, the non-metallic polymer was also reported to enhance the rate of the same reaction by 6-fold, indicating rather poor imprinting efficiency according to the authors.⁷⁶



Scheme 1.11-Synthesis of the Aldolase type II mimic proposed by Matsui *et al.* using an imprinting approach: (a) Imprinting adduct; (b) Adduct incorporated into the polymer by polymerisation reaction; (c) MIP after template removal; (d) MIP with the loaded substrate (catalysis).⁷⁶

Other successful examples include enantioselective metallic MIP catalysts that can recognise chiral molecules. These include: rhodium imprinted catalysts that were demonstrated by Locatelli and co-workers to catalyse the asymmetric hydride transfer reduction of chiral ketones;⁹⁰ titanium chiral cavities⁹¹ that showed enhanced reactivity in the catalysis of Diels-Alder reaction compared to their non-imprinted analogues. There was also a number of other non-enzymatic reactions tackled by molecular imprinting, such as Pd(II) catalysed cross-coupling,⁹² selective oxidation of alkenes using Zn(II)-porphyrin scaffold,⁹³ showing good to moderate results.

MIPs have also been tested in the area of enzyme mimicry to evaluate their activity for a variety of reactions, including phosphate ester hydrolysis. Sode and Say investigated the ability of MIPs to hydrolyse phosphate ester bonds. Taking inspiration from the enzyme phosphotriesterase, which contains four-histidine cluster coordinated to divalent metals (Figure 1.25) in its active site, Sode⁹⁴ prepared Co(II)-imidazole complex in a similar manner. This complex was coordinated to the paraoxon analogue (6:1 stoichiometry) and incorporated into the polymer. The quantity of active sites inside the polymer was only roughly estimated and relatively modest catalytic rates have been reported. Polymers imprinted with Co(II) accelerated P-O bond cleavage reaction by 20-fold compared to a solution of pure imidazole, and by 100-fold regarding pure Co(II) solutions. No comparison to the non-imprinted cobalt-imidazole complex has been reported. Further work on this system showed, that substituting Co(II) to Zn(II) and addition of methacrylic acid (backbone monomer) resulted in the some improvement in the catalytic activity. Importantly, similar activities of the imprinted and non-imprinted polymers for this reaction according to the authors signified random incorporation of the functional metallomonomers in to the polymers.

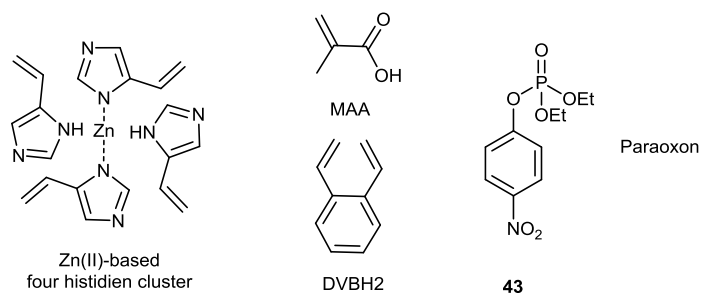
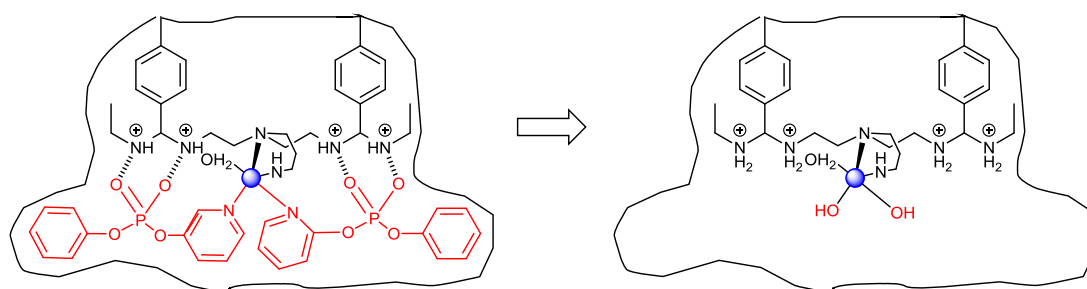


Figure 1.25- Metal-based four histidine cluster used by Sode et al. for the catalysis of paraoxon.⁹⁴

Say and co-workers^{95,96} built on this work, and also investigated the abilities of metal-imprinted polymers in the area of biomimetic hydrolysis of phosphate esters. In their work they tested a number of metal ions coordinated with methacryloyl-histidine monomers as well as to the ethyl paraoxon **43**. Although the authors do not specify how the catalyst loading was assessed and how the template remained unhydrolysed during polymerisation conditions, it was mentioned that the pH has a critical effect on the paraoxon hydrolysis. They demonstrated that imprinted catalyst showed enhanced activity in the hydrolysis of paraoxon compared to the non-imprinted polymers and free catalysts. Interestingly, among the catalysts tested, systems with Cu(II) showed the highest hydrolytic activity reaching rate enhancements of 356 times over the uncatalysed reaction. The higher catalytic activity is believed to be due to the higher affinity of the metal to the substrate, as dramatic increase in the affinity constant was observed with Cu(II).

The most prominent example of a hydrolytically active metal-based imprinted polymer in enzyme biomimicry thus far is a carboxypeptidase A mimic (Scheme 1.12).⁹⁷ The TSA approach was used to prepare this polymer imprinted with the Zn(II) metal coordinated to the phosphate transition state analogue. Following polymerisation, both template and metal were removed and the polymer was loaded with Cu(II) and resulted in the polymeric tetrahedral cavity, which was used to recognise carbonate substrates.

As opposed to the aforementioned studies, in this work more detailed investigations were carried out to assess the formation and coordination behaviour of the metal complex prior to polymerisation by NMR and UV-Vis spectroscopic techniques. This provided a better understanding of the microenvironment inside the polymeric cavity. The careful design of the system was reflected in high catalytic rates achieved by the carboxypeptidase A mimic.



Scheme 1.12- Carboxypeptidase A mimic prepared using metal-based MIP approach. ⁹⁷

It is important to note that the majority of the polymeric matrices discussed in this section are 'bulk' polymers or insoluble macroporous networks which are highly cross-linked rigid polymeric networks. It was found, that the nature of the material hampers the catalytic activity of the system due to some binding site heterogeneity. Also, rigid polymers were shown to slow down the diffusion of the substrate and/or resulting products.

In an effort to improve upon this issue, scientists utilised various approaches. One of them was the use of silica surface-imprinted catalysts, developed by Tada and co-workers.⁹⁸ Indeed, this method resulted in some improvements being achieved with this method, such as easier access of the substrates to the active sites. However, the scope of application of these silica-based catalysts remains limited only to certain reaction types, such as hydrogenation of ketones. Therefore, scientists then focused on the development of the more flexible materials which can better mimic the nature of the natural enzymes and consequently improve their catalytic features.

In the last decade, the attention turned to microgels and nanogels that have been evaluated as matrices for the preparation of molecular imprinted metal catalysts with the aim of achieving higher catalytic efficiencies.

1.4.5. Materials in Molecular Imprinting

1.4.5.1. Microgels and Nanogels

Molecular imprinted polymers present an attractive synthetic alternative to natural enzymes due to their ability to withstand conditions that are normally detrimental for natural enzymes: high temperatures and pressures as well as the presence of organic solvents. Additionally, MIPs show resistance to mechanical stress, treatment with acids and bases and thus can maintain their integrity and can be stored for long period of times.

These advantages combined with cheap and easy access to the precursor materials and reagent and short reaction times (few hours to a few days) bring attractive prospects in the area of catalysis.^{6,67}

One of the most widely used methods for the preparation of rigid (bulk) MIPs is radical polymerisation in solution by photochemical or thermal initiators. However, the major disadvantage of MIPs prepared in this manner, is that they have to be ground and sieved according to particle size, which is not only problematic and time-consuming, but also can generate heterogeneity in particle size. Moreover, such rigid nature of the polymers does not show complementarity with the flexible and adaptable nature of the natural enzymes. Furthermore, it is difficult for the reactants molecules to access the imprinted sites inside the polymer and the easy access is provided only by the sites the ones located on the surface.⁹⁹ For this reason some researchers started to evaluate soft materials, like gels, as potential new matrices.

Among the different synthetic approaches for the preparation of microgels and nanogels, high dilution radical polymerisation, developed by Graham at Strathclyde University, presents interesting advantages. This approach facilitates the *intramolecular* cross-linking over the *intermolecular* process (Figure 1.26) and results in the generation of materials with micro or nano size with high degree of cross-linking, that have larger surface area (surface to volume ratio), narrower size range and colloidal stability. Such properties facilitate extraction of the print molecule and its subsequent rebinding to the imprinted cavities and thus present advantages in the area of catalysis.⁶

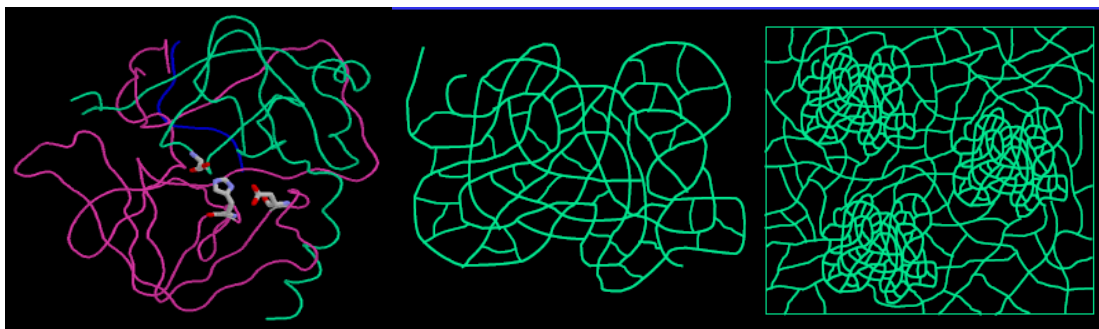


Figure 1.26- a) Natural enzymes: radius of gyration 5-15nm; molecular weight 30000 – 50000; soluble; b) Intramolecularly crosslinked macromolecules: radius of gyration <15nm; molecular weight 40000 – 20000; soluble; c) Macro gels obtained by usual crosslinking polymerisation; 3Dimensional infinite network; insoluble.⁶

The polymerisation conditions and factors that influence the generation of such materials have been explored by a number of research groups. For example, Graham *et al.* found, that macrogelation of the materials (the loss of their colloidal stability) occurs when the concentration of the monomer is above certain level. It is therefore necessary ensure that the monomers and solvent are used at appropriate amounts.⁶ Biffis and co-workers built up on this finding and thoroughly investigated such conditions at high degrees of cross-linking which resulted in successful generation of microgels with molecular recognition abilities.¹⁰⁰

The Resmini group presented the first example of the imprinted microgels that showed catalytic activity in carbonate hydrolysis. The MIP system consisted of the polymerisable amino acids functional monomers that were templated with phosphonate transition state analogue to form an MIP adduct, which was then incorporated in the hydrophilic acrylamide-based polymers. Compared to the background reaction as well as to the non-imprinted analogue (prepared without the phosphonate template), these materials displayed significantly enhanced hydrolytic rates.¹⁰¹

Further developments in this field led to the synthesis of soluble nanogel-based materials in 2006, which was described as highly homogeneous macromolecules, whose dimensions and molecular weight were measured to be close to those of natural enzymes.¹⁰² This discovery resulted in further progress in the area making nanogels more appealing candidates for imprinted catalysis. A number of such materials showed the ability to facilitate energetically demanding reactions, such as C-C bond formation.¹⁰³ One of the most successful examples include generation of the first aldolase type-I enzyme mimics.¹⁰⁴

Stable molecularly imprinted nanogels present interesting synthetic alternatives to natural enzymes and open new possibilities in the field of hydrolytic enzyme mimics. This can be attributed to the fact, that such non biological materials showed the possibility to reproduce not only enzyme's dimensions but also mimic the selectivity of the active sites. In particular, metal-based MIP nanogels offer great potential as one of the most interesting approaches to mimic natural enzymes.

1.5. Bibliography

1. a) F. Mancin, P. Scrimin and P. Tecilla, *Chem. Commun.*, 2012, **48**, 5545-5559; b) F. Mancin, P. Scrimin, P. Tecilla and U. Tonellato, *Chem. Commun.*, 2005, 2540-2548.
2. a) M. Diez-Castellnou, F. Mancin and P. Scrimin, *J. Am. Chem. Soc.*, 2014, **136**, 1158-1161; b) O. Iranzo, A. Y. Kovalevsky, J. R. Morrow and J. P. Richard, *J. Am. Chem. Soc.*, 2003, **125**, 1988-1993; c) A. Tamilselvi and G. Mugesh, *Chem. Eur. J.*, 2010, **16**, 8878-8890.
3. J. Emsley and D. Hall, *The Chemistry of Phosphorus*, Harper & Row, London, 1976.
4. S. C. L. Kamerlin and J. Wilkie, *Org. Biomol. Chem.*, 2007, **5**, 2098-2108.
5. R. F. Hudson, *Structure and Mechanism in Organophosphorus Chemistry*, Academic Press. Inc, London, 1965.
6. R. Jorge, PhD Thesis, Queen Mary University of London, 2011.
7. M. Burnworth, S. J. Rowan and C. Weder, *Chem. Eur. J.*, 2007, **13**, 7828-7836.
8. L. M. Eubanks, T. J. Dickerson and K. D. Janda, *Chem. Soc. Rev.*, 2007, **36**, 458-470.
9. H. S. Hewage, K. J. Wallace and E. V. Anslyn, *Chem. Commun.*, 2007, 3909-3911.
10. T. C. W. Convention, *Organisation for the Prohibition of Chemical Weapons* <https://www.opcw.org/protection/protection-against-chemical-weapons/>, visited August 2016
11. <http://www.us.gov.krd/aboutkurdistan/halabja-genocide/>, visited September 2016.
12. Y. Yang, J. A. Baker and J. R. Ward, *Chem. Rev.*, 1992, **92**, 1729-1743.
13. F. M. Raushel, *Curr. Opin. Microbiol.*, 2002, **5**, 288-295.
14. B. K. Singh and A. Walker, *FEMS Microbiol. Rev.*, 2006, **30**, 428-471.
15. A. A. Wang, W. Chen and A. Mulchandani, *Biotechnol. Bioeng.*, 2005, **91**, 379-386.
16. S. Yair, B. Ofer, E. Arik, S. Shai, R. Yossi, D. Tzvika and K. Amir, *Crit. Rev. Biotechnol.*, 2008, **28**, 265-275.
17. D. M. Munnecke, *Biotechnol. Bioeng.*, 1979, **21**, 2247-2261.
18. S. H. Chough, A. Mulchandani, P. Mulchandani, W. Chen, J. Wang and K. R. Rogers, *Electroanalysis*, 2002, **14**, 273-276.

19. N. Y. Liu, X. P. Cai, Y. Lei, Q. Zhang, M. B. Chan-Park, C. M. Li, W. Chen and A. Mulchandani, *Electroanalysis*, 2007, **19**, 616-619.
20. H. Yin, S. Ai, J. Xu, W. Shi and L. Zhu, *J. Electroanal. Chem.*, 2009, **637**, 21-27.
21. H. D. Lu, I. R. Wheeldon and S. Banta, *Protein Eng. Des. Sel.*, 2010, **23**, 559-566.
22. A. J. Russell, J. A. Berberich, G. E. Drevon and R. R. Koepsel, *Annu. Rev. Biomed. Eng.*, 2003, **5**, 1-27.
23. G. Aragay, F. Pino and A. Merkoçi, *Chem. Rev.*, 2012, **112**, 5317-5338.
24. F. Aguilar-Perez, P. Gomez-Tagle, E. Collad-Fregoso and A. K. Yatsimirsky, *Inorg. Chem.*, 2006, **45**, 9502-9517.
25. D. R. Edwards, C. T. Liu, G. E. Garret, A. A. Neverov and R. S. Brown, *J. Am. Chem. Soc.*, 2009, **131**, 13738- 13748.
26. K. M. Deck, T. A. Tseng and J. N. Burstyn, *Inorg. Chem.*, 2002, **41**, 669-677.
27. R. K. Totten, P. Ryan, B. Kang, S. J. Lee, L. J. Broadbelt, R. Q. Snurr, J. T. Hupp and S. T. Ngyen, *Chem. Commun.*, 2012, **48**, 4178-4180.
28. B. Kang, J. W. Kurutz, K. T. Youm, R. T. Totten, J. T. Hupp and S. T. Ngyen, *Chem. Sci.*, 2012, **3**, 1938-1944.
29. M. J. Katz, J. E. Mondloch, R. K. Totten, J. K. Park, S. T. Nguyen, O. K. Farha and J. T. Hupp, *Chem. Int. Ed.*, 2014, **53**, 497-501.
30. T. J. Bandoz, M. Laskoski, J. Mahle, G. Mogilevsky, G. W. Peterson, J. A. Rossin and G. W. Wagner, *J. Phys. Chem. C*, 2012, **116**, 11606-11614.
31. S. Moon, Y. Liu, J. T. Hupp and O. K. Farha, *Angew. Chem. Int. Ed.*, 2015, **54**, 6795-6799.
32. M. J. Katz, S. Moon, J. E. Mondloch, M. H. Beyzavi, C. J. Stephenson, J. T. Hupp and O. K. Farha, *Chem. Sci.*, 2015, **6**, 2286-2291.
33. M. Komiyama and J. Sumaoka, *Curr. Opin. Chem. Biol.*, 1998, **2**, 751-757.
34. M. Friedman and J. R. Knowles, *J. Am. Chem. Soc.*, 1985, **107**, 6126-6127.
35. N. Y. Chang and C. Lim, *J. Phys. Chem. A*, 1997, **101**, 8706-8713.
36. J. K. Bashkin, *Curr. Opin. Chem. Biol.*, 1999, **3**, 752-758.
37. J. Florian and A. Warshel, *J. Am. Chem. Soc.*, 1997, **119**, 5473-5474.
38. J. R. Cox and O. B. Ramsay, *Chem. Rev.*, 1964, **64**, 317-352.
39. K. A. Holbrook and L. Ouellet, *Can. J. Chem.*, 1958, **36**, 686-690.
40. D. E. Wilcox, *Chem. Rev.* 1996, **96**, 2435-2458.
41. R. Breslow and C. Schmuck, *J. Am. Chem. Soc.*, 1996, **118**, 6601-6605.

42. Q. Yang, J. Q. Xu, Y. S. Sun, Z. G. Li, Y. G. Li and X. H. Qian, *Bioorg. Med. Chem. Lett.*, 2006, **16**, 803-806.
43. S. R. Kirk and Y. Tor, *Chem. Commun.*, 1998, 147-148.
44. J. Chin, *Curr. Opin. Chem. Biol.*, 1997, **1**, 514-521.
45. R. R. Klinke and B. König, *J. Chem. Soc., Dalton Trans.*, 2002, 121-130.
46. S. J. Franklin, *Curr. Opin. Chem. Biol.*, 2001, **5**, 201-208.
47. J. Chin and M. Banaszczyk, *J. Am. Chem. Soc.*, 1989, **111**, 4103-4105.
48. J. A. Connolly, M. Banaszczyk, R. C. Hynes and J. Chin, *Inorg. Chem.*, 1994, **33**, 665-669.
49. J. Chin, *Acc. Chem. Res.*, 1991, **24**, 145-152.
50. J. Chin, M. Banaszczyk, V. Jubian and X. Zou, *J. Am. Chem. Soc.*, 1989, **111**, 186-190.
51. J. Chin and X. Zou, *J. Am. Chem. Soc.*, 1988, **110**, 223-225.
52. R. Hettich and H. Schneider, *J. Am. Chem. Soc.*, 1997, **119**, 5638-5647.
53. K. Hegetschweiler, D. Kuppert, J. Huppert, M. Stracka and M. Kaupp, *J. Am. Chem. Soc.*, 2004, **126**, 6728-6738.
54. J. Kim, *J. Korean Chem. Soc.*, 1998, **42**, 240-244.
55. D. A. Knight, J. B. Delehanty, E. R. Goldman, J. Bongard, F. Streich, L. W. Edwards and E. L. Chang, *Dalton Trans.*, 2004, **13**, 2006-2011.
56. F. Mancin and P. Tecilla, *New J. Chem.*, 2007, **31**, 800-817.
57. T. Koike and E. Kimura, *J. Am. Chem. Soc.*, 1991, **113**, 8935-8941.
58. L. Bonfa, M. Gatos, F. Mancin, P. Tecilla and U. Tonellato, *Inorg. Chem.*, 2003, **42**, 3943-3949.
59. M. Subat, K. Woinaroschy, C. Gerstl, B. Sarkar, W. Kaim and B. Köing, *Inorg. Chem.*, 2008, **47**, 4661-4668.
60. N. H. Williams, J. Cheung and J. Chin, *J. Am. Chem. Soc.*, 1998, **120**, 8079-8087.
61. L. Marchetti and M. Levine, *ACS Catal.*, 2011, **1**, 1090-1118.
62. A. A. Neverov, Z.-L. Lu, C. I. Maxwell, M. F. Mohamed, C. J. White, J. S. W. Tsang and R. S. Brown, *J. Am. Chem. Soc.*, 2006, **128**, 16398-16405.
63. C. T. Liu, A. A. Neverov and R. S. Brown, *J. Am. Chem. Soc.*, 2008, **130**, 13870-13872.
64. M. F. Mohamed, A. A. Neverov and R. S. Brown, *Inorg. Chem.*, 2009, **48**, 11425-11433.

65. M. Zhaoa, S. S. Xuea, X. Q. Jianga, L. Zhengb, L. N. Jia and Z. W. Mao, *J. Mol. Cat. A: Chem.*, 2015 **396**, 346–352.
66. A. Schiller, R. Scopelliti and K. Severin, *Dalton Trans.*, 2006, 3858–3867.
67. M. Resmini, *Anal. Bioanal. Chem.*, 2012, **402**, 3021–3026.
68. M. J. Whitecomb, C. Alexander and E. N. Vulfson, *Synlett.*, 2000, **6**, 911–923.
69. S. C. Zimmerman and N. G. Lemcoff, *Chem. Commun*, 2014, 5–14.
70. G. Wulff and K. Knorr, *Bioseparation*, 2002, **10**, 257–276.
71. F. H. Dickey, *Proc. Natl. Acad. Sci. U. S. A.*, 1949, **35**, 227–229.
72. G. Wulff and A. Sarhan, *Angew. Chem. Int. Edit.*, 1972, **11**, 341–343.
73. L. Andersson, B. Sellergren and K. Mosbach, *Tetrahedron Lett.*, 1984, **25**, 5211–5214.
74. K. Mosbach, *Sci. Am.*, 2006, **295**, 86–91.
75. O. Ramström and K. Mosbach, *Curr. Opin. Chem. Biol.*, 1999, **3**, 759–764.
76. J. N. Matsui, I. A. Karube and I. Mosbach, *J. Org. Chem.*, 1996, **61**, 5414.
77. X. C. Liu and K. Mosbach, *Macromol. Rapid Commun.*, 1998, **19**, 671–674.
78. K. Morihara, M. Kurokawa, Y. Kamata and T. Shimada, *J. Chem. Soc., Chem. Commun.*, 1992, 358–360.
79. B. Sellergren and K. J. Shea, *Tetrahedron Asymm.*, 1994, **5**, 1403–1406.
80. G. Wulff, T. Gross and R. Schonfeld, *Angew. Chem. Int. Ed. Engl.*, 1997, **36**, 1962–1964.
81. X.-C. Liu and K. Mosbach, *Macromol. Rapid Commun.*, 1997, **18**, 609–615.
82. S. Striegler, *J. Chromatogr. B*, 2004, **804**, 183–195.
83. K. Severin, *Curr. Opin. Chem. Biol.*, 2000, **4**, 710–714.
84. A. Jorge, M. Chernobryva, S. E. J. Rigby, M. Watkinson and M. Resmini, *Chem. Eur. J.*, 2016, **22**, 3764–3774.
85. A. G. Mayes and M. J. Whitcombe, *Adv. Drug Delivery. Rev.*, 2005, **57**, 1742–1778.
86. Y. Fujii, K. Matsutani and K. Kikuchi, *J. Chem. Soc., Chem. Commun.*, 1985, 415–417.
87. H. Kubo, T. N. Player, S. Shinoda, H. Tsukube, H. Nariai and T. Takeuchi, *Anal. Chim. Acta*, 2004, **504**, 137–140.
88. A. J. Moro, P. J. Cywinski, S. Korsten and G. J. Mohr, *Chem. Commun.*, 2010, **46**, 1085–1087.

89. A. L. Jenkins and S. Y. Bae, *Anal. Chim. Acta*, 2005, **542**, 32-37.
90. F. Locatelli, P. Gamez and M. Lemaire, *J. Mol. Catal. A: Chem.*, 1998, **135**, 89-98.
91. B. P. Santora, A. O. Larsen and M. R. Gagne, *Organometallics*, 1998, **17**, 3138-3140.
92. A. N. Cammidge, N. J. Baines and R. K. Bellingham, *Chem. Commun.*, 2001, 2588-2589.
93. J. F. Hull, E. L. O. Sauer, C. D. Incarvito, J. W. Faller, G. W. Brudvig and R. H. Crabtree, *Inorg. Chem.*, 2009, **48**, 488-495.
94. T. Y. Yamazaki, Z. Meng, K. Mosbach and K. Sode, *Anal. Chim. Acta*, 2001, **435**, 209-214.
95. M. Erdem, R. Say, A. Ersöz, A. Denizli and H. Türk, *React. Funct. Pol.*, 2010, **70**, 238-243.
96. R. Say, *Anal. Chim. Acta*, 2006, **579**, 74-80.
97. J. Liu and G. Wulff, *Angew. Chem. Int. Ed.*, 2004, **43**, 1287-1290.
98. M. Tada and Y. Iwasawa, *Coord. Chem. Rev.*, 2007, **251**, 2702-2716.
99. M. Tada and Y. Iwasawa, *J. Mol. Catal. A: Chem.*, 2003, **199**, 115.
100. A. Biffis, N. B. Graham, G. Siedlaczek, S. Stalberg and G. Wulff, *Macromol. Chem. Phys.*, 2001, **202**, 163-171.
101. S. C. Maddock, P. Pasetto and M. Resmini, *Chem. Commun.*, 2004, 536-537.
102. G. Wulff, B. Chong and U. Kolb, *Angew. Chem. Int. Ed.*, 2006, **45**, 2955-2958.
103. Z. Y. Chen, Z. D. Hua, J. Wang, Y. Guan, M. P. Zhao and Y. Z. Li, *Appl. Catal. A-Gen.*, 2007, **328**, 252-258.
104. D. Carboni, K. Flavin, A. Servant, V. Gouverneur and M. Resmini, *Chem. Eur. J.*, 2008, **14**, 7059-7065.

Chapter 2: Design and Synthesis of Macrocyclic Ligands with the View to Generate Small-Molecule Co(III) and Zn(II)-based Catalysts for Phosphate Ester Hydrolysis

2.1. Project Strategy: Introduction and Aims

The central focus of this project was the development of a number of artificial metal-based catalysts for phosphate ester hydrolysis. The major effort in this work was directed towards the enhancement of their hydrolytic efficiency through a) the use of the molecular imprinting (MIP) technique in nanogels and b) modification of the structural design of such small-molecule complexes. The first key requirement for this project was careful selection of the basic catalytic unit. The rationale behind the choice of such basic metal-ligand unit combined with the use of the molecular imprinting technique to prepare metal-containing polymers that could act as biomimetic enzyme-like catalysts, is described below. Subsequently, the aims of the second part of the project, which focuses on the structural design of the catalyst, are depicted.

2.1.1. Part One: Co(III)-based MIP Nanogels as Catalysts for Phosphate Ester Hydrolysis

2.1.1.1. Choice of the Basic Catalytic Unit

The choice of the basic catalytic unit **16** presented in Figure 2.1 was not only guided by the promising literature precedent¹⁻⁷ but was also based on the expertise developed in the Watkinson and Resmini groups in the synthesis and coordination chemistry of Co(III) complexes of the type *cis*-[Co(N₄)(X)(Y)]ⁿ⁺, where N₄ is a macrocyclic tetraamine ligand, such as cyclen.^{8,9} Such tetraamine Co(III) complexes are extensively used as phosphatase models by other research groups and remain one of the most active mimetic systems for phosphate ester hydrolysis.^{1,2,10} Various examples of azamacrocyclic Co(III) complexes as attractive candidates for phosphate ester hydrolysis have already been presented in Chapter 1, see section 1.3.3.2.2.^{4,7,11-13}

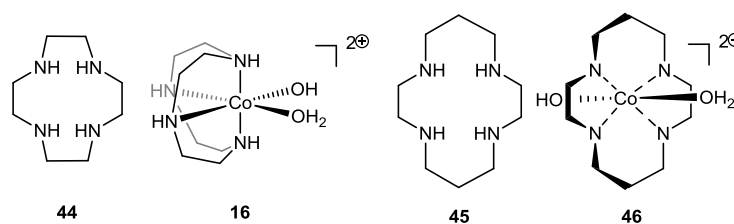


Figure 2.1- Structures of the tetraamine cyclen and cyclam ligands **44** and **45** respectively and their corresponding Co(III) complexes **16** and **46**.^{6,14}

In particular, the $[\text{Co}(\text{cyclen})(\text{OH}_2)\text{OH}]^{2+}$ catalytic unit presents a number of advantageous features for the development of artificial phosphatases. Firstly, not only do macrocyclic tetraamine ligands have a remarkable ability to coordinate metal ions, but due to the variety of the size of the macrocyclic cavity they are also able to regulate the coordination environment of the metal, which is very beneficial in the preparation of the metal complexes.^{6,15} For example, complexation between rigid cyclen **44** (Figure 2.1) and the Co(III) metal ion only results in a *cis*-configuration in the geometry at the central cation, which is an essential feature for high hydrolytic efficiency. In contrast, Co(III) *trans*-complexes of the cyclam derivative **45** (Figure 2.1) are inactive, as the aqua-hydroxo ligands that take part in ester hydrolysis are not in close proximity.^{4,6} Among the various transition metals (e.g. Cu(II) and Ni(II)) that are also used for such tetraamine-based systems, Co(III) is frequently utilised for the hydrolysis of phosphate esters.¹⁰ One of the reasons for this is the kinetic inertness of the Co(III) cation that results in exchange of the two substitutionally active ligands in *cis*-positions at a relatively slow rate with $K_{\text{ex}} = 12 \text{ s}^{-1}$ measured for the aqua-hydroxo cyclen-based Co(III) complex, which is known to be advantageous for mechanistic studies.¹⁶ Additionally, no competitive oxidative mechanisms have been observed for Co(III) promoted phosphate ester hydrolysis (compared with Cu(II) for example), which further simplifies mechanistic studies.¹⁰ Also, cobalt presents a less toxic alternative compared to Cu(II) and Ni(II), which adds another benefit to the metal. In addition and most importantly, **16** was established by Chin *et al.* as one of the most active mimetic systems for phosphate ester hydrolysis, showing rate enhancements of up to 10^7 in the hydrolysis of BNPP.⁶ Work by other groups has also demonstrated that the dinuclear functionalised derivative of **16** can facilitate hydrolysis of supercoiled DNA 10 million times faster compared to the uncatalysed reaction.¹⁷

However, the substitutional inertness of the Co(III) cation is, on the other hand, a major disadvantage for such complexes when used as phosphatase mimics, because it results in

Chemical reaction scheme showing the synthesis of macrocyclic phosphonate **47** from macrocyclic cobalt complex **16** and 4-nitrophenyl phosphonic acid **7**. The reaction proceeds via a two-step mechanism:

- Coordination of the cobalt center to the phosphonate group of **7**, forming a five-membered ring intermediate.
- Intramolecular nucleophilic attack of the macrocyclic ligand's terminal hydroxyl group on the phosphorus atom, displacing the phenoxide group.

The final products are macrocyclic phosphonate **47** and 4-nitrophenoxide **6**.

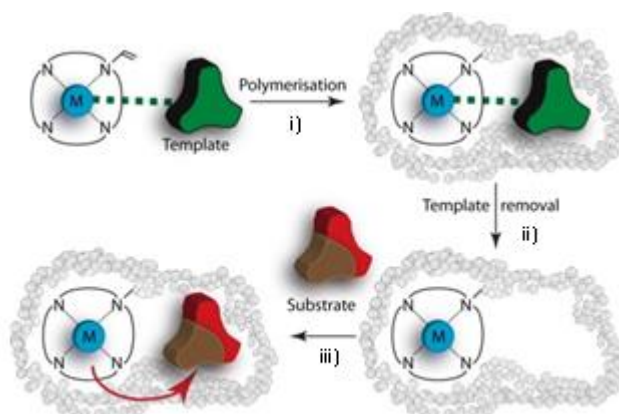
Although it is known that rational design of the ligand system is crucial for the catalytic efficiency gain, it was recently discovered that placing such small-molecule complexes in a low polarity environment (including lower polarity solvent, such as MeOH and EtOH as well as larger supramolecular structures), that closely mimic the dielectric environment of the active sites of enzymes, results in high catalytic activity and turnover with reduced catalytic load.^{20,21} This phenomenon is supported by a number of studies discussed in Chapter 1, section 1.3.3.2.5. Preliminary work carried out in the Watkinson and Resmini groups demonstrated that a Co(III)-cyclen complex with ligands incorporating polymerisable units can form an imprinted nanogel particle once polymerisation has taken place, using the molecular imprinting technique. The nanogel matrix particles formed supported the Co(III)-cyclen units and afforded an increased phosphate hydrolysis reaction turnover, even with a low catalytic load.⁸

67

approach in catalysis of phosphate ester hydrolysis. The main features of the molecular imprinting technique are described below.

2.1.1.2. Use of the Molecular Imprinting Methodology

The molecular imprinting technique has great potential in providing a novel tool in the area of enzyme mimics. It offers a possibility to mimic the structure of enzymes (Chapter 1, section 1.3.2), by forming a polymeric particle with the embedded metal-ligand complex, thereby leading to the generation of catalysts with high efficiency.²⁸ This methodology involves a number of key steps. The first is the assembly of the molecular imprinting (MIP) adduct, which requires the synthesis of the polymerisable derivative of the basic catalytic unit **16** and its subsequent complexation with the strategically chosen template. The second step requires the incorporation of this MIP adduct into the nanogel polymer matrix, which is followed by the removal of the template.²⁹ This results in the generation of catalytically active Co(III)-based nanogels with the free three-dimensional cavity inside the polymer that can be used for the hydrolysis of phosphate ester substrates and is illustrated in Scheme 2.2.⁹



Scheme 2.2- Overall design of the metal-based MIP catalyst for phosphate ester hydrolysis, which consists of the following steps: i) coordination of the polymerisable tetraamine-based metal complex to the template (substrate analogue) to form an imprinting adduct; ii) formation of the metal-based nanogel; iii) removal of the template and generation of the three-dimensional cavity, complementary in size and shape to the template, which results in the generation of the catalytic MIP.

The reasons behind the selection of certain units that comprise the MIP adduct are explained below:

i) Choice of the polymerisable derivative

The choice of the polymerisable unit that allows the incorporation of the metal complex into the nanogel was based on previous findings by Watkinson and Resmini *et al.* It was

demonstrated that in a study of several polymerisable Co(III) complexes, the styrene-functionalised complex **48** (Figure 2.2) showed the most efficient incorporation, and hence resulted in higher polymerisation yields.^{8,9}

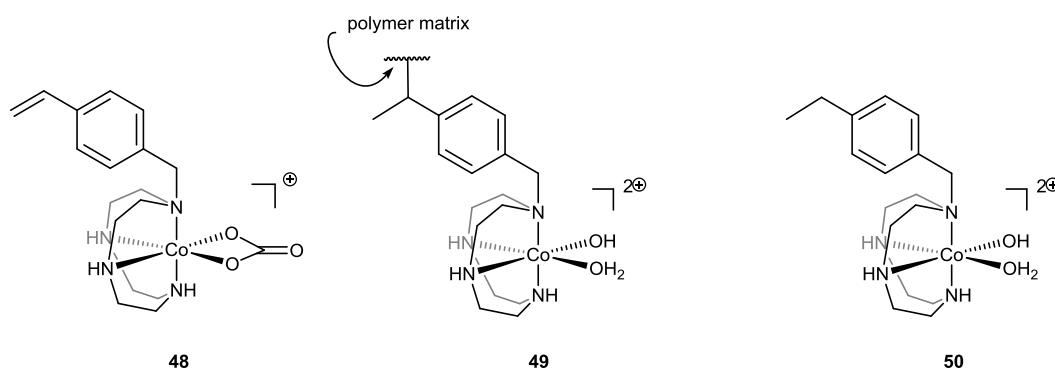


Figure 2.2- Structures of the polymerisable carbonate Co(III) complex **48**, **48** integrated into the polymer matrix to form **49**, and **50**- the non-polymerisable analogue of **48**.^{8,9}

However, it was previously reported by Knight *et al.* that alkylation at a single nitrogen atom of Co (III) cyclen complexes resulted in a 25% reduction in activity.¹¹ Therefore, it was decided to synthesise the structurally similar non-polymerisable analogue **50** (Figure 2.2), which can act as a mimic of the active site within the nanogel. Once incorporated into the nanogel by radical polymerisation, the terminal double bond on the alkyl chain of **48** is converted into a single bond to form **49**. Thus, metal complex integrated into the polymer becomes structurally analogous to the non-integrated complex **50**,⁸ which allows more accurate investigation of the effect of incorporation of the complex into the nanogel polymer on the phosphatase activity of this metal complex.

ii) Choice of the target templates and the substrate

It was shown previously by Watkinson and Resmini that the strategic choice of templates is crucial for the molecular imprinting strategy. Their preliminary studies demonstrated that the nature of the template affects the oxidation state and the coordination geometry around the metal ion, which in turn influences both the recognition properties and catalytic activity of the molecular imprinted nanogels.⁸ Templates are chosen according to several characteristics. For example, they should be structurally similar to the substrate and provide stable interactions with the metal complex (e.g. the MIP adduct needs to withstand polymerisation conditions at 70°C).

It was decided to continue using the previously employed templates phosphonate **51** and carbonate **52** (Figure 2.3). The phosphonate template **51** is a cognate template and was

chosen because of its structural similarity to substrate **7**, whereas the carbonate template **52** (is structurally unrelated to the substrate) and does not resemble the substrate structure and is known to coordinate metal ion in the bidentate manner. For this reason **52** was deemed to be an attractive candidate for the catalytic studies using the MIP approach, as it could be used as an analogue of the non-imprinted polymer required for the reference in the study of NPP hydrolysis.^{8,9}

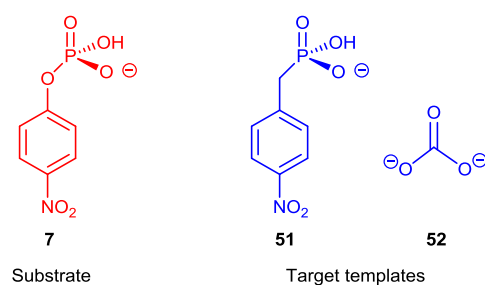
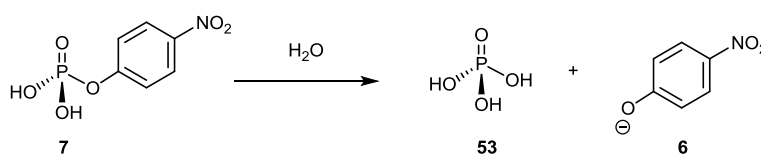


Figure 2.3- Structures of the substrate *p*-nitrophenyl phosphate (NPP) **7** and target templates: *p*-nitrophenyl phosphonate **51** and carbonate **52**.^{8,9}

In the field of enzyme mimics for phosphate ester hydrolysis, the substrate NPP (*p*-nitrophenyl phosphate) **7** is most frequently used by a wide range of researchers as it provides benefits for mechanistic studies, which are outlined in Chapter 3, section 3.1.1.³⁰ **7** was also previously used in the Watkinson and Resmini groups as a good model substrate for nerve agent hydrolysis.⁸ Therefore, the hydrolytic studies were focused on the hydrolysis of **7**, which produces the highly chromophoric and bright yellow *p*-nitrophenolate unit **6** during the hydrolysis reaction, allowing its progress to be monitored by UV-Vis spectroscopy (Scheme 2.3).^{30,31}



Scheme 2.3- Spontaneous hydrolysis of **7** to give phosphoric acid **53** and *p*-nitrophenolate **6**.

2.1.2. Part Two: Development of the Small-Molecule Metal Complexes for the Phosphate Ester Hydrolysis

The second objective of this study was to systematically investigate the effect of the structural modification of the cyclen ligand backbone on the hydrolytic activity of its metal complexes towards phosphate ester cleavage. Additionally, click-based tripodal ligands

were used to prepare a range of their d-block metal complexes as potential catalysts for phosphate ester hydrolysis and are presented in Chapter 4.

2.1.2.1. Cyclen-based Metal Complexes

Given the numerous literature reports that emphasise the importance of the tetraamine ligand structure on the hydrolytic activity of the corresponding Co(III) complexes as phosphatase models (Chapter 1 section 1.3.3.2.2), in this work it was planned to extend the library of cyclen-based Co(III) complexes by preparing their structurally modified derivatives presented in Figure 2.4, with a view to investigate the effect of ligand structure on the catalytic efficiency of the cobalt complex. The rationale behind the choice of these structural modifications will be extensively discussed in the following sections of this chapter.

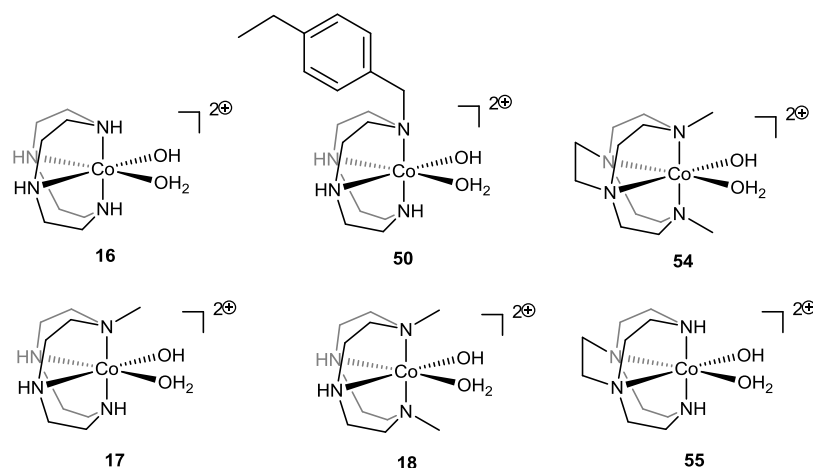
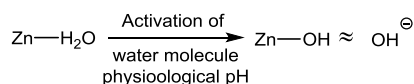


Figure 2.4- Structures of the target cyclen-based Co(III) complexes.

Although tetraamine Co(III) complexes are amongst the most frequently used to investigate phosphate ester hydrolysis reactions, the role of other metal ions should not be underestimated in P-O cleavage. There is an increasing number of reports where macrocyclic Zn(II) complexes are extensively studied as phosphatase models and show catalytic activity in hydrolysing certain phosphates, such as BNPP.^{32,33} The effect of the structure of such complexes on their hydrolytic efficiency is also widely investigated (Chapter 1, section 1.3.3.2.3). It is known that unlike Co(III) ion, Zn(II) is not substitutionally inert and is able to exchange ligands rapidly, which prevents the formation of the four-membered chelate **47**³⁴ (Scheme 2.1), which hampers the activity of the complex. Moreover, not only is Zn(II) known to form thermodynamically stable complexes, but it is also able to activate water molecules, which leads to the generation of the 'Zn-OH'

nucleophile at physiological pH, as shown in Scheme 2.4.³⁵ Furthermore, the Zn(II) cation is present in the active site of many naturally occurring phosphatases³² and possesses moderate Lewis acidity. The redox inertness of the Zn(II) ion, which possesses a full d¹⁰ configuration, also rules out the competitive oxidative cleavage of P-O bond.³⁴ Thus, considering these characteristics Zn(II)-based complexes are ideal candidates for the study of hydrolytic catalysis.



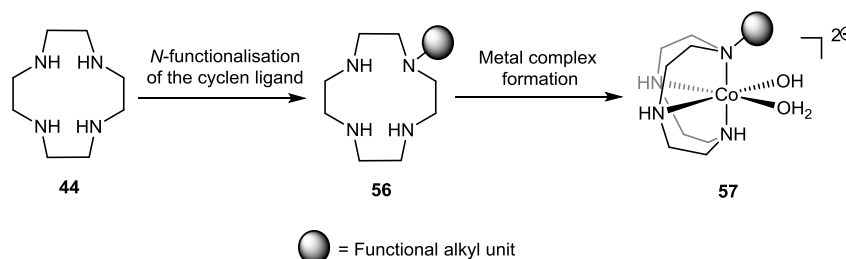
Scheme 2.4- Activation of water molecule by Zn(II) cation (charges omitted) to generate hydroxide nucleophile at physiological pH.³⁵

Nevertheless, according to literature data, Zn(II) complexes show lower rate accelerations in phosphate ester hydrolysis compared with the other commonly employed metal ions, such as Cu(II), Co(III) and Ni(II).³⁴ Therefore, another objective was to prepare analogous cyclen-based Zn(II) complexes in order to investigate the effect of the metal ion on the catalytic hydrolysis of phosphate esters in such complexes. The proposed mechanistic details and other features of Zn(II)-based catalysed hydrolysis of phosphate esters will be more extensively discussed in Chapter 3.

The following sections of this chapter will present the design, synthesis and full characterisation of the small-molecule cyclen-based Co(III) complexes.

2.2. Introduction to the Synthesis of the Functionalised Tetraamine Ligands

Generic diagram for the synthesis of *N*-functionalised azamacrocyclic Co(III) and Zn(II) complexes is shown in the Scheme 2.5.



Scheme 2.5- Generic scheme for the synthesis of the *N*-functionalised cyclen-based Co(III) complexes, that involves incorporation of the alkyl unit onto the cyclen ligand 44 (this figure represents alkylation only on one nitrogen atom, but one to all four nitrogen atoms on cyclen can be functionalised, which will be shown later) and subsequent formation of the metal complex.

The first step in this process is the synthesis of *N*-alkylated cyclen derivatives followed by their complexation with the metal ion. Overall, the chemistry of azamacrocycles is very versatile due to their remarkable ability to coordinate metal ions. Consequently, the design and synthesis of *N*-alkylated tetraamines continues to be of great interest due to the broad range of biomedical applications of their complexes. For example, cyclen is a key intermediate in the synthesis of medical imaging agents, such as MRI and PET contrast agents, fluorescent probes and metal recovery agents.³⁶ Additionally, it is used in anti-cancer³⁷ and anti-HIV drug development³⁸ in the pharmaceutical field. The following section will depict the main methods used by researchers to achieve the synthesis of functional cyclen-based derivatives.

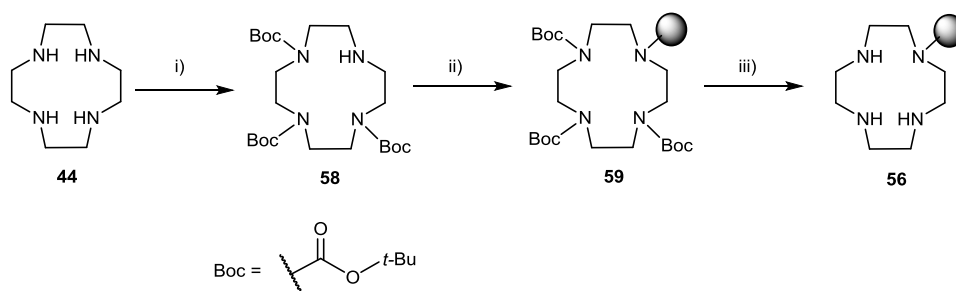
2.2.1 Methods for Generation of *N*-functionalised Macrocyclic Ligands

There are three main methodologies established for the selective *N*-alkylation of cyclen:³⁹

- i. synthesis from acyclic precursors;
- ii. selective alkylation through *N*-acylated precursors;
- iii. selective alkylation through tetracyclic intermediates.

Methods involving acyclic precursors are only employed in cases when *C*-functionalisation (on the ethylene bridges between nitrogen atoms) is required instead of *N*-alkylation. A major disadvantage of this strategy is that a new synthetic route has to be designed with each different alkyl chain, which results in extremely time consuming synthesis as well as low yields of the target compounds. Thus, this method is rarely used nowadays.

The other two approaches: alkylation through the *N*-acylated precursor and *N*-functionalisation *via* tetracyclic intermediates have received much more interest and remain among the most frequently used methods for macrocycle functionalisation. The second method was previously utilised by Watkinson *et al.*²⁴ This 'classical' protection method is depicted in Scheme 2.6 below and involves acylation of cyclen on the three nitrogen atoms with Boc protecting groups, which is followed by the selective mono-alkylation with the target alkyl group on the remaining nitrogen and subsequent removal of the Boc protecting groups. This approach is also time-consuming as it requires laborious purification procedures by column chromatography that can lead to low yields of the target products. Therefore, this route was not initially chosen in this project.



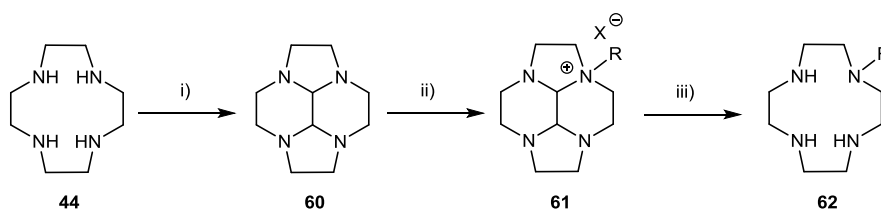
Scheme 2.6- Generic synthetic scheme for the *N*-functionalisation of cyclen 44 *via* Boc route: i) protection of the three cyclen nitrogens, ii) alkylation of the remaining free nitrogen with the target alkyl unit and iii) removal of the protecting Boc groups to give *N*-functionalised cyclen 56.²⁴

The last method, which is depicted in Scheme 2.5, is known to be one of the most efficient to obtain *N*-functionalised azamacrocycles. It requires the synthesis of the tetracyclic bisaminal intermediate, which allows selective mono- and di-*N*-alkylation and is then followed by the removal of the bisaminal bridge providing access to *N*-functionalised macrocycles.⁴⁰ Based on the available expertise in the group in utilising this route,⁸ it was decided to use it for the target ligand synthesis in this project.

2.3. Results and Discussion

2.3.1. Synthesis of the Non-bridged Mono- and Di-alkylated Cyclen-based Derivatives

The first objective was to prepare selectively *N*-functionalised cyclen derivatives and a generic strategy towards such ligands *via* bisaminal **60** is depicted in Scheme 2.7.



Scheme 2.7- General strategy towards *N*-functionalisation of cyclen *via* bisaminal 60: i) formation of the tetracyclic intermediate X; ii) mono- (or di-alkylation- shown later) of 60; iii) removal of bisaminal bridge.³⁶

The efficient bisaminal synthesis, which was first developed by Weisman *et al.*, was chosen⁴⁰ as this methodology has proven to be very efficient when applied by the Watkinson and Resmini research groups, and has allowed new target products to be prepared in high yields and short times, without laborious purification procedures, such as column chromatography.^{8,9} Overall, this synthetic route begins with the preparation of the tetracyclic bisaminal intermediate **60**. The different basicity of the four nitrogen atoms in the bisaminal then allows selective *N*-alkylation of cyclen with an appropriate electrophile, such as an alkyl or aryl halide, leading to the formation of mono- or di-alkylated quaternary ammonium salts. These salts are subsequently deprotected by hydrolysing the aminal bridge leading to selectively *N*-alkylated macrocycles with the ‘free’ cyclen cavity.^{36,41}

The first step of this methodology - synthesis of tetracyclic bisaminal intermediate **60**, involves a condensation reaction of cyclen **44** with glyoxal.⁴² This intermediate presented in Figure 2.5 possesses a folded *cis*-configuration, which results in different reactivity of the opposing nitrogen pairs. The two nitrogens whose lone pairs point out from the convex site of the structure (the *exo* nitrogens) possess greater nucleophilicity than the other pair.⁴³

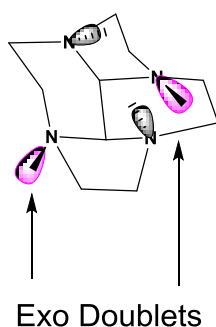
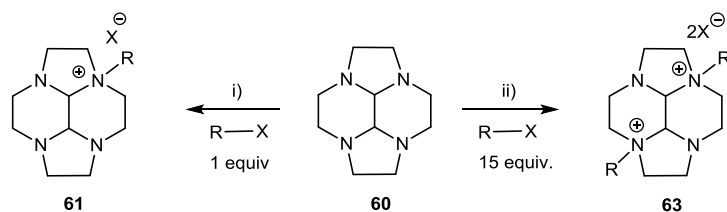


Figure 2.5- Molecular structure of bisaminal 60.⁴³

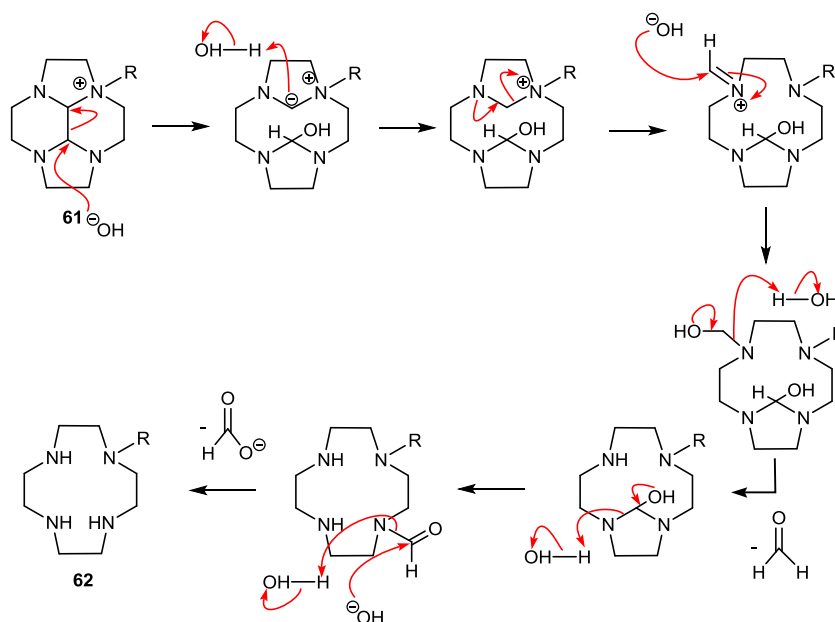
Therefore, this tetracyclic intermediate can be selectively mono- and di-alkylated on these nitrogens. The key feature of this process is the precipitation of the mono- and di-alkylated quaternary ammonium salts from the reaction solvent chosen; mono-alkylation occurring

in toluene and di-alkylation in MeCN.⁴¹ The number of equivalents of the target electrophile is also important: one equivalent is required to obtain the mono-alkylated products whereas 15 equivalents of the electrophile are needed for the formation of a di-alkylated derivative (Scheme 2.8). The resulting precipitated solids that form under these conditions can then be isolated by a simple Büchner filtration in good to excellent yields, typically 83-98%. Very recently, Archibald *et al.*⁴⁴ reported that quaternary ammonium bisaminal salts can be prepared by mechanochemical alkylation, which involves grinding bisaminal intermediate with stoichiometric amounts (instead of large excesses in the case of di-alkylation) of an appropriate electrophile in the presence of small amount of MeCN, whilst also significantly reducing reaction times from 16 hours (required for the synthesis in solution) to only 30 minutes. However, this procedure was not attempted as all target compounds were already prepared in sufficient amounts at the time of its publication.



Scheme 2.8- General scheme for the formation of mono- and di-*N*-alkylated bisaminal intermediates: i) R-X (1 equiv.), toluene, RT, 16 h, under N₂; ii) R-X (15 equiv.), MeCN, RT, 16 h, under N₂.⁴¹

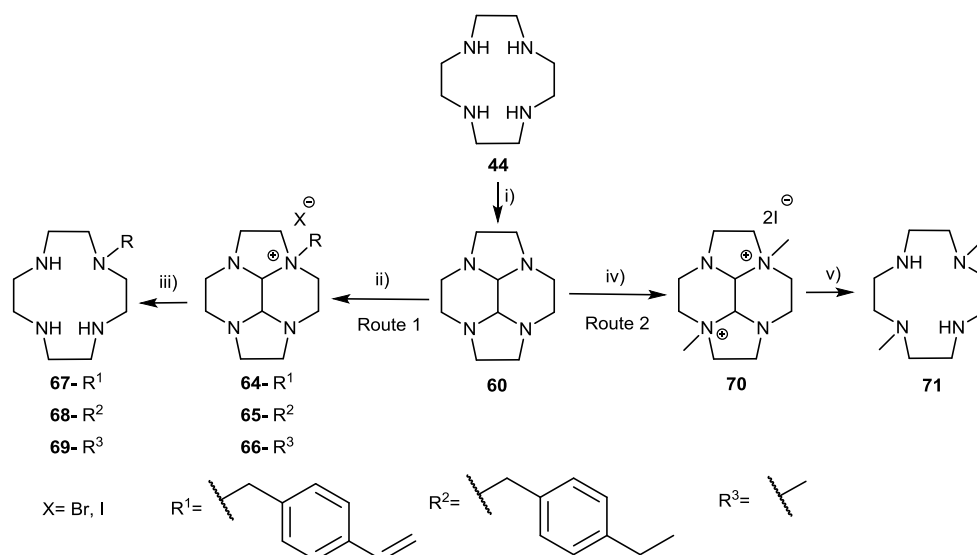
The final synthetic step requires basic hydrolysis of the bisaminal. To the best of our knowledge, no validated mechanism for this reaction has yet been reported. Baker *et al.*³⁶ have proposed a mechanism shown in Scheme 2.9, which starts with a hydroxide nucleophile attacking one of the carbons on the ethylene bridge, resulting in the rate-determining formation of ylide. Subsequent loss of formaldehyde and formate fragments then leads to the formation of the deprotected cyclen ligand. The *N*-alkylated quaternary ammonium salts thus formed are then easily deprotected with EtOH solution of hydroxylamine (NH₂OH).



Scheme 2.9- Mechanism of the bisaminal hydrolysis proposed by Baker and co-workers.³⁶

However, this last step is often the most challenging and our group has previously found that the structure of the electrophile used and the number of nitrogen atoms alkylated (mono- or di-alkylation) can significantly affect the purity of the isolated product as well as the yields of the reaction.⁸ This observation was confirmed in the work presented here. Nonetheless, as this synthetic methodology offers the opportunity to introduce various alkyl groups into the cyclen moiety, it was considered as the best starting point of the ligand synthesis.

The synthetic route for the preparation of the desired ligands **67**, **68**, **69** and **71** is depicted in Scheme 2.10.

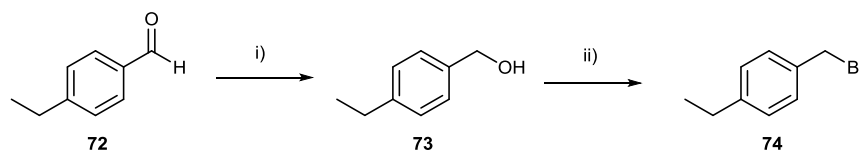


Scheme 2.10- Synthetic route for the target 'free' *N*-functionalised cyclen ligands. Conditions: i) Glyoxal (0°C), MeOH, RT, 95%; ii) 64-*R*¹ *p*-vinylbenzyl chloride (1 equiv.), 65-*R*² *p*-ethylbenzyl bromide (1 equiv.) or 66-*R*³ methyl iodide (1 equiv.), toluene, 16 h, RT; 64-*R*¹ = 95%, 65-*R*² = 91%; 66-*R*³ = 94%; iv) methyl iodide (15 equiv.), MeCN, 16 h, RT, yield 98%; iii) and v) NH₂OH (aq), EtOH, 45°C, 20 h; 67-*R*¹ = 20%, 68-*R*² = 18%, 69-*R*³ = 37%, 71 = 87%.

In the first step, the tetracyclic bisaminal intermediate **60** was synthesised by condensation of glyoxal with cyclen in MeOH at room temperature. It was previously found in our group⁹ that if the addition of the aqueous glyoxal solution into the MeOH cyclen solution was carried out at low temperature (0°C) the target bisaminal is formed in almost quantitative yield. Following this procedure, **60** was isolated simply by removal of the solvent and trituration of the crude mixture with Et₂O several times; the ethereal fractions were then combined and reduced to dryness affording **60** as a white hygroscopic solid in 95% yield.

Initially, the focus was on the synthesis of **67**, referred to as the polymerisable cyclen derivative, which was previously prepared in our group (albeit in an impure state),⁸ with the view to improve its purity. As shown in Scheme 2.10, commercially available *p*-vinylbenzyl chloride was used to alkylate bisaminal **60** in toluene, which resulted in the isolation of the monoquaternary salt **64** in 95% yield. Subsequent hydrolysis of **64** using an EtOH solution of aqueous NH₂OH, followed by 10% KOH (w/v) was undertaken as reported⁴¹ and gave the crude product in 65% yield, which required further purification. A standard purification procedure for such ligands involving the formation of its hydrochloride salt, basification and extraction with CHCl₃ was carried out and resulted in the isolation of the pure **67** in a disappointingly low yield of 20%, most probably due to the product decomposition under the harsh conditions used.⁴⁵ Nonetheless, pure ligand **67** was then taken forward for the synthesis of the corresponding Co(III) complex.

The second step was to prepare the non-polymerisable analogue of **67**. *p*-Ethylbenzyl bromide was identified as an ideal electrophile for the alkylation of the bisaminal.



Scheme 2.11- Synthesis of the *p*-ethylbenzyl bromide **74**. Conditions: i) NaBH₄, MeOH, 1h, RT, 82%; ii) PBr₃ (0°C), 1h, RT, 78%.⁴⁶

Initially, various routes were attempted towards the preparation of the desired alkyl halide, including modification of the alcohol and aldehyde groups. Firstly, direct chlorination of the commercially available *p*-ethylbenzyl alcohol **73** was attempted using concentrated HCl.⁴⁶ However, the desired *p*-ethylbenzyl chloride was obtained in a very low yield due to multiple side products being formed, which in turn resulted in complicated purification process. Thus, considering the prohibitively high cost of **73**, this synthetic route was deemed to be inefficient and was abandoned. Therefore, another procedure towards more reactive *p*-ethylbenzyl bromide electrophile **74** was chosen,⁴⁶ which first required the conversion of the commercially available **72** into **73** and subsequent conversion to **74** (Scheme 2.11). Using this procedure, **72** was successfully converted into **73** in good yield. Moreover, it was found that direct bromination of **73** without any solvent resulted in the synthesis of pure **74**, which did not require any further purification. This was used in the synthesis of **65** as shown in Scheme 2.10 and resulted in the immediate precipitation of target **65**. In order to obtain the maximum yield, the reaction mixture was stirred for 20 hours and the target product was then isolated by suction filtration as a white powder that did not require further purification in excellent yield. Mono-alkylation of **60** results in the loss of symmetry and a very complex ¹H NMR spectra, as has been previously reported.^{41,47} However, **65** can be easily identified by two identical doublets that appear in its ¹H NMR spectra, as illustrated in Figure 2.6. Each doublet integrates to one proton and corresponds to one of the protons on the ethylene bisaminal bridge carbons.⁴⁷

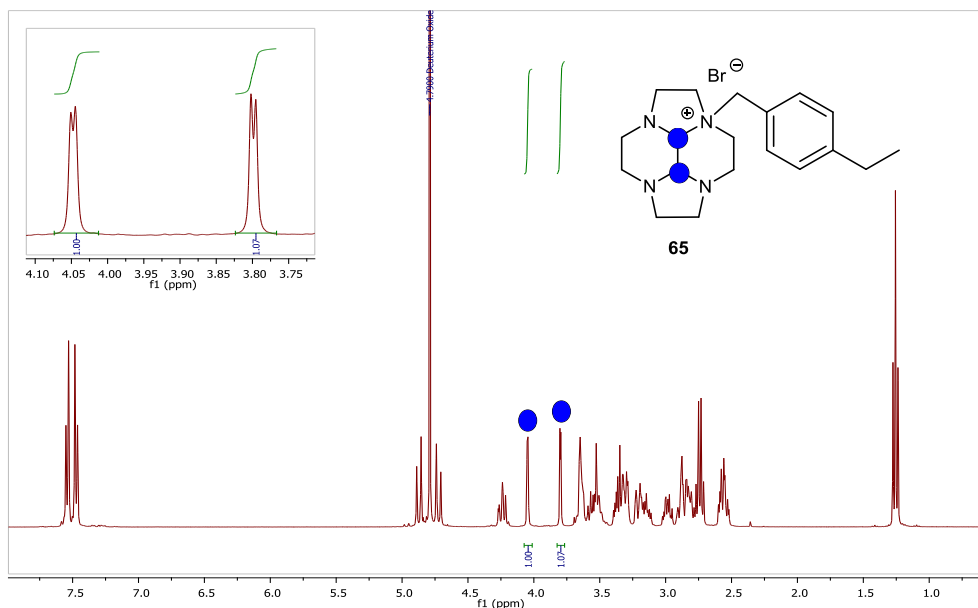


Figure 2.6- ^1H NMR spectrum of pure **65** in D_2O . Insert: Enlarged part of this spectrum with the two doublets corresponding to the two protons on the bisaminal bridge carbons highlighted with blue circles.

The subsequent deprotection of **65** to afford the target cyclen derivative **68**, proved to be rather more challenging than in the case of its polymerisable derivative **67** and also required additional purification procedures that consequently resulted in a low overall yield. Hydrolysis of **65** using an EtOH solution of aqueous NH_2OH was undertaken as reported. However, isolation of **68** using a common work-up method that involves basifying the reaction mixture with 10% KOH (w/v) and extracting the resulting aqueous layer with DCM, resulted in the isolation of very impure **68** and this method was deemed unsuitable for its isolation. Hence, an acid-base work up was employed. The crude product obtained in 62% yield was first converted to its hydrochloride salt, which was isolated. The salt was then basified and extracted with CHCl_3 , which resulted in the isolation of the pure ligand **68**, but only in 18% yield, presumably because of decomposition of the product under the harsh conditions used, as in the case with its polymerisable analogue **67**. Nevertheless, a sufficient amount of this ligand was obtained to form the required Co(III) and Zn(II) complexes.

Mono-methyl bisaminal salt **66** was prepared in a similar way to the reported protocol using iodomethane in 94% yield.⁴¹ Conversion of **66** to **69** was again performed as shown in Scheme 2.10, however, both basic work-up with 10% KOH and the acid-base work-up method developed for **68** resulted in the isolation of impure **69**, which in both cases

contained the same unknown species; this was also reported by Baker *et al.*³⁶ Therefore **69** was converted to its hydrochloride salt which was recrystallised in water and EtOH³⁶ giving much purer material, however, some impurities remained. Therefore, a second round of this purification step was performed to remove these impurities. Unsurprisingly, these extra purification steps resulted in a low yield of 37% of the *N*-functionalised ligand **69**.

For the preparation of ligand **71**, alkylation of **60** with an excess of methyl iodide in MeCN resulted in the precipitation of **70** as a white solid that was collected in 98% yield.⁴¹ As the di-alkylated bisaminal is symmetrical, its ¹H NMR spectrum is much less complicated than those of mono-alkylated analogues and shows a characteristic singlet at 4.5 ppm corresponding to the protons on the ethylene bridge (Figure 2.7).

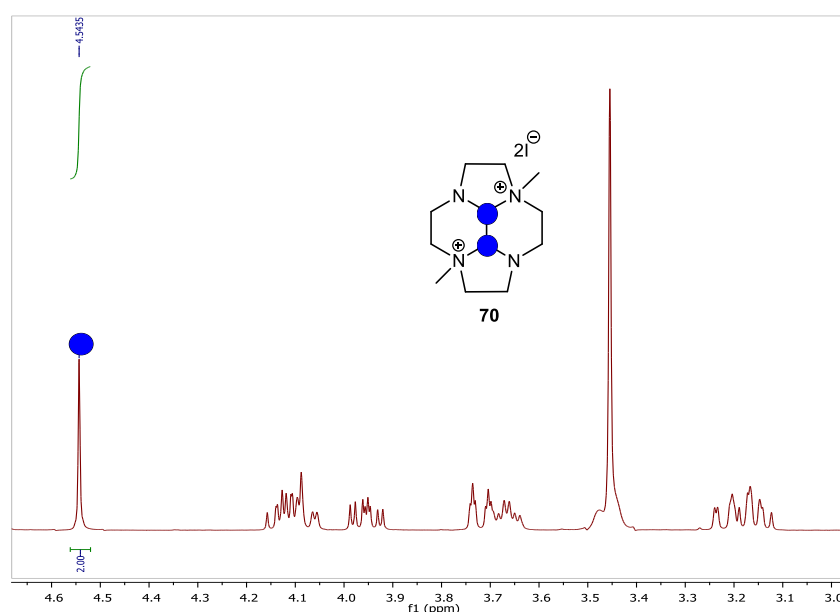


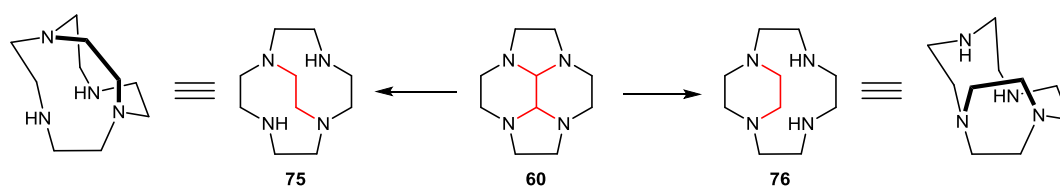
Figure 2.7- ¹H NMR spectrum of the pure di-methylated bisaminal **70**.

In this case, the deprotection step proceeded cleanly without any complications and the need for further purification procedures. Simple hydrolysis of the ethylene bridge with NH₂OH followed by acid-base work up afforded pure product **71** in 87% yield.

2.3.2. Introduction to Ethylene-bridged Azamacrocycles: Special Characteristics

In the previous section it was explained that an efficient bisaminal synthetic route can be used to selectively obtain *N*-alkylated ligands with the ‘free’ or non-bridged macrocyclic cavity, which is achieved by a complete removal of the bisaminal bridge from the *N*-alkylated quaternary ammonium salts using an EtOH solution of aqueous NH₂OH. The modification and extension of this bisaminal synthetic pathway allows the synthesis of

bridged macrocycles by introducing the internal ethylene bridge between nonadjacent nitrogen atoms (cross-bridge as in **75**) or between adjacent ones (side-bridge as in **76**) in the macrocyclic backbone.⁴⁸ Molecular structures and proposed conformations of the cross- and side-bridged cyclen units are shown in Scheme 2.12 below. Weisman, Wong and collaborators were first to report cross-bridging of polyazacycloalkanes using bisaminal chemistry.⁴⁹ Later, Kolinsky adopted this methodology to prepare side-bridged macrocycles.⁴⁸



Scheme 2.12- Cyclen bisaminal 60 and its cross- and side-bridged derivatives 75 and 76 respectively. Proposed conformations of 75 and 76.⁴⁸

N-Functionalised bridged macrocyclic derivatives continue to attract a significant amount of interest for a number of reasons. It was discovered, that modification of the macrocycle topology by linking two nitrogens of the parent ligand with an ethylene bridge imparts interesting characteristics, including their coordination behaviour, electrochemical properties and basicity.

Firstly, an internal two-carbon bridge in the macrocyclic moiety introduces further strain and rigidity into the ligand backbone, which makes bridged derivatives more configurationally restricted compared to their unbridged analogues.¹⁵ As a consequence, structurally reinforced cross-bridged bicyclic tetraamines adopt a locked conformation with all four nitrogen lone pairs pointing inside the ligand cavity. This conformation leads to formation of more kinetically stable metal complexes, as the bridge also reinforces a better alignment between nitrogen lone pairs and metal d-orbitals, as illustrated in Figure 2.8. This prevents dissociation of the metal cation from the ligand cavity, even under harsh acidic conditions. Hence, the increased kinetic stability of their metal complexes makes bridged ligands preferred candidates for metal chelation in a number of applications including biomimicry, bioimaging and catalysis.⁴⁹⁻⁵²

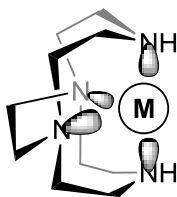


Figure 2.8- Proposed molecular conformation of the cyclen-cross-bridged ligand **75** with metal cation inside the ligand cavity, with nitrogen lone pairs pointing towards the metal.^{49d}

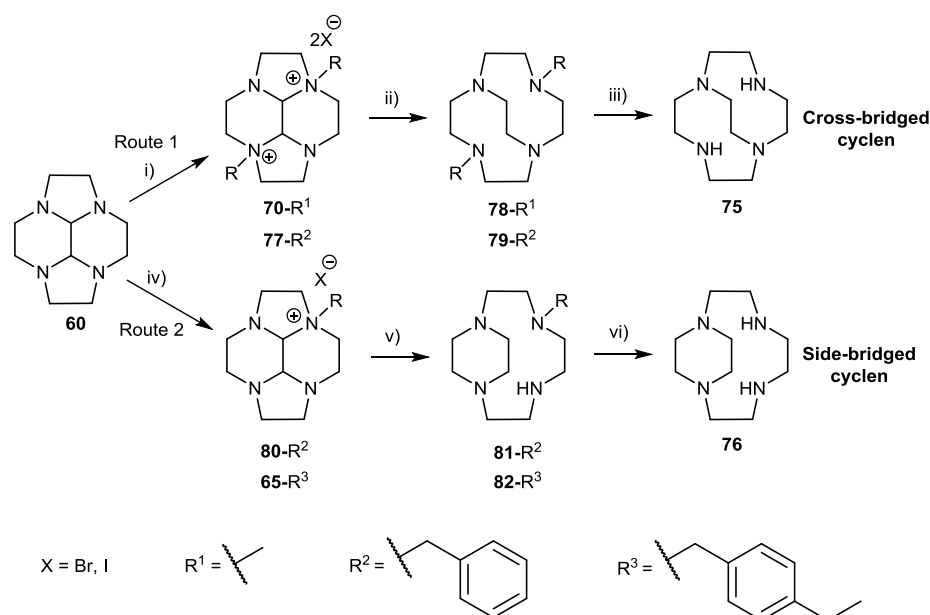
Moreover, this also ensures a *cis*-geometry of the metal complex. In particular, it is important for cyclam-based ligands (Figure 2.1, section 2.1.1.1), which are larger and allow a mixture of *trans*- and *cis*- isomers of the metal complexes to be formed. It has been also reported by Ware *et al.*,⁵⁰ that additional alkylation on the nitrogen in the macrocyclic backbone impacts the electronic properties and redox behaviour of the corresponding metal complex, which in turn can potentially affect their hydrolytic activities towards target substrates. This will be discussed in detail later in this chapter and in Chapter 3.

Furthermore, it was demonstrated by Weisman *et al.*,^{49d} that ethylene-bridged ligands are remarkably basic and act as proton sponges due to the presence of the secondary and tertiary aliphatic amines, and their pK_a s lie outside the normal range. For example, according to Weisman, the cyclam analogue of ligand **75** has a $pK_{a_2} > 24$ and $pK_{a_1} = 10.8$,^{49d,50} which indicates unusually high basicity of this ligand and is similar to DBU or guanidine bases, which have high pK_a s of 13.5 ± 1.5 .⁵³ The proton sponge nature of these ligands makes complexation with certain metal cations challenging under protic conditions due to the competition between protons and the metal ion for the nitrogen lone pairs. Therefore, dry conditions and elimination of any source of protons is crucial in such cases.⁵¹ Only the strongest binding transition metal ions, such as Cu(II) and Ni(II) can complex with these ligands under protic conditions.^{49d} Additionally, it has been reported that significant interactions occur between the solvent and such ligands.^{49d} Therefore, it was postulated, that $CDCl_3$ solvent should be avoided for the purposes of NMR spectroscopy. Instead, solvents such as C_6D_6 or CD_3CN , should be used.

The key reasons for the introduction of the internal ethylene bridge into the cyclen backbone (together with the addition of *N*-alkyl substituents to the ligand) in this project were to explore how this affects the geometry and Lewis acidity of Co(III) and Zn(II) complexes and consequently their hydrolytic activity towards phosphate ester hydrolysis.

2.3.2.1. Synthesis of the Ethylene-bridged Ligands

Overall, in the bisaminal approach towards the synthesis of the bridged macrocycles, the formation of the *N*-alkylated quaternary ammonium salts is followed by their reductive cleavage with an excess of NaBH₄ in EtOH to give a bicyclic ring system. It is known that two types of bridged macrocycles can be made depending on the number of alkylation sites in the quaternary ammonium salt. For example, symmetrical bis-*N*-functionalisation is required to obtain a cross-bridged macrocycle, whereas mono-*N*-functionalisation is necessary for the synthesis of the side-bridged ligand. Finally, when benzylic pendant arms are present they can be readily removed by catalytic hydrogenation to obtain unsubstituted cross- or side-bridged macrocyclic ligands. The synthetic pathways for the target ligands are depicted in Scheme 2.13 below.^{49d}



Scheme 2.13- Synthesis of ethylene-bridged cyclen ligands *via* bisaminal **60**. Conditions: i) 70-*R*¹- methyl iodide or 77-*R*²- benzyl bromide, MeCN, 16 h, RT; 70-*R*¹= 98%, 77-*R*²= 90%; ii) NaBH₄, EtOH, RT, 5 days; 78-*R*¹= 83%, 79-*R*²= 72%; iii) Pd/C 20%, H₂ g, AcOH, 27 %; iv) 80-*R*²- benzyl bromide or 65-*R*³- *p*-ethylbenzyl bromide, toluene, 16 h, RT; 80-*R*²= 96%, 65-*R*³= 91%; v) NaBH₄, EtOH, RT, 5 days; 81-*R*²= was not isolated (see text), 82-*R*³= 64%; vi) synthetic step was not carried out (see text).

Weisman *et al.*^{49d} proposed a reduction mechanism for the di-*N*-alkylated quaternary ammonium salt with NaBH₄, which involves the conversion of the tetracyclic bisaminal **60** into the tricyclic iminium ion in the rate-determining step. This is followed by the addition of hydride to the iminium ion. After formation of the second iminium ion and the subsequent addition of hydride, the symmetrically di-*N*-alkylated cross-bridged cyclen ligand is formed. Although reduction in EtOH with a large excess (40 equiv.) of NaBH₄ is

slow and requires five days to complete, it is normally remarkably clean and in some cases no purification procedures are required. Alder and co-workers previously attempted to improve on the efficiency of this step by using higher temperatures or larger proportions of water. However, their efforts proved to be unsuccessful due to side-product formation, which was suggested to be a result of iminium ion hydrolysis.^{49d}

Prior to the NaBH₄ reduction method reported by Weisman *et al.*,^{49d} other conditions were also used to prepare ethylene-bridged tetraazamacrocycles. For example, Alder *et al.* used LiAlH₄ as the reducing agent in ethereal solvents for the reductive cleavage of tricyclic α -amino ammonium salts to prepare a range of bicyclic diamines. However, the use of harsher reducing agents, such as LiAlH₄ should be avoided due to their dangerous pyrophoric properties. Therefore, NaBH₄ reductive cleavage in EtOH *via* the bisaminal pathway has been proved to be more efficient and versatile compared to other methods mentioned above and is generally preferred for the synthesis of bridged macrocycles.^{49d}

It is noteworthy that very recently Archibald and co-workers developed a novel method towards the synthesis of bicyclic macrocycles, which involves mechanochemistry (as also mentioned in section 2.3.1) combined with efficient microwave heating for a faster reaction.⁴⁴ The most significant advantage of this method is that it dramatically reduces the overall reaction time for the syntheses of the target ligands. Archibald *et al.* demonstrated that the second reduction step can be carried out using only 10 molar equivalents of NaBH₄ (as opposed to 40 equivalents in solution) and heating the reaction by microwave irradiation reduces the reaction time from 5 days to 30 minutes as well as improving the yield of the product. Therefore, this methodology is an attractive alternative to a conventional solution chemistry approach towards the synthesis of tetraazamacrocyclic derivatives. Unfortunately, this discovery was revealed just before the completion of this work when all target compounds were already prepared. However, it will be worth considering this alternative method for the future investigations in this field in our research group.

In this work, as shown in Scheme 2.13, in order to obtain ligand **78**, **70** was reacted with 40 molar equivalents of NaBH₄ in EtOH under inert conditions at room temperature for 5 days, leading to the formation of **78**, which was followed by basic work up and pure **78** was isolated in good yield. In some cases, purification of **78** by Kugelrohr distillation

(0.05 mmHg, 80-100°C) was required.⁴⁹ **78** was then used for the preparation of the corresponding metal complexes.

It has been suggested by Ware *et al.*⁵⁰ that although highly basic, **78** is not technically a proton sponge. It was reported that the triprotonated **78** [**78** H₃]³⁺ has three pK_a values 2.0, 5.8 and 11.3 respectively, which lie within the normal pH range for polyamines.⁵³ This means that protic solvent conditions can be used for the preparation of the metal complexes of this ligand. This property will be discussed in more detail in the next section. Despite this, ¹H NMR studies of **78** in CDCl₃ showed shifts in the peaks upfield after subsequent runs of the same NMR solution over time, indicating that interactions occur between CDCl₃ and tertiary nitrogens in the ligand. ¹H NMR spectra of **78** taken at different time intervals are shown in Figure 2.9. On the other hand, ¹H NMR spectra in C₆D₆ did not show any peak shifts over time. Thus, it was decided to run ¹H NMR of such ligands in C₆D₆.

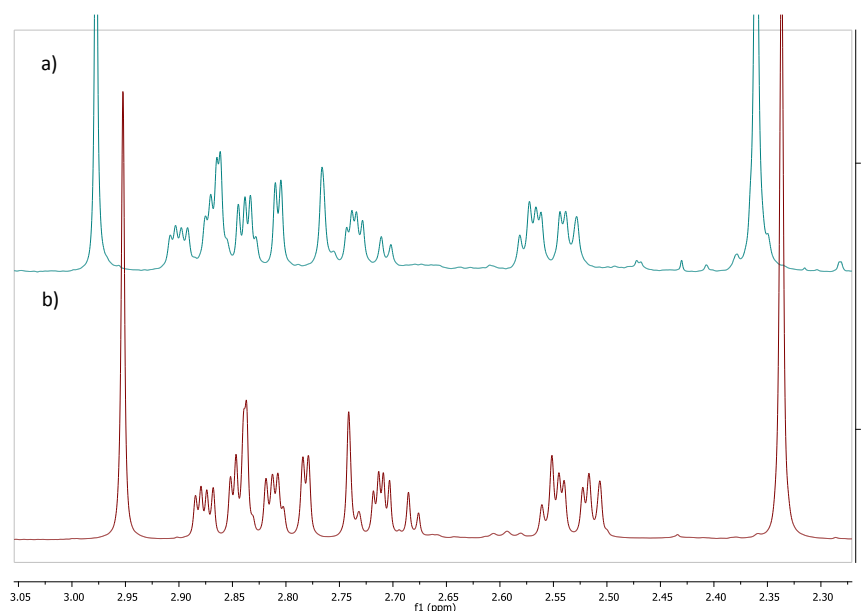


Figure 2.9- ¹H NMR spectra of **78** in CDCl₃ taken at different times: a) spectrum taken shortly after distillation of **78**; b) spectrum of the sample taken after 2 hours.

Synthesis of the unsubstituted ethylene-bridged cyclen requires the presence of the highly reactive *N*-alkyl pendant arms in the macrocyclic moiety, which then can subsequently be removed by catalytic hydrogenation after cross-bridge formation. Thus, di-benzyl bisaminal intermediate **77** was prepared in excellent yield using an excess of commercially available benzyl bromide.⁴⁹ **79** was prepared similarly to the **78** with an excess of NaBH₄. However, compared to **78**, synthesis of the di-benzylated cross-bridged cyclen ligand did not require

any further purification procedures and resulted in the isolation of the pure product in a 72% yield. It was then also used for the preparation of corresponding metal complexes.

Finally, the synthesis of ligand **75** was achieved by the removal of the benzylic groups through their hydrogenation in acetic acid over Pd/C. 20% Pd/C was used and proved to be an efficient catalyst for this particular reaction in comparison to 5% Pd/C that showed no activity at all. It is reported that the purity of product is sensitive to reaction times, e.g. longer reaction times result in the contamination of the product with an *N*-acetyl derivative of **75**.⁵⁴ Therefore, reaction was monitored by ¹H NMR every 30 minutes and de-benylation was complete after 2 hours. Nevertheless, this reaction did result in the isolation of the 73% of the mono-*N*-acetyl derivative **83** (impurity, which structure is shown in Figure 2.10) in the crude mixture of **75**. In order to remove this impurity, the crude product was converted to its hydrochloride salt. However, it was not possible to isolate this salt from the EtOH solution due to the 'slurry-like' nature of this material.

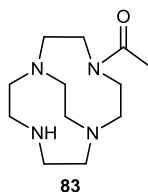


Figure 2.10- Structure of the mono-*N*-acetyl derivative **83**.

Likewise, alternative separation of the desired **75** from the impurity by Kugelrohr distillation (0.05 mmHg, 80-100°C) did not result in the isolation of the pure product and lead to its decomposition.⁵⁴ Thus, purification of crude **75** proved to be very challenging and no pure product could be isolated. Nonetheless, previous studies in the Watkinson group showed that addition of a metal ion to this type of the ligand can result in facile hydrolysis of the amide group.⁵⁵ Therefore, in anticipation of hydrolysis occurring upon complex formation the crude ligand **75** was taken forward for metal complex formation.

The mono-benzyl bisaminal **80** was prepared in almost quantitative yield. Unfortunately, the reductive cleavage of **80** did not proceed cleanly. Prolonging the reaction time from 5 to 15 days as well as further purification of the crude mixture by both distillation and *via* formation of its hydrochloride salt did not result in the isolation of pure **81** and the identity of the impurity could not be established. In addition, due to the availability of **65**, its reductive cleavage with an excess of NaBH₄ was also carried out with the aim to prepare

mono-*N*-alkylated side-bridged **82**.⁵⁶ In contrast to **81**, pure **82** was isolated in 64% yield. However, further attempts to repeat this reaction failed and many impurities were present that could not be identified by ¹H NMR spectroscopy. Purification procedures, such as distillation and isolation of pure **82** as its hydrochloride salt were not successful and the pure product could not be obtained. As a consequence of such purification issues, this route to compound **76** was not pursued further, although a small amount of the pure ligand **82** was used for the synthesis of the corresponding metal complex. In light of the low catalytic activity of the mono-alkylated Co(III) cyclen complexes that was subsequently observed (Chapter 3), this line of investigation was not pursued further.

2.3.3. Small-Molecule Biomimetic Systems: Synthesis, Structure and Characterisation of the Cyclen-based Co(III) and Zn(II) Complexes

With the six structurally modified cyclen-based ligands in hand it was set to synthesise their corresponding Co(III) and Zn(II) complexes with the view to study the effect of the structural modifications on their efficiency towards phosphate ester hydrolysis. Extensive examination of a variety of related reports revealed, that there are two major factors that affect the catalytic activity of tetraamine metal complexes:^{4,16,32}

- Basicity of the labile ligands
- Structure of the macrocyclic ligand backbone

The former can be regulated by adjusting the pH conditions in the hydrolytic reaction mixture and this factor will be discussed in detail later in this chapter and in Chapter 3. The major part of this chapter is focused on the thorough and systematic investigation of the effects of ligand structures on the properties of their complexes with an end goal to test their ability to hydrolyse phosphate ester bonds. It will be explored how structural modifications affect the following characteristics of the target metal complexes:

- i) physical and chemical properties (coordination geometry, ligand exchange);
- ii) electronic properties (redox potentials and Lewis acidity of the metal in the metal-ligand complex);
- iii) hydrolytic efficiency towards phosphate ester hydrolysis (which will be extensively discussed in Chapter 3).

Based on a number of reports that study the relationship between the ligand structure and behaviour of the corresponding metal complexes, it is striking that complexes so closely related in structure can show a dramatic difference in hydrolytic efficiency.^{4,32} Thus, the

ligand topology is particularly important in the design of small-molecule catalysts because even small structural modifications can remarkably affect their physical, chemical and electronic properties, together with their hydrolytic activity. In particular, it was demonstrated by Chin and co-workers,⁴ that the major factor that determines the catalytic efficiency of tetraamine Co(III) complexes is the ease of formation of the four-membered chelate between metal complex and substrate in the rate determining step of the hydrolytic mechanism (as shown in Scheme 2.1 in section 2.1.1.1). The researchers also identified two structural features that influence the ease of such strained four-membered ring intermediate formation:

- N_{eq} -Co- N_{eq} angle size opposite the chelate⁴
- *N*-Alkylation on the axial nitrogens of the ligand⁷

Current efforts are directed to increase the hydrolytic efficiency of these complexes by designing ligand systems that can facilitate the formation of the four-membered ring chelate. However, it is also important to note, that steric hindrance (Chapter 1, section 1.3.3.2.2) is not the only effect exerted on the metal complex by *N*-alkylation of amine ligands. Another major contribution to the effect of *N*-alkylation on the properties of the corresponding metal complexes is attributed to its influence on the interaction of this metal complex with the solvent.⁵⁷ Addition of the alkyl substituent to the nitrogen atom in amine ligand prevents the formation of hydrogen bonds of the type $M-N-H\cdots O$ with the solvent, which contribute to the outer sphere solvation energy. The lack of such hydrogen bonds reduces charge delocalisation from the metal to the solvent, thus leading to the increased charge density on the central metal cation, thus increasing its Lewis acidity in the *N*-alkylated complexes.⁵⁷ For example, Hegg *et al.* showed that alkylation of the 1,4,7-triazacyclononane Cu(II) di-chloride complex with the three isopropyl groups makes it a better catalyst for the anaerobic hydrolysis of DNA. They suggest that increased charge density on the copper cation upon *N*-alkylation might also contribute to the gain in catalytic activity of the complex.⁵⁸

The findings described above appear to suggest that the effect of *N*-alkylation is counterintuitive: on the one hand it increases steric hindrance that leads to the decrease in hydrolytic efficiency of the metal complex, but on the other hand it also increases Lewis acidity of the central metal cation, which should result in hydrolytic efficiency gain. Despite the considerable efforts made by a number of research groups to investigate the factors

that influence the phosphatase activity of small azamacrocyclic metal complexes, available literature is still lacking studies where the two factors that are influenced by *N*-alkylation are systematically investigated in a series of metal complexes with the view to establish which effect has a more pronounced influence on the hydrolytic efficiency of the target complex. Moreover, the role of the ethylene cross-bridge on the catalytic activity of the tetraamine Co(III) towards phosphate ester hydrolysis remains unexplored. Thereby, it was also of interest to study the Lewis acidity of **55** and examine its effect on NPP hydrolysis.

As was mentioned in section 2.1.2.2 of this chapter, analogous cyclen-based Zn(II) complexes were also prepared and the following sections will discuss the synthesis and characterisation of the target cyclen-based metal complexes in detail.

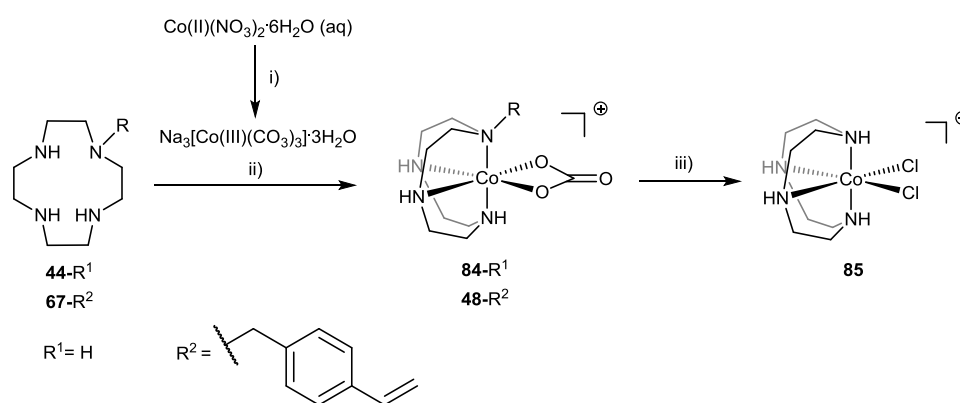
2.3.3.1. Small-Molecule Hydrolytic Agents: Synthesis and Characterisation of the Tetraamine Co(III) Complexes

Co(III)-amine-aqua complexes ($[\text{Co}(\text{NH}_3)_x(\text{H}_2\text{O})_{6-x}]^{3+}$) are model compounds of an inert metal complex and have been extensively studied for more than 130 years.⁵⁹ Such complexes are known to have very inert Co-N bonds and somewhat more labile Co-O bonds, allowing ligand substitution to occur at the coordination sphere of the metal. Moreover, the diamagnetic nature of the Co(III) centre is especially valuable to allow mechanistic investigations of ligand exchange reactions by conventional ^1H NMR techniques. In particular, tetraamine Co(III) complexes $[\text{Co}(\text{N}_4)\text{XY}]^{2+}$ (in the family of amine-aqua complexes) are at the forefront of coordination chemistry to date. Based on the numerous published reports, the syntheses of the target $[\text{Co}(\text{L})(\text{OH}_2)\text{OH}]^{2+}$ (where L= cyclen or its derivatives) readily occurs *via* di-chloride precursors, which can be obtained by various methods, such as:

- i. Aerial oxidation of a buffered solution of $\text{Co(II)Cl}_2 \cdot 6\text{H}_2\text{O}$ and the ligand in the presence of NaNO_2 , with subsequent conversion of the NO_2^- complex to the di-chloride species by addition of concentrated HCl ;⁶⁰
- ii. Direct aerial oxidation of a buffered solution of Co(II)Cl_2 and ligand;⁶¹
- iii. Reaction of the ligand and $\text{Na}_3[\text{Co(III)}(\text{CO}_3)_3] \cdot 3\text{H}_2\text{O}$ in MeOH , followed by treatment with HCl ;¹¹

According to the literature, the most common method for generating di-chloride species is *via* Co(II) salts and direct oxidation of the metal to Co(III) (method i and ii). However, some

structurally modified cyclen ligands cannot be complexed directly with $\text{CoCl}_2 \cdot 6\text{H}_2\text{O}$, which will be further discussed in this chapter. Previously, method iii was utilised in the Watkinson and Resmini groups and proved to be viable and efficient for such systems.^{8,9} For these reasons, target di-chloride Co(III) complexes were prepared from the Co(III) carbonate salt as illustrated in Scheme 2.14. This synthetic method involves the reaction of the ligand with the $\text{Na}_3[\text{Co}(\text{CO}_3)_3] \cdot 3\text{H}_2\text{O}$ salt to prepare the $[\text{Co}(\text{L})\text{CO}_3]\text{HCO}_3$ complexes, which can be converted to $[\text{Co}(\text{L})\text{Cl}_2]\text{Cl}$ species by successive addition of 35% HCl. These reactions can be visually followed by a colour change, which will be discussed later.



Scheme 2.14- Synthetic scheme for the synthesis of target $[\text{Co(III)(L)Cl}_2]\text{Cl}$ complexes *via* the carbonate species exemplified using ligand **44-R¹** (and **67-R²** only to prepare carbonate species). Conditions: i) NaHCO_3 , H_2O , 1 h, 0°C , 75%; ii) $\text{Na}_3[\text{Co}(\text{CO}_3)_3] \cdot 3\text{H}_2\text{O}$, $\text{MeOH}/\text{H}_2\text{O}$ 1:1, 65°C , **84-R¹** = 87%; **48-R²** = 67%; iii) 35% HCl, MeOH, **85** = 75%.

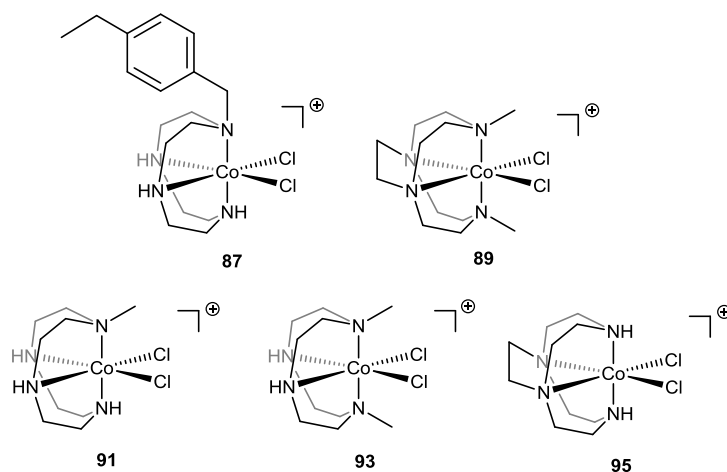


Figure 2.11- Yields of the di-chloride complexes and their corresponding carbonate precursors prepared *via* the scheme shown above: **87** = 86% (carbonate **86** = 81%); **89** = 65%, (carbonate **88** = 78%); **91** = 78% (carbonate **90** = 88%), **93** = 89% (carbonate **92** = 83%); **95** = 77% (carbonate **94** = 97%).

Seven Co(III) carbonate cyclen-based complexes were generated as dark pink solids in good yields 67-97%, by refluxing ligands **44**, **67**, **68**, **78**, **69**, **71** and **75** with $\text{Na}_3[\text{Co}(\text{CO}_3)_3] \cdot 3\text{H}_2\text{O}$ in

MeOH:H₂O for 16 hours.^{8,11} The colour change of the reaction solutions from olive green to dark pink indicated the presence of the carbonato species in the reaction mixture. Despite the highly basic properties of ligand **78**, aprotic conditions were not necessary to successfully obtain [Co(**78**)CO₃]₂HCO₃.⁵⁰ Advantageously, the longer reaction time of 5 days lead to higher yields of this complex of ligand **78**. UV-Vis and ¹H NMR spectroscopy confirmed the presence of the octahedral diamagnetic Co(III) carbonate complexes. Moreover, slow Et₂O/Pet.Ether (1:1) diffusion into a solution of [Co(**68**)CO₃]₂HCO₃ in MeOH gave crystals of [Co(**68**)CO₃]₂MeCO₃ suitable for single crystal X-ray diffraction and its crystal structure is shown in Figure 2.12 below.

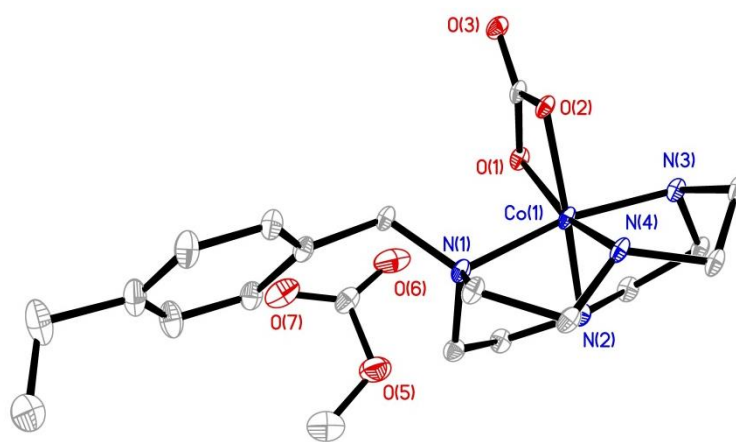


Figure 2.12- ORTEP⁶² reference plot showing the single crystal X-ray structure of [Co(**68**)CO₃]₂MeCO₃ with 50% probability displacement ellipsoids, with hydrogen atoms omitted for clarity.

It is evident, that the complex adopts a distorted *cis*-octahedral configuration, in which the cyclen ligand folds to fit around the cobalt ion and occupies two axial and two equatorial sites on the metal. The remaining two equatorial sites are occupied by a *cis*-coordinated carbonate ligand. The selected bond lengths and bond angles corresponding to [Co(**68**)CO₃]₂MeCO₃ are presented in Table 2.2.

A more detailed inspection of the crystal structure reveals, that the Co-N(1) bond length, is slightly longer (2.02 Å) than all other Co-N bond lengths in the complex (1.92-1.95 Å). This structural observation can be attributed to the alkylation of the axial N(1), which makes it a poorer σ-donor and hence causes bond elongation.⁵⁷ The axial N(1)-Co-N(4) and equatorial N(2)-Co-N(3) bond angles of 168.08° and 100.75° respectively indicate a slight distortion from ideal octahedral geometry around the metal, which is consistent with the literature data⁶³ and will be discussed in detail later in this section. It can also be seen, that the benzylic pendant arm points away from the metal centre to minimize steric strain. To our

knowledge, $[\text{Co}(\mathbf{68})\text{CO}_3]\text{MeCO}_3$ is the first isolated and structurally characterized Co(III) complex of this ligand, which presents the first crystallographic report of the MeCO_3^- anion that most likely was formed by a reaction between MeOH and a carbonate dianion.

Given that $[\text{Co}(\mathbf{78})\text{CO}_3]\text{HCO}_3$ can be successfully obtained using a protic MeOH:H₂O solvent mixture, it was decided to attempt complexation of ligands **79** and **82** with $\text{Na}_3[\text{Co}(\text{CO}_3)_3]\cdot 3\text{H}_2\text{O}$ under the same conditions. However, this did not result in the formation of the desired target metal complexes. Due to the low catalytic activity of the mono- and di-alkylated complexes that subsequently observed, this line of investigation was not pursued further.

Successive treatment of MeOH solutions of each of the prepared carbonate complexes with concentrated HCl lead to the generation of the di-chloride species *via* ligand exchange, and was accompanied by a significant colour change from dark pink to violet, as previously reported and as shown in Figure 2.13.^{8,11} Evaporation of the solvents under vacuum, resuspension in MeOH, (and subsequent filtration to remove any insoluble materials) resulted in the desired di-chloride Co(III) complexes as dark violet powders in yields from 65% to 89%. It is important to note, that treatment of complex $[\text{Co}(\mathbf{75})\text{CO}_3]\text{HCO}_3$ **94**, that contained mono-*N*-acetyl Co(III) carbonate derivative in the product mixture, with concentrated HCl resulted, as anticipated, in complete hydrolysis of the amide bond⁵⁵ and isolation of the di-chloride analogue **95** without mono-*N*-acetyl cyclen-based derivative according to its ¹H NMR spectrum.

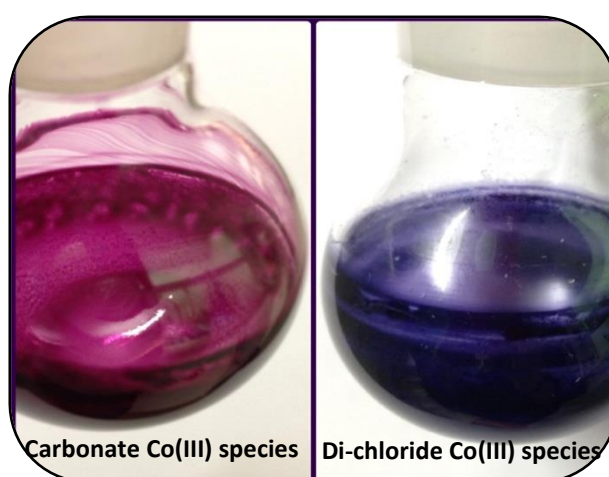


Figure 2.13- Colour change upon conversion of carbonate Co(III) species (dark pink) to Co(III) di-chloride species (violet) of the cyclen-based ligands.

UV-Vis spectroscopic studies of the [Co(III)Cl₂]Cl complexes reported here confirmed typical characteristics for Co(III) cyclen-based tetraamine species: a low spin diamagnetic d⁶ electronic configuration, (which was also indicated by the sharp ¹H NMR spectra) and distorted octahedral coordination geometry around the central cobalt atom.⁵⁹ For all six di-chloride cobalt complexes a major band was observed with λ_{max} between 543 nm and 589 nm, which corresponds to a cobalt d-d transition (¹A_{2g} ← ¹A_{1g})⁵¹ and is characteristic of all *cis*-di-chloride cyclen-based cobalt complexes. UV-Vis spectra of [Co(**44**)Cl₂]Cl **85** in DMSO and of complexes **87**, **91**, and **93** in MeOH, contain two bands in the same region as summarised in Table 2.1. On the other hand, the spectra of **89** and **95** in MeOH contain three absorption bands, which is uncommon for octahedral *cis*-[Co(N₄)X₂]X complexes. This phenomenon can be explained by the presence of the ethylene cross-bridge on **89** and **95**, which distorts the octahedral geometry of the complex more strongly than the other ligands. This results in sufficient splitting of the ¹T_{1g} energy level and gives rise to the extra absorption band observed at 411 nm (¹E_{1g} ← ¹T_{1g}) for **89** and 400 nm **95**. The spectrum of **89** is similar to the one published by Busch *et al.*⁵¹ and is shown in Figure 2.14. Moreover, the results show that the extinction coefficients of **89** and **95** are 671 and 486 M⁻¹cm⁻¹ respectively for a d-d transition at 340 nm (¹A_{1g} ← ¹T_{2g}) and are significantly higher than those of the other di-chloride complexes, which fall in the range between 183 and 264 M⁻¹cm⁻¹ in this region. As with Busch *et al.*⁵¹, a likely explanation for this observation is that the stronger distortion of the octahedral geometry leads to higher extinction coefficients due to the relaxation of symmetry. Extinction coefficients for the six complexes in the other two regions of 550 and 400 nm fall within the range between 100 and 224 M⁻¹cm⁻¹, which consistent with literature data.⁵¹

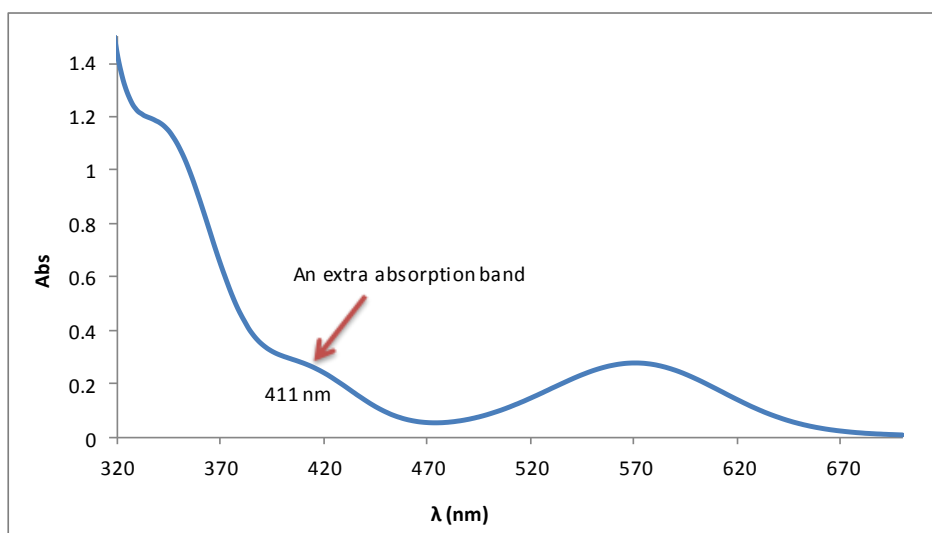


Figure 2.14- UV-Vis spectrum of **89** showing an extra absorption band at 411 nm.⁵¹

Table 2.1- Visible electronic spectra data for [Co(L)Cl₂]Cl complexes (5mM solutions in MeOH).

¹= in DMSO solution

Complex	Absorption in nm (extinction coefficient M ⁻¹ cm ⁻¹)		
	¹ A _{1g} / ¹ A _{2g} (¹ T _{1g})	¹ A _{1g} / ¹ E _g (¹ T _{1g})	¹ A _{1g} / ¹ T _{2g}
85 ¹	563 (148)	-	394 (155)
87	570 (224)	-	395 (264)
91	567 (183)	-	395 (212)
93	589 (192)	-	400 (183)
89	572 (168)	411 (154)	340 (671)
95	543 (100)	400 (131)	337 (486)

Needle-like X-ray quality crystals of **89** were also obtained by slow diffusion of Et₂O into a MeOH solution of the complex. The crystal structure of complex **89** presented in Figure 2.15 a) is very similar to the one previously published by Busch *et al.*⁵¹ Again, the axial N(1)-Co-N(4) angle of 170° deviates from the ideal 180°, whilst the equatorial N(2)-Co-N(3) bond angle of 88.05° is very close to the ideal one of 90°. The crystal structure of **89** was also compared to the one of [Co(cyclen)Cl₂]Cl (Figure 2.15 b)) previously obtained in Watkinson and Resmini groups.⁸

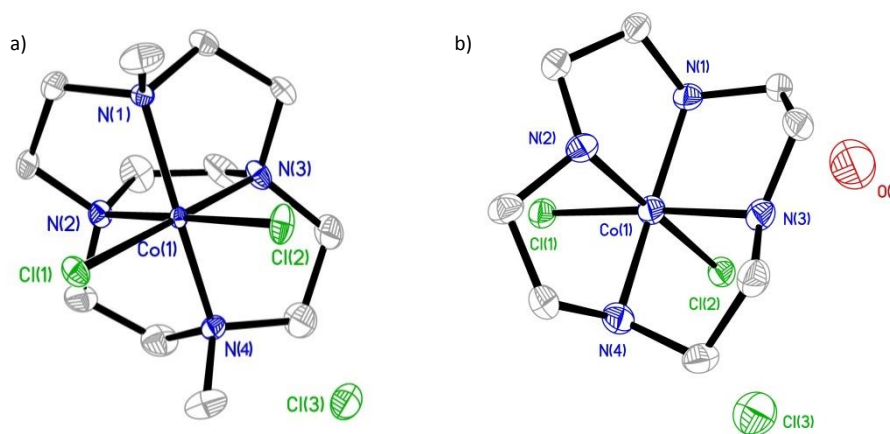


Figure 2.15- ORTEP⁶² reference plot of the single crystal X-ray structures of a) [Co(78)Cl₂]Cl **89** (from this work) and b) [Co(cyclen)Cl₂]Cl **8** with 50% probability displacement ellipsoids, with hydrogen atoms omitted for clarity.

Comparisons of the crystallographic values of **89** with those of the unbridged cyclen-based Co(III) complex allows a more detailed investigation of the effect of the topological constraints on the cyclen ligand. Selected bond lengths and bond angles of these two complexes, as well as carbonate complex **86** are shown in Table 2.2. As in the case with **86**, it was observed, that the axial N(1)-Co and N(4)-Co bond lengths on **89** are slightly longer (2.00 Å) than the two equatorial N(2)-Co and N(3)-Co bond lengths (1.94 Å) on the same complex as well as all the other Co-N bond lengths (1.93-1.97 Å) on [Co(cyclen)Cl₂]Cl.

Finally, and most importantly, Chin *et al.* demonstrated that the size of the N_{eq}-Co-N_{eq} bond angle opposite to the O-Co-O chelate ring affects the flexibility of the tetraamine metal complex. It has been suggested, that larger bond angles opposite the four-membered rings better stabilise four-membered Co(III) complexes. It was found that mono *N*-alkylation on cyclen with *p*-ethyl benzylic moiety leads to a small reduction in the N_{eq}-Co-N_{eq} equatorial angle in carbonate Co(III) complexes from 103.1° (reported for [Co(cyclen)CO₃]HCO₃)⁶³ to 100.7° in **86**. It was also reported Chiampolini *et al.*⁶⁴ that incorporation of the two methyl groups on the [Co(cyclen)CO₃]HCO₃ complex resulted in N_{eq}-Co-N_{eq} angle of 101.7°, which is very similar to this angle in **86**. Consequently, based on this finding with carbonate complexes, it can be postulated that mono- and di-*N*-alkylation on di-chloride Co(III) cyclen-based complexes might lead to smaller equatorial N_{eq}-Co-N_{eq} angles compared to non-alkylated complexes. It can be clearly seen, however, that O-Co-O angle is unsurprisingly not affected by *N*-alkylation and its size remains very similar upon structural modifications, as shown in Figure 2.20.

Table 2.2- Selected bond lengths (Å) and bond angles (°) in the cationic complexes of cyclen-based ligands.

	[Co(68)CO ₃]HCO ₃ ⁶³	[Co(78)Cl ₂]Cl	[Co(44)Cl ₂]Cl ⁸
<i>Bond lengths</i>			
Co-N(1)	2.024(2)	2.009(2)	1.972(8)
Co-N(2)	1.923(2)	1.940(2)	1.944(8)
Co-N(3)	1.934(2)	1.945(2)	1.930(7)
Co-N(4)	1.948(2)	2.001(2)	1.972(8)
<i>Bond angles</i>			
N(1)-Co-N(2)	86.31 (1)	84.79 (9)	83.9 (3)
N(2)-Co-N(3)	100.75(1)	88.05(9)	95.8(3)
N(3)-Co-N(4)	85.98 (1)	84.64 (9)	85.5 (3)
N(1)-Co-N(4)	168.08(1)	168.96(9)	165.0(3)
X(1)-Co-X(2)	69.14(9)¹	87.72(3)²	88.04(1)²
^a Footnote ¹ X=O, ² X=Cl			

Additionally, it was observed that this N_{eq}-Co-N_{eq} angle in cyclen-based Co(III) complexes is reduced from 103.1° when bidentate ligand such as carbonate is present, to 95.8° in complexes with mono-dentate ligands such as [Co(cyclen)Cl₂]Cl. It was also found that the N(2)-Co-N(3) angle in complex **89** is 88°, which considerably smaller than the reported 95.8° N(2)-Co-N(3) angle in [Co(cyclen)Cl₂]Cl complex. Based on the literature data, this reduction in the size of the angle from 95.8° to 88° in the N_{eq}-Co-N_{eq} can be attributed to the additional conformational strain in the ligand structure created by the ethylene cross-bridge⁵¹, which is illustrated in Figure 2.16. Thus, based on the published data, it can be confirmed in this work that inclusion of the ethylene bridge into the cyclen moiety imparts additional strain to the molecule. Additionally, X-Co-Y angles opposite N_{eq}-Co-N_{eq} angles in the complexes presented in this work match with the reported values for both bidentate and monodentate chelates. O(1)-Co-O(2) angle in carbonate complex **86** is 69.1° which is similar to the reported 68.4° O-Co-O angle in [Co(cyclen)CO₃]HCO₃⁶³ and 68.6° in [Co(**71**)CO₃]HCO₃,⁶⁴ whereas the Cl(1)-Co-Cl(2) angles in [Co(cyclen)Cl₂]Cl and [Co(**78**)Cl₂]Cl are, as expected, larger and are 88.04° and 87.72° respectively.

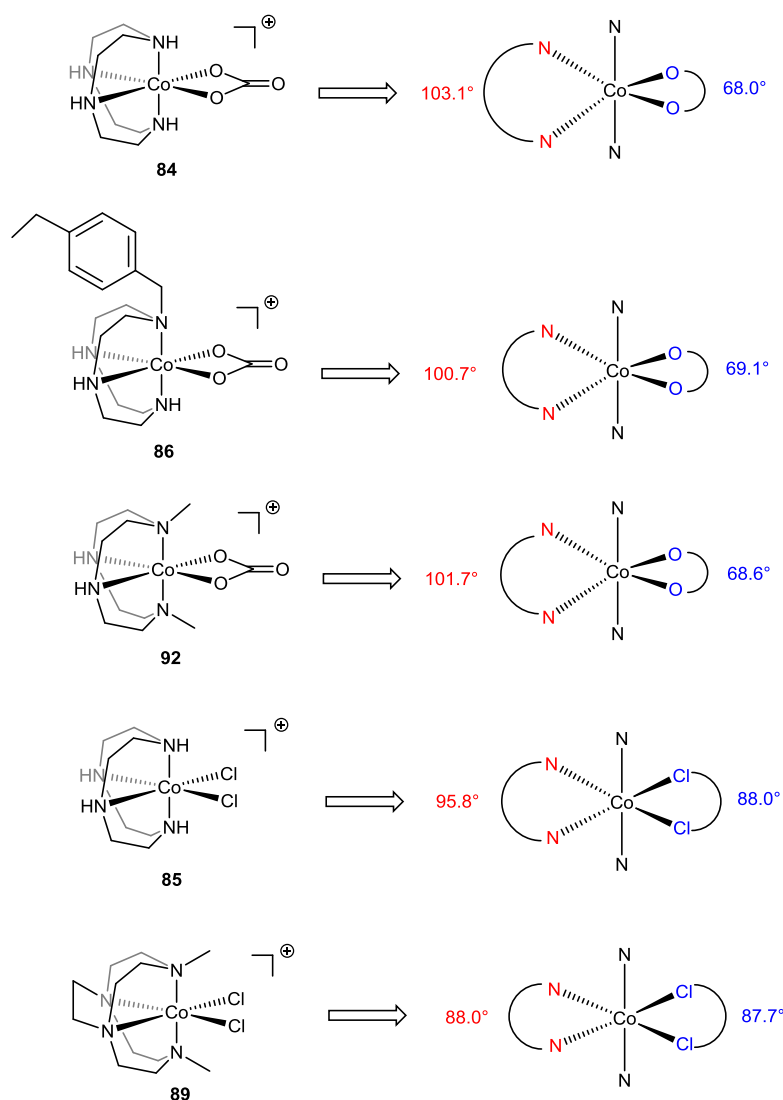


Figure 2.16- Structures of the four [Co(cyclen)(X)(Y)]⁺ complexes, when X,Y are monodentate and bidentate ligands, illustrating the N_{eq}-Co-N_{eq} and X-Co-Y angles reported^{8,63,64} (X,Y = CO₃²⁻ and Cl) and found in this work.

Literature data suggests that the presence of three configurational isomers of the [Co(L)Cl₂]Cl complex is possible.⁶⁵ Based on NMR techniques it was revealed that such isomerisation occurs due to the different configuration of the amine (equatorial (N1) and (N3)) protons that are diametrically opposed (occupy *syn,syn*, *anti,anti* or *syn-anti* positions) to the chloride anions. In this work, the presence of several isomers of these complexes was confirmed by their ¹H NMR spectra in D₂O, that contain a number of multiplets as shown in Figure 2.17 a). It can be speculated, that this indicates not only the existence of *syn,syn*, *anti,anti* and *syn-anti* isomers in the solution, but also the presence of the di-chloride, di-aqua, aqua-hydroxo and hydroxo-hydroxo species due to ligand exchange on the cobalt cation in water. In contrast, such isomers were not identified when the spectrum of the complex was obtained in CD₃OD (Figure 2.17 b)).

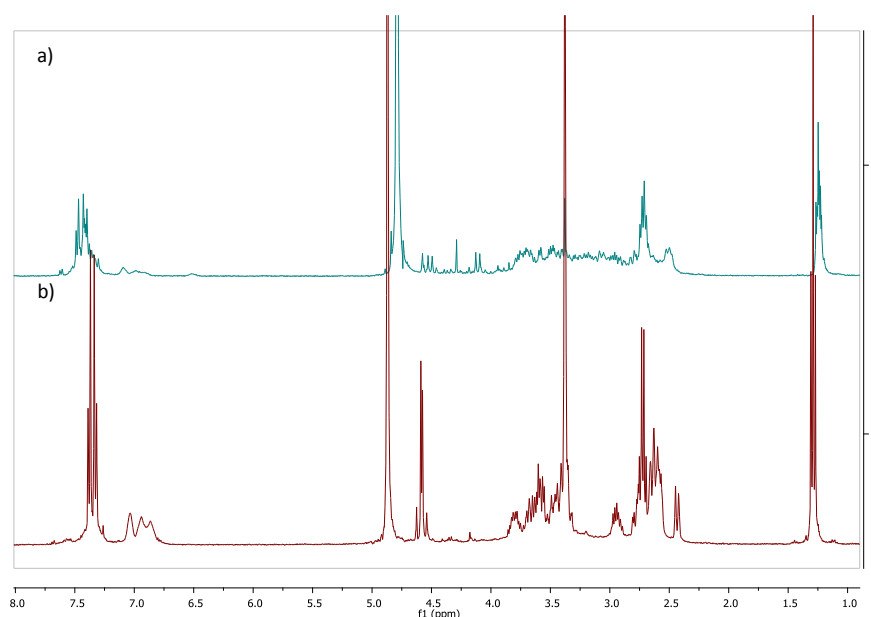


Figure 2.17- a) ^1H NMR spectrum of **87** in D_2O indicating the presence of several isomers; b) ^1H NMR spectrum of **87** in CD_3OD .

2.3.3.2. Other Methods for the Synthesis of Cyclen-based Co(III) Complexes

It is noteworthy, that our attempts to obtain complex **89** directly from $\text{CoCl}_2 \cdot 6\text{H}_2\text{O}$ based on a previously published procedure¹¹ that has been used for other cyclen derivatives, was not successful. Addition of 35% HCl to a stirred solution of **78** in MeOH with the Co(II) salt at room temperature resulted in a colour change from dark brown to bright blue as reported. Evaporation of the solvents after 4 hours resulted in the isolation of both blue and violet solids. The identity of the blue solid was determined with the help of the isolation of X-ray quality crystals, which show that a tetrahedral $[\text{CoCl}_4]^{2-}$ anion lies outside of the protonated ligand cavity, as illustrated in Figure 2.18. Broad peaks in the ^1H NMR (d_6 -DMSO) spectrum in combination with three characteristic absorption peaks for a Co(II) species in its UV-Vis spectrum in DMSO also supported the presence of the paramagnetic high spin Co(II) species.

Conversely, the violet solid appeared to be a Co(III) complex based on its UV-Vis and NMR spectra, although its ^1H NMR spectrum indicates the formation of a significantly different complex to that formed using standard syntheses *via* the carbonato species as shown in Figure 2.19. Therefore, for the purposes of the kinetic experiments this procedure was assumed to be unreliable and was not pursued further.

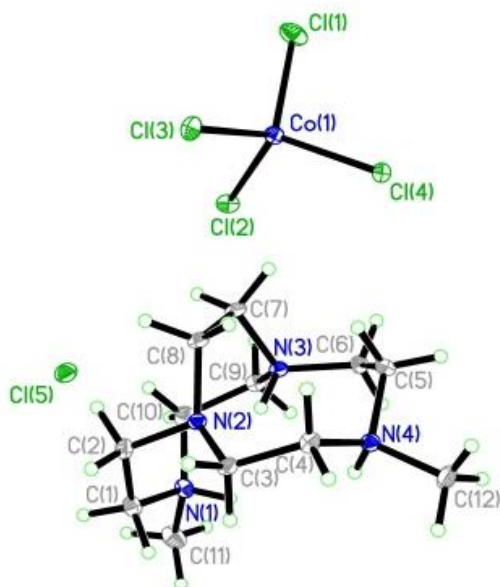


Figure 2.18- ORTEP⁶² reference plot showing the single crystal X-ray structure of $[78H_3][CoCl_4][Cl]$ 96 with 50% probability displacement ellipsoids.

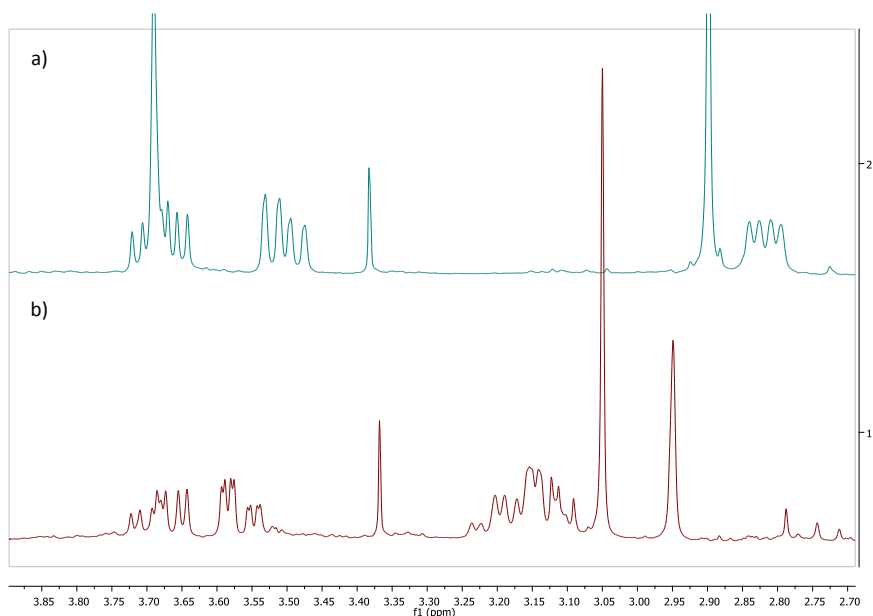
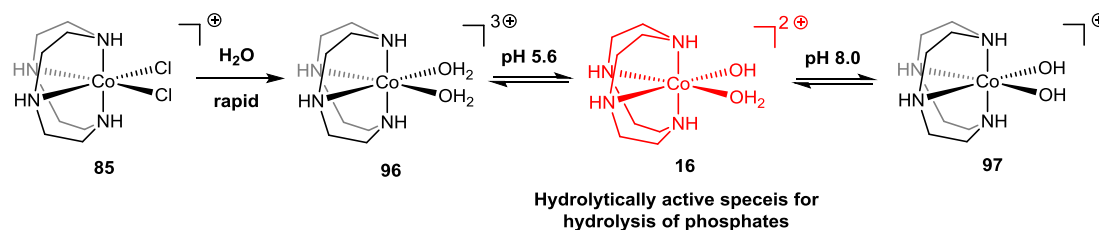


Figure 2.19- 1H NMR spectra of a) 89 and b) the violet solid in D_2O showing the presence of Co(III) species in both cases, however also demonstrating the variation in structures between the two compounds.

2.3.3.3. Generation of the Hydrolytically Active $[Co(L)(OH_2)OH]^{2+}$ Species

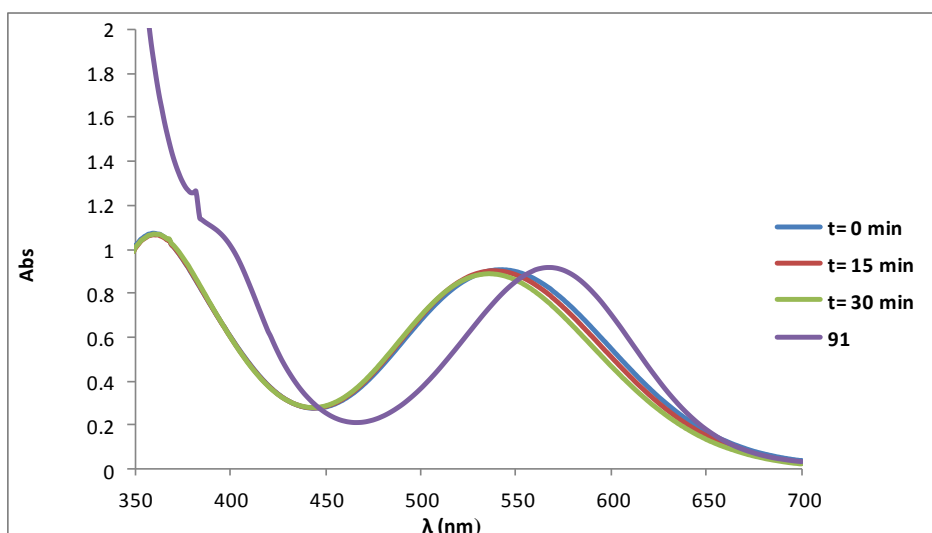
After all six $[Co(L)Cl_2]Cl$ complexes were isolated and fully characterised, it was necessary to obtain the hydrolytically active $[Co(L)(OH_2)OH]^{2+}$ species. The generation of such species was carried out following a well-established literature procedure,² which involves the dissolution of the di-chloride precursor species in HEPES buffer (10 mM, pH 7.2) and

addition of 2 equivalents of 0.1 M NaOH solution (Scheme 2.15). However, the time-scale for the ligand exchange to occur differed noticeably. For example, in some cases, heating at 50°C for 30 minutes was required to promote ligand exchange, whereas other complexes showed almost immediate ligand exchange.¹¹



Scheme 2.15- Scheme for the conversion of the di-chloride species 85 to hydrolytically active aqua-hydroxo species 16.

The dissolution of [Co(**44**)Cl₂]Cl and [Co(**75**)Cl₂]Cl in HEPES and NaOH mixtures resulted in UV-Vis spectra with an almost immediate shift in the absorbance bands from 394 and 563 nm (observed for di-chloride species) to 360 and 520 nm, which are characteristic peaks for the aqua-hydroxo species and are consistent with the literature.⁸ This observation thus suggests, that [Co(**44**)Cl₂]Cl and [Co(**75**)Cl₂]Cl undergo rapid aquation in water to give the catalytically active species [Co(**44**)(OH₂)OH]²⁺ and [Co(**75**)(OH₂)OH]²⁺, which is accompanied by the colour change from violet to light red. However, it was observed that aquation of **87**, **93**, **91** and **89** was much slower. When their spectra were recorded in HEPES, the major band between 567 and 589 nm (di-chloride species) did not shift immediately. Therefore, according to Kinght *et al.*¹¹ the solutions of these complexes in water were heated at 50°C and were monitored by UV-Vis spectroscopy. The shift of the major absorbance band from 570-590 nm region to 540 nm (aqua-hydroxo) region occurred after 30 minutes. A corresponding change in colour from violet to pink was observed. The UV-Vis spectrum in Figure 2.20 shows shift in the visible band from di-chloride species to the aqua-hydroxo for **91**. The spectrum demonstrates that there is an almost immediate shift in wavelength from 567 nm to 549 nm upon dissolution of the di-chloride complex in HEPES, which indicates the ligand exchange from di-chloride to di-aqua (t= 0 min). This is followed by a slower ligand exchange from di-aqua to aqua-hydroxo (t= 30 min) and corresponds to the wavelength shift to 540 nm.



Scheme 2.20- UV-Vis spectra showing the ligand exchange from di-chloride species **91** (purple band) to aqua-hydroxo species **17** (green band) over time. Purple band: di-chloride species dissolved in MeOH; blue-green bands: di-chloride species dissolved in HEPES (10 mM, pH 7.2) with 2 equiv. of 0.1 M and heated at 50°C for 30 min.

The shifts in wavelengths as well as the colour changes observed (Figure 2.21) due to the ligand exchange are presented in Table 2.3 for all the complexes. Interestingly, the aquation rate does not correlate with hydrolytic activity of the complexes (Chapter 3, section 3.2.2). For example, both **85** and **95** show an almost immediate ligand exchange, while hydrolytic activity of the corresponding **55** towards phosphate ester hydrolysis is more than nine times lower than that of **16**. It can be hypothesised that the reduction in angle size on cyclen upon the incorporation of the ethylene cross-bridge does not affect the aquation rate, whereas the additional steric hindrance imposed by the *N*-alkyl substituents on the corresponding ligands is likely to influence the time taken for the ligand exchange on the complexes.

Table 2.3- Comparison of the visible spectra absorption bands and colour change upon aquation of the di-chloride Co(III) complexes.

Major UV-Vis bands (nm)						
	[Co(44)XY] ⁿ⁺	[Co(68)XY] ⁿ⁺	[Co(78)XY] ⁿ⁺	[Co(71)XY] ⁿ⁺	[Co(69)XY] ⁿ⁺	[Co(75)XY] ⁿ⁺
Di-chloride species	563	570	572	589	567	543
Colour	pink	violet	violet	violet	violet	violet
Aqua-hydroxo species	520	540	540	554	540	530
Colour	light red	pink	pink	pink	pink	pink

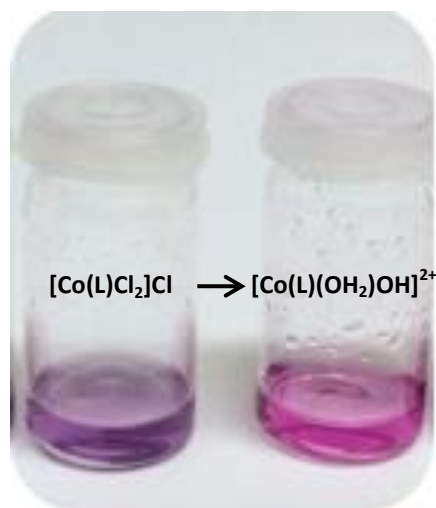


Figure 2.21- Colour change from violet to pink upon ligand exchange on the Co(III) centre from di-chloride to aqua-hydroxo species for complex **89** after 30 min at 50 °C.

2.3.3.4. Electrochemical Studies on the $[\text{Co}(\text{L})\text{Cl}_2]\text{Cl}$ and $[\text{Co}(\text{L})(\text{OH}_2)\text{OH}]^{2+}$ Complexes

Electrochemical studies of six $[\text{Co}(\text{L})\text{Cl}_2]\text{Cl}$ complexes were performed in MeOH and half-wave reduction potentials were measured by cyclic voltammetry separately using tetrabutylammonium tetrafluoroborate $n\text{-Bu}_4\text{NBF}_4$ as the supporting electrolyte. Cyclic voltammogram of **85** and **93** (representative of all the *N*-alkylated Co(III) complexes presented in this work) are shown in Figure 2.22 a) and b) respectively. They both present irreversible reduction potentials of -0.57 V and -0.20 V (relative to a standard calomel reference electrode (SCE)) respectively at a scan rate of 50 mV s^{-1} . This type of reduction wave is attributed to Co(III)/(II) couple and is known to be typical for octahedral tetraamine Co(III) complexes.^{66,67}

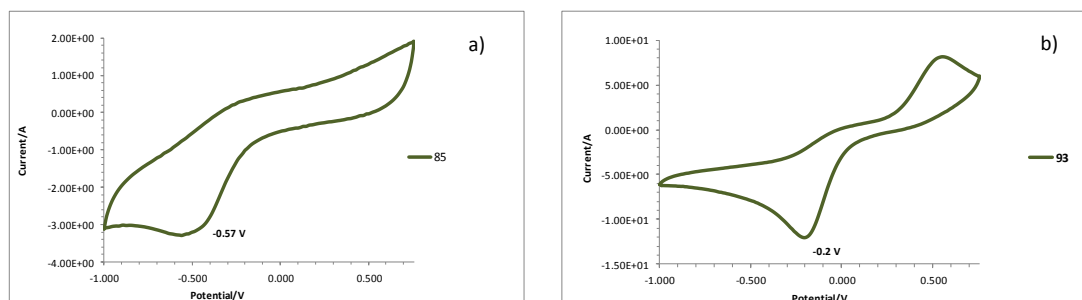


Figure 2.22- Cyclic voltammograms at glassy carbon using calomel reference electrode in MeOH ($n\text{-Bu}_4\text{NBF}_4$ is a supporting electrolyte; scan rate= 50 mV s^{-1}) of 5 mM solutions of **85** and **93**.

Analysis of the cyclic voltammograms of the presented complexes revealed that the introduction of the alkyl functional moiety to the cyclen ligand results in two major

differences: i) the shape of the voltammogram from the broad (non-alkylated cyclen) to more defined and sharp peak; and ii) shift of the reduction potentials to the more positive values. The CVs of all five *N*-alkylated complexes display essentially the same reduction potentials. Table 2.4 shows that complexes **95**, **89**, **91**, **87** and **93** exhibit anodically shifted reduction potentials, which is consistent with the hypothesis that *N*-alkylation induces more positive reduction potentials, making Co(III) a stronger Lewis acid.^{50,57} This phenomenon is known to be caused mainly by the loss of hydrogen bonds from the complex to the solvent of the type M-N-H \cdots O upon *N*-alkylation, which leads to the loss of stabilisation by solvation. Thus, the lack of such hydrogen bonds prevents charge delocalisation from the complex to the solvent resulting in the increased charge density on the central cation making it a harder Lewis acid in the *N*-alkylated complexes, as discussed in the section 2.3.3. In some of the *N*-alkylated complexes a similar oxidation wave is observed at approximately 0.5 V, which is not ligand-based. A small reduction wave at approximately 0.25 V is observed in the voltammogram of **89**, which can be attributed (based on literature results) to the presence of other minor configurational isomers and/or dinuclear species.

Reduction potentials vs SCE and vs SHE (standard hydrogen electrode) for the target six di-chloride cyclen Co(III) complexes are reported in Table 2.4.

Table 2.4- Reduction potentials vs SCE and vs SHE (SCE+0.250 V) for the six di-chloride Co(III) complexes.

Complex	E_{red} (V) vs SCE	E_{red} (V) vs SHE
85	-0.57	-0.32
95	-0.39	-0.14
89	-0.33	-0.08
91	-0.30	-0.05
87	-0.20	0.05
93	-0.20	0.05

Reduction potentials represented by the Co(III) complexes in this work are in the range from -0.32 to 0.05 V (vs SHE) and fall well within the range of the expected potentials reported for similar Co(III) complexes. For example, reduction potentials for the *N*-alkylated cyclen-based Co(III)/(II) couples observed by Ware *et al.*⁵⁰ range from -0.31 to -0.13 V vs SHE although reported for cyclen-based Co(III) with 8-quinolinolato-based ligands at scan rate 100 mV s⁻¹. Other related (hexaamine)Co(III) complexes that are known to span a

range of over 0.9 V, with the lowest potential (-0.63 V vs SHE) measured for [Co-(trans-diammac)]³⁺ and the highest potential (0.28 V vs SHE) found for [Co(tmen)₃]³⁺.⁶⁶

Reduction potentials of aqua-hydroxo species of the corresponding cyclen-based Co(III) complexes were also measured in HEPES (10 mM, pH 7.2) and 0.1 M NaOH (conditions required for the conversion of di-chloride species to the aqua-hydroxo analogues), which also acted as a supporting electrolyte at scan rate of 50 mV s⁻¹. A similar trend was observed for the aqua-hydroxo analogues with anodic shift in reduction potentials for the *N*-alkylated complexes with the exception of **55** and **50**, which unlike their di-chloride analogues showed a cathodic shift from -1.0 to -1.20 V as shown in Figures 2.23 and 2.24 below. This shift in **55** is consistent with the results published by Ware *et al.* for the similar cyclen-based Co(III) complexes.⁵⁰ However, in **50** this value is debatable due to the broadness of the reduction peak.

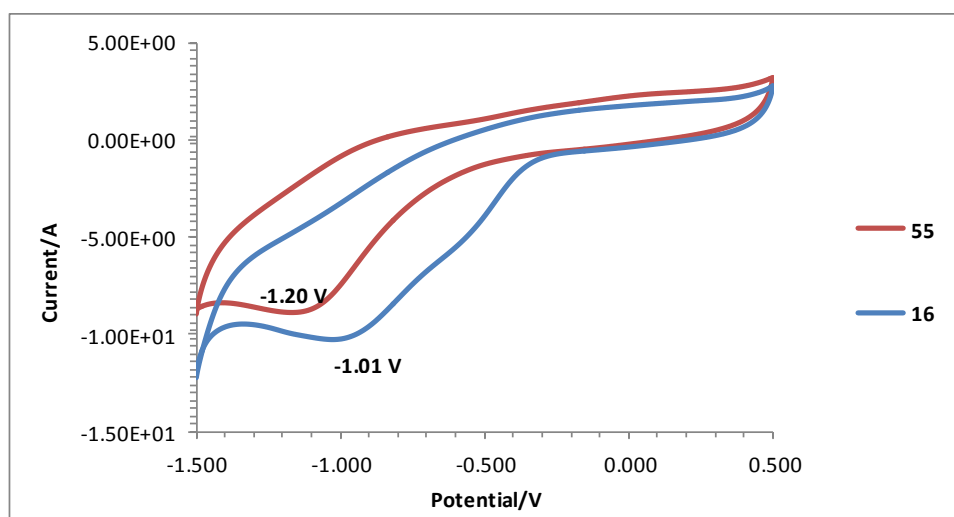


Figure 2.23- Cyclic voltammograms at glassy carbon using calomel reference electrode (scan rate= 50 mV s⁻¹) of 5 mM solutions of **16** and **55** in HEPES (10 mM, pH 7.2), showing a cathodic shift in reduction potential from -1.01 V to -1.20 V upon ethylene-cross-bridge incorporation.

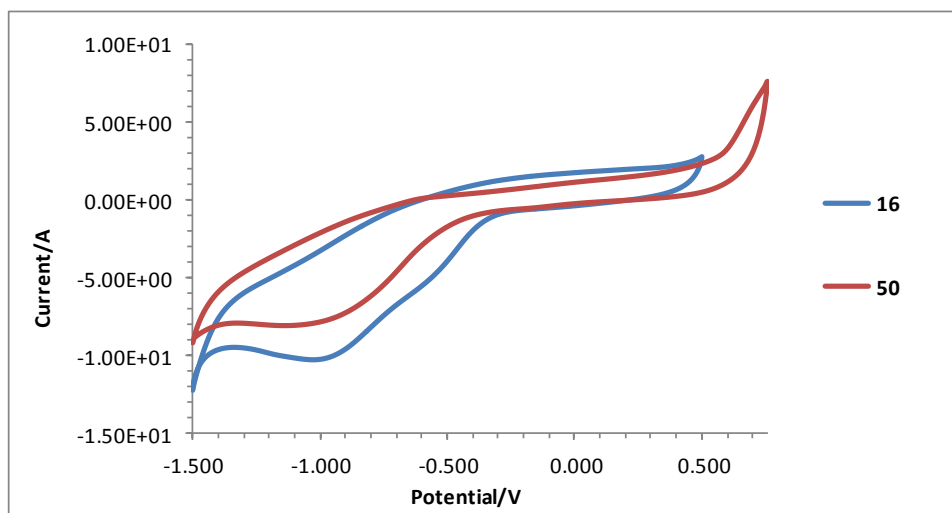


Figure 2.24- Cyclic voltammograms at glassy carbon using calomel reference electrode (scan rate= 50 mV s⁻¹) of 5 mM solutions of **16** and **50** in HEPES (10 mM, pH 7.2).

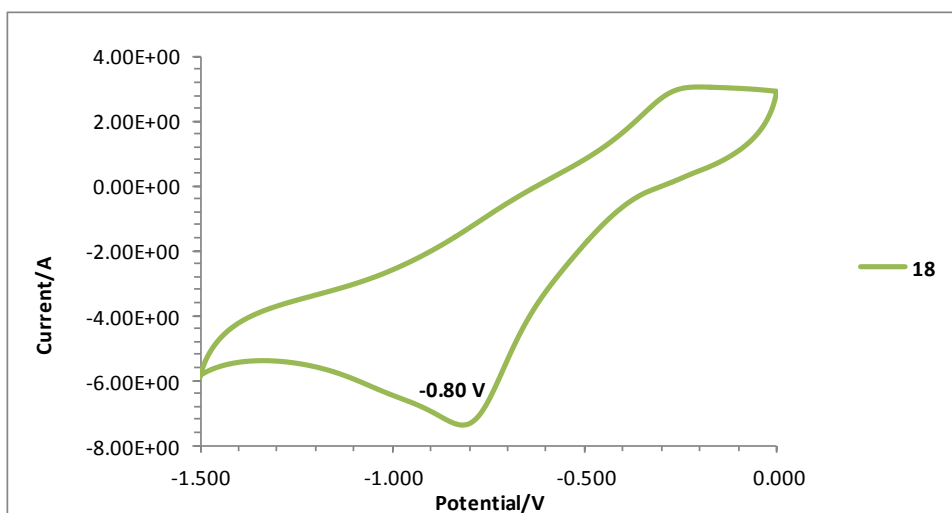


Figure 2.25- Cyclic voltammograms at glassy carbon using calomel reference electrode (scan rate= 50 mV s⁻¹) of 5 mM solutions of **18** in HEPES (10 mM, pH 7.2).

The change of the labile ligands on the central cobalt atom from di-chloride to aqua-hydroxo also leads to a small cathodic shift in reduction potentials: di-chloride cobalt complexes showed reduction potentials in the range of -0.57 to -0.20 V, whereas the range observed for the aqua-hydroxo species was from -0.8 to -1.20 V (see Table 2.5). Cyclic voltammogram of **18** is shown in Figure 2.25 as an example.

Table 2.5- Reduction potentials vs SCE and vs SHE (SCE+0.250 V) for the six aqua-hydroxo Co(III) complexes.

Complex	E_{red} (V) vs SCE	E_{red} (V) vs SHE
50	-1.20	-0.95
55	-1.20	-0.95
16	-1.01	-0.76
17	-0.92	-0.67
54	-0.81	-0.56
18	-0.80	-0.55

2.3.3.5. Generation of Zn(II) Complexes Using Cyclen-based Ligand Derivatives

Analogous cyclen-based Zn(II) complexes were also prepared based on published literature procedures.^{54,68} The synthesis of Zn(II) complexes of general structure $[\text{Zn}(\text{L})\text{OH}_2](\text{ClO}_4)_2$, where L is an appropriate cyclen ligand, required (in contrast to the corresponding Co(III) complexes) only one step: complexation of the ligand with $\text{Zn}(\text{ClO}_4)_2 \cdot 6\text{H}_2\text{O}$ salt in MeOH or MeCN solvent under reflux. Subsequent addition of Et_2O in the reaction mixture resulted in the separation of Zn(II) complexes as beige solids in very good yields from 70% to 88% as reported, with the exception of complex **102**. This only gave a 47% yield of the desired complex, which remained contaminated with *ca.* 30% of the analogous complex of the *N*-acetyl impurity **83** (Figure 2.10, section 2.3.2.1) albeit in significantly reduced amounts compared to that in the crude ligand mixture used of 73%, presumably due to Lewis acid activated amide cleavage.⁵⁵ ^1H NMR spectroscopy was sufficient to confirm the identity of the diamagnetic Zn(II) complexes. Six complexes represented in Figure 2.26 were then tested as catalysts for phosphate ester hydrolysis, which will be discussed in detail in the next chapter.

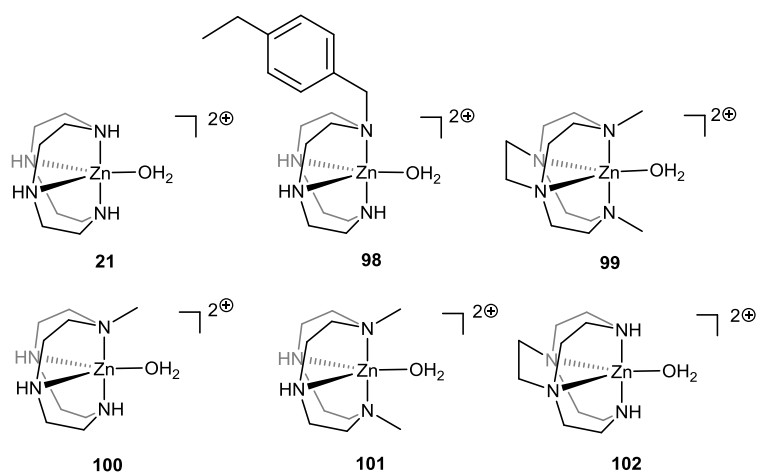


Figure 2.26- Structures of the target cyclen-based Zn(II) complexes. Yields: 21 = 81%, 98 = 88%, 99 = 70%, 100 = 81%, 101 = 85%, 102 = 47%.

2.4. Conclusions

In conclusion, a bisaminal synthetic strategy was utilised to efficiently prepare five *N*-alkylated cyclen-based ligands in good to excellent yields (in 3-4 steps). In particular, a novel non-polymerisable ligand **68** was designed and synthesised. The purification procedure that involves the formation of the hydrochloride salt of **68** with the help of concentrated HCl, was used and successfully afforded pure **68**. The purity of its polymerisable derivative **67** (previously synthesised in the Watkinson and Resmini groups) was also successfully improved using the same purification procedure.

Corresponding cyclen-based $[\text{Co(III)Cl}_2]\text{Cl}$ complexes **85**, **87**, **91**, **93**, **89** and **95**, were prepared *via* the formation of intermediate Co(III) carbonate complexes in good to excellent yields. Their characterisation by NMR and UV-Vis spectroscopies, CV and X-ray crystallography confirmed the expected presence of the diamagnetic low spin Co(III) metal in a pseudo-octahedral geometry in these metal complexes. The crystal structures of the novel complex **86** as well as **89** were obtained and extensively studied and compared to the previously obtained crystal structure of $[\text{Co(cyclen)Cl}_2]\text{Cl}$ complex. Overall, UV-Vis, X-ray and cyclic voltammetry data also confirmed the hypothesis that even small structural modifications on tetraamine ligands (such as *N*-alkylation) result in significant changes in the properties of their corresponding metal complexes, such as distortion of the coordination geometry around the metal ion, rates of labile ligand exchange and the Lewis acidity of the metal in the complex. The effects of axial *N*-methylation as well as incorporation of the cross-bridge into the cyclen cavity on the hydrolytic activity of the Co(III) complexes will be demonstrated in the next chapter. Finally, six di-chloride Co(III) complexes were successfully converted to the corresponding hydrolytically active aqua-hydroxo species in HEPES (10 mM, pH 7.2) by the addition of two equivalents of aqueous NaOH, which could be followed by the shift of the wavelength in the visible region and was accompanied by the corresponding colour change from violet to pink.

In addition, analogous cyclen-based Zn(II) complexes of the ligands were prepared and isolated as beige solids in good to excellent yields with the view to investigate the effect of metal cation on the catalytic activity of such complexes towards phosphate ester hydrolysis.

2.5. Bibliography

1. J. Chin and M. Banaszczyk, *J. Am. Chem. Soc.*, 1989, **111**, 4103-4105.
2. J. Chin and X. Zou, *J. Am. Chem. Soc.*, 1988, **110**, 223-225.
3. J. Chin, M. Banaszczyk, V. Jubian and X. Zou, *J. Am. Chem. Soc.*, 1989, **111**, 186-190.
4. J. Chin, *Acc. Chem. Res.*, 1991, **24**, 145-152.
5. J. A. Connolly, M. Banaszczyk, R. C. Hynes and J. Chin, *Inorg. Chem.*, 1994, **33**, 665-669.
6. R. Hettich and H. Schneider, *J. Am. Chem. Soc.*, 1997, **119**, 5638-5647.
7. J. Kim, *J. Korean Chem. Soc.*, 1998, **42**, 240-244.
8. R. Jorge, PhD Thesis, Queen Mary University of London, 2011.
9. A. Jorge, M. Chernobryva, S. E. J. Rigby, M. Watkinson and M. Resmini, *Chem. Eur. J.*, 2016, **22**, 3764-3774.
10. F. Mancin, P. Scrimin and P. Tecilla, *Chem. Commun.*, 2012, **48**, 5545-5559.
11. D. A. Knight, J. B. Delehanty, E. R. Goldman, J. Bongard, F. Streich, L. W. Edwards and E. L. Chang, *Dalton Trans.*, 2004, **13**, 2006-2011.
12. J. B. Delehanty, T. C. Stuart, D. A. Knight, E. R. Goldman, D. C. Thach, J. E. Bongard and E. L. Chang, *RNA*, 2005, **11**, 831-836.
13. J. B. Delehanty, J. E. Bongard, D. C. Thach, D. A. Knight, T. E. Hickey and E. L. Chang, *Bioorg. Med. Chem.*, 2008, **16**, 830-837.
14. A. L. Reiff, E. M. Garcia-Frutos, J. M. Gil, O. P. Anderson and L. S. Hegedus, *Inorg. Chem.*, 2005, **44**, 9162-9174.
15. N. Bernier, J. Costa, R. Delgado, V. Félix, G. Royal and R. Tripier, *Dalton Trans.*, 2012, **40**, 4514-4526.
16. N. E. Brasch, D. A. Buckingham, C. R. Clark and A. Rogers, *Inorg. Chem.*, 1998, **37**, 4865-4871.
17. C. S. Jeung, J. B. Song, Y. H. Kim and J. Suh, *Bioorg. Med. Chem. Lett.*, 2001, **11**, 3061-3064.
18. M. Shibata, *Modern synthesis of Co(III) complexes*, Springer-Verlag, New York, 1993.
19. J. Chin, M. Banaszczyk, V. Jubian and X. Zou, *J. Am. Chem. Soc.* 1989, **111**, 186-190.
20. a) M. Diez-Castellnou, F. Mancin and P. Scrimin, *J. Am. Chem. Soc.*, 2014, **136**, 1158-1161; b) O. Iranzo, A. Y. Kovalevsky, J. R. Morrow and J. P. Richard, *J. Am. Chem. Soc.*, 2003, **125**, 1988-1993; c) A. Tamilselvi and G. Mugesh, *Chem. Eur. J.*, 2010, **16**, 8878-8890.

21. L. Marchetti and M. Levine, *ACS Catal.*, 2011, **1**, 1090-1118.
22. J. E. W. Scheuermann, K. F. Sibbons, D. M. Benoit, M. Motevalli and M. Watkinson, *Org. Biomol. Chem.*, 2004, **2**, 2664-2670.
23. a) G. Ilyashenko, G. De Faveri, S. Masoudi, R. Al-Safadi and M. Watkinson, *Org. Biomol. Chem.*, 2013, **11**, 1942-1951; b) K. Shastri, E. W. C. Cheng, M. Motevalli, J. Schofield, J. S. Wilkinson and M. Watkinson, *Green Chem.*, 2007, **9**, 996-1007.
24. a) K. Jobe, C. H. Brennan, M. Motevalli, S. M. Goldup and M. Watkinson, *Chem. Commun.*, 2011, **47**, 6036-6038; b) E. Tamanini, A. Katewa, L. M. Sedger, M. H. Todd and M. Watkinson, *Inorg. Chem.*, 2009, **48**, 319-324; c) E. Tamanini, S. E. J. Rigby, M. Motevalli, M. H. Todd and M. Watkinson, *Chem. Eur. J.*, 2009, **15**, 3720-3728; d) J. Pancholi, D. J. Hodson, K. Jobe, G. A. Rutter, S. M. Goldup and M. Watkinson, *Chem. Sci.*, 2014, **5**, 3528-3535.
25. S. C. Maddock, P. Pasetto and M. Resmini, *Chem. Commun.*, 2004, 536-537.
26. D. Carboni, K. Flavin, A. Servant, V. Gouverneur and M. Resmini, *Chem. Eur. J.* 2008, **14**, 7059-7065; b) M. Resmini, *Anal. Bioanal. Chem.*, 2012, **402**, 3021-3026.
27. A. Servant, K. Haupt and M. Resmini, *Chem. Eur. J.* 2011, **17**, 11052-11059.
28. M. Resmini, *Anal. Bioanal. Chem.*, 2012, **402**, 3021-3026.
29. K. Severin, *Curr. Opin. Chem. Biol.*, 2000, **4**, 710-714.
30. K. A. Holbrook and L. Ouellet, *Can. J. Chem.*, 1958, **36**, 868-690.
31. M. Resmini, R. Vigna, C. Simms, N. J. Barber, E. P. Hagi-Pavli, A. B. Watts, C. Verma, G. Gallacher and K. Brocklehurst, *Biochem. J.*, 1997, **326**, 279-287.
32. T. Koike and E. Kimura, *J. Am. Chem. Soc.*, 1991, **113**, 8935-8941.
33. M. Subat, K. Woinaroschy, C. Gerstl, B. Sarkar, W. Kaim and B. Köing, *Inorg. Chem.*, 2008, **47**, 4661-4668.
34. L. Bonfa, M. Gatos, F. Mancin, P. Tecilla and U. Tonellato, *Inorg. Chem.*, 2003, **42**, 3943-3949.
35. W. Kaim and B. Schwederski, *Bioinorganic Chemistry: Inorganic Elements in the Chemistry of Life: An Introduction and Guide*, Wiley, 1993.
36. W. C. Baker, M. J. Choi, D. C. Hill, J. L. Thompson and P. A. Petillo, *J. Org. Chem.*, 1999, **64**, 2683-2689.
37. A. Khan, J. D. Silversides, L. Madden, J. Greenman and S. J. Archibald, *Chem. Commun.*, 2007, 416-418.
38. L. Ronconi and P. J. Sadler, *Coord. Chem. Rev.*, 2007, **251**, 1633.
39. M. Suchy and R. H. E. Hudson, *Eur. J. Org. Chem.*, 2008, 4847-4865.

40. G. R. Weisman, S. C. H. Ho and V. Johnson, *Tetrahedron Lett.*, 1980, **21**, 335-338.
41. J. Rohovec, R. Gyepes, I. Císařová, J. Rudovský and I. Lukeš, *Tetrahedron Lett.*, 2000, **41**, 1249-1253.
42. G. Hervé, H. Bernard, N. Bris, M. Baccon, J. Yaouanc and H. Handel, *Tetrahedron Lett.*, 1999, **40**, 2517-2520.
43. S. Develay, R. Tripier, F. Chuburu, M. Baccon and H. Handel, *Eur. J. Org. Chem.*, 2003, **16**, 3047-3050.
44. B. H. Abdulwahaab, B. P. Burke, J. Domarkas, J. D. Silversides, T. J. Prior and S. J. Archibald, *J. Org. Chem.* 2016, **81**, 890-898.
45. L. M. P. Lima, D. Esteban-Gómez, R. Delgado, C. Platas-Iglesias and R. Tripier, *Inorg. Chem.*, 2012, **51**, 6916-6927.
46. a) D. E. Ward and C. K. Rhee, *Can. J. Chem.*, 1989, **67**, 1206-1211; b) C. A. Martin, P. M. McCrann, M. D. Ward, G. H. Angelos and D. A. Jaeger, *J. Org. Chem.*, 1984, **49**, 4392-4396.
47. M. Argese, M. Brocchetta, M. Miranda, A. Ferraris, P. Dapporto, P. Paoli and P. Rossi, *Tetrahedron*, 2007, **63**, 6915-6923.
48. N. Bernier, M. Allali, R. Tripier, F. Conan, V. Patinec, S. Develay, M. Baccon and H. Handel, *New J. Chem.*, 2006, **30**, 435-441.
49. a) G. R. Weisman, M. R. Rogers, E. H. Wong, J. P. Jasinski and E. S. Paight, *J. Am. Chem. Soc.*, 1990, **112**, 8604-8605; b) G. R. Weisman, E. H. Wong, D. C. Hill, M. E. Rogers, D. P. Reed and J. C. Calabrese, *Chem. Commun.*, 1996, 947-948; c) T. J. Hubin, J. M. McCormick, S. R. Collinson, N. W. Alcock and D. H. Busch, *Chem. Commun.*, 1998, 1675-1676; d) E. H. Wong, G. R. Weisman, D. C. Hill, David P. Reed, M. E. Rogers, J. S. Condon, M. A. Fagan, J. C. Calabrese, K. Lam, I. A. Guzei, and A. L. Rheingold, *J. Am. Chem. Soc.*, 2000, **122**, 10561-1572.
50. J. Y. Chang, G. Lu, R. J. Stevenson, P. J. Brothers, G. R. Clark, K. J. Botting, D. M. Ferry, M. Tercel, W. R. Wilson, W. A. Denny and D. C. Ware, *Inorg. Chem.*, 2013, **52**, 7688-7698.
51. T. J. Hubin, N. W. Alcock, H. J. Clase, L. L. Seib and D. H. Busch, *Inorg. Chim. Acta*, 2002, **337**, 91-102.
52. J. Lichty, S. M. Allen, A. I. Grillo, S. J. Archibald and T. H. Hubin, *Inorg. Chim. Acta*, 2004, **357**, 615-618.
53. J. Clayde, N. Greeves, S. Warren and P. Wothers, *Organic Chemistry*, OUP Oxford, 2001.

54. W. Niu, E. H. Wong, G. R. Weisman, D. C. Hill, D. J. Tranchemontagne, K. C. Lam, R. D. Sommer, L. N. Zakharov and A. L. Rheingold, *Dalton Trans.*, 2004, 3536-3547.
55. T. Emiliano and M. Watkinson, unpublished results.
56. R. Smith, D. Huskens, D. Daelemans, R. E. Mewis, C. D. Garcia, A. N. Cain, T. N. C. Freeman, C. Pannecouque, E. Clercq, D. Schols, T. J. Hubin and S. J. Archibald, *Dalton Trans.*, 2012, **41**, 11369-11377.
57. D. Meyerstein, *Coord. Chem. Rev.*, 1999, **185-186**, 141-147.
58. E. L. Hegg and J. N. Burstyn, *Inorg. Chem.*, 1996, **35**, 7474.
59. K. Hegetschweiler, D. Kuppert, J. Huppert, M. Stracka and M. Kaupp, *J. Am. Chem. Soc.*, 2004, **126**, 6728-6738.
60. J. P. Collman, and W. Schneider, *Inorg. Chem.* 1966, **5**, 1380-1384.
61. M. E. Sosa and M. L. Tobe, *J. Chem. Soc., Dalton Trans.*, 1985, 475-477.
62. L. J. Farrugia, *J. Appl. Cryst.*, 1997, **30**, 565.
63. J. H. Loehlin, *Acta Cryst.*, 1976, **B32**, 3063.
64. J. Giusti, S. Chimichi and M. Ciamfolini, *Inorg. Chim. Acta*, 1984, **88** 51-54.
65. a) D. Buckingham, C. R. Clark and A. J. Rogers, *Inorg. Chim. Acta*, 1995, **240**, 125-134; b) M. E. Sosa and M. L. Tobe, *J. Chem. Soc., Dalton Trans.*, 1985, 475-477; c) S. E. Castillo-Blum and M. E. Sosa-Torres, *Polyhedron*, 1995, **14**, 223-229.
66. P. Comba and A. F. Sickmuller, *Inorg. Chem.*, 1997, **36**, 4500-4507.
67. F. B. Johansson, A. D. Bond, U. G. Nielsen, B. Moubaraki, K. S. Murray, K. J. Berry, J. A. Larrabee and C. J. McKenzie, *Inorg. Chem.*, 2008, **47**, 5079-5092.
68. W. Niu, E. H. Wong, G. R. Weisman, L. N. Zakharov, C. D. Incarvitoc, A. L. Rheingold, *Polyhedron*, 2004, **23**, 1019-1025.

Chapter 3: Phosphatase-like Activity of Small-Molecule Metal Complexes and Imprinted Polymers

3.1. Introduction

The previous chapter presented the work done on the synthesis and characterisation of small-molecule metal catalysts, which provided information on how the coordination environment (e.g. $N_{eq}\text{-Co-}N_{eq}$ angle size, steric strain) and Lewis acidity of the target complexes are affected as a result of their structural modifications by *N*-alkylation. Given the fundamental importance of the tetraamine ligand structure in the phosphatase-like activity of the corresponding metal complexes,¹⁻³ a number of *N*-alkylated metal-based tetraamine complexes were prepared to investigate the effect of such structural modifications on their hydrolytic activity towards phosphate ester hydrolysis. In particular, as a novel contribution to this area of research, it was planned to compare the relevant significance of the two factors affected by *N*-alkylation - $N_{eq}\text{-Co-}N_{eq}$ angle size (opposite to the four-membered chelate) and Lewis acidity of the Co(III) cation- on the hydrolytic activity of these complexes and identify the dominant factor, which affects their phosphatase-like efficiency the most.

Literature reports suggest that a lower polarity of the environment around the metal complex enhances its hydrolytic activity towards phosphate ester bond cleavage (Chapter 1 section 1.3.3.2.5 and Chapter 2, section 2.1).⁴⁻⁶ Thus, the study of the effect of the incorporation of these small-molecule metal complexes into low polarity molecular imprinted polymers was one of the objectives of this work, with the aim to increase the phosphatase-like activity of such systems.

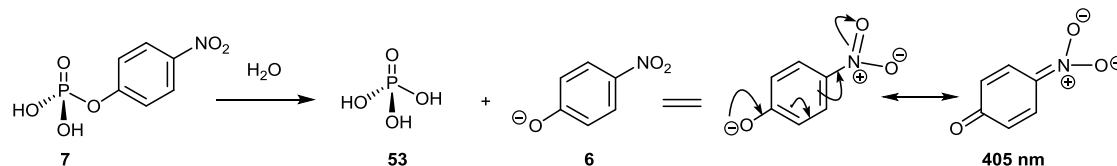
In this chapter the study of the phosphatase activity of the different complexes and the results obtained will be described and discussed. The first section will focus on the data related to the small-molecule Co(III) and Zn(II) complexes while the last two sections will discuss the data obtained with Co(III)- imprinted polymers. It is important to highlight at this stage that while the synthesis of Co(III) and Zn(II) complexes were entirely done by the candidate, the imprinted polymers were already available in the research group as a result of previous work carried out by Dr. Jorge.^{7,8} For clarity of understanding, some information regarding the synthesis and characterisation of the imprinted polymers will be given,

however, this will be kept at a minimum and Dr. Jorge's contribution will be acknowledged at all stages.

3.1.1. The Choice of Reaction: Selection of the pH and the Target Substrate *p*-Nitrophenyl Phosphate (NPP) and Bis(*p*-Nitrophenyl) Phosphate (BNPP)

The investigation of the hydrolytic activity of the target metal complexes (**16**, **50**, **17**, **18**, **55** and **54**) including MIP nanogels (**P1** and **P2**) required careful selection of the reaction conditions, of the target substrate and the appropriate methodology. In particular it was very important to ensure that such parameters, once established were kept constant, to ensure acquisition of reliable data.

The majority of the hydrolytic investigations in this project were focused on the hydrolysis of the *p*-nitrophenyl phosphate (NPP) **7**, a substrate that releases *p*-nitrophenolate **6** as one of the products (Scheme 3.1), which is a very good chromophore, with an absorption band at 405 nm, as a result of the delocalisation of the aromatic electrons outside the benzylic ring in the deprotonated form. This wavelength falls well into the visible region of the UV-Vis (light) spectrum.^{9,10}



Scheme 3.1- Spontaneous hydrolysis of *p*-nitrophenyl phosphate (NPP) **7** to give phosphoric acid **53** and *p*-nitrophenolate **6**.⁹

Analysis of the relevant literature data revealed that amongst a wide variety of phosphate substrates used to study the mechanism of phosphate ester hydrolysis, NPP is one of the most commonly used.^{2,5,10} The monophosphate ester is known to have slower hydrolysis rates in comparison to bisphosphates,⁹ a fact that together with a simpler mechanism allows more accurate kinetic studies. Holbrook and Ouellet⁹ reported that the uncatalysed hydrolysis of NPP at 68 - 82°C, in HEPES at pH 7-9 is not appreciable due to its slow rate, therefore allowing the kinetic data to be used without subtracting the background reaction, at least over a period of 48 hours. It was decided to study the NPP hydrolysis in aqueous buffered solutions (e.g. HEPES) and at 25°C as opposed to 50-70°C as normally reported in the literature,^{10,11} which result in higher rates of spontaneous NPP cleavage. In order to

calculate the yield of *p*NP released after the hydrolysis reaction, Lambert-Beer Law (Eq 3.1) was used.

$$A = \varepsilon lc \quad \text{Eq 3.1}$$

The molar extinction coefficient at 405 nm for a given conditions (25°C, pH 7.2) was already identified by previous researchers and was also confirmed in the Watkinson and Resmini groups: $\varepsilon_{\text{pH}14}(\lambda_{\text{max}}(\text{H}_2\text{O}) = 405 \text{ nm}) = 16963 \text{ M}^{-1}\text{cm}^{-1}$.^{7,8} Furthermore, the effect of the pH on ε can be mathematically calculated using the equation below (Eq 3.2), where ε_{pH} is the extinction coefficient at any measured pH and ε_{max} is the extinction coefficient at pH 14.

$$\varepsilon_{\text{pH}} = \frac{\varepsilon_{\text{max}}}{\left(1 + \frac{10^{-\text{pH}}}{10^{-\text{pKa}}}\right)} \quad \text{Eq 3.2}$$

The uncatalysed hydrolysis of the NPP substrate **7** at pH 7.2 (HEPES) and 25°C is negligible, and therefore the absence of the background rate together with the absorption at 405 nm after 48 hours clearly simplifies the hydrolytic studies.⁹

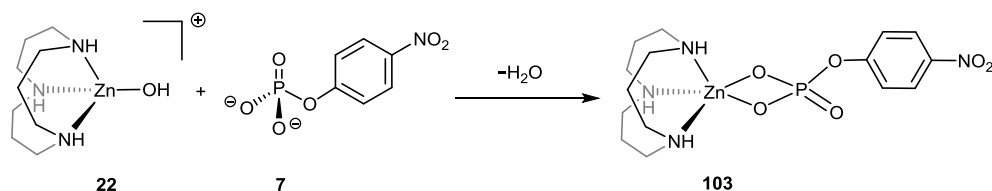
Careful consideration was given when evaluating the pH of the solutions to be used. It was determined, that the rate of the spontaneous NPP hydrolysis increases with the decrease in pH: at pH 2.6-2.7, when NPP is present mainly in the protonated form, the hydrolysis is appreciable, whereas at pH 9.0, when NPP is largely present in the ionised form, the rate of NPP hydrolysis is negligible (as mentioned previously in this section).⁹ However, in the context of this project the target pH range for the tetraamine Co(III) complexes was targeted around 7.0-7.2, because the hydrolytically active aqua-hydroxo species of the metal complex $[\text{Co}(\text{cyclen})(\text{OH}_2)\text{OH}]^{2+}$ can only exist between pH 5.6 and 8.0 (pK_a values of the aqua-hydroxo ligands on the Co(III) centre).¹⁰⁻¹² The hydrolytic studies with the tetraamine Co(III) complexes were therefore carried out at pH 7.2 and HEPES buffer (pH range of 6.8 and 8.2) was used to maintain the pH of the solution. Moreover, Basallote and colleagues established that HEPES buffer is one of the most ‘innocent’ biological buffers.¹³ It was found, that due to its ability to auto-aggregate, HEPES buffer has the least possibility to affect the progress of the formation of the tetraamine Co(III) bis-hydroxo bridged or $(\mu\text{-OH})_2$ species (the feature that will be discussed later in this chapter), in comparison to the other buffers, such as Tris (2-Amino-2-hydroxymethyl-propane-1,3-diol), MES (2-(*N*-morpholino)ethanesulfonic acid) or PIPES (piperazine-*N,N'*-bis(2-ethanesulfonic acid), which inhibit the formation of such species. This finding was based on the spectroscopic

changes observed when the UV-Vis spectra of the reaction in non-buffered medium was compared to the one in Tris and MES buffered solutions, while these spectroscopic characteristics were not affected when HEPES reaction media was used. This feature can be attributed to the complexation of Tris and MES buffers with the metal complex in an outer-sphere fashion and formation of some aggregates that prevent further progress of the reaction. Therefore, Tris, MES and PIPES buffers were avoided for such kind of studies in this research group and HEPES buffer was chosen.

It was found by Kimura *et al.*³ that there is a relationship between the pH value and the hydrolytic activity of azamacrocyclic Zn(II) complexes. Results showed, that higher pHs (up to 11) ensure higher concentration of Zn(II) species bound to the deprotonated water molecule, which leads to higher rates of the phosphate ester hydrolysis. It was therefore planned to study hydrolytic activity of the target tetraamine Zn(II) complexes at pH 9.0 and 10.0 using appropriate buffers - CAPS buffer (50 mM) and CPASO buffer (50 mM) respectively.^{3,14,15}

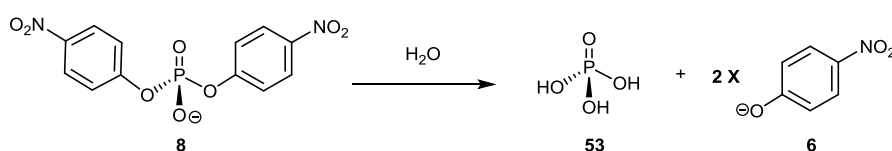
As one of the objectives of this work was the investigation of the hydrolytic activity of a range of Co(III) and Zn(II) complexes, **7** was selected as the substrate for kinetic studies with Co(III) complexes, to allow benchmarking against literature data.^{2,16} In the case of azamacrocyclic Zn(II) complexes, **7** is known to be a non-suitable substrate for these complexes and therefore was replaced by BNPP **8**, frequently used in other works.³

It is known that natural Zn(II)-based phosphatases (e.g alkaline phosphatases) are inhibited by di-anionic phosphate anions, such as NPP.^{17,18} This phenomenon was experimentally proven by Kimura *et al.*³ who showed that NP^{2-} phosphodianions have strong interactions with azamacrocyclic Zn(II) complex (with affinity constants having $\log K(A^-)$ values of 3.1 and 3.5, which are higher than 2.6 of acetate anion) and form 1:1 complexes like **103** shown in Scheme 3.2 (which is not known to be the case with macrocyclic Co(III)-based complexes). They observed, that 1,4,7-triazacyclododecane Zn(II) complex **22** showed no hydrolytic activity in the presence of NP^{2-} dianion in aqueous solution at 35°C due to the very low concentration of the reactive Zn(II)-OH⁻ species available to attack phosphate ester bond.



Scheme 3.2- Formation of the hydrolytically inactive azamacrocyclic Zn(II) complex **103** resulting from the coordination of complex **22** to the di-anionic phosphate ester **7**.³

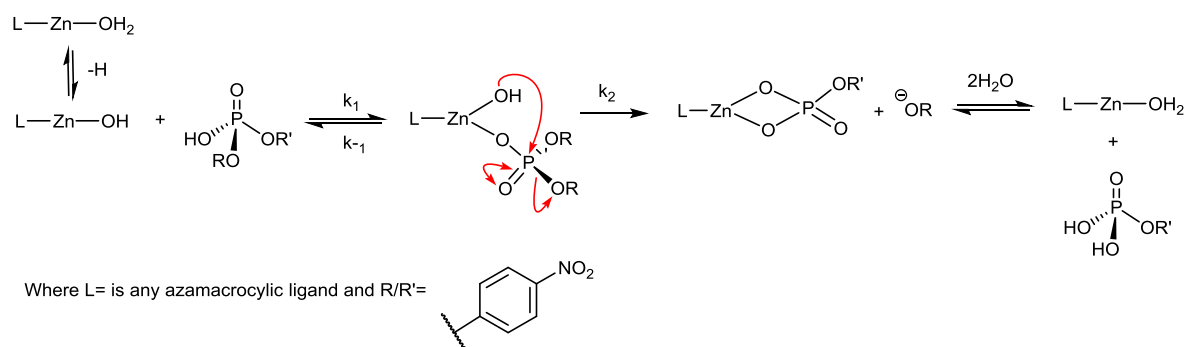
Alternatively, mono-anionic phosphate diesters, such as BNPP **8** shown in Scheme 3.3 are known to only weakly coordinate Zn(II) cations and are frequently used to investigate the hydrolytic activity of azamacrocyclic Zn(II) complexes. It was shown that in the presence of **8** in aqueous solution, sufficient amount of hydrolytically active Zn(II)-OH⁻ species are generated for the P-O bond cleavage to occur.³ Therefore, based on these findings, **8** was chosen as a target substrate to evaluate the hydrolytic activity of the tetraamine Zn(II)-based complexes in this PhD project.



Scheme 3.3- Spontaneous hydrolysis of bis(*p*-nitrophenyl) phosphate (BNPP) **8** to give phosphoric acid **53** and two molecules of *p*-nitrophenolate **6**.¹⁹

Also, the reported rate constant $K_{\text{obs}} = 1.1 \times 10^{-11} \text{ s}^{-1}$ at pH 7.0 and 25°C for the uncatalysed BNPP cleavage reflects the slow progress of this reaction at the reported conditions.^{19,20} Thus, like with **7**, the absence of the background rate together with the absorbance at 405 nm after 48 hours in the BNPP hydrolysis, simplifies catalytic studies. The uncatalysed hydrolysis reaction of **8** is depicted in Scheme 3.3.

The proposed mechanism for the phosphate ester bond cleavage by cyclen-based Zn(II) complex is depicted in Scheme 3.4. It involves deprotonation of the metal coordinated water molecule and coordination of the metal unit to the substrate oxygen atom, which is followed by the nucleophilic attack of the metal bound hydroxide and simultaneous departure of the leaving group. Subsequent deprotonation and de-complexation of the substrate occurs to restore the catalyst.



Scheme 3.4- Generally accepted mechanism for the Zn(II)-mediated hydrolysis of phosphate esters, which involves deprotonation of Zn(II)-bound nucleophile, coordination of the substrate to the metal complex, which is followed by the intramolecular nucleophilic substitution. Subsequent regeneration of hydrolytically active Zn(II) species then occurs.¹⁵

As with Co(III) complexes,^{21,22} azamacrocyclic Zn(II) complexes are also consistently used in excess when studying phosphate ester hydrolysis. Due to the biological relevance of Zn(II) cation, there is still a strong interest in exploring the factors, such as ligand structure, nucleophile and substrate activation, which can tune the reactivity of the azamacrocyclic Zn(II) complexes, although compared to cobalt the knowledge related to zinc is considerably less.^{3,14}

The next section will discuss the results obtained in the hydrolytic studies of the uncatalysed NPP and BNPP cleavage and promoted by the tetraamine Co(III) and Zn(II) small-molecule complexes. The key reasons for the differences in their hydrolytic activities will be highlighted and discussed.

3.2. Phosphate Ester Hydrolysis: Uncatalysed and Promoted by Small-Molecule *N*-Functionalised Tetraamine Co(III) and Zn(II) Complexes

3.2.1. Studies of the Uncatalysed NPP Hydrolysis

Although the uncatalysed hydrolysis of **7** was studied at elevated temperatures (e.g. 68-82°C) over a wide range of pHs (e.g. 2.6- 9.0)⁹ and its rate was determined, to our knowledge, there is a lack of reports that investigate the spontaneous hydrolysis of **7** at 25°C over long periods of time (e.g. longer than 48 hours). Thus, it was of interest to determine the time required to obtain an appreciable quantity of the hydrolytic *p*NP product in the absence of any catalyst, so that kinetic studies with polymers could be carried out for longer period of times. In this work the uncatalysed hydrolysis of **7** was monitored in HEPES buffer (10 mM, pH 7.2), at 25°C for nine days (*ca.* 220 hours). The substrate concentration was fixed at [S] 100 μM, 400 μM and 600 μM and the homogenous

solutions were kept in sealed test tubes in thermostatic bath at a constant temperature of 25°C. An increase in absorbance at 405 nm was measured, which was accompanied by the colour change from clear to yellow - a characteristic colour of *p*-nitrophenolate **6**, and the product was quantified. Figure 3.1 presents the *p*NP product concentration calculated after 9 days at [S] 100 μ M, 400 μ M and 600 μ M. It is clearly demonstrated that the increase in product concentration parallels the increase in substrate concentration with **7** at 600 μ M giving the highest quantity of **6** (81 μ M) compared to **7** at 100 μ M and 400 μ M which resulted in the release of 36 μ M and 73 μ M of **6**, respectively.

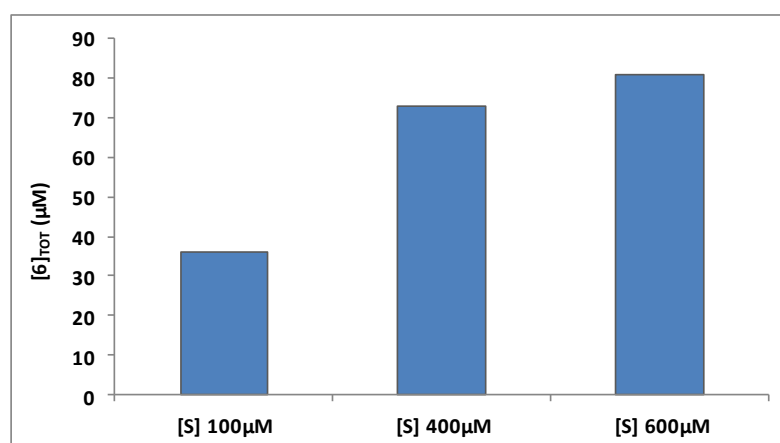


Figure 3.1- Total product *p*NP **6** (μ M) formed in the uncatalysed hydrolysis of **7** at [S] 100 μ M, 400 μ M and 600 μ M, after 9 days in HEPES (10 mM, pH 7.2) at 25°C.

These results also show that the rate of the uncatalysed NPP cleavage is slow at 25°C and pH 7.2 in HEPES buffer taking approximately nine days to reach an appreciable *p*NP concentration. This is in accord with the finding by Holbrook and Ouellet.⁹

In line with this result, it was also observed in this PhD study, that the concentration of the *p*NP product after 48 hours in aqueous solution at 25°C was estimated as being < 1 nM with [S] 400 μ M, with the product being close to the limit of detection. The absence of a background rate clearly simplified the kinetic studies of the NPP cleavage promoted by Co(III) complexes, which will be discussed in the next section.

3.2.2. Phosphate Ester Hydrolysis Promoted by Cyclen-based Co(III) Complexes

This section reports the work done to evaluate how the variation in structure of the small-molecule tetraamine Co(III) complexes affects their efficiency to promote hydrolysis of the simple phosphate monoester **7**. Here the hydrolytic activity of the six *N*-functionalised cyclen-based Co(III) complexes is examined and discussed.

In a typical hydrolytic experiment, Co(III) mediated hydrolysis of **7** was monitored with each cobalt complex used in three fold excess (1200 μM) over substrate **7** (400 μM). The target cyclen-based Co(III) complexes are shown in Figure 3.2.^{1,8}

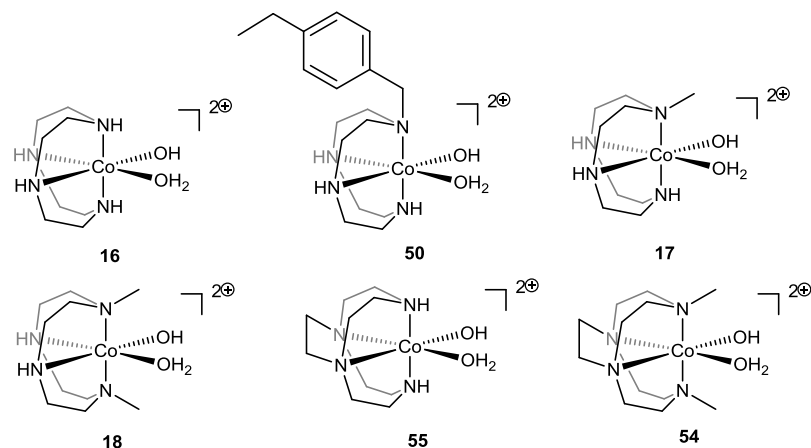


Figure 3.2- Structures of the target cyclen-based Co(III) complexes used to promote hydrolysis of substrate **7**.

It is important to highlight that stock solution of each Co(III) complex had to be prepared fresh before each hydrolytic experiment. This is because the literature data appear to suggest that such tetraamine Co(III) complexes presented here have poor stability in aqueous solutions and after *ca.* 6 hours tend to form hydrolytically inactive dimers like **104**, which is shown in Figure 3.3. This was reported by Basallote *et al.*¹³ and was not further investigated as part of this project.

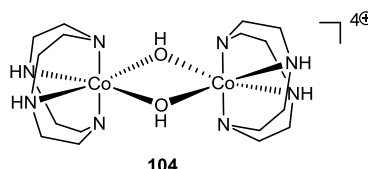


Figure 3.3- Structure of the hydrolytically inactive cyclen-based Co(III) bis-hydroxo bridged or $(\mu\text{-OH})_2$ species.¹³

In order to obtain accurate kinetic data the UV-Vis spectrometer was always calibrated with the appropriate blank solution to eliminate absorption due to the cobalt species with λ_{max} in the region between 520-540 nm. All solutions were kept in closed test tubes in a thermostatic bath at a constant temperature of 25°C between measurements. The increase in absorbance at 405 nm was monitored at set time intervals for 48 hours. The final absorbance at 48 hours was used to calculate the yield of *p*NP product obtained. The pH of the solutions was also measured at the end of each reaction and found to be pretty much constant (7.2 \pm 0.2). Each experiment was repeated three times to obtain reliable data.

Figure 3.4 illustrates the variation in the *p*NP yield % after 48 hours in the NPP hydrolysis promoted by Co(III) complexes **16**, **50**, **17**, **18**, and **54**. Interestingly there seems to be a specific trend that can be observed. The data demonstrate that unsubstituted [Co(cyclen)(OH₂)OH]²⁺ complex **16** presents the highest hydrolytic activity among the six complexes, resulting in 75% yield of *p*NP obtained after 48 hours. Comparison of the data for complex **16** with the remaining five complexes appears to suggest that any attempt to modify the ligand structure results in a decrease in hydrolytic activity. Firstly, when the original complex **16** is modified at a single point, *via* substitution at one of the nitrogen atoms of the cyclen ligand either with a methyl group or a larger *p*-ethyl benzyl unit, there is a small drop in activity going from 75% to 68% and 66% for complexes **50** and **17** respectively. This is in accord with the findings published by Kim *et al.*,² indicating that mono-methylated cyclen-based Co(III) complex catalyses phosphodiester BNPP at a slower rate compared to the unsubstituted cyclen.

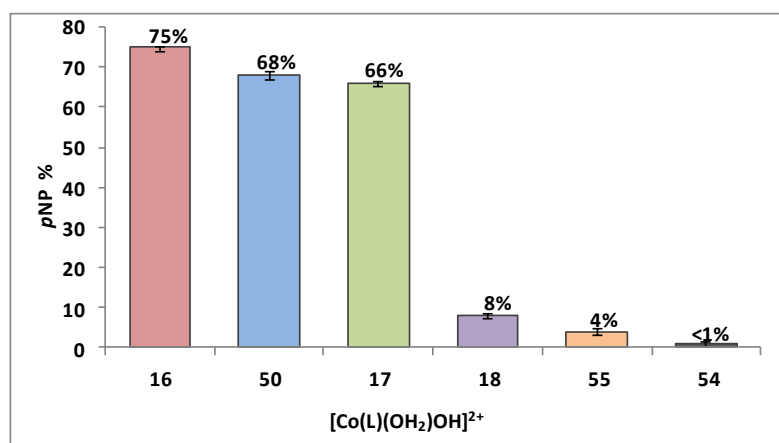
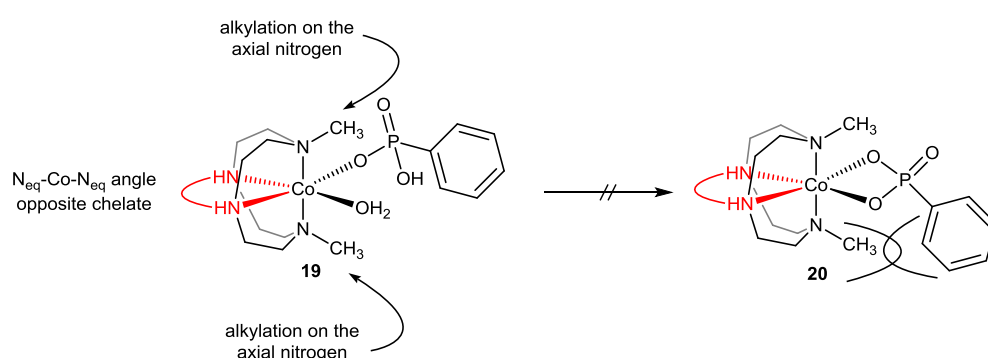


Figure 3.4- Yield of the *p*NP product obtained in the hydrolysis of substrate **7** (400 μ M) promoted by Co(III) complexes **16**, **50**, **17**, **18**, **55** and **54** (1200 μ M each) after 48 hours.

This result is further supported by the previous finding that mono-*N* alkylation of cyclen-based Co(III) complexes of such type leads to a 25% decrease in their activity towards the cleavage of supercoiled DNA.²³

Unlike mono-alkylation, the introduction of a second *N*-methyl group in **18** causes a dramatic decrease in hydrolytic activity of its complex leading to only 8% of the *p*NP yield being produced. This result confirms the hypothesis postulated by Kim *et al.*,² that incorporation of the second alkyl group on to the cyclen moiety creates a steric strain during the ring closure to form a four-membered chelate. Inhibition of the four-membered

ring formation on the Co(III) complex results in the significant reduction of the phosphate ester hydrolysis rate. Scheme 3.5 represents the result of the ^1H NMR-based binding studies between **18** and phenyl phosphonate, where the formation of the four-membered ring is inhibited by the steric hindrance created by the second methyl group on the cyclen moiety. This is consistent with the finding by Kim and colleagues, that the rate of the BNPP hydrolysis catalysed by **18** was about 1000 slower compared to the non-alkylated cyclen Co(III) complex **16**. Although the kinetic data for complexes **16**, **17** and **18** were previously reported in the literature, it was decided to repeat these experiments in order to have data that could be compared with the phosphatase-like activity of the ethylene cross-bridged complexes tested here.



Scheme 3.5- Binding of the phenyl phosphonate to **18 to form **19**: Inhibition of the four-membered ring chelate formation due to steric interactions between the methyl group on the cobalt complex and phenyl ring on the phosphonate, proposed by J.Kim *et al.*²**

In order to elucidate the effect of the ethylene cross-bridge on the activity of the cyclen Co(III) complex, hydrolytic activity of complex **55** towards NPP cleavage was tested. As illustrated in Figure 3.4, the yield of *p*NP product drops remarkably from 75% to 4% upon ethylene bridge incorporation, which is most likely to be attributed to the reduced $\text{N}_{\text{eq}}\text{-Co-}\text{N}_{\text{eq}}$ size in **55** compared to the one in **16**.⁷ This is consistent with the finding by Chin *et al.*²² that a decrease in the $\text{N}_{\text{eq}}\text{-Co-}\text{N}_{\text{eq}}$ angle on the tetraamine ligand leads to a decrease in rate of the corresponding Co(III) complex-mediated phosphate ester hydrolysis by 300 times. As it was discussed in detail in Chapter 2 (section 2.3.3.1), crystal structure of complex **89** revealed that its $\text{N}_{\text{eq}}\text{-Co-}\text{N}_{\text{eq}}$ angle is approximately 8° smaller than that in the non-bridged complex **85**, as shown in Figure 3.5. Additionally, incorporation of the ethylene cross-bridge into the cyclen moiety in **55** resulted in the decrease in its redox potential, which is reflected in the decrease of its Lewis acidity.²⁴ This work demonstrates for the first time the effect of the ethylene cross-bridge on the activity of the cyclen-based Co(III) complex towards NPP cleavage, showing that a resulting decrease in $\text{N}_{\text{eq}}\text{-Co-}\text{N}_{\text{eq}}$ angle by 8° as well

as slight drop in Lewis acidity is reflected in the remarkable drop of the hydrolytic activity of the cobalt complex.

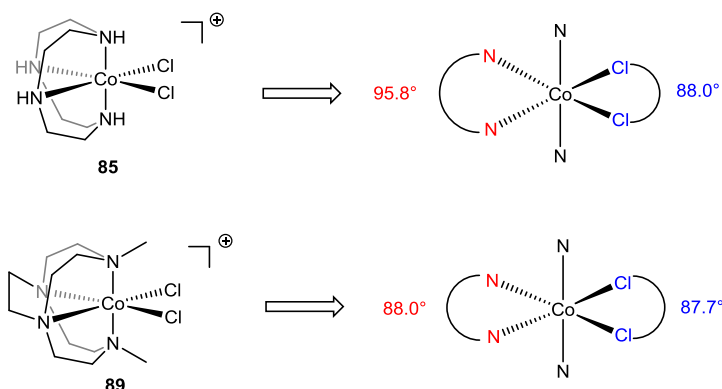


Figure 3.5- Structures of the two complexes **85**⁷ and **89**, illustrating the reduction of the N_{eq}-Co-N_{eq} angle upon ethylene cross-bridge incorporation.

The combination of the di-*N*-trans methylation and an ethylene cross-bridge on the cyclen moiety completely hampered the hydrolytic activity of the corresponding Co(III) complex **54** towards **7** under the chosen conditions, which resulted in <1% *p*NP yield, and no appreciable absorbance at 405 nm was detected after 48 hours. Interestingly, it was found by Hegg *et al.*²⁵ that triple alkylated 1,4,7-triazacyclononane (or azamacrocyclic) Cu(II) complex performed better in the hydrolysis of DNA compared to the non-alkylated one. The authors tentatively proposed that this higher activity might be attributed to the increase in Lewis acidity of the Cu(II) cation upon *N*-alkylation (as discussed extensively in Chapter 2, section 2.3.3). However, the experimental evidence presented in this work combined with the literature findings reveal that the effect of the steric strain and the N_{eq}-Co-N_{eq} angle size on the efficiency of the tetraamine Co(III) complexes in the hydrolysis of **7** is significantly more pronounced than a small increase in Lewis acidity of the cobalt cation as a result of *N*-alkylation (the latter is demonstrated by cyclic voltammetry experiments with the Co(III) complexes discussed in Chapter 2, section 2.3.3.4).

To summarise, the data presented here clearly demonstrate that the efficiency of the tetraamine Co(III) complexes towards phosphate ester hydrolysis is highly sensitive to the ligand structure. Any attempt to modify the cyclen ligand structure by *N*-alkylation appeared to result in the decrease of the hydrolytic activity of its corresponding Co(III) complex towards the NPP hydrolysis. It was observed that *N*-alkylation of cyclen at a single nitrogen reduced the complex activity only by 7% - 9%, whereas subsequent di-alkylation lead to a significant drop in hydrolytic activity of the corresponding Co(III) complexes by

67% - 71%. Also, alkylation at all four nitrogens of the cyclen ligand completely hampered the activity of the corresponding Co(III) complex. It is noteworthy, that regardless of the increased Lewis acidity on Co(III) cation due to *N*-alkylation (in complexes **50**, **17**, **18** and **54**) these complexes showed a drop in their hydrolytic activity. According to this data, it can be postulated that the reduction in the N_{eq} -Co- N_{eq} angle size is the most significant factor that impacts the activity of the tetraamine Co(III) complexes, compared to the steric interactions created by the axial *N*-alkylation. In this work, it was shown for the first time that the effect of the steric strain is more pronounced in the complex activity than the increased Lewis acidity on the cobalt cation.

In the contribution towards the progress in artificial phosphatases, these results confirm the superior role of the rational design of the small-molecule metal complexes over the Lewis acidity of the metal.

3.2.3. Phosphate Ester Hydrolysis Promoted by Cyclen-based Zn(II) Complexes

This section presents the kinetic data obtained while studying the hydrolytic activity of cyclen-based Zn(II) complexes in the hydrolysis of phosphate esters. The tetraamine Zn(II) complexes that were prepared and evaluated with the di-anionic substrate **7** are shown in Figure 3.6. The kinetic studies were first carried out on **7** to demonstrate the absence of any activity, as reported in the literature.³ This was then followed by the study of complexes efficiency towards the mono-anionic phosphate diester BNPP **8**.

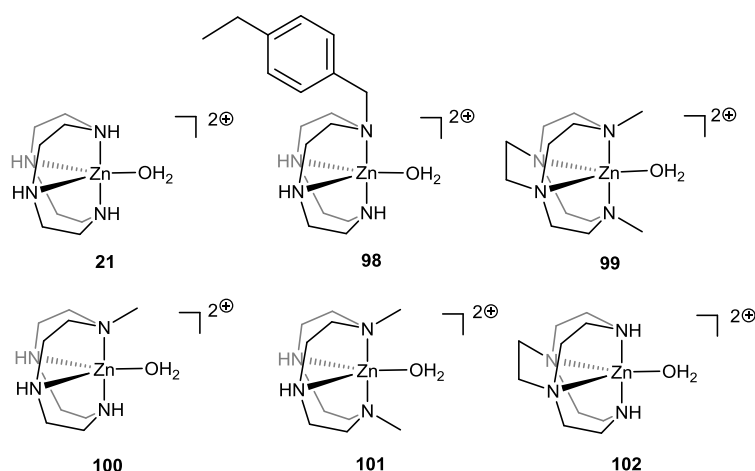


Figure 3.6- Structures of the target cyclen-based Zn(II) complexes prepared in this work to study hydrolysis of the BNPP substrate.

The kinetic data for the hydrolysis of **7** and **8** mediated by Zn(II)-based tetraamine complexes is presented and discussed in the next section.

3.2.3.1. Hydrolytic Studies With **7**

As expected, all six cyclen-based Zn(II) complexes showed no activity in promoting hydrolysis of **7**, when used in threefold excess (1200 μM) over the substrate (400 μM) in HEPES (10 mM, pH 7.2) at 25°C after 48 hours, as no appreciable absorbance at 405 nm was detected. Thus, this result confirms the finding by Kimura *et al.*³ that di-ionic phosphate ester binds to Zn(II) ion and inhibits its efficiency by significantly reducing the amount of the hydrolytically active species,^{17,18} as mentioned earlier in section 3.1.1. In light of these findings, the hydrolytic activity of the Zn(II) complexes towards **7** was not pursued further at higher pHs.

3.2.3.2. Hydrolytic Studies With **8**

The hydrolytic activity of Zn(II) complexes **21** and **100** towards mono-anionic **8** was first tested at pH 9.0 (50 mM CAPS buffer) and pH 10.0 (50 mM CPASO buffer) at 35°C based on literature reports.²⁰ The results were compared to the background hydrolysis of **8**. According to the UV-Vis spectroscopy, there was no evidence of any meaningful absorbance values at 405 nm for the BNPP cleavage at 400 μM substrate in the absence or presence of **21** and **100** at both pHs after 48 hours.

Based on the reported rate constants (K_{obs}) for the uncatalysed hydrolysis of **8** in HEPES of $5.8 \times 10^{-6} \text{M}^{-1}\text{s}^{-1}$ (at 25°C, pH 7.9), the amount of the *p*NP product released after 48 hours in the solution with [**8**] 400 μM was calculated to be less than 1 nM and hence non-detectable by UV-Vis.²⁰ This finding is in accord with the literature results. Also, like with **7**, the absence of the background rate together with the absorbance at 405 nm after 48 hours in the hydrolysis of **8** simplifies catalytic studies. It can be also concluded, that in these studies the increase in pH from the reported 7.2 to pH 9.0 and 10 did not show any appreciable effect on the spontaneous hydrolysis of **8**.

The reported second order rate constants (K_{BNP}) for the BNPP hydrolysis promoted by **100**²⁶ and **21**²⁰ are $5.2 \times 10^{-6} \text{M}^{-1}\text{s}^{-1}$ and $=2.1 \times 10^{-5} \text{M}^{-1}\text{s}^{-1}$ respectively at 35°C and pH 9.3 (CHES buffer). Thus, given these rate constant values, it can be estimated that the amount of *p*NP product produced after 48 hours should be only 1.8 μM and 7.5 μM respectively, which indicates < 2% yield. Provided no appreciable absorbance at 405 nm in the BNPP hydrolysis for **21** and **100** after 48 hours at pH 9.0 and 10.0, the results obtained are in accord with the literature data.

As a consequence of the very low activity of these two Zn(II) complexes at pH 9.0 and 10.0 at 35°C this line of investigation was not pursued further at wider pH range. Additionally, the effect of higher temperatures on the hydrolytic reaction was not pursued further due to the time constraints of this PhD project.

3.2.4. Molecular Imprinted Polymers as an Alternative to Small-Molecule Metal Complexes

In addition to studying the factors that influence the reactivity of small-molecule complexes and the effect of using different metals, researchers have investigated alternative approaches to enhance the hydrolytic efficiencies of these complexes. As already mentioned in Chapter 1, section 1.3.3.2.5 and Chapter 2, section 2.1.1.2, the environment around the metal complex was shown to play a significant role in its activity.⁴⁻⁶ For example, it was found that placing such small-molecule complexes in low polarity environments (e.g. solvents, such as MeOH and EtOH; larger polymeric matrices) that closely mimic enzyme's dielectric active sites, results in high catalytic activity and turnover with reduced catalytic load.

3.2.4.1. *Why Molecular Imprinted Nanogels?*

Among the postulated methods, the use of metal-based molecular imprinted polymers has attracted considerable interest as an alternative to the non-imprinted small-molecule hydrolytic agents for a variety of reasons. One of them is that the hydrophobic nature of the polymer creates a non-polar environment around the metal-ligand complex, which mimics the dielectric constant of the natural enzyme and thus leads to the increased hydrolytic activity of the system.²⁷ Another very important aspect of incorporating small-molecule metal complexes into a polymer matrix is that it allows reducing the catalytic load of the target system. To date the non-integrated metal-ligand complexes have been shown to promote phosphate ester hydrolysis only when used in excess, which means that they act as real reagents, not as 'true' catalysts. Integrating such small molecule complexes into the gel polymers *via* the molecular imprinting technique presents an advantageous alternative to improve the performance of small hydrolytic agents by reducing their load for the reaction to promote phosphate ester hydrolysis.⁸ There is a clear interest in developing a system that can carry out such hydrolytic reactions in a very efficient way with low catalytic load. It was therefore decided to use the molecular imprinting technique to

evaluate how the incorporation of the hydrolytic unit inside a nanogel matrix would impact its activity. The basic concept of the molecular imprinting strategy together with the synthesis and incorporation of the polymerisable complex into the polymeric matrix have already been described in Chapter 2, section 2.1.1.2.²⁸ For clarity of understanding the key structures of the polymerisable monomers and templates are provided here in Figure 3.7. The polymers and polymerisable functional monomers **48** and **105** described in the next section were prepared and characterised by Dr. Jorge⁸ and for this reason their synthesis and properties are not discussed and repeated in detail.

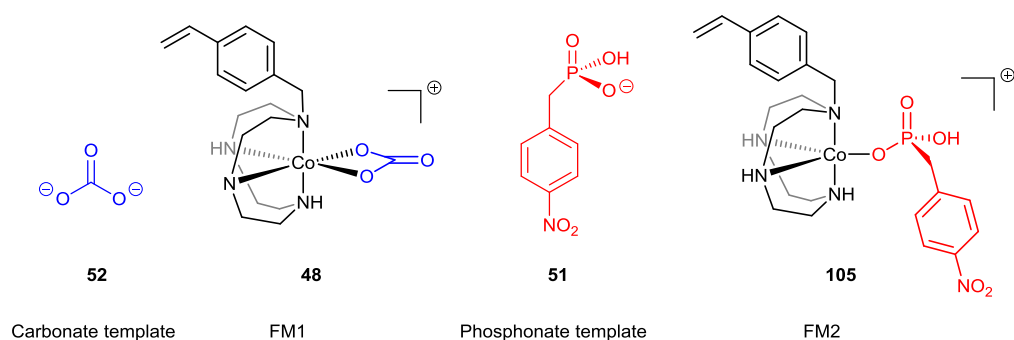


Figure 3.7- Structures of the target templates: *p*-nitrophenyl phosphonate (NPPA) **51** and carbonate **52**; structures of the target functional monomers **FM1 48** and **FM2 105**.⁸

3.2.4.2. MIP Nanogel Synthesis and Characterisation⁷

As already briefly explained in Chapter 1, nanogels are “crosslinked polymer particles that possess a size comparable to the statistical dimensions of non-cross-linked macromolecules (10 - 100 nm), which can exist as stable colloidal solutions in appropriate solvents”.⁷

Based on the significant expertise in the Resmini group^{29,30} in the synthesis of highly cross-linked nanogels, two sets of MIP nanogels **P1** (imprinted with carbonate template **52**) and **P2** (imprinted with phosphonate template **51**) were synthesised by high-dilution radical polymerisation.⁸ This involved diluting all the polymeric components in DMSO and leaving to co-polymerise at 70°C over a fixed period of time (*ca.* 4 days). Each polymer consisted of the following components: 10% of an appropriate polymerisable hydrolytic unit, 10% of the acrylamide backbone monomer **106**, 80% of methylene bis-acrylamide cross-linker **108** and 1% of AIBN radical initiator **106**, as shown in Figure 3.8.

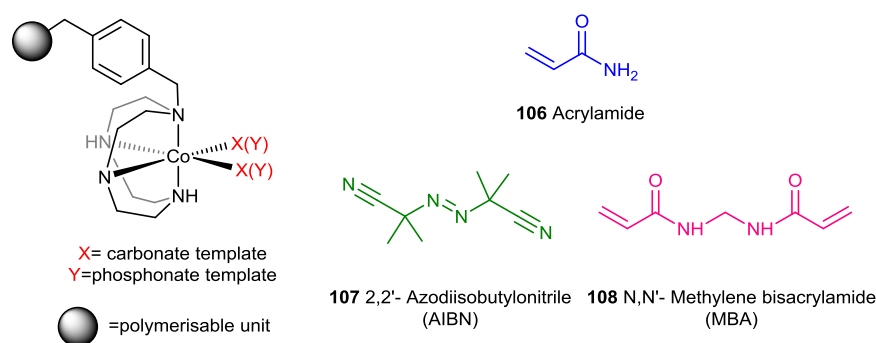


Figure 3.8- Selected monomers, cross-linker and radical initiator for the synthesis of the hydrolytic nanogels P1 and P2.⁸

The overall monomer concentration with respect to the solvent or C_M value was set to be 0.5%. After the polymerisation reaction, the polymer solutions were treated with dilute HCl to remove the template molecule followed by dialysis, to allow formation of the hydrolytically active Co(III) aqua-hydroxo species. This was followed by freeze-drying of the dialysed solutions to isolate two sets of nanogels that both contained hydrolytically active Co(III) aqua-hydroxo species: **P1** (imprinted with complex **48**) and **P2** (imprinted with complex **105**) with yields of 16% and 19% respectively. The non-imprinted nanogel **P0**, which did not contain any imprinted metallomonomer was also synthesised in 81% yield.⁸ Isolated nanogels were characterised in terms of their aqueous solubility, size, and % of the metallomonomer incorporation using various techniques, such as DLS (Dynamic Light Scattering) and FAAS (Flame Atomic Absorption Spectroscopy). **P1** and **P2** nanogels with particle size of 12 ± 2 nm and 6 ± 1 nm, respectively, were found to be highly soluble in water with **P1**: 9 mg/ml H₂O and **P2**: 7 mg/ml H₂O as expected, given their hydrophilic components. Key characteristics of both nanogels are summarised in Table 3.1.

Table 3.1- Chemical composition and characterisation of MIPs P1 and P2.⁸

Polymer	Template	Acrylamide	MBA (%)	C_M (%)	Size(nm)	Solubility H ₂ O(mg/ml)	%Co content
P1	52	10%	80%	0.5	12 ± 2	9	36
P2	51	10%	80%	0.5	6 ± 1	7	20

Prior to the incorporation into the nanogels, metallomonomers **48** and **105** were characterised by UV-Vis and EPR (**105** only) spectroscopies in DMSO.⁸ The results showed that whilst carbonate complex **48** was diamagnetic with predominantly octahedral geometry around central Co(III) cation with low spin, phosphonate complex **105** almost

exclusively adopted trigonal bipyramidal geometry around Co(II) atom with high spin d^7 electron configuration and thus showed paramagnetic behaviour. This clearly indicates that the nature of the template in these complexes affects the coordination geometry and the oxidation state of the cobalt atom. The EPR of the MIP **P2** imprinted with **105** was run after the polymerisation took place to ensure the presence of the paramagnetic species inside the polymer in the DMSO solution after the polymerisation conditions. The data confirmed that this was the case. Interestingly, after the template removal both nanogels appeared to have diamagnetic Co(III) species according to the UV-Vis and EPR data⁸ (not shown here). Prior to the hydrolytic studies in this work, the UV-Vis spectra of both nanogels **P1** and **P2** were obtained again by the candidate to ensure the presence of the Co(III) species in the polymers and their spectra are shown in Figure 3.9.

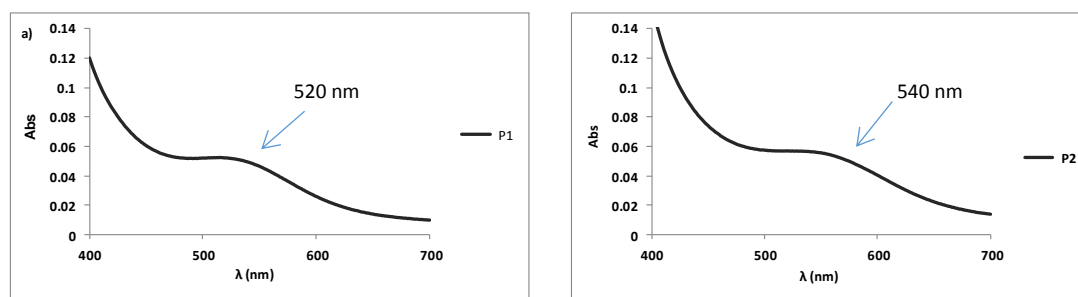


Figure 3.9- UV-visible spectra (run by the candidate) of P1 a) (100 μ M [Co]) and P2 b) (100 μ M [Co]) in HEPES (10 mM, pH 7.2) that were prepared by Dr. Jorge approximately five years ago and contain Co(III) aqua-hydroxo species.

Firstly, each spectrum has a single broad absorption band that is characteristic of Co(III) diamagnetic species, thereby confirming that both polymers contain Co(III) aqua-hydroxo metallomonomers. It can be also seen that **P1** and **P2** nanogels result in different absorption wavelengths with λ_{max} at 520 nm and 540 nm respectively, most likely as a consequence of different geometries (which are 'frozen' or imprinted in the polymeric cavities) of the cobalt complexes inside the nanogels. Most importantly comparison of these data with the original ones obtained by Dr. Jorge⁸ confirmed that the material had remained unchanged over a 3 year period.

Another key feature of the molecular imprinting is that once the polymerisable metallomonomer is incorporated in the polymer matrix, the terminal double bond on its alkyl chain is converted into a single bond by radical polymerisation process. Therefore, as explained in Chapter 2, section 2.1.1.2, structural non-integrated analogue **50** was prepared in order to investigate the effect of the *p*-ethyl benzyl moiety on the hydrolytic activity, which in turn allows more accurate evaluation of the impact of the polymeric

matrix on the phosphatase-like activity of this metal complex. As previously mentioned in section 3.2.2 of this chapter and shown again in Figure 3.10 here, the hydrolytic activity of non-polymerisable complex **50** was 7% lower compared to the non-alkylated cyclen Co(III) complex in aqueous solution at 25°C when both complexes were used in excess over the NPP substrate. This finding is in line with the results obtained by Knight *et al.*,²³ showing that alkylation at a single nitrogen atom of such Co(III) cyclen complexes resulted in 25% reduction in activity.

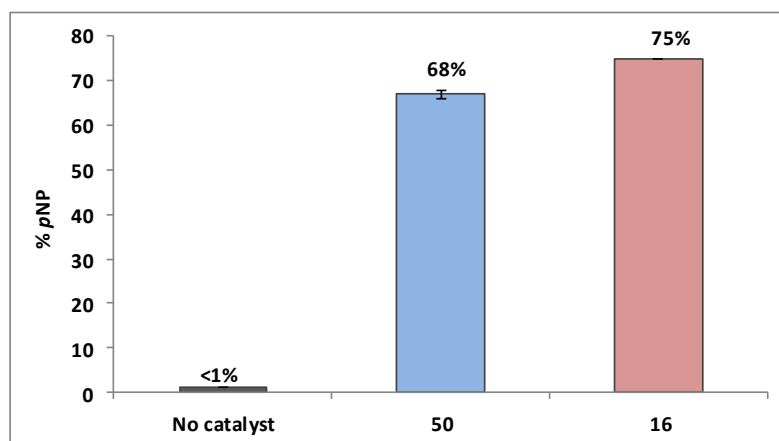


Figure 3.10- Yield of the pNP product obtained after 48 hours in the hydrolysis of substrate **7** (400 μM) without catalyst, promoted by Co(III) complexes **50** (1200 μM) and **16** (1200 μM).

The next section will present and discuss the results obtained in the study of phosphatase-like activity of the non-imprinted Co(III) complexes (used at low catalytic loads this time) versus Co(III)-based MIP nanogels. Key hydrolytic features of **P1** and **P2** nanogels will be also highlighted and explained.

3.2.5. Hydrolytic Studies Using Imprinted *Versus* Non-Imprinted Co(III) Complex Polymers

3.2.5.1. Hydrolytic Studies Using Catalytic Amounts of the Non-Imprinted Co(III) Complexes **16** and **50**

To ensure accurate evaluation of the nanogel matrix on the Co(III) complex activity towards NPP hydrolysis, it was important to study the performance of the free Co(III) complexes at the same concentration as present in **P1** and **P2** nanogels during hydrolytic studies. Thus, the investigations started by testing the performance of Co(III) complexes **16** and **50** at 23% catalytic load, the same one used for the hydrolytic studies with the nanogels.

In the experiment, solutions containing 100 μM of **16** and **50** separately were each made to react with 442 μM NPP substrate solution at 25°C in HEPES for 9 days. The amounts of total *p*NP product **6** released in each 'catalysed' reaction were then compared with that of the uncatalysed reaction and are shown in Figure 3.11. The data demonstrate, that the concentrations of **6** obtained in the 'catalysed' reaction by **16** and **50** are pretty much equal and furthermore it can be considered similar to the amount of the product obtained *via* the spontaneous NPP hydrolysis.

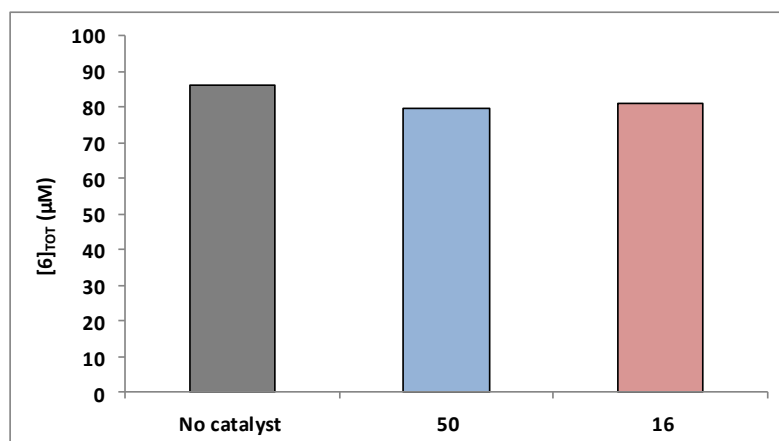


Figure 3.11- Total product **6** (μM) produced after 9 days in the hydrolysis of substrate **7** (442 μM) without catalyst, hydrolysed by **50** (100 μM) and by **16** (100 μM).

These results clearly indicate that the complexes do not promote phosphate ester hydrolysis when used in low catalytic loads. Quite the opposite, there seems to be a small inhibitory effect of these complexes on the hydrolysis of NPP, which results in the lower pace of the NPP hydrolysis involving both Co(III) complexes compared to the background reaction. This is likely to be a consequence of the irreversible binding of the second hydrolysis product to the Co(III) complex forming the four-membered chelate ring as in **47** and thus hampering the activity of the complex (as was already explained in Chapter 2, section 2.1.1.1 and is in line with the similar preliminary studies done by Dr. Jorge).^{8,22}

The hydrolytic activity of these Co(III) complexes integrated inside the nanogels are evaluated and discussed in the next section.

3.2.6. Evaluation of the Catalytic Activity of the Co(III)-Imprinted Nanogels

It is worthwhile mentioning here, that previous studies in the Watkinson and Resmini groups determined that extinction coefficient and hence the absorbance of **6** was not altered in the presence of the nanogel matrix and remained the same,⁷ which means that

the absorbance values could be taken as true values in the catalytic studies with the nanogels.⁷

In order to evaluate the efficiency of **P1** and **P2** nanogels, hydrolytic experiments were consistently carried out in HEPES buffer, at pH 7.2 and at 25°C for 9 days. The only difference with the free Co(III) complexes was that 0.1 M NaOH was not added to the nanogel stock solution (to ensure the presence of the aqua-hydroxo cobalt species), because nanogels **P1** and **P2** already contained aqua-hydroxo Co(III) species as described earlier in this chapter. To ensure that both nanogel solutions contained an equimolar amount of the imprinted cobalt complex (100 µM), different amounts of the nanogels were used given different % of Co(III) species incorporated into the polymers (section 3.2.4.2). For accurate data the UV-Vis spectrometer was always calibrated with the appropriate blank polymer solution to eliminate absorption due to the cobalt species in the nanogels. The hydrolytic activity of both nanogels was studied by comparing the concentration of the *p*NP product produced after the catalysed and uncatalysed NPP hydrolysis reaction at different substrate concentrations and at different time intervals. The results obtained are discussed below.

3.2.6.1. Catalytic Activity at Different Substrate Concentrations

To evaluate the effect of substrate concentration on the catalytic activity of both nanogels, the concentration of the cobalt active site in the polymers was fixed at [Co] 100 µM, and the concentration of the NPP substrate **7** varied between 442 µM and 664 µM, which represents the 23% and 15% catalytic loads respectively (or in other words means that complex:substrate ratio less than one) compared to the substrate. The total amount of **6** released was measured after nine days and compared to that produced in the background reactions.

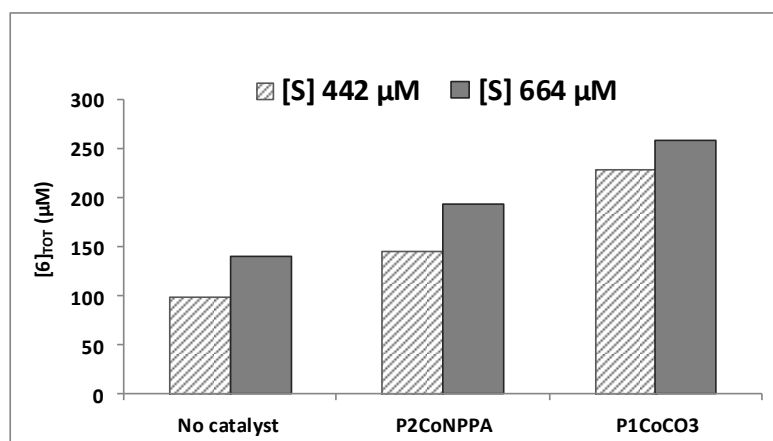


Figure 3.12- Total product **6** (μM) formed after 14 days in the hydrolysis of substrate **7** (442 μM and 664 μM) without catalyst, catalysed by **P1** (100 μM [Co]) and **P2** (100 μM [Co]).

Figure 3.12 illustrates the total concentration of hydrolysis product **6** obtained at [S] 442 μM and 664 μM after the spontaneous and catalysed hydrolysis of **7** after 9 days. The data clearly demonstrates that the amount of the product obtained after the reaction in the presence of both nanogels is higher compared to the uncatalysed phosphate ester hydrolysis at both substrate concentrations. This indicates, that regardless of the substrate concentration used, both MIP nanogels **P1** and **P2** show increased efficiency in catalysing NPP hydrolysis over the background reaction and when compared to the small-molecule complexes **16** and **50** when used in low catalytic loads. This result proves the catalytic efficiency gain in the small-molecule Co(III) complexes as a result of incorporation into the nanogellic polymers through the imprinting strategy. The data also suggests that **P1** (imprinted with the carbonate template) has enhanced activity compared to **P2** (imprinted with the cognate phosphonate template) and the rationale behind this phenomenon will be suggested in section 3.2.6.3.

3.2.6.2. Catalytic Activity Over Time

The investigations continued to establish if the same reactivity trend was consistent over longer periods of time. The total amount of **6** was measured at fixed time intervals (for the spontaneous NPP hydrolysis, and catalysed by **P1** and **P2**) at fixed [S] 442 μM and [Co] 100 μM in both nanogels.

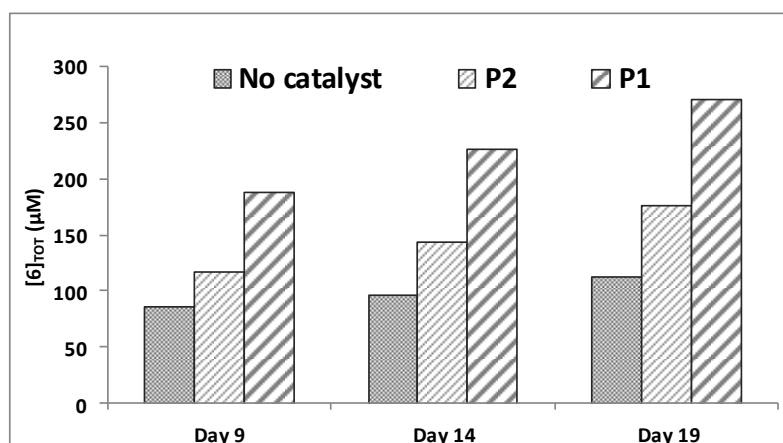


Figure 3.13- Total product **6** (μM) formed after 9, 14 and 19 days in the hydrolysis of substrate **7** ($442 \mu\text{M}$) without catalyst, catalysed by **P1** ($100 \mu\text{M}$ [Co]) and **P2** ($100 \mu\text{M}$ [Co]).

Figure 3.13 shows the total concentration of hydrolysis product **6** obtained at $[S] 442 \mu\text{M}$ after the spontaneous and catalysed NPP hydrolysis after day 9, 14 and 19. The data demonstrates, that the total $[p\text{NP}]$ concentration is gradually increasing over time and then levels off after 19 days (not shown here) for the catalysed and uncatalysed NPP hydrolysis. The results also seem to suggest that the same trend in the NPP hydrolysis is maintained over time: both nanogels show higher amount of **6** produced compared to the uncatalysed reaction, with **P1** imprinted with the carbonate template being consistently more efficient promoter of phosphate ester hydrolysis than **P2** imprinted with the cognate phosphonate template.

3.2.6.3. Factors that Influence the Catalytic Activity of **P1** and **P2**: The Effect of Template Structure

In order to establish whether nanogels show catalytic turnover, the amount of product formed as a result of the background reaction was subtracted from the total amount of the product produced in the presence of **P1** and **P2**. The net product obtained for both nanogels on day 9, 14 and 19 is depicted in Figure 3.14. It is clear, that **P1** is a more efficient catalyst than **P2** and it operates with the turnover, with $130 \mu\text{M}$ and $158 \mu\text{M}$ product being formed on day 14 and 19 respectively. This finding is very significant because it demonstrates that small-molecule tetraamine Co(III) complexes that are normally required in great excess to accelerate chemical reactions can be converted from real reagents to the ‘true’ catalysts giving turnover, once incorporated into the polymeric matrices using the molecularly imprinted technique. Interestingly, given the identical cobalt concentration in both polymers, it is evident, that the difference in their activity is a consequence of

morphological changes occurring during the imprinting process as a result of the different templated structures.

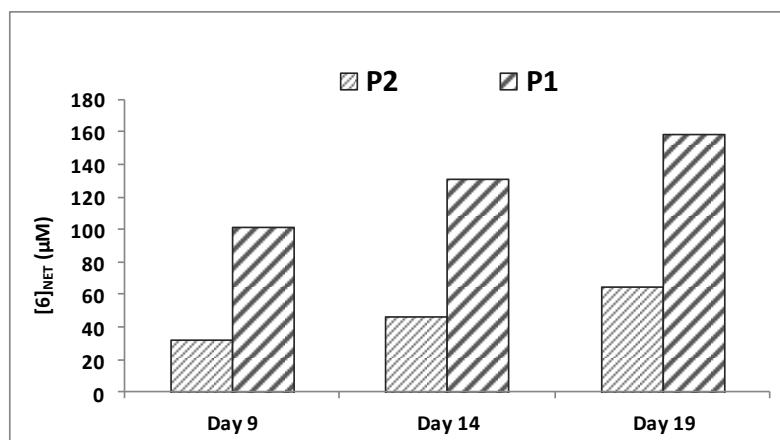


Figure 3.14- Net product 6 (μM) formed by P1 ($100 \mu\text{M}$ [Co]) and P2 ($100 \mu\text{M}$ [Co]) in the hydrolysis of substrate 7 ($442 \mu\text{M}$) on day 9, 14 and 19 (the data here have been corrected for the uncatalysed reaction).

The systematic characterisation studies in this work show that the nature of the polymerisable unit and the structure of the template impacts the coordination geometry and oxidation state of the Co(III) complexes, which can be maintained during the polymerisation process. This leads to the generation of the nanogels imprinted with both pseudo-octahedral Co(III) and trigonal bipyramidal Co(II) structures. The subsequent removal of the template results in both nanogels with catalytically active Co(III) aqua-hydroxo species in the cavities. Given the variation in catalytic activity observed, it can be deduced that the coordination geometry around the Co(III) atom can be ‘frozen’ inside the polymeric matrix as a result of the imprinting approach and such morphological differences in the polymeric matrices are responsible for the different molecular recognition capabilities.

It seems reasonable to suggest that significantly enhanced efficiency in both nanogels compared to the free complexes can be attributed due to the template site disfavours the formation of the post-hydrolysis complex **47**, which inhibits the catalytic cycle. Moreover, better performance of **P1** over **P2** can be an effect of the different morphologies in the active site of the polymer due to the difference in coordination environment between **FM1** and **FM2**. **P1** nanogel retains more strained octahedral coordination geometry due to the significantly smaller structure of the carbonate template compared to the phosphonate and resulting trigonal bipyramidal geometry. This at first site counterintuitive and surprising result becomes clear when the structural differences of the

templates are further examined in more detail and their effect on the hydrolytic efficiency of the metal complexes is compared. As discussed in Chapter 2, section 2.3.3.1, analysis of the crystal structure of [Co(**68**)(CO₃)]MeCO₃ confirmed the O-Co-O angle to be rather strained (O(1)-Co(1)-O(2) = 68° which is very similar to that seen in other Co(III) complexes containing bidentate carbonate ligands mentioned in this work and in the Cambridge Crystallographic Database.^{31,32} In contrast, the equivalent angle in Co(II) complex with phosphate chelates is considerably larger at 76°. ³³ Most importantly, as has been already discussed in this thesis (Chapter 2, section 2.3.3.1 and Chapter 3, section 3.2.2), it was shown that it is the size of the N_{eq}-Co-N_{eq} angle opposite the four-membered chelate like in **47**, that plays a key role in determining the hydrolytic efficiency of the tetraamine Co(III) complexes. Larger N_{eq}-Co-N_{eq} angles tend to stabilise the formation of the opposite four-membered chelate and result in higher hydrolytic efficiencies compared to that observed in the complexes with the smaller angles.²² It is generally accepted, that Co(III) complexes with tightly coordinated bidentate ligands, such as carbonate in **48**, have larger opposing N_{eq}-Co-N_{eq} angles, compared to the ones with monochelating ligands, such as phosphonates in **105**. Further analysis of the crystal structure of [Co(**68**)(CO₃)]MeCO₃ showed, that its N_{eq}-Co-N_{eq} is 103 ° compared to 95.8 ° for the same complex with the monodentate ligands, such as chlorides.⁷

Overall, it can be concluded, that a combination of factors is likely to contribute to the enhanced catalytic activity in **P1** and **P2**. First, there is a decrease in polarity around the Co(III) complexes inside the nanogel compared to the bulk aqueous solutions, which is known to be an enhancing factor for the similar systems.⁴ The second factor is the considerably strained coordination geometry of **48**, which results from the tight binding angle of the carbonate ligand and may better destabilize the post-hydrolysis product **47** in the polymer compared with **105** with phosphonate geometry. Moreover, based on the literature findings, larger N_{eq}-Co-N_{eq} bond angle in carbonate Co(III) complex **48** compared to that in **105** (with the phosphonate template) leads to higher rates of the P-O bond cleavage.²²

3.3. Conclusions

To summarise, hydrolytic studies in this work showed that it takes approximately 9 days to obtain an appreciable quantity of the *p*NP product in the NPP substrate hydrolysis reaction, confirming its slow rate in aqueous solutions at 25 °C.

The activity of six tetraamine Co(III) complexes towards P-O bond cleavage was tested, and results revealed that any modification on the cyclen ligand by *N*-alkylation lead to a decrease in the their efficiency in hydrolysing NPP substrate **7**. It was observed that di-alkylation resulted in more significant drop compared to the mono-alkylation, an effect that can be attributed to the steric hindrance inhibiting the post-hydrolysis Co(III) four-membered chelated formation.² Moreover, the reduction in N_{eq} -Co- N_{eq} size opposite this four-membered chelate together with the slight decrease in the Lewis acidity upon the ethylene-cross-bridge incorporation in the cyclen moiety, gave a remarkable decrease in the corresponding Co(III) complex activity from 75% to 4% chemical yield of the *p*NP product obtained. The results demonstrated that the effect of the reduced N_{eq} -Co- N_{eq} angle size is more pronounced on the hydrolytic efficiency of the Co(III) complexes, compared to the influence of steric hindrance. Interestingly, it was found, that both steric hindrance has more significant effect on the hydrolytic activity of the complexes, than the increase in Lewis acidity of the Co(III) cation resulting from the *N*-alkylation. Thus, structural modifications are key in the phosphatase-like activity of such tetraamine Co(III) complexes. Unlike Co(III) complexes, analogous Zn(II) complexes did not show any detectable activity towards BNPP hydrolysis even at higher temperatures and pHs. This result might potentially be attributed to the weaker Lewis acidity in Zn(II) ion compared to Co(III) cation. Most importantly, it was shown for the first time, that small-molecule cyclen-based Co(III) complexes normally required in large excess to promote P-O cleavage, can in fact be used in 15 % catalytic loads with turnover once incorporated into the larger nanogel polymer *via* the imprinting approach. The catalytic efficiency gain could be attributed to the lower polarity in the nanogels compared to the bulk aqueous solution.⁴ Moreover, it was demonstrated that the structure of the template in metallomonomers **FM1** and **FM2** used to imprint the polymers is key in determining the MIPs activity. It was shown that **P1** MIP imprinted with the structurally smaller carbonate template **52** resulted in the higher hydrolytic efficiency compared to **P2** MIP imprinted with the larger cognate phosphonate template **51**, as a result of the more strained coordination geometry and larger N_{eq} -Co- N_{eq} bond angle in **48**.

3.4. Bibliography

1. J. Chin and X. Zou, *J. Am. Chem. Soc.*, 1988, **110**, 223-225.
2. J. Kim, *J. Korean Chem. Soc.*, 1998, **42**, 240-244.
3. T. Koike and E. Kimura, *J. Am. Chem. Soc.*, 1991, **113**, 8935-8941.
4. a) M. Diez-Castellnou, F. Mancin and P. Scrimin, *J. Am. Chem. Soc.*, 2014, **136**, 1158-1161; b) A. A. Neverov, Z.-L. Lu, C. I. Maxwell, M. F. Mohamed, C. J. White, J. S. W. Tsang and R. S. Brown, *J. Am. Chem. Soc.*, 2006, **128**, 16398-16405.
5. F. Mancin, P. Scrimin and P. Tecilla, *Chem. Commun.*, 2012, **48**, 5545-5559.
6. L. Marchetti and M. Levine, *ACS Catal.*, 2011, **1**, 1090-1118.
7. R. Jorge, PhD Thesis, Queen Mary University of London, 2011.
8. A. Jorge, M. Chernobryva, S. E. J. Rigby, M. Watkinson and M. Resmini, *Chem. Eur. J.*, 2016, **22**, 3764-3774.
9. K. A. Holbrook and L. Ouellet, *Can. J. Chem.*, 1958, **36**, 868-690.
10. J. Chin and X. Zou, *J. Am. Chem. Soc.*, 1988, **110**, 223-225.
11. J. Chin, M. Banaszczyk, V. Jubian and X. Zou, *J. Am. Chem. Soc.*, 1989, **111**, 186-190.
12. N. E. Brasch, D. A. Buckingham, C. R. Clark and A. Rogers, *Inorg. Chem.*, 1998, **37**, 4865-4871.
13. M. Bassallote, M. Martínez and M. Vázquez, *Dalton Trans.*, 2014, **43**, 11048-11058.
14. M. Subat, K. Woinaroschy, C. Gerstl, B. Sarkar, W. Kaim and B. Köing, *Inorg. Chem.*, 2008, **47**, 4661-4668.
15. L. Bonfa, M. Gatos, F. Mancin, P. Tecilla and U. Tonellato, *Inorg. Chem.*, 2003, **42**, 3943-3949.
16. M. Zhaoa, S. S. Xuea, X. Q. Jianga, L. Zhengb, L. N. Jia and Z. W. Mao, *J. Mol. Cat. A: Chem.*, 2015, **396**, 346-352.
17. R. K. Morton, *Biochem. J.*, 1955, **61**, 232-240.
18. H. N. Fernley, P. G. Walker, *Biochem. J.*, 1967, **104**, 1011-1018.
19. M. J. Young, D. Wahnnon, R. C. Hynes, and J. Chin, *Int. J. Chem. Kinet.*, 2012, 398-403.
20. A. Yatsimirsky, *Coord. Chem. Rev.*, 2005, **249**, 1997-2011.
21. M. Shibata, *Modern Synthesis of Co(III) Complexes*, Springer-Verlag, New York, 1993.
22. J. Chin, *Acc. Chem. Res.*, 1991, **24**, 145-152.
23. D. A. Knight, J. B. Delehanty, E. R. Goldman, J. Bongard, F. Streich, L. W. Edwards and E. L. Chang, *Dalton Trans.*, 2004, **13**, 2006-2011.

24. J. Y. Chang, G. Lu, R. J. Stevenson, P. J. Brothers, G. R. Clark, K. J. Botting, D. M. Ferry, M. Tercel, W. R. Wilson, W. A. Denny and D. C. Ware, *Inorg. Chem.*, 2013, **52**, 7688-7698.
25. E. L. Hegg and J. N. Burstyn, *Inorg. Chem.*, 1996, **35**, 7474.
26. E. Kimura, Y. Kodama, T. Koike: and M. Shire, *J. Am. Chem. Soc.* 1995,**117**, 8304-8311.
27. M. Resmini, *Anal. Bioanal. Chem.*, 2012, **402**, 3021-3026.
28. K. Severin, *Curr. Opin. Chem. Biol.*, 2000, **4**, 710-714.
29. S. C. Maddock, P. Pasetto, M. Resmini, *Chem. Commun.*, 2004, 536-537.
30. a) D. Carboni, K. Flavin, A. Servant, V. Gouverneur and M. Resmini, *Chem. Eur. J.* 2008, **14**, 7059-7065; b) M. Resmini, *Anal. Bioanal. Chem.*, 2012, **402**, 3021-3026.
31. J. H. Loehlin, *Acta Cryst.*, 1976, **B32**, 3063.
32. J. Giusti, S. Chimichi and M. Ciamfolini, *Inorg. Chim. Acta*, 1984, **88** , 51-54.
33. A. S. Kumbhar, M. S. Deshpanden and R. J. Butcher, *Cryst. Eng. Comm.*, 2008, **10**, 1520-1523.

Chapter 4: Synthesis and Characterisation of Complexes of Tripodal 'Click'-based Ligands as Potential Small-Molecule Catalysts for Phosphate Ester Hydrolysis

4.1. Introduction

The central idea of this project was further extended by deviating from the use of traditional macrocyclic Co(III)-based systems as phosphatase mimics to the development of novel d-block metal complexes of 'click'-based tripodal ligands. Although there are some reports on the coordination behaviour, structural properties, and some catalytic applications (that will be discussed later in this chapter) of these type of complexes, such as **109**¹ (Figure 4.1), no previous studies have reported their use in enzyme mimicry towards the hydrolysis of phosphate esters. Thus, these 'click'-based metal complexes can potentially open a new line of investigation in the development of catalysts for phosphate ester hydrolysis.

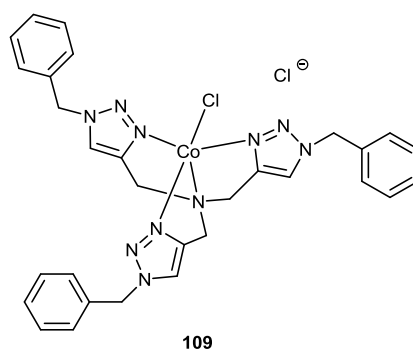


Figure 4.1- Structure of the reported TBTA-based Co(II) complex **109**, where Co(II) is coordinated to TBTA in a capped tetrahedral coordination geometry (one of the most commonly reported geometries in 1:1 metal-ligand complexes of this type).¹

This chapter presents the key features of this approach, such as the design, synthesis and characterisation of the tripodal 'click' ligands and their corresponding d-block metal complexes. The first part of the chapter describes the rationale behind the choice of the target 'click'-based ligands and their corresponding metal complexes as potential candidates for phosphate ester hydrolysis. The following section outlines and discusses the main synthetic challenges encountered in the preparation of the target ligands and their metal complexes. Thereafter, the final part focusses on the extensive and systematic investigation of their coordination and redox chemistry with a range of techniques,

including single crystal X-ray crystallography, EPR spectroscopy, cyclic voltammetry and UV-Vis spectroscopy.

4.1.1. The Choice of Triazole-based Tripodal Ligands and Their Corresponding Metal Complexes as Potential Promoters of Phosphate Ester Hydrolysis

At present, the use of small-molecule d-block metal complexes that can promote hydrolytic cleavage of phosphate ester bonds is central in the area of phosphatase metalloenzyme mimicry.² In particular, metal complexes of multidentate nitrogen chelating ligands are being increasingly investigated. The existence of the *N*-donor in the histidine amino acid residue present in the active sites of many natural hydrolytic enzymes has motivated researches to extensively study multiple *N*-donor ligands containing pyridine and/or triazole-based functional moieties that show some resemblance to imidazole.³ For example, imidazole-based ligand **42** shown in Figure 4.2 has been successfully used to prepare Cu(II) and Zn(II) complexes which showed rate accelerations over the uncatalysed cleavage of the BNPP with rate constants of $k_1 = 7.6 \times 10^{-6} \text{ mM min}^{-1}$ and $k_1 = 2.7 \times 10^{-5} \text{ mM min}^{-1}$ respectively.⁴

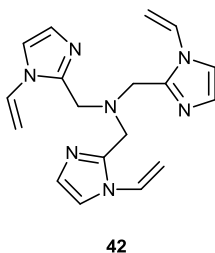


Figure 4.2- Chemical structure of the imidazole-based tripodal ligand that was used by Severin *et al.* to prepare hydrolytically active Zn(II) and Cu(II) complexes.⁴

Interestingly, Yang *et al.*⁵ reported that 1,2,4-triazole-based di-Cu(II) complex (L=3,5-bis(bis(pyridine-2-ylmethyl)amino)methyl)-4*H*-1,2,4-triazole-4-amine) where two Cu(II) cations are bridged by a 1,2,4-triazole of the ligand, gave 7.2×10^7 -fold rate enhancement in the hydrolytic cleavage of double stranded DNA at 37°C over the uncatalysed reaction. Despite the fact that multiple 1,2,3-triazole-based metal complexes have not yet been tested for their ability to promote phosphate ester bond cleavage, there is an increasing interest in the literature in the synthesis of 'click'-generated tetradentate tripodal ligands that show strong chelating abilities to a number of metal cations.^{1,6-10} In this work, it was decided to prepare a range of 1,2,3-triazole tripodal ligands (and their corresponding metal complexes) that could pave the way for the development of novel hydrolytically active small-molecule metal complexes in enzyme mimicry for several reasons: 1) polyamine *N*-

chelate ligands are known to form stable metal complexes;⁶ 2) coordinated metals can potentially contain one labile nucleophilic hydroxide anion to promote P-O bond cleavage;¹ 3) the 1,2,3-triazole shows structural similarities to imidazole;³ 4) they can be easily prepared in one or two steps from the commercially available materials in large quantities; 5) they can be readily tuned sterically and electronically due to the modularity of the ‘click’ reaction used to prepare them.^{1,10,11} Figure 4.3 presents the general structure of the tripodal amine ligand and structures of the three 1,2,3-triazole based tripodal ligands used in this work: tris[(1-benzyl-1*H*-1,2,3-]triazol-4-yl)methyl]amine (TBTA) **110**,¹² the fully conjugated analogue of TBTA- TPTA **111**¹¹ and the more hydrophilic TBTA version- TCTA **112**.¹³ These nitrogen-rich ligands have three side arms, each containing aromatic-substituted triazole moieties that provide π -stacking interactions within and between the molecules. N₂ and N₃ nitrogen donors on each of the three triazole moieties together with the tertiary central amine can potentially bond to the metal cation and their different basicity allows for selective metal coordination.⁶

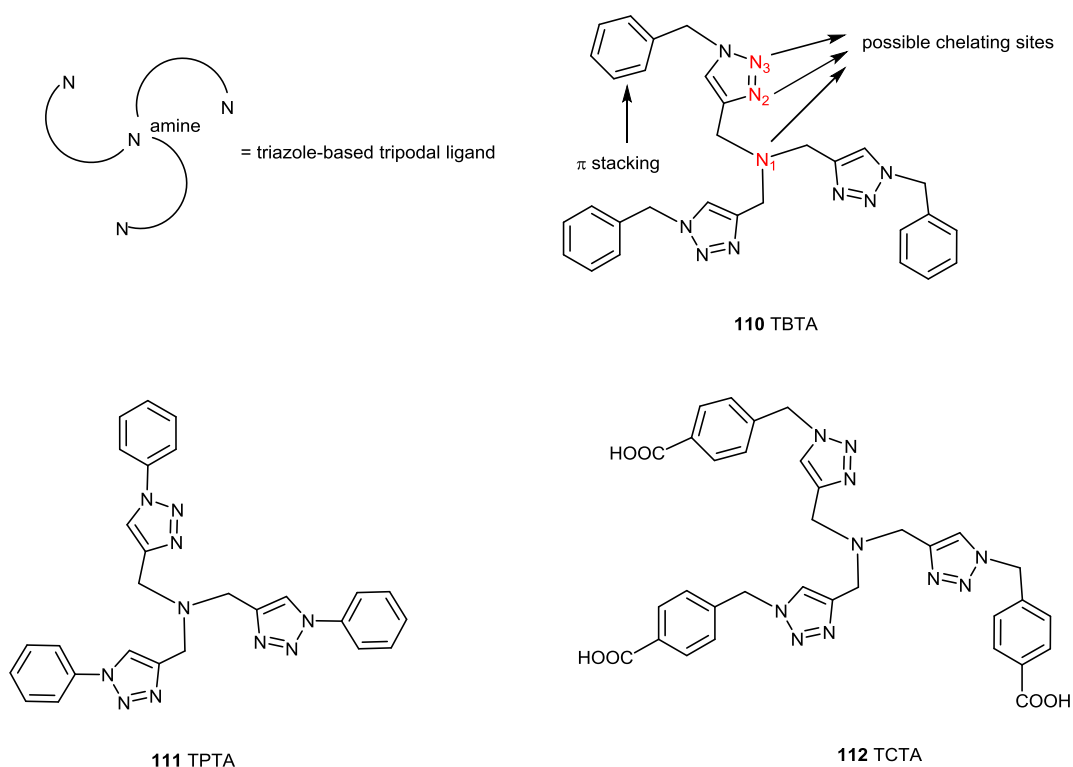


Figure 4.3- Structures of the 1,2,3-triazole ligands **110**, **111** and **112** used in this work.

The chelating abilities of such ligands are attributed to the ‘click’ triazole functional moiety, and they are extensively compared in the literature to the pyridine-based ligands, such as TMPA **113** (Figure 4.4). For example, two tripodal Co(II) complexes of ligands **113** and **110** were compared by Sweinfurth *et al.*¹ It was found, that Co-N(triazole) bond distances in

[Co(**110**)Cl]Cl complex **109** are 0.03-0.05 Å shorter compared to the equivalent Co-N(pyridine) distances in [Co(**113**)Cl]Cl complex **114** (Figure 4.4). However, the distances between the metal and central amine nitrogen (Co-N(amine)) in [Co(**110**)Cl]Cl and [Co(**113**)Cl]Cl are 2.350(3) Å and 2.184(6) Å respectively, indicating that Co-N bond in **109** is longer than in **114** and is acting as a capping bond. Thus, the coordination geometry in **109** is described as capped tetrahedral or pseudo-tetrahedral 4+1, whereas **114** adopts trigonal bipyramidal geometry.

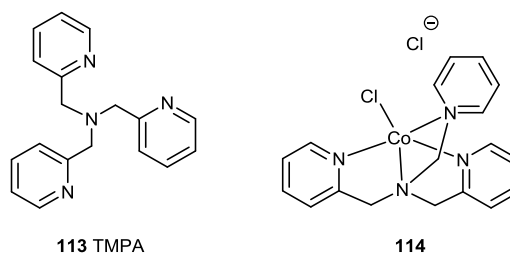


Figure 4.4- Structures of pyridine-based TMPA ligand **113** and its corresponding Co(II) complex **114**.^{1,3}

Metal complexes (e.g. Co(II)) of the triazole-like tripodal ligands, such as AMPT **115** (Figure 4.5) have been also investigated and the coordination geometry of their Co(II) complexes was reported to be pseudo-tetrahedral (or capped tetrahedral) as in the case of the 1,2,3-triazole-based metal complexes.¹

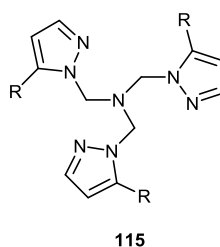


Figure 4.5- Chemical structure of the triazole-like tripodal AMPT ligand **115**.¹

It is also known that due to the presence of the triazole-based functional groups (or side arms), such 'click'-based ligands possess large structural flexibility unlike the more rigid terpyridine ligands.¹ This phenomenon results in a wider range of coordination modes in the corresponding triazole-based metal complexes, compared to the analogous pyridine-based complexes, which has been the subject of investigations by Schweinfurth and co-workers.^{1,6-9} For example, the Co(II) centre in **114** adopts the expected trigonal bipyramidal geometry, whereas its complex with **110** results in an unusual five-coordinate capped tetrahedral geometry, which will be discussed in detail in section 4.4.2.5. Another interesting example was presented by Donnelly *et al.*¹⁰ who reported the single crystal X-

ray crystal structure of an unusual dinuclear Cu(I) complex of the TBTA ligand, produced under anaerobic conditions. In this complex each Cu(I) cation adopts a distorted tetrahedral geometry with one triazole unit from each TBTA ligand bridging between two metal centres: three coordination sites on Cu(I) in this complex are occupied by the nitrogens of the triazole groups from one TBTA molecule, with the fourth being coordinated to the medial and proximal nitrogen from the triazole group of another TBTA molecule within the dimer. Moreover, in some cases like in the Ni(II) complex **116**⁸ (Figure 4.6), the TBTA ligand was shown to act as a tridentate ligand as opposed to the regular tetradentate ligand, which demonstrates the unpredictable nature of the coordination chemistry of such ligands.

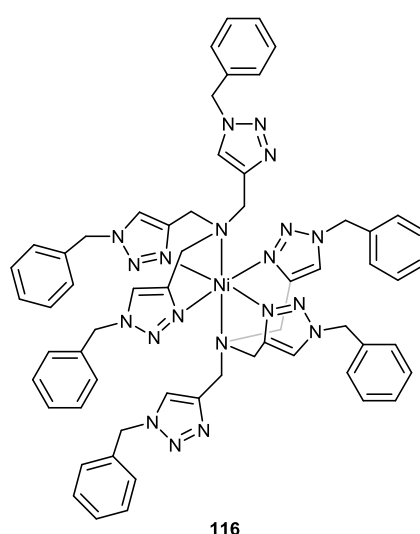


Figure 4.6- Structure of the $[\text{Ni}(\text{TBTA})_2](\text{BF}_4)_2$ complex showing the pseudo-octahedral geometry.⁸

Additionally, the use of such 'click'-based tripodal ligands in coordination chemistry received considerable attention because their corresponding metal complexes are known to exhibit some peculiar properties, such as the magnetic behaviour of the metal ions. Sweinfurth *et al.* demonstrated that complexing Co(II) with TBTA resulted in the generation of the spin-crossover of the Co(II) centre in **109** at elevated temperatures.⁶

The effect of structural modifications in the triazole-based ligands on the properties of their corresponding metal complexes has not been reported yet. However, metal complexes of various structurally related tripodal *N*-donor ligands were prepared and their coordination, magnetic and redox properties investigated and compared. For example, comparative studies of the two Cu(II) complexes of pyridine-based ligands **113** and **117** (Figure 4.7), by Karlin *et al.*³ showed that small structural variations in these ligands lead to significant

changes in the coordination geometry of their corresponding complexes. In **113**, where central nitrogen is connected to pyridine by one methylene bridge, a trigonal pyramidal coordination mode with Cu(II) was observed, whereas in the complex with the analogous ligand **117** with two methylene bridges, a pseudo-octahedral geometry was reported.

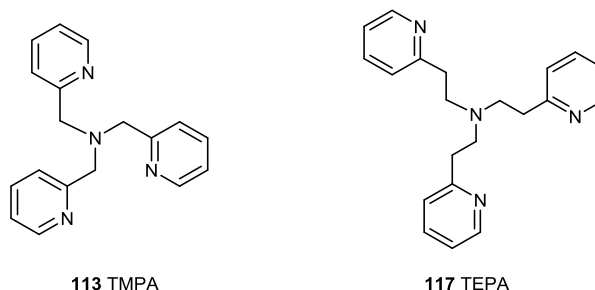


Figure 4.7- Chemical structures of the two pyridine-based tripodal ligands TMPA **113** and TEPA **117**.³

Consequently, the corresponding metal complexes of the triazole-based ligands are tested in various fields, such as electron transfer, electro- and coordination chemistry and magnetism.^{1,6} They also have found widespread applications in the areas of chemosensing, diagnostics and transition metal catalysis. This includes a) the generation of triazole-based sensors;¹³ b) luminescent lanthanide-based systems with versatile photophysical properties;¹¹ c) the synthesis of ‘click’-derived metal complexes as rate-accelerating agents in ‘click’ reactions or them being employed as precatalysts for the homopolymerisation of ethylene.⁷ Thus, due to the expanding range of their applications, the design and synthesis of such ligands and their corresponding metal complexes continues to be of great interest. In this work it was first decided to design and prepare a number of metal complexes with **110** and its structural derivatives **111** and **112** and characterise them using a range of techniques, such as single crystal X-ray crystallography, UV-Vis and EPR spectroscopies, the measurement of magnetic moments using the Evan’s NMR method as well as cyclic voltammetry. These methods were also used to examine how small structural variation in the ‘click’-derived triazole ligand can tune the coordination, electronic, magnetic and electrochemical properties of their corresponding metal complexes.^{1,7-9} Due to the poor water solubility of TBTA, another objective was to prepare its more hydrophilic analogue **112** in order to improve the aqueous solubility of its corresponding metal complexes, which is important for their potential use in phosphatase enzyme mimicry.

The following sections will briefly introduce and outline the merits of ‘click’ chemistry as a facile and effective tool for the synthesis of such triazole-derived compounds.

4.1.2. The Cu(I)-Catalysed Azide-Alkyne Cycloaddition (CuAAC) or 'Click' Reaction

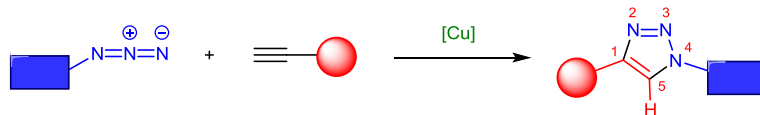
The term 'click' chemistry was first coined by Barry Sharpless to describe a facile and effective way to covalently join two simple units together.¹⁴ According to the author, the main features of a desirable click reaction are simple reaction conditions, which include the use of benign or easily removed solvents (e.g. water) and product isolation by simple non-chromatographic methods, such as distillation and crystallisation, generation of little or no toxic by-products, stereospecificity, short reaction times and high yields. Click chemistry should normally have readily available starting materials and reagents, provide a wide scope of applications and be modular.

'Click'-chemistry covers a wide range of reaction types:

- i. Cycloaddition reactions, including the Diels-Alder family of transformations and the Huisgen 1,3-dipolar cycloaddition of an azide and an alkyne;
- ii. The thiol-ene reaction (or alkene hydrothiolation);
- iii. 4+1 Cycloadditions between isonitriles (isocyanides) and tetrazines;
- iv. The ring opening of strained heterocycles, such as epoxides and aziridines;
- v. 'Non-aldol' carbonyl chemistry, such as the formation of ureas, aromatic heterocycles and amides;
- vi. Additions to carbon-carbon multiple bonds, such as epoxidation, dihydroxylation and Michael addition reactions.

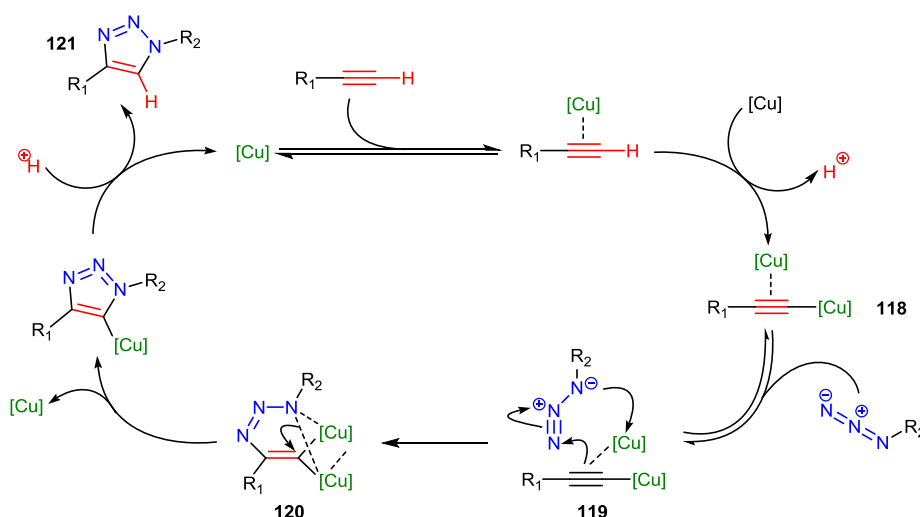
In particular, the Cu(I)-catalysed cycloaddition of an azide and alkyne or CuAAC has been termed the "premier example of a 'click' reaction" by Sharpless. Due to its experimental simplicity, mild reaction conditions, regioselectivity and very high yields, the CuAAC reaction has become increasingly popular since its discovery in 2001 and remains one of the most commonly used reactions by chemists for the synthesis of complex molecular architectures. For example, the high thermodynamic driving force of the 'click' reaction (normally greater than 20 kcal mol⁻¹) favours the formation of the most desirable product, which can be easily isolated without the need for laborious chromatographic purification techniques.¹⁴

Compared to the thermal Huisgen 1,3-dipolar cycloaddition, which involves concerted addition of a 1,3-dipole to a multiple bond, the Cu(I) catalysed cycloaddition of an azide and a terminal alkyne results in the formation of only the 1,4-disubstituted 1,2,3-triazoles, which is formed with complete regiocontrol as shown in Scheme 4.1.¹⁵



Scheme 4.1- Schematic representation of the Cu(I)-catalysed reaction between an azide and an alkyne, which results in the regioselective formation of the 1,4-triazole.¹⁵

Although it was previously hypothesised that σ -bound Cu(I) acetylide species exhibited catalytic activity in the cycle, further detailed studies allowed a better understanding of the mechanistic details to be established. For example, a number of calorimetric and isotopic experiments by Fokin *et al.*¹⁵ provided experimental evidence that the active cycloaddition complex **118** (Scheme 4.2), which is responsible for the regiocontrol, contains two copper atoms: the first is coordinated to the acetylene through weak and reversible π -interactions, which lowers the pK_a of the terminal alkyne proton and allows formation of the species, whilst a second is strongly bound to the acetylide by a σ -bond.



Scheme 4.2- Catalytic mechanism for a typical CuAAC reaction with two copper atoms proposed by Fokin *et al.*¹⁵

The CuAAC reaction mechanism proposed by Fokin *et al.* (Scheme 4.2) involves: 1) the formation of the dinuclear Cu(I) catalytic species **118**; 2) reversible coordination of these species with an azide *via* the proximal nitrogen to form complex **119**; 3) nucleophilic attack from the β -carbon of the acetylide to the proximal nitrogen resulting in the formation of the first covalent C-N bond in **120**; 4) the formation of the second C-N bond, which results in ring-closure and generation of the 1,2,3-triazole bridge between the two 'click' precursors; 5) proton transfer that regenerates the free copper catalyst and liberates the desired triazole product **121**. Although the understanding of the CuAAC mechanism has progressed significantly, further studies by Fokin *et al.*¹⁵ revealed that there are a number

of other reactive off-cycle intermediates in equilibria with the catalytically active species such as oligomeric copper acetylide complexes that are difficult to isolate and identify, due to their instability and high reactivity.¹² Nonetheless, this 'click' reaction remains a widely used and robust method to generate covalent links in a vast number of systems due to its experimental and operational simplicity. It has found a large number of applications in organic synthesis and coordination chemistry, such as the generation of large supramolecular structures and metal chelators.^{1,16} This reaction is also used in drug development, the synthesis of biomedical imaging agents, such as fluorescent probes, as well as biomimetic polymers, dendrimers and chains.¹³ In the case of coordination chemistry, there are a large number of groups that utilise the CuAAC reaction including the Watkinson group,¹⁶ to deliver efficient metal chelators, which then can be used to prepare a wide range of complexes with various metals including transition metals^{1,6-10} and lanthanides.¹¹

4.1.2.1. 'Click'-based Methods for the Generation of the Triazole-based Ligands

There are several sets of conditions that are currently used by researchers to prepare 'click'-derived triazole-based ligands, involving the use of the following:

- i. Cu(II) species and reducing agents;¹²
- ii. Cu(I) species and a base;¹⁷
- iii. Cu(I)-polytriazole ligand complex (including Cu(I) complexes with poorly-coordinating anions such as $[\text{Cu}(\text{MeCN})_4]\text{PF}_6$ and $[\text{Cu}(\text{MeCN})_4]\text{BF}_4$).¹⁸

The first method is one of the most commonly utilised to generate triazole linkages and has also been extensively used in the Watkinson group¹⁶ to develop fluorescent Zn(II) chelating probes for monitoring the trafficking of Zn(II) both *in vitro* and *in vivo*. It requires the use of the *in situ* reducing agent sodium ascorbate, which allows the generation of the catalytically active Cu(I) species from Cu(II) salts. Such reactions normally involve the use of organic solvents and gentle heating. These conditions are also very often employed in effective and facile one-pot CuAAC reactions, which allow the *in situ* synthesis of organic azides prior to the addition of the alkyne-based substrate. This two-step one-pot methodology avoids the isolation of azide intermediates, which is especially useful for low molecular weight azides as they can be explosively unstable and difficult to handle. Moreover, this one-pot reaction allows the synthesis of molecules with multiple triazole units without extra manipulations that decrease the efficacy of the reaction.¹⁸

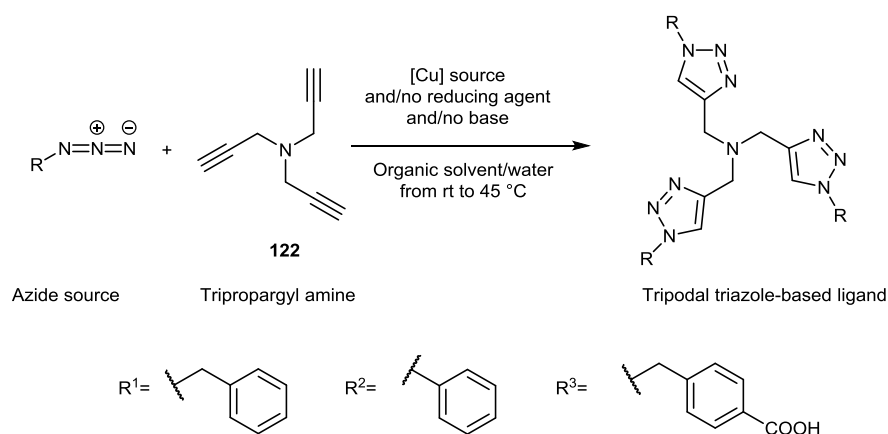
The second approach involves the direct use of active Cu(I) species without the presence of a reducing agent. The DIPEA-based reaction conditions were successfully used by Horne *et al.*¹⁹ to generate 1,2,3-triazole amino acid precursors for peptide synthesis. Advantageously, the absence of sodium ascorbate broadens the applications of this CuAAC method, as the oxidised species of the reducing agent (e.g. dehydroascorbate) may be detrimental to biomarcomolecules, as also described below.¹³

The third method, which involves the use of a Cu(I) catalyst with an appropriate triazole-based chelating ligand has become increasingly popular since Fokin *et al.*¹⁸ first discovered the rate-accelerating abilities of a Cu(I) complex of the TBTA ligand. It was found that the TBTA ligand can stabilise the Cu(I) centre from aerial oxidation and hence maintain the active Cu(I) species, which avoids the use of reductants as well as strict anaerobic conditions. Moreover, the absence of the sodium ascorbate reducing agent is also advantageous for CuAAC-based bioconjugation reactions, which require the use of protein or DNA-based substrates. The *in situ* formation of the Cu(I) complex of TBTA also considerably accelerated the CuAAC reaction and lead to excellent yields (84%) after 24 hours, as opposed to 21% for the equivalent Cu(II)-based CuAAC reaction using sodium ascorbate, according to a study by Fokin *et al.* Although TBTA remains amongst the most popular chelating ligands for the CuAAC reaction, its poor water solubility somewhat limits its applications, such as in bioconjugation. Interestingly, a Cu(I) complex of a more hydrophilic *p*-carboxylate version of TBTA **112** proved to be more efficient than that of TBTA and provided higher rate accelerations in CuAAC bioconjugation, as well as synthetic coupling reactions.¹³ For example, a 97% yield was detected after 60 minutes with **112**, compared to 84% with **110** after 24 h in the generation of a single 'click' unit.

4.2. Synthesis of Tripodal 'Click'-based Ligands

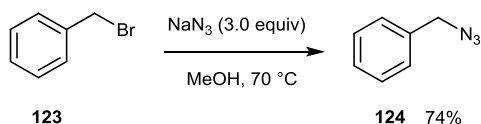
4.2.1. TBTA and Derivatives

The TBTA ligand **110** and its derivatives **111** (TPTA) and **112** (TCTA) were prepared and the generic strategy for their synthesis is depicted in Scheme 4.3. Several synthetic methods were tested in order to establish the most suitable ones, which allowed the generation of the target ligands in short times, without lengthy purification procedures and also in high yields.



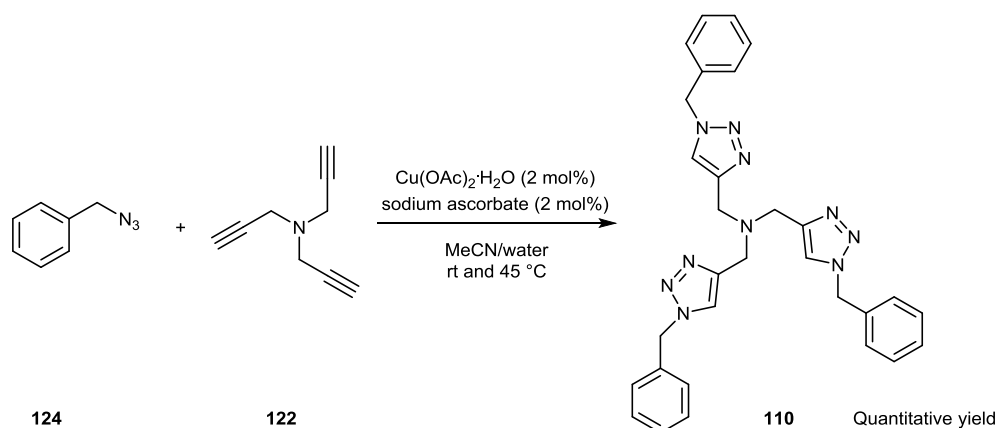
Scheme 4.3- Generic scheme for the synthesis of the target tripodal 1,2,3-triazole-based ligands *via* CuAAC reactions.

The first objective was to prepare the TBTA ligand **110** (R=Bn) using the methodology established by Fokin *et al.*,¹² which proved to be efficient and high yielding and is depicted in Scheme 4.3. This synthetic method starts with mixing tripropargylamine **122** and the azide with the Cu(II) species (e.g. Cu(OAc)₂·H₂O or CuSO₄·5H₂O). The reaction is then initiated by the addition of the *in situ* reducing agent, which results in the generation and maintenance of the catalytically active Cu(I) species. This allows the use of strict inert atmospheres and anhydrous solvents to be avoided. The isolation of several intermediates (e.g. species that contain only one or two 1,2,3-triazole moieties) was possible and it therefore proved important to monitor the reaction by thin layer chromatography (TLC) to ensure the conversion to the triple-‘click’ target product.



Scheme 4.4- Synthesis of benzyl azide **124**.²⁰

Prior to the synthesis of the TBTA ligand **110**, benzyl azide **124** had to be prepared. As shown in Scheme 4.4, this could be achieved in good yield as reported.



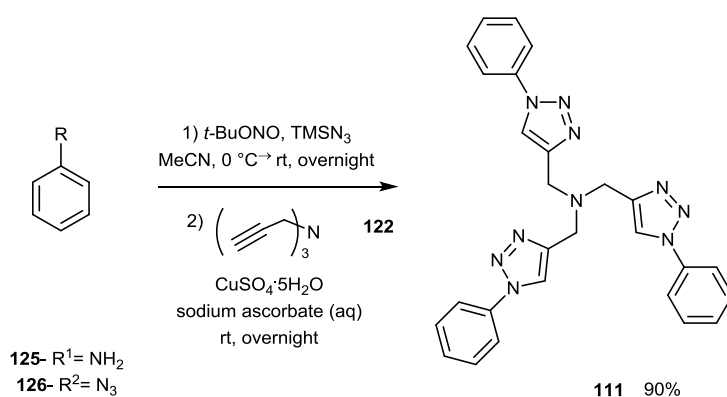
Scheme 4.5- Synthesis of the TBTA ligand **110**.¹²

The synthesis of TBTA shown in Scheme 4.5 involved mixing tripropargylamine **122** with the benzyl azide **124** (1.7 equiv.) in MeCN and adding this mixture to the catalytic $\text{Cu(OAc)}_2 \cdot \text{H}_2\text{O}$ (2 mol%) dissolved in MeCN under an inert atmosphere. This was followed by the addition of the sodium ascorbate reducing agent as an aqueous solution (2 mol%). This reaction mixture was then gently heated at 45°C for 5 hours and an additional 1.7 equiv. of benzyl azide were added and the reaction allowed to proceed for another 24 hours. The reaction mixture was then monitored by TLC, which showed the full consumption of **122** and the absence of unwanted intermediates resulting from single and double ‘click’ reactions. The remaining copper catalyst was removed from the crude reaction mixture using aqueous ammonia and brine solution. Ligand **110** was then isolated by recrystallisation from MeOH/Et₂O mixture as a beige solid in quantitative yield, compared to the reported 98% yield.¹² Additionally, when the reaction scale was increased from 0.1 g to 1 g, longer reaction times (up to five days) as well as a larger excess of benzyl azide **124** (five equiv. compared to the 3.4 equiv. on the 0.1 g scale) were required to obtain **110** in the same yield.

Initially, due to the availability of the azidobenzene **126** in the laboratory, the synthesis of **111** was attempted utilising the methodology applied for **110**, using $\text{CuSO}_4 \cdot 5\text{H}_2\text{O}$ as a source of the copper catalyst instead of $\text{Cu(OAc)}_2 \cdot \text{H}_2\text{O}$. The TLC of the reaction mixture after 20 hours showed the presence of unwanted reaction intermediates, presumably some resulting from single and double ‘click’ reactions and thus an additional two equivalents of **126** were added, and the reaction mixture stirred for another 16 hours. Unexpectedly, this resulted in multiple products forming which were difficult to identify. According to Baschiery *et al.*,¹¹ a possible explanation for this is the formation of destructive side

reactions resulting from Cu(I)-mediated generation of reactive oxygen species. Thus, the method was deemed unsuitable due to the isolation of the crude product in very small quantities, which also required laborious purification by column chromatography. As an alternative strategy, the removal of the remaining copper catalyst from the crude reaction mixture using aqueous ammonia solution was followed by attempts to recrystallise the product from the crude reaction mixture, which were unsuccessful. Due to the availability of a more efficient alternative route this methodology was not pursued further.

Barral *et al.*²¹ have reported an efficient high-yielding one-pot synthetic method to generate 'click'-triazole containing compounds with multiple triazole linkages. This approach involves the *in situ* synthesis of azides from their corresponding anilines, followed by their CuAAC reaction with an alkyne. This protocol was subsequently used by Baschiery *et al.*¹¹ to prepare the TPTA ligand and its derivatives and was employed in this work.

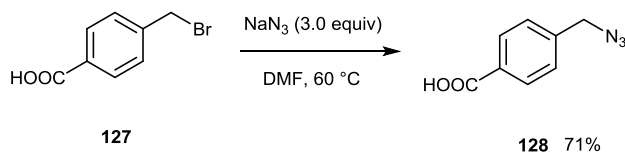


Scheme 4.6- One-pot synthesis of TPTA ligand **111** via azidobenzene intermediate **126**.¹¹

This one-pot synthesis shown in Scheme 4.6 started with reacting aniline **125** with *t*-BuONO and (CH₃)₃SiN₃ (TMSN₃) at room temperature in MeCN for 20 hours under inert conditions to form aryl azide **126** *in situ*. Without any intermediate work-up procedure, **122** and the CuSO₄·5H₂O/sodium ascorbate mixture in water were then added to the reaction mixture and the resulting solution stirred at room temperature for 20 hours. A portion of **111** precipitated from the solution, which was collected by filtration as a pale yellow solid and the supernatant was subjected to a work-up resulting in a further portion of **111** being isolated. ¹H NMR spectra of both portions were identical and indicated the formation of pure **111** in an excellent combined 90% yield. In comparison, Baschiery *et al.*¹¹ used flash column chromatography over neutral Al₂O₃ to obtain pure **111** in a lower yield of 61%. According to the authors, the lower yield might be attributed to the autocatalytic activity of this type of ligand. Conveniently, the one-pot synthesis of **111** did not require any elevated

temperatures, additional equivalents of an azide or longer reaction times at larger scale, as was the case with **110**.

Prior to the synthesis of **112**, the *p*-carboxylic benzyl azide **128** was prepared using the reported literature procedure, as shown in Scheme 4.7. Acidification of the aqueous reaction mixture with the dilute HCl resulted in the precipitation of the white solid, which was then isolated by filtration and lead to pure **128** in 71% yield as reported.²²



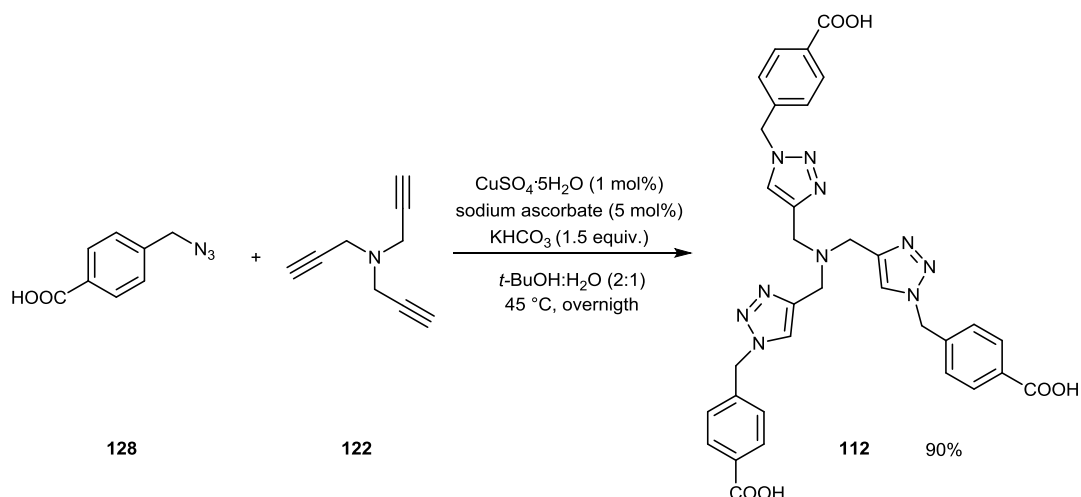
Scheme 4.7- Synthesis of the *p*-carboxylic benzyl bromide **128**.²²

It is important to mention, that **127** showed poor solubility in water as well as in common polar organic solvents, such as MeOH and MeCN (except DMSO and DMF). As a result, **128** did not show any reactivity with **122** in MeCN when the TBTA-based procedure was employed, which resulted in the recovery of starting materials. The synthesis of ligand **112** using the CuAAC method in which the TBTA complex is generated *in situ* by reaction of the ligand and $[\text{Cu}(\text{MeCN})_4]\text{PF}_6$ (1 mol%) in a 2:1 mixture of *t*-BuOH:H₂O¹⁸ was also unsuccessful and also resulted in the isolation starting materials.

It is worth mentioning here, that the preparation of the TBTA-based Cu(I) catalyst was also attempted separately to ensure complex formation, which could then be used as a catalyst for the CuAAC reaction. This required ligand **110** and 1 equiv. of $[\text{Cu}(\text{MeCN})_4]\text{PF}_6$ to be mixed in degassed DCM and MeCN at room temperature. After *ca.* 2 hours, degassed Et₂O was added to the reaction mixture, which resulted in the formation of a cloudy solution. This was then kept in the freezer at -20°C, which is reported to result in the formation of a sticky solid,¹⁸ however, none appeared even after two weeks. Due the availability of another more viable synthetic procedure towards ligand **112**, this methodology was not pursued further.

In an attempt to solve the problem of the solubility of **128**, another procedure reported by Horne *et al.*¹⁹ used to prepare triazole-based compounds with the same carboxylic acid moiety was utilised. This methodology involved the reaction between **128** and **122** in MeCN with a DIPEA base, which resulted in high solubility of **128** in MeCN. Cu(I)I was added to

initiate the reaction, which did not require the addition of the *in situ* reducing agent. After heating the reaction mixture at 60°C for 20 hours the reaction solution was decanted and a beige solid subsequently precipitated with the addition of an excess of EtOAc or Et₂O, which according to the ¹H NMR spectrum in DMSO-d₆ contained the target product, together with the starting material **128** and DIPEA base. However, before any attempts to isolate pure product from this crude mixture were made, another more viable procedure was found.



Scheme 4.8- Synthesis of the *p*-carboxylic TBTA ligand **112**.¹³

The key feature of the alternative method reported by Hong *et al.*¹³ is the use of the base KHCO₃, which resulted in the formation of the potassium salt of the acid, thereby solving the solubility issues. This CuAAC reaction between **122** and **128** with CuSO₄·5H₂O and sodium ascorbate was carried out in a 2:1 *t*-BuOH:H₂O mixture under gentle heating at 45°C for 16 hours (Scheme 4.8). The acidification of the aqueous reaction solution with glacial acetic acid to pH 3-4 resulted in precipitation of a beige solid, which was isolated and further purified by recrystallization giving pure **112** in an excellent yield of 90%, compared with the reported 80%.

Overall, three structurally similar ‘click’-derived tripodal and potentially tetradentate ligands **110**, **111** and **112** were prepared in excellent yields using CuAAC-based synthetic approaches with a number of variations applied. Additionally, **111** was prepared without the need for laborious column chromatography in a higher yield than the reported procedure.

4.2.2. Synthesis and Characterisation of Triazole-based d-Block Metal Complexes

With the three triazole-based tripodal ligands **110**, **111** and **112** in hand the preparation of a range of their corresponding chloride and perchlorate complexes with Co(II), Cu(II), Ni(II), Mn(II) and Zn(II) metal ions was undertaken for a number of reasons. First, it was of interest to investigate the effect of structural modifications of the ligands on the coordination chemistry and electrochemical behaviour of their corresponding metal complexes. Moreover, the role of the anion on the chemical and physical properties of the complexes was also examined to see what effects, if any, the use of coordinating versus poorly coordinating anions had.

4.2.2.1. Preparation of the Chloride and Perchlorate Metal Complexes

Established literature protocols were used to prepare target metal complexes of the 'click'-derived tripodal tetradentate ligands **110** and **111**.^{1,7,11} A range of metal complexes were prepared by reacting the target ligands with the corresponding metal salt in an appropriate solvent at room temperature. Any precipitate formed was removed by filtration, followed by the isolation of the desired complex by precipitation with Et₂O. The resulting solids were then isolated by filtration and dried under vacuum to afford the desired metal complexes.

TBTA-based metal chloride complexes were prepared in MeCN using a 1:1 metal:ligand ratio in all cases with the exception of the reaction with MnCl₂·4H₂O, which was carried out in MeOH due to the poor solubility of the metal salt in MeCN. Complex formation could be easily observed visually by the colour change that occurred for almost all complexes, with the exception of the Mn(II) and Zn(II)-based ones, which, as expected, remained colourless. The dichloride TBTA-based complexes were isolated in yields between 74% and 84%, with the exception of [Cu(**110**)Cl]Cl **129** which gave a 54% yield. The complexes showed good solubility in MeOH and MeCN except [Mn(**110**)Cl]Cl **131** which was soluble in MeOH but not in MeCN. Unfortunately all of the complexes reported here showed poor aqueous solubility. Similarly, perchlorate complexes of the TBTA ligand were prepared in MeCN. The removal of the reaction precipitate and isolation of the products by precipitation with Et₂O afforded solids in 73% to quantitative yields, except for the [Mn(**110**)](ClO₄)₂ **135**, which resulted in a lower yield of 41%. The perchlorate complexes also showed good solubility in both MeOH and MeCN, but were also insoluble in water. Additionally, complexation between the TBTA and Na₃[Co(CO₃)₃]·3H₂O was attempted, but due to solubility issues the reaction failed.

Due to the partial solubility of the TPTA in MeCN, the metal complexes of **111** were prepared in MeOH. However, $[\text{Cu}(\mathbf{111})](\text{ClO}_4)_2$ **142** and $[\text{Ni}(\mathbf{111})](\text{ClO}_4)_2$ **143** could not be isolated from MeOH and therefore were prepared in MeCN. Initially a 1:1 metal:ligand ratio was used in all cases. However, in the case of $[\text{Mn}(\mathbf{111})](\text{ClO}_4)_2$ **144** following the isolation of X-ray quality crystal structures, two equivalents of the ligand were used as a result of the complex stoichiometry (Section 4.4.2.4). Furthermore, isolation of the Zn(II)-based TPTA crystals of $[\text{Zn}(\mathbf{111})\text{Cl}]\text{Cl}$ **141** also showed a 2:1 metal: ligand stoichiometry in the unit cell and consequently two equivalents of ZnCl_2 were used subsequently. The TPTA chloride metal complexes were isolated in good to excellent yields from 79% to 86%, with the exception of the $[\text{Mn}(\mathbf{111})\text{Cl}]\text{Cl}$ **140** that resulted in 62% yield. TPTA perchlorate complexes were also isolated in good yields ranging from 70% to 85%.

Due to the very poor solubility of **112** in both MeOH and MeCN, its complexes could not be prepared under the same conditions used for TBTA and TPTA. Therefore, the reaction between **112** and the appropriate metal salt was attempted in DMSO using 1 equiv. of each $\text{CoCl}_2 \cdot 6\text{H}_2\text{O}$ and ZnCl_2 . A colour change was observed in the Co(II)-based solution from blue to purple, but attempts to obtain X-ray quality crystals from this solution were not successful. In the case of the Zn(II) complex, the ^1H NMR spectrum in DMSO-d_6 of the sample taken from this solution showed an upfield shift in peaks compared to the free ligand peaks, indicating the coordination of Zn(II) ion to the ligand had occurred, as illustrated in Figure 4.8. However, attempts to obtain X-ray quality crystals also failed and neither complex could be isolated. As a result of these solubility issues the coordination chemistry of this ligand was not pursued any further.

Overall all the complexes prepared generally have good solubility in common polar organic solvents, such as MeOH, MeCN and DMSO. They also are air-stable for long periods of time.

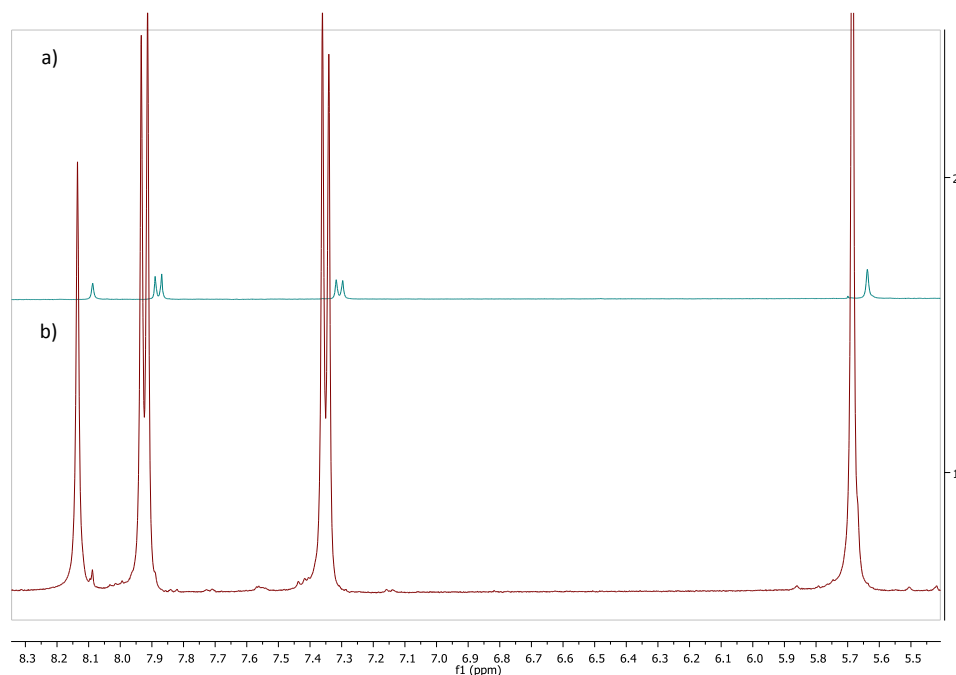


Figure 4.8- Stacked ^1H NMR spectra of a) $[\text{Zn}(\mathbf{112})\text{Cl}]\text{Cl}$ and b) ligand **112** in DMSO-d_6 showing an upfield chemical shift in protons of **112** upon its complexation with Zn(II) .

4.2.2.2. Characterisation of the Complexes

The complexes presented here were characterised, where possible, by single crystal X-Ray crystallography and UV-Vis and EPR spectroscopies. Their magnetic moments were measured using the Evan's NMR method and their electrochemistry was investigated using cyclic voltammetry. When the complexes were diamagnetic their ^1H NMR spectra were also recorded. Their stoichiometry was also analysed by high resolution mass spectroscopy (HRMS). The conditions for the characterisation studies reported in this work are briefly outlined in the experimental section.

4.2.2.2.1. Characterisation of Co(II) Complexes

Electronic spectra for **109** and **137** were obtained from MeCN solutions and two very similar UV-Vis spectra were obtained exhibiting spectroscopic features that are indicative of paramagnetic Co(II) species with a high spin d^7 electron configuration.²³ Traditionally, Co(II) species with this electron configuration are expected to give rise to three absorption bands. However, each spectrum obtained in this work for **109** and **137** contains six bands, with one broad band with λ_{max} between 510 nm and 517 nm and five other bands with λ_{max} in the region between 586 nm and 690 nm. The UV-Vis spectrum of $[\text{Co}(\mathbf{111})\text{Cl}]\text{Cl}$ **137** is shown in Figure 4.9 as an example and the data for both complexes is given in Table 4.1. Due to the lack of the spectroscopic characterisation of such Co(II) complexes in the literature, the unequivocal assignment of the visible absorption bands (as was done with the tetraamine Co(III) d^6 complexes in Chapter 2, section 2.3.3.1) becomes complicated.

The appearance of the broad absorption band at 517 nm was unexpected, as this type of band is indicative of the diamagnetic low spin d^6 Co(III) species (see Chapter 2, section 2.3.3.1). Interestingly, Sweinfurth *et al.*⁹ have recently presented an X-ray structure of a rare case of the dinuclear $[(\text{TBTA})\text{Co}(\mu\text{-OH})_2\text{Co}(\text{TBTA})](\text{BF}_4)_4$ complex, in which each Co(III) atom is coordinated to one TBTA ligand in a distorted octahedral manner with the metal ions joined by hydroxo bridges, which gave a visible absorption band with λ_{max} at 501 nm ($\epsilon = 200 \text{ M}^{-1}\text{s}^{-1}$). Thus, this result shows the possibility of the formation of Co(III) species coordinated to the tetradentate-tripodal ligands.

Table 4.1- Visible electronic spectral data for the Co(II) complexes **109** and **137** (2.5 mM solutions in MeCN).

137	Wavelength (nm)	517	590	613	634	660	688
	$\epsilon (\text{M}^{-1} \text{s}^{-1})$	202	232	236	265	216	204
109	Wavelength (nm)	510	589	610	631	663	691
	$\epsilon (\text{M}^{-1} \text{s}^{-1})$	210	188	280	274	188	200

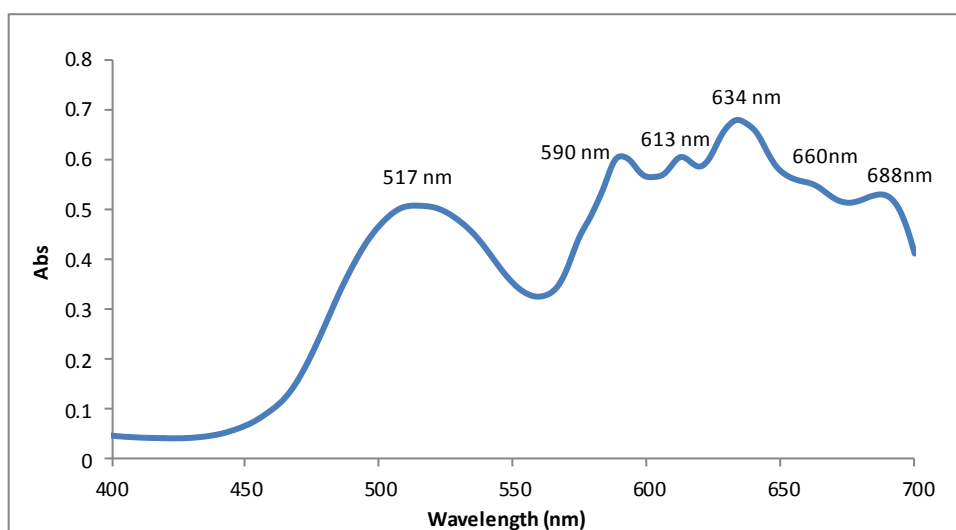


Figure 4.9- The UV-Vis spectrum of **137** run in MeCN solution.

Based on this result it might seem plausible to consider the presence of some Co(III) species coordinated to the TBTA ligand, which may have formed due to aerial oxidation. Additionally, another dinuclear TBTA-based Co(II) complex (which has Co(II) in the distorted octahedral coordination geometry) reported by Sweinfurth *et al.*⁹ gave two shoulders in its UV-vis spectrum with λ_{max} at 377 nm and 538 nm. The combination of these observations may suggest the presence of a mixture of compounds (mononuclear and dinuclear species) or dimeric species in **109** and **137**, which may be mixed valence. Moreover, the crystal structure for the mononuclear $[\text{Co}(\text{TBTA})\text{Cl}]\text{BF}_4$ complex was reported by Sweinfurth *et al.*,¹

where the Co(II) ion is coordinated to a central TBTA nitrogen atom and to one nitrogen from each of the three triazole rings of the ligand and to one chloride anion. This coordination mode is described as 4+1 coordination geometry or capped tetrahedral and will be discussed in detail in section 4.2.2.2.5. Similar 5-fold coordination geometry was reported for Co(II) complexes with the related AMPT ligand **115**.¹ However, to date, no UV-Vis spectral data has been reported for the mononuclear [Co(TBTA)Cl]Cl complex. Based on the crystal structure reported, it is reasonable to suggest the presence of such a mononuclear Co(II) species with this 4+1 coordination geometry in solution for **109** and **137**. No major difference was detected between the UV-Vis spectra of the Co(II) complexes **109** and **137** indicating that switching the substituent on the triazole ring in the 'click'-derived tripodal ligand has no significant effect.

In order to gain further evidence for the cobalt oxidation state in the complexes and to identify metal's electronic configuration, magnetic moments for **109** and **137** were experimentally determined by the Evan's NMR method. The values obtained for **109** and **137** were calculated to be 4.2 μ_B and 4.6 μ_B respectively based on an assumed 1:1 metal: ligand stoichiometry i.e. [Co(L)Cl]Cl, which are within the range of those reported for the paramagnetic Co(II) high spin d^7 species.²⁴ These results are also consistent with those reported by Schweinfurth *et al.*,¹ who measured the magnetic moment for [Co(TBTA)Cl]BF₄ to be approximately 4.2 μ_B at 300 K. Similar values have also been reported for the structurally similar Co(II) complexes of TMPA **113** and AMPT **115** ligands¹ (shown in section 4.2). The combination of the relevant literature data and the results obtained in this work using Evan's NMR and UV-Vis spectroscopies thus support the presence of mainly paramagnetic magnetically dilute high spin d^7 Co(II) species in **109** and **137** as it has been reported that dinuclear Co(II) complex of the TBTA ligand (in which two Co(II) ions are connected by chloranilic acid), display a larger magnetic moment of 6.30 μ_B ⁹ at room temperature, a value in the expected range for the presence of two high spin Co(II) centres. This also leads to the conclusion that small structural variation in the 'click'-derived tetradentate tripodal ligands are not likely to affect the spin state of the coordinated Co(II) cation. Considering the magnetic moment values reported for **109** and **137** in this work, the presence of the dinuclear Co(II) species with the TBTA and TPTA ligands based on the evidence associated with their UV-Vis spectra and electrochemical studies (see later), becomes debatable.

Comparative electrochemical studies of complexes **109** and **137** resulted in very similar cyclic voltammograms being recorded in MeCN, with two irreversible one-electron reduction waves being observed in the range of -1.30 and -2.10 V and two unrelated oxidation processes at 1.35 V and 1.71 V (vs a calomel reference electrode (SCE)). The data for both complexes **109** and **137** are presented in Table 4.2. The cyclic voltammogram of **137** is presented in Figure 4.10 as an example. The oxidation-reduction peak related to the unidentified impurity, which is present in the blank solution, can be also observed (Chapter 6, section 6.1).

Table 4.2- Redox potentials of **137** and **109** (0.1 M *n*-Bu₄NBF₄ solution of the supporting electrolyte, scan rate =50 mV s⁻¹) reported vs SCE.

Compound	E _{red} (V)	E _{ox} (V)
137	-1.83	1.35
	-1.30	1.71
109	-2.10	1.35
	-1.73	1.70

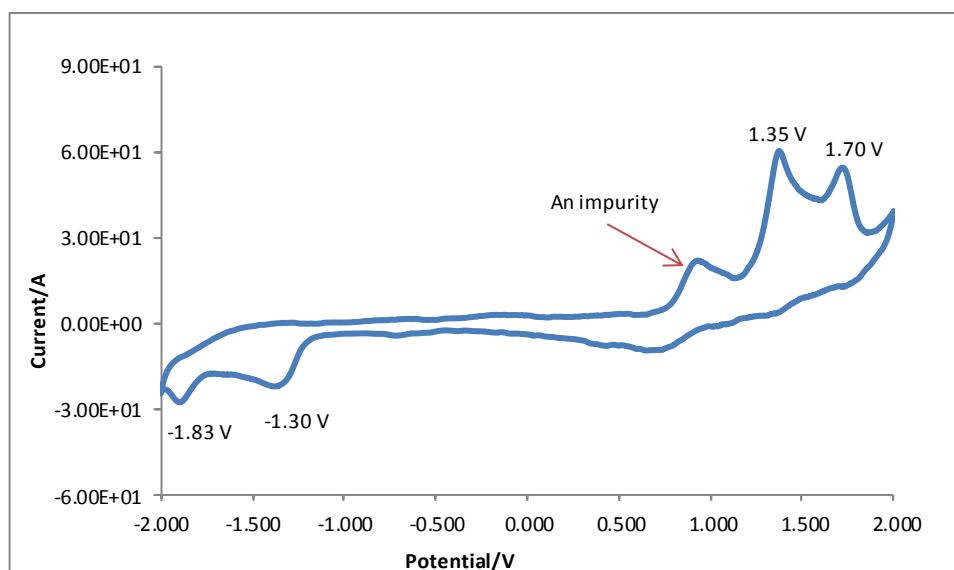


Figure 4.10- Cyclic voltammogram at glassy carbon using a calomel reference electrode in MeCN (*n*-Bu₄NBF₄ is the supporting electrolyte; scan rate= 50 mV s⁻¹) of 2.5 mM solutions of **137**.

According to Schweinfurth *et al.*,⁹ the irreversibility might point towards the decomposition of a dimeric Co(II) species upon oxidation. In their electrochemical studies of the dinuclear Co(II) complex of the TBTA ligand, they reported an ill-defined irreversible process, which was thought to be a result of the decomposition of the Co(II) complex upon oxidation. The authors proposed several factors that are likely to contribute to the irreversible redox

chemistry, including the need for structural reorganisation on oxidation from Co(II) to Co(III). Donnelly *et al.*¹⁰ have also proposed, based on the electrochemical studies of the complex [Cu(TBTA)Cl]Cl, that the electrochemical irreversibility could be attributed to significant structural reorganisations at the metal centre.

Additionally, HRMS supports the presence of the mononuclear Co(II)-ligand species for both **109** and **137** with 1:1 molecular ions being observed of stoichiometry [Co(L)Cl]Cl in both cases and no molecular ions relating to dimers being observed. Unfortunately, numerous attempts to grow crystals of **109** and **137** using various techniques with the view to gain more detailed structural evidence were not successful.

In summary, there is clear evidence for the formation of high spin d^7 [Co(L)Cl]Cl species for both **109** and **137**. Additionally, by comparison with literature data there is some evidence pointing towards the presence of a mixture of these mononuclear complexes together with Co(II) and possibly Co(III) or mixed valent TBTA/TPTA-based dimers in solution. A more detailed study using alternative techniques such as X-band or more advanced high-frequency EPR spectroscopy and single crystal X-ray diffraction are required to elucidate the nature of the species present in **109** and **137**.

4.2.2.2.2. Characterisation of Cu(II) Complexes

Single crystals of [Cu(**111**)Cl₂] **138** suitable for X-ray diffraction studies were isolated from a mixture of CD₃CN/MeCN/TMS used to measure the magnetic moment of the complex by the Evan's NMR method and are shown in Figure 4.11.

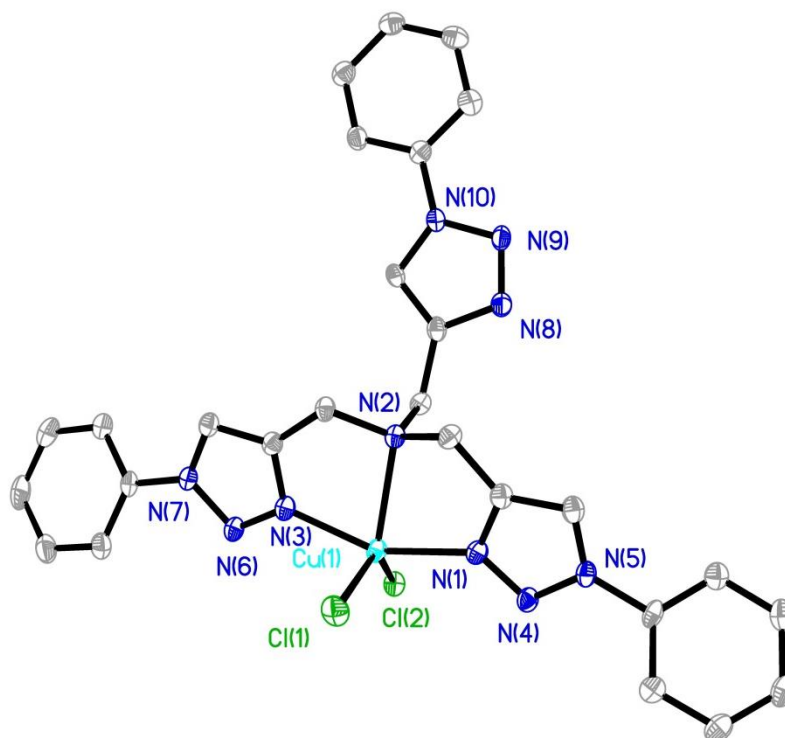


Figure 4.11- ORTEP²⁵ plot showing the single crystal X-ray structure of **138** with 50% probability displacement ellipsoids, with hydrogen atoms omitted for clarity.

The crystal structure reveals that the Cu(II) centre in **138** is coordinated by only two nitrogen atoms of the triazoles of the TPTA ligand as well as its central tertiary amine donor. Additionally, there are two chloride ions coordinated. This is in contrast to the crystal structure of the analogous [Cu(TBTA)Cl]Cl¹⁰, where the Cu(II) centre is in a distorted trigonal bipyramidal coordination environment, and to other related mononuclear complexes including [Co(TBTA)Cl]BF₄,¹ [Ce(TPTA)(NO₃)₃]NO₃,¹¹ [Ni(**110**)(OH₂)Cl]Cl **130** and [Zn(**111**)Cl]₂[ZnCl₄] **141** (this work) in which the central metal ion is coordinated to all three triazole donors. The situation when only two triazole moieties are bound to the metal atom with the non-coordinated third triazole arm is known to be common for homoleptic metal complexes in which one metal is coordinated to two TBTA ligands. This phenomenon has also been observed in this work (see section 4.2.2.2.4) as well as in the case of the reported analogous [Ni(TBTA)₂](BF₄)₂,⁸ [Co(TBTA)₂](BF₄)₂ and [Fe(TBTA)₂](BF₄)₂⁷ complexes. This unusual coordination mode can potentially be attributed to the high degree of binding flexibility, which results in large number of coordination modes of such ‘click’-derived ligands, compared to the tetrapyridine ligands. To the best of our knowledge, not only is this the first example of such coordination geometry with Cu(II) and triazole-based tripodal ligands, it is also the first isolated X-ray crystal of a TPTA-based transition metal complex. It

also indicates that switching the substituent on the triazole moiety of the ligand does affect the coordination mode of the ligand around the metal centre in the solid state in this case.

Table 4.3- Selected bond lengths (Å) and bond angles (°) for the X-ray crystal structure of **138** with estimated standard deviations (esds).

<i>Bond lengths (Å)</i>		<i>Bond angles (°)</i>	
Cu-N(1)	2.0591(10)	N(2)-Cu-N(1)	78.34(4)
Cu-N(2)	2.1223(10)	N(2)-Cu-N(3)	78.94(4)
Cu-N(3)	2.0270(10)	N(3)-Cu-N(1)	156.08(4)
Cu-Cl(1)	2.2177(3)	Cl(1)-Cu-Cl(2)	109.188(13)
Cu-Cl(2)	2.4430(4)	N(2)-Cu-Cl(1)	152.98(3)
		N(2)-Cu-Cl(2)	97.78(3)

Closer inspection of the crystal structure of **138** revealed that the average Cu-N bond distance is 2.06 Å, which is within the reported range of bond lengths in such complexes. Interestingly, the Cu-N(2) distance in **138** is 2.12 Å, which is shorter than the normally reported distance (e.g. 2.24 Å -2.35 Å) between the metal and tertiary nitrogen donor in such complexes but is comparable to the distance of 2.12 Å reported for [Cu(TBTA)Cl]Cl by Donnelly *et al.*¹⁰ Additionally, the Cu-Cl(1) and Cu-Cl(2) bond lengths are 2.21 Å and 2.44 Å respectively, with the 2.21 Å being in the reported range in related complexes,³ whereas 2.44 Å is much longer compared to those reported for similar heteroleptic complexes of 'click'-derived tripodal ligands¹⁰ and appears to be amongst the longest Cu(II)-Cl bonds reported. The angle between the triazole nitrogen atoms and Cu(II) (N(3)-Cu-N(1)) is 156.08° and is the largest valence angle in the X-ray structure; and that between the tertiary amine, copper and Cl(2) is 97.78°. Based on these angles, the Addison parameter was calculated to be 0.97,²⁶ which is very close to 1 and thus indicates the presence of the trigonal bipyramidal geometry with the triazole ligands occupying the axial positions, whereas the tertiary nitrogen and chloride ligands occupy the equatorial positions. The related TBTA-based Cu(II) crystal structure reported by Donnelly *et al.*,¹⁰ also reveals that Cu(II) is in a distorted trigonal bipyramidal CuN₄Cl coordination environment.

UV-Vis spectra of the four Cu(II) complexes reported here- [Cu(**110**)Cl]Cl **129**, [Cu(**110**)](ClO₄)₂ **133**, [Cu(**111**)Cl₂] **138**, [Cu(**111**)](ClO₄)₂ **142**, showed very similar characteristics containing two very broad bands with the λ_{max} in the region between 650 nm and 900 nm, which are similar to those reported for the tetradentate Cu(II) complex

[Cu(TMPA)Cl]PF₆ which adopts trigonal bipyramidal geometry.³ Cu(II) complexes presented here also displayed a peak in the UV region at 360 nm, which is most likely related to a metal-to-ligand charge transfer (MLCT) transition.

More reliable evidence about the oxidation state of the copper ion in **129**, **133**, **138** and **142** was derived from the magnetic moment values obtained by the Evan's NMR method. Experimentally determined values of 1.6 μ_B for **133** and 1.7 μ_B for **138** and **142**, were approximately in the range of magnetic moment values (1.7-2.2 μ_B) typically reported for magnetically dilute spin-only values for Cu(II) d⁹ species.²⁴ The 2.6 μ_B value obtained for complex **129** falls outside the range of the reported values for reasons which are unclear, but may indicate that the stoichiometry of the complex is different to that assumed. Further evidence about coordination environment in the four Cu(II) complexes was obtained by EPR spectroscopy and electrochemical studies.

EPR spectra of **138**, **129**, **142** and **133** are presented in Figure 4.12 and were recorded in MeOH and are characteristic of axial d⁹ Cu(II) species. These signals arise due to the hyperfine interactions between the unpaired Cu(II) electron and the two ⁶³Cu and ⁶⁵Cu nuclei (*I*=3/2). The spectra show that *g*_{||} values are in the range of 2.31-2.44, and *g*_⊥ values are in the range of 2.07-2.13. *g*_⊥ values are closer to 2.0 compared to the *g*_{||} values which are >2.0, which is suggestive of the significant distortion in these Cu(II) complexes.²⁷ EPR data are in line with the magnetic moments measurements for **138**, **142** and **133**. In contrast the spectrum for **129** is poorly-resolved, which like the magnetic moment measurement, perhaps indicates either that the sample is impure or that a mixture of species exists in the solid state.

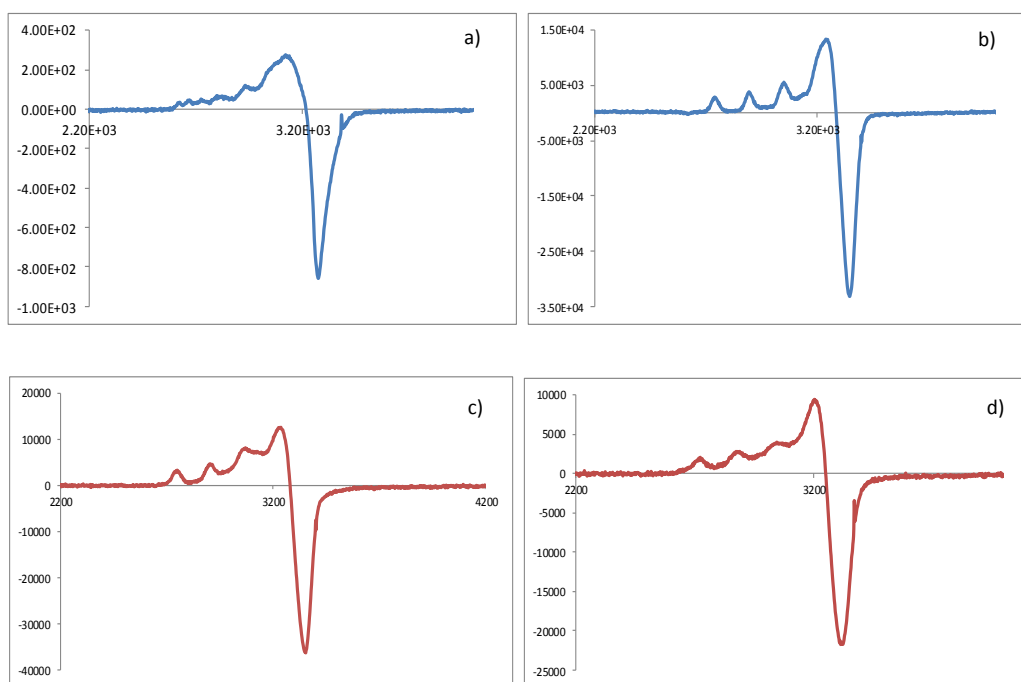


Figure 4.12- EPR spectra of Cu(II) complexes in MeOH recorded at 50 K: a) **129**; b) **138**; c) **133**; d) **142**.

Additionally, the electrochemical behaviour of these four Cu(II) complexes was evaluated. On comparing cyclic voltammograms of **129** and **138**, it was observed that both complexes display two quasi-reversible reduction waves and related oxidation waves at similar values (given for **129**) of 0.12 V and 0.86 V (E_{red}) and 0.26 V and 1.06 V (E_{ox}) vs SCE as shown in Figure 4.13. However, Donnelly *et al.*¹⁰ have reported that the [Cu(TBTA)Cl]Cl monomer in DMSO exhibited only single reversible oxidation-reduction process at $E = -0.18$ V (vs.Fc/Fc⁺), corresponding to a Cu(II)/Cu(I) couple. Redox potentials for **129**, **133**, **138** and **142** vs SCE are shown in Table 4.4

Table 4.4- Redox potentials of **129**, **133**, **138** and **142** (0.1 M *n*-Bu₄NBF₄ and *n*-Bu₄NClO₄ solutions of supporting electrolytes for the chloride and perchlorate species respectively, scan rate = 50 mV s⁻¹) reported vs SCE.

Compound	E_{red} (V)	E_{ox} (V)
129	0.12	0.26
	0.86	1.06
133	0.24	0.42
	0.32	0.25
138	0.23	0.31
	0.52	1.28
142	0.25	0.35
	0.56	1.25

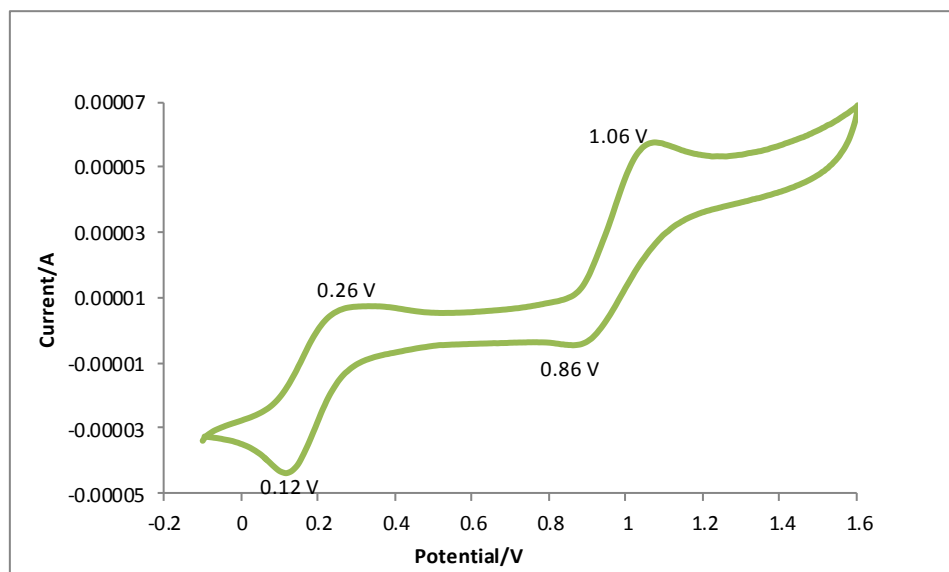


Figure 4.13- Cyclic voltammogram at glassy carbon using a calomel reference electrode in MeCN (*n*-Bu₄NBF₄ is the supporting electrolyte; scan rate= 50 mV s⁻¹) of 2.5 mM solutions of **129**.

Based on the other available literature regarding the electrochemistry of Cu(II) complexes with ligands containing four nitrogen donor atoms, the reduction peaks in Figure 4.13 are likely to correspond to the Cu(III)/Cu(II) and Cu(II)/Cu(I) processes.^{27,28} The presence of two reduction peaks for the Cu(II) complexes reported here might also potentially be explained by the formation of dinuclear species in the solution. However, no evidence of such phenomenon was obtained in this work. It is also worthwhile noting, that there is a strong anodic stripping peak (not shown here) observed at -0.25 V for all four Cu(II) complexes reported here, which is typical of Cu(II) complexes and has been previously reported²⁹ but was not mentioned by Donnelly *et al.*¹⁰ in their studies. The electrochemical analysis of the corresponding Cu(II) perchlorate complex **142**, showed that the nature of the anion did not affect the electrochemistry of the complex and the redox potentials remained very similar to those of **138**. On the other hand, the corresponding redox potentials of the TBTA-based perchlorate complex **133** appeared in the 0.0 to 0.5 V region (compared to 1.06 V oxidation peak with the chloride complex), which is likely to be an effect of the poorly-coordinating nature of the perchlorate anion. Apparent anodic stripping remained at the same value in these perchlorate complexes.

Additionally, the presence of the mononuclear Cu(II):ligand species [Cu(L)Cl] was confirmed for **129** and **138** by HRMS, whereas for **133** and **142** ions of stoichiometry [Cu(L)] were observed.

Overall, a combination of single crystal X-ray crystallography, cyclic voltammetry, magnetic moments and high resolution mass spectrometry would seem to indicate the presence of paramagnetic Cu(II) d^9 species of general formulation $[\text{Cu}(\text{L})]$ have been formed in **129**, **133**, **138** and **142**. Most importantly, the structure of $[\text{Cu}(\mathbf{111})\text{Cl}_2]$ has been established in this work.

4.2.2.2.3. Characterisation of Ni(II) Complexes

Slow diffusion of Et_2O into the MeCN solution of **130** lead to the generation of the X-ray quality crystals of $[\text{Ni}(\mathbf{110})(\text{OH}_2)\text{Cl}]\text{Cl}$, the structure of which is shown in Figure 4.14 with selected bond lengths and angles contained in Table 4.5.

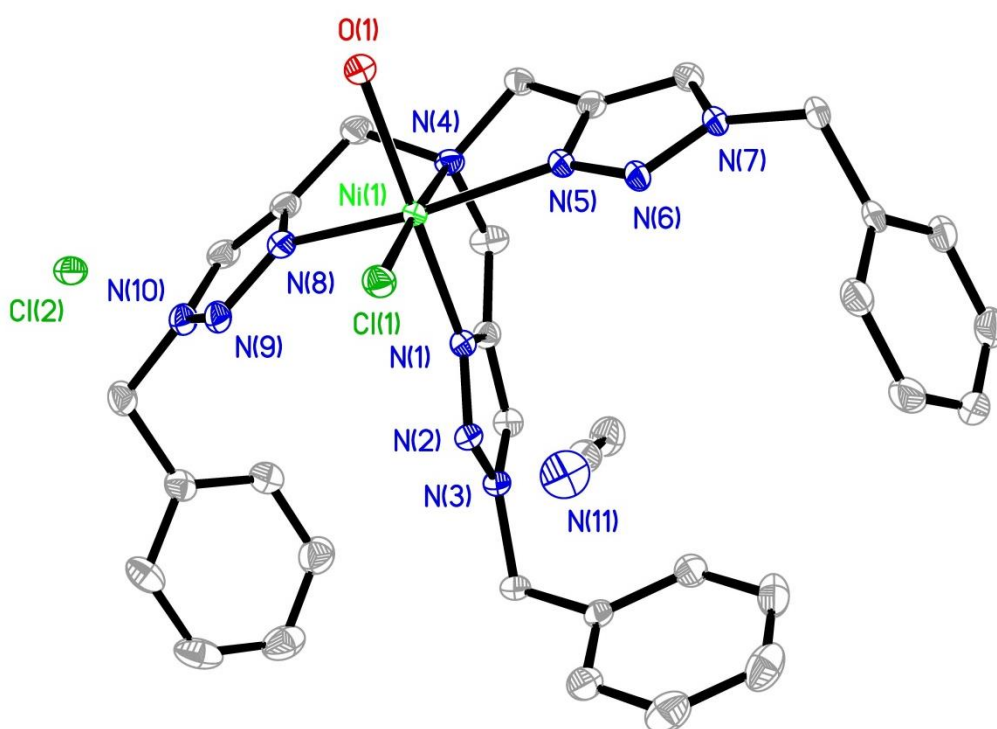


Figure 4.14- ORTEP²⁵ plot showing the single crystal X-ray structure of **130** with 50% probability displacement ellipsoids, with hydrogen atoms omitted for clarity.

Analysis of the X-ray structure revealed that the complex displays a distorted octahedral geometry as expected for d^8 Ni(II), where the TBTA ligand binds Ni(II) in a tetradentate fashion through all of its nitrogen donors. Additionally, one chloride anion and a water molecule complete the coordination sphere.

Table 4.5- Selected bond lengths (Å) and bond angles (°) for the X-ray crystal structure of **130 with estimated standard deviations (esds).**

<i>Bond lengths(Å)</i>		<i>Bond angles(°)</i>	
Ni-N(1)	2.0601(15)	N(4)-Ni-O(1)	91.18(6)
Ni-N(4)	2.2125(16)	N(5)-Ni-O(1)	89.69(6)
Ni-N(5)	2.0663(15)	N(8)-Ni-O(1)	90.60(6)
Ni-N(8)	2.1162(16)	Cl(1)-Ni-O(1)	90.71(4)
Ni-Cl(1)	2.3737(5)	N(1)-Ni-O(1)	170.92(6)
Ni-O(1)	2.0850(14)	N(4)-Ni-N(5)	77.50(6)
		N(8)-Ni-Cl(1)	102.27(5)

Closer examination of the crystal structure revealed that the Ni-N(triazole) (N(1), N(5) and N(8)) bond distances are between 2.06 Å and 2.11 Å, which is in accord with those reported for the homoleptic $[\text{Ni}(\text{TBTA})_2](\text{BF}_4)_2$ complex.⁸ The Ni-N(4) bond, on the other hand, is longer and at 2.21 Å, which is also very similar to the reported 2.24 Å distance in the related $[\text{Ni}(\text{TBTA})_2](\text{BF}_4)_2$ complex.⁸ The Ni(1)-O(1) bond length of 2.08 Å is very similar to the 2.10 Å Ni-O distances observed in the other related complexes.^{29,30} In contrast, the Ni-Cl(1) bond is 2.37 Å, which is much longer than all of the other coordination bonds in the structure. Additionally, it was observed, that the O(1)-Ni-N(1) bond angle is 170.92° in **130**, which points towards distortion from the ideal octahedral geometry. The other axial-Ni-equatorial bond angles are similar to the ones reported for $[\text{Ni}(\text{TBTA})_2](\text{BF}_4)_2$ and are in the range between 77.50° and 102.27°, which also indicates distorted octahedral geometry. Thus, the differences in bond lengths and angles indicate a more strained structure and results in a relaxation of symmetry. The presence of a chloride anion balances the charge on the cationic complex. Additionally, one MeCN solvent molecule was also observed in the unit cell. This work presents the first example of a heteroleptic complex of the TBTA ligand with Ni(II). Previously only a homoleptic TBTA-based Ni(II) complex $[\text{Ni}(\text{TBTA})_2](\text{BF}_4)_2$ has been reported by Sweinfurth *et al.*,⁸ in which two TBTA ligands were coordinated to the central Ni(II) atom in a distorted octahedral fashion by the two tertiary amine nitrogens and four of the six triazole-based nitrogen donors, with the third triazole-based pendant arm remaining uncoordinated in each ligand.

In order to obtain further evidence for the presence of an octahedral d⁸ Ni(II) paramagnetic species in $[\text{Ni}(\textbf{110})\text{Cl}(\text{OH}_2)]\text{Cl}$ **130**, $[\text{Ni}(\textbf{110})](\text{ClO}_4)_2$ **134**, $[\text{Ni}(\textbf{111})\text{Cl}]\text{Cl}$ **139** and

[Ni(**111**)](ClO₄)₂ **143**, alternative spectroscopic measurements together with electrochemical studies were carried out. The four Ni(II) complexes reported in this work presented similar UV-Vis spectra with four absorption bands being observed with λ_{max} in the region between 350 nm and 360 nm (most likely corresponding to MLCT transitions) and around 545-585 nm, with further third and fourth absorption bands around λ_{max} values of 790 nm and beyond the 900 nm limitation of the spectrometer. The characteristic spectrum of **130** is shown in Figure 4.15. It is similar to those reported for polypyridyl ligand complexes of Ni(II) and is characteristic of d⁸ Ni(II) in a pseudo-octahedral coordination.³¹ According to Hadadzadeh *et al.*,³¹ there are three spin-allowed transitions known for such octahedral Ni(II) complexes from the ³A_{2g} ground state to the three triplet excited states: ³A_{2g}(³F) → ³T_{2g}, ³A_{2g}(³F) → ³T_{1g}(³F) and ³A_{2g}(³F) → ³T_{1g}(³P), with reported molar absorptivity values (ε) being in the range of 18 to 27 M⁻¹ s⁻¹. Thus, the three absorption bands observed in the spectra reported here are most likely to correspond to these transitions and also show similar molar absorptivity values that are presented in Table 4.6 for the four Ni(II) complexes.

Table 4.6- UV-Vis spectral data for Ni(II) complexes **130**, **134**, **139** and **143** (2.5 mM solutions in MeCN).

130	Wavelength (nm)	367	580	790	900 (approx.)
	ε (M ⁻¹ s ⁻¹)	69	17	7	11
134	Wavelength (nm)	350	545	774	900 (approx.)
	ε (M ⁻¹ s ⁻¹)	60	20	10	12
139	Wavelength (nm)	360	582	785	900 (approx.)
	ε (M ⁻¹ s ⁻¹)	41	16	8	12
143	Wavelength (nm)	360	542	771	900 (approx.)
	ε (M ⁻¹ s ⁻¹)	65	19	6	12

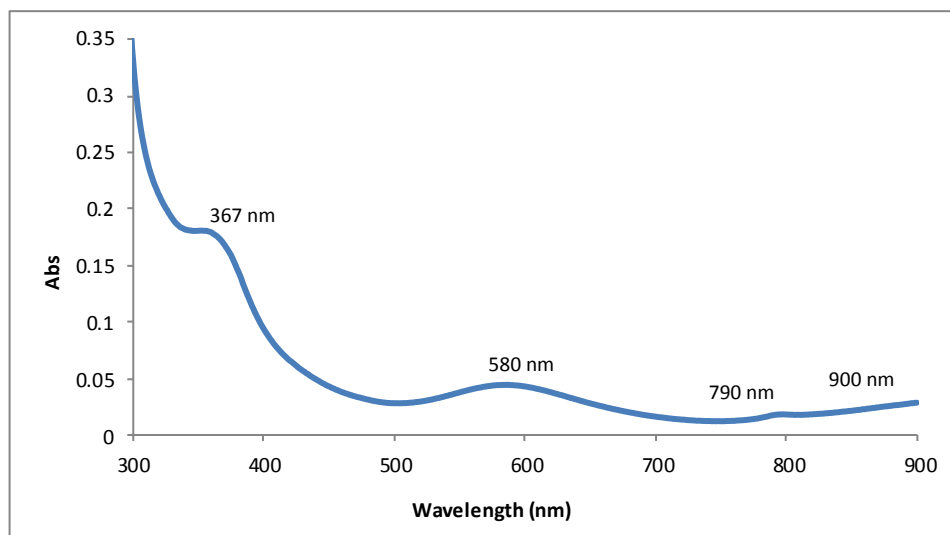


Figure 4.15- UV-Vis spectra of **130** run in MeCN solution.

The experimentally obtained magnetic moments were $2.8 \mu_B$ and $2.7 \mu_B$ for **130** and **134** respectively and $2.9 \mu_B$ for both **139** and **143**, which are in accord with the reported 2.9 - $3.3 \mu_B$ range for magnetically dilute Ni(II) d^8 species.²⁴ The data thus reflects the presence of the paramagnetic Ni(II) d^8 species with two unpaired electrons for **130**, **134**, **139** and **143**.

The electrochemical studies of the two Ni(II) chloride complexes **130** and **139** gave similar cyclic voltammograms with very similar E_{red} values of -1.65 V and -1.11 V (given for complex **130** vs SCE), which may tentatively be assigned to the Ni(II)/Ni(I) reduction couples. The second reduction peak at -1.11 V is very broad and ill-defined. This data is contrary to the reported polypyridyl Ni(II) d^8 complexes,³¹ which exhibited a quasi-reversible redox Ni(III)/Ni(II) couple at positive electrode potentials. There is also a small oxidation peak observed for **130** at -1.75 V, which is absent in the analogous TPTA complex for reasons which are unclear. The CV of **130** is presented in Figure 4.16. The presence of the poorly-coordinating perchlorate anion results in a slight cathodic shift of the reduction values for the Ni(II) perchlorate complex **134** and **143** with the shape remaining very similar to the corresponding chloride complexes **130** and **139**. Thus it seems reasonable to suggest that the anion does not exhibit any significant effect on the electrochemistry of the triazole-based Ni(II) complexes. Redox potentials for all four Ni(II) complexes vs SCE are presented in Table 4.7.

Table 4.7 -Redox potentials of **130**, **134**, **139** and **143** (0.1 M *n*-Bu₄NBF₄ and *n*-Bu₄NClO₄ solutions of supporting electrolytes for the chloride and perchlorate species respectively, scan rate= 50 mV s⁻¹) reported vs SCE.

Compound	E _{red} (V)	E _{ox} (V)
130	-1.11	-1.75
	-1.65	
134	-1.20	-
	-1.78	
139	-1.12	-
	-1.43	
143	-1.30	-
	-1.74	

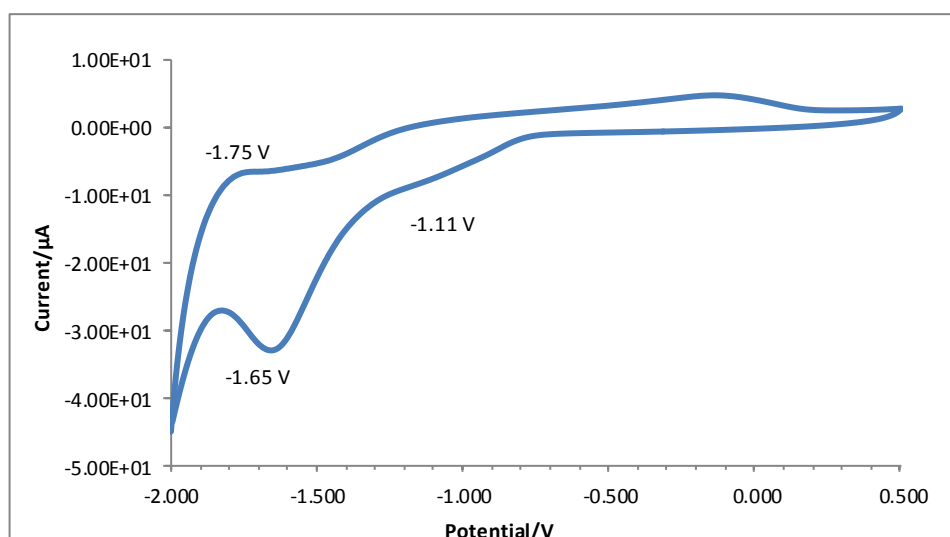


Figure 4.16- Cyclic voltammogram at glassy carbon using a calomel reference electrode in MeCN (*n*-Bu₄NBF₄ is the supporting electrolyte; scan rate= 50 mV s⁻¹) of 2.5 mM solution of **130**.

HRMS also confirmed the presence of the species of [Ni(II)L] stoichiometry for **130** and **139** and of [Ni(L)] stoichiometry for **134** and **143**.

Overall, the combination of single crystal X-ray crystallography, UV-Vis spectroscopy, magnetic moment measurements together with electrochemical studies determined the presence of d⁸ Ni(II) species in a pseudo-octahedral coordination geometry in all of the complexes prepared.

4.2.2.2.4. Characterisation of Mn(II) Complexes

X-ray quality crystals of $[\text{Mn}(\mathbf{111})_2](\text{ClO}_4)_2$ **144** were also obtained by slow diffusion of Et_2O into a MeOH solution of the complex and its structure is depicted in Figure 4.17 with selected bond lengths and angles contained in Table 4.8. It can be seen that, in **144** the central Mn(II) ion is coordinated to the two TPTA ligands in a pseudo-octahedral manner. Four triazole nitrogens (N(2), N(3), N(4) and N(6)) and two tertiary amine nitrogen donors (N(1) and N(5)), bind to the Mn(II) ion, while the third triazole ring from each TPTA ligand remains uncoordinated. A similar mode of binding has previously been observed in homoleptic TBTA-based Co(II), Fe(II) and Ni(II) complexes^{7,8} and octahedral geometry is known to be common for Mn(II) d^5 high spin complexes with tetradentate nitrogen donor ligands, such as azamacrocycles.³²

More extensive examination of this crystal structure revealed, that the Mn-N(2), Mn-N(3), Mn-N(4) and Mn-N(6) (Mn-N(triazole)) distances are 2.16 Å, 2.21 Å, 2.17 Å and 2.22 Å respectively. The Mn-N(2) and Mn-N(4) lengths fall within the range of reported distances in the similar systems with other metals, whereas Mn-N(3) and Mn-N(6) are longer than commonly reported M-N(triazole) distances in such metal complexes. Also, the Mn-N(1) and Mn-N(5) bond lengths are 2.53 Å and 2.47 Å respectively, which are significantly longer than those observed in the related cations $[\text{Co}(\text{TBTA})_2](\text{BF}_4)_2$, $[\text{Fe}(\text{TBTA})_2](\text{BF}_4)_2$ ⁷ and $[\text{Ni}(\text{TBTA})_2](\text{BF}_4)_2$.⁸ Interestingly, in the case of $[\text{Mn}(\mathbf{111})_2](\text{ClO}_4)_2$, the N(2) and N(4) triazole nitrogens from each TPTA ligand are *trans*- to each other, whereas the other two triazole nitrogens together with the central amine donors are present in *cis*-positions.

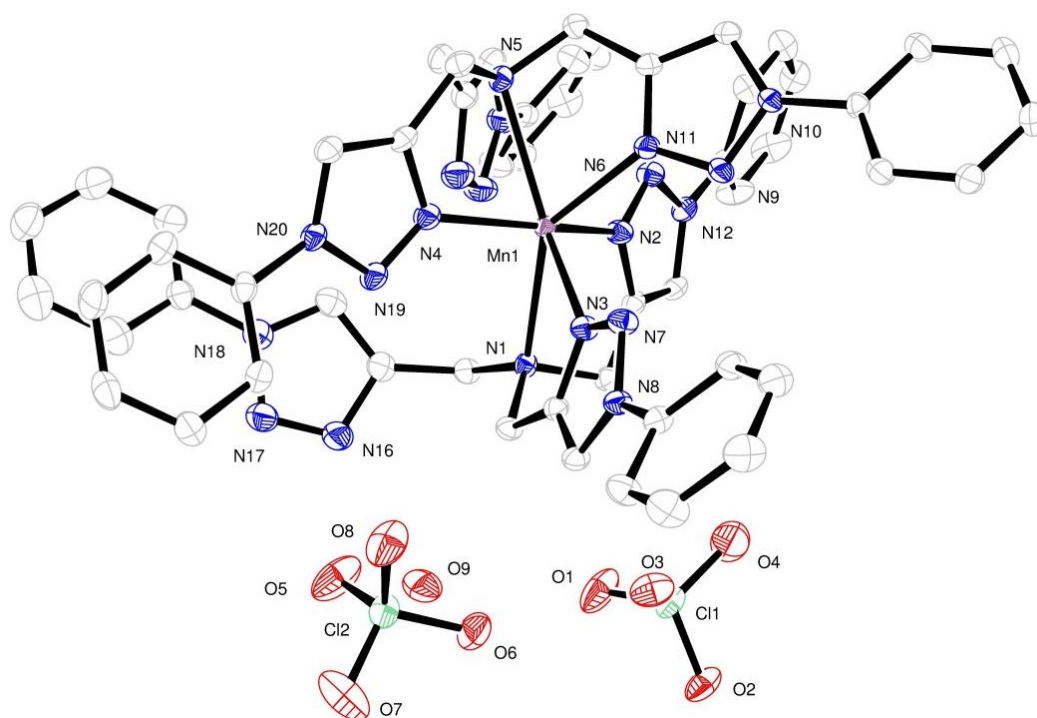


Figure 4.17- ORTEP²⁵ reference plot showing the single crystal X-ray structure of **144** with 50% probability displacement ellipsoids, with hydrogen atoms omitted for clarity.

This is in contrast to the similar reported metal complexes, where the central amine donors of each TBTA ligand occupy the *trans*-positions in the octahedron and the four triazole nitrogen donors are in *cis*-positions to each other. Additionally, the N(2)-Mn-N(4) bond angle is 155.72°, which deviates considerably from the ideal 180° angle in octahedral geometry. The other bond angles in **144** are in the range between 70.20° and 111.63°, which also reveals some deviation from ideal geometry. Two perchlorate anions are also present in **144** to balance the charge on the complex.

Table 4.8- Selected bond lengths (Å) and bond angles (°) for X-ray crystal structure of **144** with estimated standard deviations (esds).

Bond lengths(Å)		Bond angles(°)	
Mn-N(1)	2.5307(17)	N(2)-Mn-N(4)	155.72(7)
Mn-N(5)	2.4781(17)	N(4)-Mn-N(1)	99.97(6)
Mn-N(2)	2.1613(17)	N(4)-Mn-N(3)	87.68(6)
Mn-N(3)	2.2132(17)	N(4)-Mn-N(5)	71.21(6)
Mn-N(4)	2.1793(17)	N(4)-Mn-N(6)	111.63(6)
Mn-N(6)	2.2263(17)	N(1)-Mn-N(3)	70.20(6)
		N(5)-Mn-N(6)	70.30(6)

In order to obtain further evidence for the presence of Mn(II) d^5 paramagnetic species in [Mn(**110**)Cl]Cl **131**, [Mn(**110**)](ClO₄)₂ **135**, [Mn(**111**)Cl]Cl **140** and [Mn(**111**)₂](ClO₄)₂ **144**, alternative spectroscopic measurements together with electrochemical studies were carried out. All of the Mn(II) complexes prepared displayed similar UV-Vis spectra exhibiting features that are indicative of paramagnetic Mn(II) species. Given the fact that d-d transitions in high spin d^5 Mn(II) complexes are both spin and Laporte forbidden, it was unsurprising to see extremely weak or no pronounced d-d bands in the spectra.²³ The only exception was complex **135**, which resulted in the electronic spectra with absorption bands that could be distinguished in the regions of 660 nm and 855 nm albeit they were also very broad and still relatively weak.

Surprisingly, only complex **131** showed any electrochemical behaviour amongst the four Mn(II) complexes reported here for reasons that are unclear. The cyclic voltammogram displayed two reversible redox processes with reduction waves at 0.90 V and 1.61 V and related oxidation waves at 0.95 V and 1.73 V (vs SCE), which may correspond to the Mn(II)/Mn(III) and Mn(III)/Mn(IV) couples respectively²⁷ (Figure 4.18). The ratios of the cathodic (i_{pc}) and the anodic (i_{pa}) currents are 0.95 and 0.93, which are very close to 1 and are indicative of the reversible one electron redox behaviour. Redox potentials for **131** vs SCE are presented in Table 4.9.

Table 4.9- Redox potentials of **131** (0.1 M *n*-Bu₄NBF₄ solution of supporting electrolyte, scan rate= 50 mV s⁻¹) reported vs SCE.

Compound	E _{red} (V)	E _{ox} (V)
131	0.90	0.95
	1.61	1.73

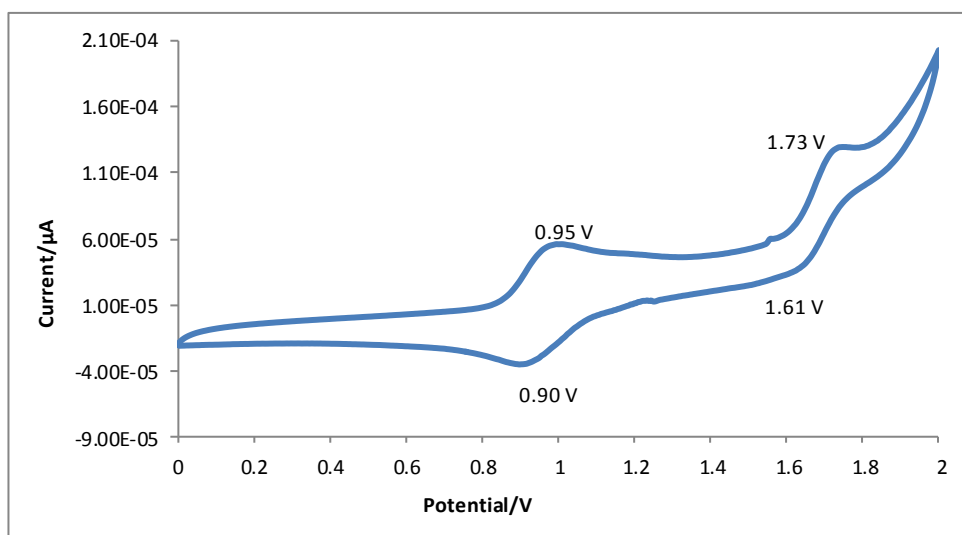


Figure 4.18- Cyclic voltammogram at glassy carbon using calomel reference electrode in MeOH ($n\text{-Bu}_4\text{NBF}_4$ is the supporting electrolyte; scan rate= 50 mV s^{-1}) of 2.5 mM solution of **131**.

Magnetic moment values for **131**, **135** and **144** were found to be $5.8 \mu_B$, $5.6 \mu_B$ and $5.3 \mu_B$ respectively based on an assumed complex stoichiometry of $[\text{Mn}(\text{L})\text{X}]$, $[\text{Mn}(\text{L})]$ and $[\text{Mn}(\text{L})_2]\text{X}_2$ and are in accord with the values expected for magnetically dilute high spin Mn(II).²⁴ Surprisingly, complex **140** gave a value of $\mu_{\text{eff}} = 6.7 \mu_B$, based on an assumed stoichiometry of $[\text{Mn}(\text{L})]$ (other assumed stoichiometries used for calculations resulted in the unreasonable μ_{eff} values), which is outside this range for reasons which are unclear as HRMS confirmed the presence of the expected mononuclear $[\text{Mn}(\text{L})\text{X}]$ species in **140**. Additionally, high resolution mass spectrometry supported the presence of a species with 1:1 metal ligand stoichiometry for both TBTA complexes. Rather surprisingly, the molecular ion that was observed for the structurally characterised complex $[\text{Mn}(\text{111})_2](\text{ClO}_4)_2$, corresponded to the presence of two ligands with no Mn(II) cation coordinated. Despite this HRMS result for **144**, together with the absence of any visible redox behaviour observed in **135**, **140** and **144**, EPR spectroscopy confirmed the presence of high spin d^5 Mn(II) species in all four complexes presented here.

EPR spectra of **131**, **140**, **135** and **144** were recorded in MeOH and are shown in Figure 4.19. The X-band EPR spectra of the four Mn(II) complexes each shows six well-resolved signals that arise due to the hyperfine interactions between the unpaired Mn(II) electrons with the ^{55}Mn nucleus ($I=5/2$). The broadening effect on the spectra is most likely to be due to spin relaxation.²⁷ The polycrystalline spectra are typical of high spin d^5 Mn(II) centres and with g values in the range of 2.01-2.04. Thus, EPR data corroborate with the Evan's NMR

data. Interestingly, it can be observed that the shape of the EPR spectrum of **131** is slightly different when compared to the other three Mn(II) complexes, perhaps indicating some subtle differences in the coordination chemistry. There was a speculation that the EPR signal in **144** might arise simply from the presence of $\text{Mn}(\text{ClO}_4)_2 \cdot 6\text{H}_2\text{O}$ in the sample as a result of it being precipitated from the reaction solution upon the addition of Et_2O . However, testing of this theory showed that the salt does not precipitate from either MeCN or MeOH under these conditions.

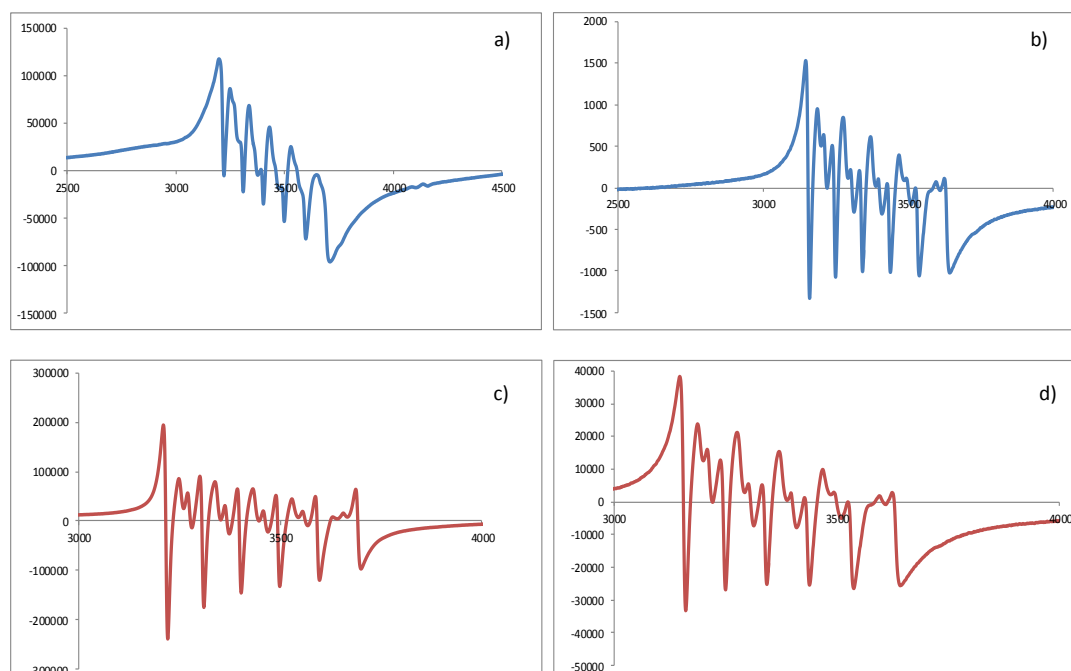


Figure 4.19- EPR spectra of Mn(II) complexes in MeOH reported at 50 K: a) **131**; b) **140**; c) **135**; d) **144**.

4.2.2.2.5. Characterisation of Zn(II) Complexes

The presence of the Zn(II) complexes $[\text{Zn}(\mathbf{110})\text{Cl}]\text{Cl}$ **132**, $[\text{Zn}(\mathbf{110})](\text{ClO}_4)_2$ **136**, $[\text{Zn}(\mathbf{111})\text{Cl}]_2[\text{ZnCl}_4]$ **141** and $[\text{Zn}(\mathbf{111})](\text{ClO}_4)_2$ **145** in solution and their purity was assessed by ^1H NMR spectroscopy. The ^1H NMR spectra of the Zn(II) complexes showed a shift in all signals when overlapped with the appropriate uncoordinated ligand, providing evidence of complex formation. This is exemplified by a stacked plot of the ^1H NMR spectra of complex **132**, showing a clear downfield shift and broadening of the signals upon Zn(II) complexation (Figure 4.20).

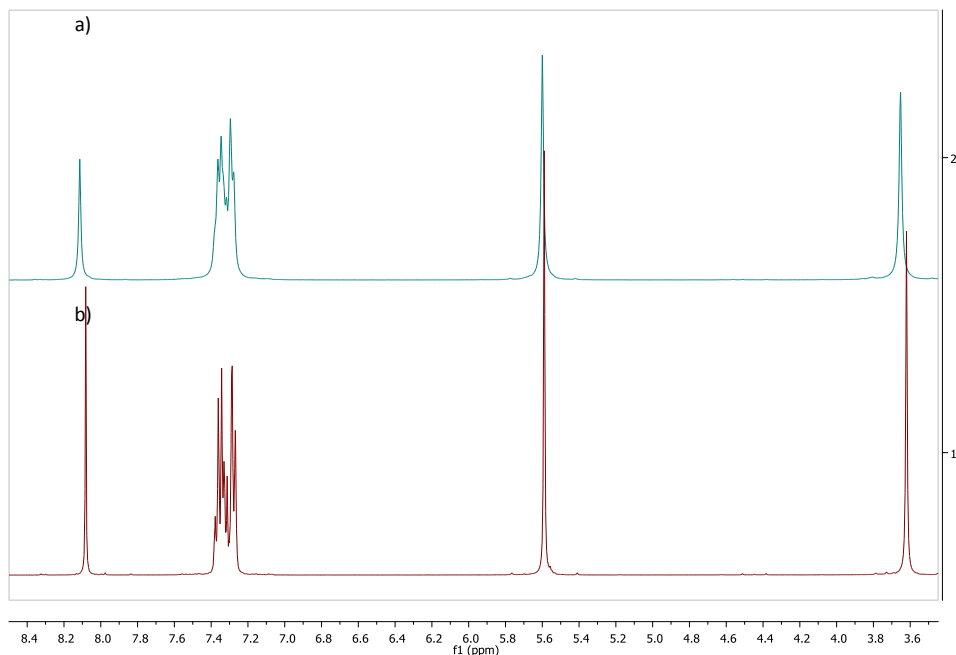


Figure 4.20- Stacked ^1H NMR spectra of the a) $[\text{Zn}(\mathbf{110})\text{Cl}]\text{Cl}$ complex **132** and b) TBTA ligand **110** in DMSO-d_6 , showing a downfield chemical shifts in the protons of **110** upon $\text{Zn}(\text{II})$ complexation.

Crystals of complex **141** suitable for single crystal X-ray diffraction were formed in CD_3OD solution and revealed there to be two similar cationic monomers in the asymmetric unit of stoichiometry $[\text{Zn}(\mathbf{111})\text{Cl}]_2[\text{ZnCl}_4]$, which are shown in Figure 4.21. Analysis of the crystals revealed it to be a heteroleptic complex in which the $\text{Zn}(\text{II})$ ions are each coordinated to one ligand through one nitrogen atom from each of the three triazole rings of the TPTA ligand with a long and weak interaction with the central tertiary amine nitrogen. Selected bond lengths and angles for both $\text{Zn}(\text{II})$ units are shown in Table 4.10, which indicate that these are very similar in both metal units. Based on the monomeric unit **1**, it was observed that the average $\text{Zn-N}(\text{triazole})$ bonds length is 2.04 \AA , which is in accord with the reported distances in similar heteroleptic complexes.¹ On the other hand, the distance between the $\text{Zn}(\text{II})$ ion and the central TPTA nitrogen is rather longer and is 2.58 \AA , as previously reported for similar heteroleptic TBTA metal complexes (*vide infra*).¹

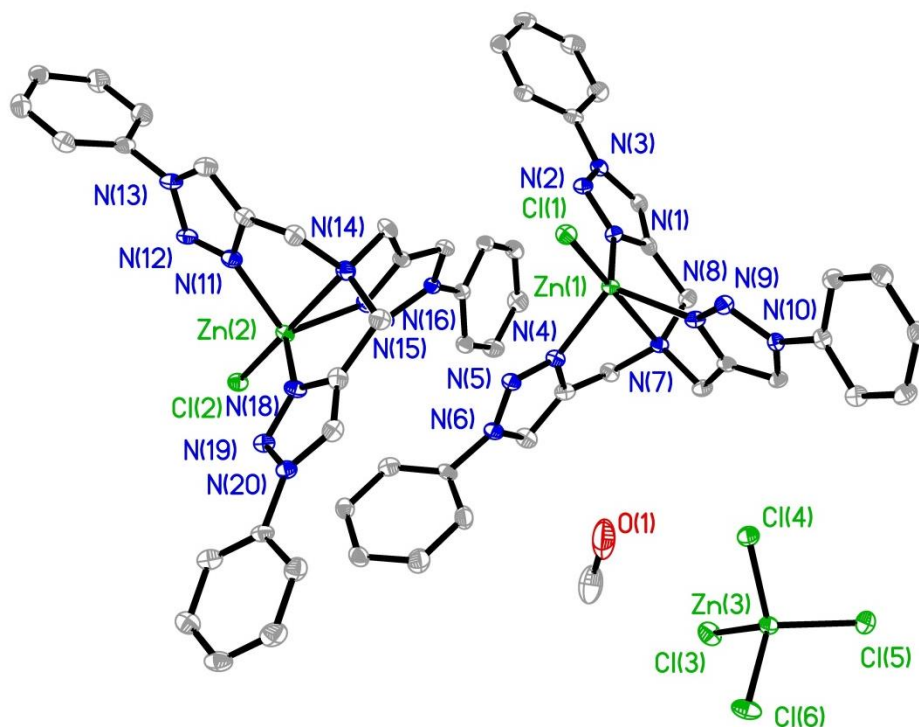


Figure 4.21- ORTEP²⁵ plot showing the single crystal X-ray structure of 141 with 50% probability displacement ellipsoids, with hydrogen atoms omitted for clarity.

Table 4.10- Selected bond lengths (Å) and bond angles (°) for the X-ray crystal of 141 with estimated standard deviations (esds).

<i>Zn(II) monomeric unit 1</i>			
<i>Bond lengths(Å)</i>		<i>Bond angles(°)</i>	
Zn(1)-N(1)	2.034(3)	N(4)-Zn(1)-N(1)	106.83(13)
Zn(1)-N(4)	2.051(3)	N(4)-Zn(1)-N(8)	109.10(13)
Zn(1)-N(8)	2.053(3)	N(8)-Zn(1)-N(1)	114.57(12)
Zn(1)-N(7)	2.585(3)	N(4)-Zn(1)-Cl(1)	107.90(9)
Zn(1)-Cl(1)	2.237(1)		
<i>Zn(II) monomeric unit 2</i>			
<i>Bond lengths(Å)</i>		<i>Bond angles(°)</i>	
Zn(2)-N(11)	2.039(3)	N(18)-Zn(2)-N(11)	107.95(13)
Zn(2)-N(18)	2.022(3)	N(18)-Zn(2)-N(15)	113.41(13)
Zn(2)-N(15)	2.047(3)	N(15)-Zn(2)-N(11)	109.08(13)
Zn(2)-N(14)	2.599(3)	N(18)-Zn(2)-Cl(2)	113.13(10)
Zn(2)-Cl(2)	2.2366(10)		

Additionally, Zn(II) is coordinated to one chloride ligand, with a bond length of 2.23 Å. with the cationic charge of the two cations in the unit cell balanced by a $[\text{ZnCl}_4]^{2-}$ anion as has been reported for a related pyridine-based complex.³³ The N-Zn-N and Cl-Zn-N bond angles in **141** range from 106.83° to 114.57° and are similar to those observed in related studies.¹ Overall, all the reported crystallographic data points towards a capped tetrahedral, or 4+1, coordination geometry around the Zn(II) ion, where the weak interactions between the zinc centres and the tertiary nitrogen donors act as a capping bonds and cause distortions in the structures from the traditional trigonal bipyramidal coordination mode. Similar five-coordinate pseudo-tetrahedral coordination geometries were reported in the case of $[\text{Co}(\text{TBTA})\text{Cl}]\text{BF}_4$ and other Co(II) complexes with similar ‘click’-derived triazole-based ligands.¹ To our knowledge, the crystal structure of **141** is the first example of for a TPTA-based Zn(II) complex.

The presence of the mononuclear Zn(II) metal-ligand complexes of general stoichiometry $[\text{Zn}(\text{L})\text{X}]$ in **132** and **141**, and of $[\text{Zn}(\text{L})]$ in **136** and **145** was confirmed by HRMS.

Electrochemical studies of the two chloride complexes **132** and **141** were performed as a blind test for all other electrochemical studies reported in this work in MeOH to ensure that the presence of electrochemical behaviour in the complexes is metal- rather than ligand-based given the redox inactivity of Zn(II). As expected, the complexes did not show any redox chemistry, thus indicating that all electrochemical changes observed for the other complexes reported herein are due to metal-based redox chemistry.

4.3. Conclusions and Final Remarks

In summary, potentially tetradentate 1,2,3-triazole-based tripodal ligands **110**,¹² **111**¹¹ and **112**¹³ were prepared in excellent to quantitative yields using efficient and experimentally simple ‘click’ CuAAC methodology. In particular, the yield of **111** was optimised from the reported yield of 61% to 90% and pure ligand could be isolated without using laborious chromatographic techniques as reported. A range of TPTA and TBTA-based d-block metal complexes have been prepared and their structural features together with their coordination, magnetic and electrochemical behaviour were investigated by various techniques where possible, such as X-ray crystallography, ¹H NMR, UV-Vis spectroscopy and Evan’s NMR spectroscopy, cyclic voltammetry, EPR spectroscopy and HRMS. d-Block metal complexes with a range of coordination modes, including capped tetrahedral, pseudo-octahedral and trigonal bipyramidal were obtained. The X-ray crystallographic data for

complexes **130**, **138**, **141** and **144** (together with a comparison with reported structures) showed that changes in the ligand structure can influence the binding mode around the metal atom, as exemplified by the $[\text{Cu}(\mathbf{111})\text{Cl}_2]$ complex **138**, where two triazole moieties coordinate to the metal compared to the reported $[\text{Cu}(\text{TBTA})\text{Cl}]\text{Cl}$.¹⁰ Some evidence was also acquired from electrochemical studies in the case of the Cu(II) complexes that the nature of the anion as well the chemical structure of the ligand can also result in changes in redox chemistry, thus influencing the Lewis acidity of the metal ion. Effective magnetic moments were measured to determine the spin state of the metal cations in the complexes and the majority fell within the expected range of values with some minor exceptions.²⁴ EPR data were in line with the magnetic moment measurements and also supported the formulated oxidation and spin states for the Cu(II) and Mn(II) complexes. Electrochemical experiments in this work confirmed that the presence of metal-based redox activity in the target complexes. Surprisingly, three Mn(II) complexes **135**, **140** and **144** did not show any electrochemistry for reasons that are unclear. Nonetheless, the stoichiometry of these complexes as formulated was supported by HRMS, with the exception of **144**, even though the structure was confirmed by single crystal X-ray crystallography. ¹H NMR spectroscopy allowed the formation of Zn(II) complex formation to be determined as evidenced by changes in the spectra. Unfortunately, due to a lack of aqueous solubility, the potential phosphatase-like hydrolytic activity of these 'click'-based metal complexes has not been tested.

4.4. Bibliography

1. D. Sweinfurth, S. Demeshko, M. M. Khusniyarov, S. Dechert, V. Gurram, M. R. Buchmeister, F. Meyer and B. Sarkar, *Inorg. Chem.*, 2012, **51**, 7592-7597.
2. F. Mancin, P. Scrimin and P. Tecilla, *Chem. Commun.*, 2012, **48**, 5545-5559.
3. K. D. Karlin, J. C. Hayes, S. Juen, J. P. Hutchinson and J. Zubieta, *Inorg. Chem.*, 1982, **21**, 4106-4108.
4. A. Schiller, R. Scopelliti and K. Severin, *Dalton Trans.*, 2006, 3858-3867.
5. D. Li, J. Tian, W. Gu, X. Liu and S. Yan, *J. Inorg. Biochem.*, 2010, **104**, 171-179.
6. D. Schweinfurth, F. Weisser, D. Bubrin, L. Bogani and B. Sarkar, *Inorg. Chem.*, 2011, **50**, 6114-6121.
7. D. Sweinfurth, S. Demeshko, S. Hohloch, M. Steinmetz, J. G. Brandenburg, S. Dechert, F. Meyer, S. Grimme and B. Sarkar, *Inorg. Chem.*, 2014, **53**, 8203-8212.
8. D. Sweinfurth, J. Krzystek, I. Schapiro, S. Demeshko, J. Kleins, J. Tesler, A. Ozarowski, C. Su, F. Meyer, M. Atanasov, F. Neese and B. Sarkar, *Inorg. Chem.*, 2013, **52**, 6880-6892.
9. D. Sweinfurth, J. Klein, S. Hohloch, S. Dechert, S. Demeshko, F. Meyer and B. Sarkar, *Dalton Trans.*, 2013, **42**, 6944-6952.
10. P. S. Donnelly, S. D. Zanatta, S. C. Zammit, J. M. White and S. J. Williams, *Chem. Commun.*, 2008, 2459-2461.
11. A. Baschieri, A. MAzzanti, S. Stagni and L. Sambri, *Eur. J. Inorg. Chem.*, 2013, 2432-2439.
12. J. E. Hein, L. B. Kransova, M. Iwasaki and V. V. Fokin, *Org. Synth.*, 2011, **88**, 238-247.
13. V. Hong, A. K. Udit, R. A. Evans and M.G. Finn, *Chem. Biochem.*, 2008, **9**, 1481-1486.
14. H. C. Kolb, M. G. Finn and K. B. Sharpless, *Angew. Chem. Int. Ed.*, 2001, **40**, 2004-2021.
15. B. T. Worrell, J. A. Malik and V. V. Fokin, *Science*, 2013, **340**, 457-460.
16. a) S. J. Krivickas, E. Tamanini, M. H. Todd and M. Watkinson, *J. Org. Chem.*, 2007, **27**, 8280-8289; b) J. Pnacholi, D. J. Hodson, K. Jobe, G. A. Rutter, S. M. Goldup and M. Watkinson, *Chem. Sci.*, 2014, **5**, 3528-3535.
17. C. D. Hein, X. Liu and D. Wang, *Pharm. Res.*, 2008, **25**, 2216-2230.
18. T. R. Chan, R. Hilgraf, K. B. Sharpless and V. V. Fokin, *Org. Lett.*, 2004, **6**, 2853-2855.
19. W. S. Horne, C. D. Stout and M. R. Ghadiri, *J. Am. Chem. Soc.*, 2003, **125**, 9372-9376.

20. L. Campbell-Verduyn, P. H. Elsinga, L. Mirfeizi, R. A. Dierckxb and B. L. Feringa, *Org. Biochem. Chem.*, 2008, **6**, 3461, 3463.
21. K. Barral, A. D. Moorhouse and J. E. Moses, *Org. Lett.*, 2007, **9**, 1809-1811.
22. J. S. Foot, F. E. Luia and R. Kluge, *Chem. Commun.*, 2009, **47**, 7315-7317.
23. C. E. Housecroft and A. G. Sharpe, *Inorganic Chemistry*, Pearson, 2007.
24. a) K. De Buysser, G. G. Herman, E. Bruneel, S. Hoste and I. Van Driessche, *Chem. Phys.*, 2005, **315**, 286-292;
b) <http://wwwchem.uwimona.edu.jm/spectra/MagMom.html>, visited September 2016.
25. L. J. Farrugia, *J. Appl. Cryst.*, 1997, **30**, 565.
26. A. W. Addison, N. T. Rao, J. Reedijk, J. Van Rijn and G. C. Verschoor, *J. Chem. Soc., Dalton Trans.*, 1984, 1349-1356.
27. S. Chandra and L. K. Gupta, *Spectrochim. Acta Part A*, 2004, **60**, 1751-1761.
28. M. A. Neelakantana, F. Rusalraj, J. Dharmaraj, S. Johnsonraja, T. Jeyakumar and M. S. Pillai, *Spectrochim. Acta Part A*, 2008, **71**, 1599-1609.
29. D. J. Chesnut, R. C. Haushalter and J. Zubieta, *Inorg. Chim. Acta*, 1999, **292**, 41-51.
30. M.-L. Sun, L. Zhang, Q.-P. Lin, J. Zhang and Y.-G. Yao, *Crystal Growth & Design*, 2010, **10**, 1464-1467.
31. H. Hadadzadeh, G. Mansouri, A. Rezvani, H. R. Khavasi, B. W. Skelton, M. Makha and F. R. Charati, *Polyhedron*, 2011, **30**, 2535-2543.
32. T. J. Hubin, J. M. McCormick, S. R. Collinson, M. Buchalova, C. M. Perkins, N. W. Alcock, P. K. Kahol, A. Raghunathan and D. H. Busch, *J. Am. Chem. Soc.*, 2000, **122**, 2512-2522.
33. J. García-Martín, R. López-Garzón, M. L. Godino-Salido, R. Cuesta-Martos, M. D. Gutiérrez-Valero, P. Arranz-Mascarós and H. Stoeckli-Evans, *Eur. J. Inorg. Chem.*, 2005, 3093-3103.

Chapter 5: Conclusions and Future Work

5.1. An Overview

The hydrolytic cleavage of phosphate ester bonds- one of the most stable units in Nature- plays a fundamental role not only in some of the key biological processes, but also in the degradation of toxic organophosphorous compounds, such as nerve agents.^{1,2} Thus far, certain classes of natural organophosphatases that show excellent substrate selectivity to certain phosphate esters remain the most efficient catalysts for such energetically demanding reactions, providing rate accelerations as high as 10^{17} over the uncatalysed reaction.³ Nevertheless, the applications of such biological enzymes are often limited due to their inherent instability and subsequent denaturation under certain experimental conditions, such as extremes of temperatures and pHs and in their intolerance of organic solvents.^{3,4}

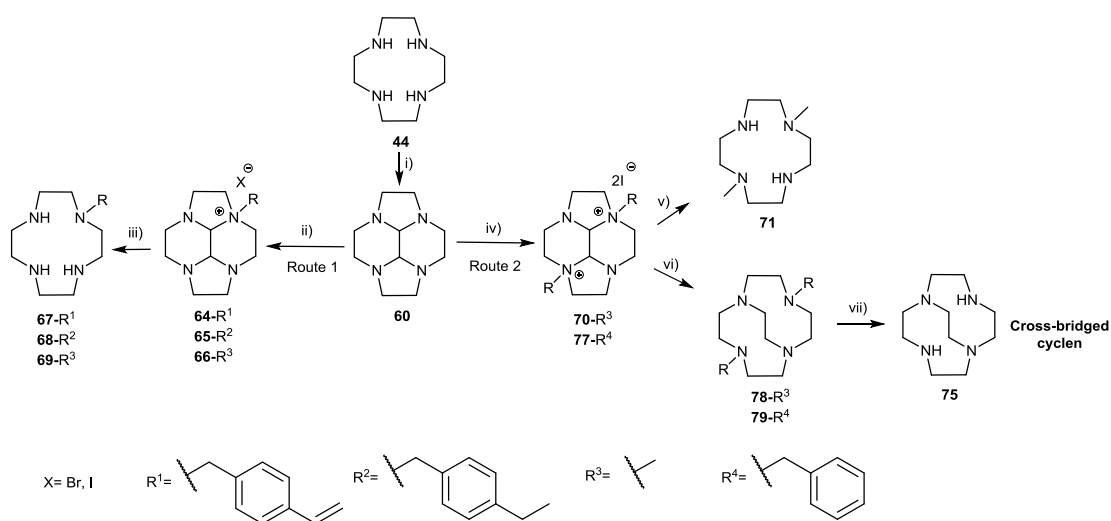
Chemists, within the broad field of biomimetic chemistry, have been long-engaged in the challenge of reproducing and even improving the efficiency of natural phosphoesterases. Their efforts resulted in the development of various interesting mimetic systems that could facilitate phosphate ester hydrolysis with impressive rate enhancements, yet these are still significantly lower than enzymatic rates.³ Amongst the synthetic alternatives explored, the vast majority were small-molecule complexes with d-block metal ions. Structural design of such hydrolytic models was believed to be central to their hydrolytic efficiency and a broad range of structure–reactivity studies were carried out in search of an ‘ideal’ synthetic model.³ However, one of the biggest disadvantages of such metallic small-molecule systems is that they are often used in large excess over the substrate and thereby are not acting as ‘real’ catalysts. In order to tackle this issue and further optimise their activity, taking an inspiration from Nature, another approach was developed with the focus on the chemical environment around the metal complex. It was demonstrated, that placing these complexes into a low polarity environment, such as low polarity solvents, large organic molecules or polymers, that closely mimic the dielectric constants of the active sites of enzymes, creating hydrophobic environments around the metal centres, resulted in higher rate enhancements compared to those obtained with the ‘free’ metal complexes.^{5,6} The use of molecular imprinting technique in nanogels is one of the strategies used to mimic the secondary coordination sphere of natural enzymes. This technique allows the generation of highly specific cavities within the three dimensional polymeric matrix, that provide the

secondary enzyme-like coordination sphere around the metal cation.⁷ This sphere involves interactions between the metal ion, functional monomer, template and substrate-interactions that have yet to be fully understood.⁴ Also, the full potential of metals in MIP systems has not been fully exploited thus far. Flexible nanogels have been identified as a flexible and most attractive matrix for novel biomimetic catalysis, giving the best mimic of the natural enzyme.⁷

5.2. Small-Molecule Tetraamine Co(III) and Zn(II) Complexes

In this work it was mainly set out to explore a) the effect of structural modifications of the small-molecule tetraamine Co(III) and Zn(II) complexes on their efficiency to facilitate phosphate ester hydrolysis and b) the effect of incorporating polymerisable tetraamine Co(III) complex on its hydrolytic activity.

The main focus of the first part of the project was focussed on the synthesis and characterisation of the tetraazamacrocyclic Co(III) complexes using Co(III) cyclen complexes as the basic metal-ligand unit. Firstly, selectively *N*-alkylated cyclen-based ligands were prepared in good to excellent yields *via* a bisaminal synthetic route and some of them had improved purity compared to the ones previously prepared in the group. This strategy allowed generation of the target ligands with the various alkyl groups in short times without laborious purification procedures and thus proved to be efficient and versatile.⁸ Certain modifications to the bisaminal synthetic route also lead to the incorporation of the ethylene bridge into the macrocyclic moiety⁹ (Scheme 5.1).



Scheme 5.1- Synthesis of *N*-functionalised cyclen ligands *via* tetracyclic intermediates.^{8,9}

Six structurally related cyclen-based $[\text{Co}(\text{L})\text{Cl}_2]\text{Cl}$ complexes were prepared from their respective $[\text{Co}(\text{L})\text{CO}_3]\text{HCO}_3$ precursors and isolated in good to excellent yields, and were then successfully converted to their corresponding hydrolytically active aqua-hydroxo species in HEPES (10 mM, pH 7.2) depicted in Figure 5.1.^{10,11}

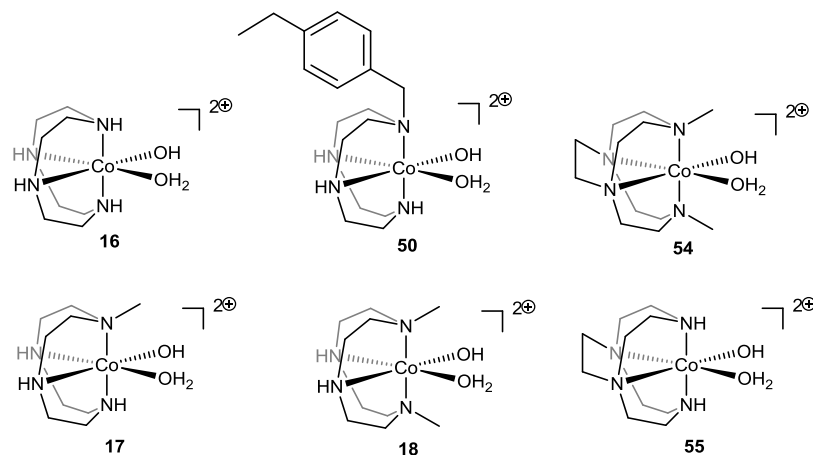
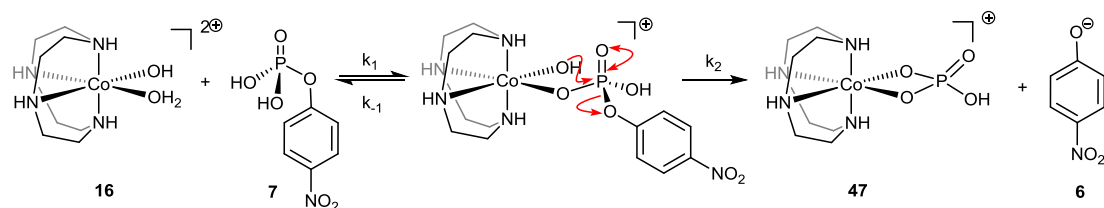


Figure 5.1- Structures of the target cyclen-based Co(III) complexes.

The coordination geometry and electrochemical behaviour of the $[\text{Co}(\text{L})\text{Cl}_2]\text{Cl}$ species was studied by a range of techniques, such as NMR and UV-Vis spectroscopies, X-ray crystallography and cyclic voltammetry, which confirmed the presence of the low spin diamagnetic d^6 Co(III) species in pseudo-octahedral geometry in these complexes. Overall, based on the results obtained, *N*-alkylation of the tetraamine ligands resulted in significant changes in the properties of their corresponding metal complexes, such as distortion of the coordination geometry around the metal ion, rates of labile ligand exchange and their Lewis acidity.



Scheme 5.2- Co(III) catalysed hydrolysis of NPP 7, which involves coordination of the substrate to the complex followed by the intramolecular nucleophilic substitution to give *p*-nitrophenolate 6 and complex 47.¹²

Importantly, the size of the $\text{N}_{\text{eq}}\text{-Co-N}_{\text{eq}}$ angle (Figure 5.2 below), which influences the ease of the four-membered ring chelate formation during the hydrolytic reaction (Scheme 5.2), was found to be one of the determining factors in the activity of the tetraamine Co(III) complexes. It was shown by Chin *et al.*¹³ that larger $\text{N}_{\text{eq}}\text{-Co-N}_{\text{eq}}$ angles facilitate the

stabilisation of the post-hydrolysis ring and result in enhanced hydrolysis of phosphate esters. Based on the comparison of the crystal structures of **89** and **85** (previously obtained in the Watkinson and Resmini groups),¹⁴ it was confirmed in this work that bidentate carbonate ligands result in larger $N_{eq}\text{-Co-}N_{eq}$ angles ($\sim 100^\circ$) when compared to the monodentate chloro coordinating ligands ($\sim 95^\circ$) in Co(III) cyclen complexes (a feature that will be discussed later in this chapter). *N*-Alkylation in carbonato complexes was found to cause slight reduction in the angle according to the $[\text{Co}(\mathbf{68})\text{CO}_3]\text{MeCO}_3$ X-ray structure compared to the previously published one of the $[\text{Co}(\text{cyclen})\text{CO}_3]\text{HCO}_3$.¹⁵

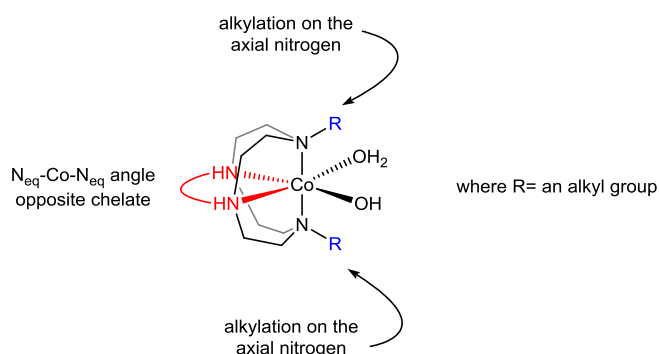
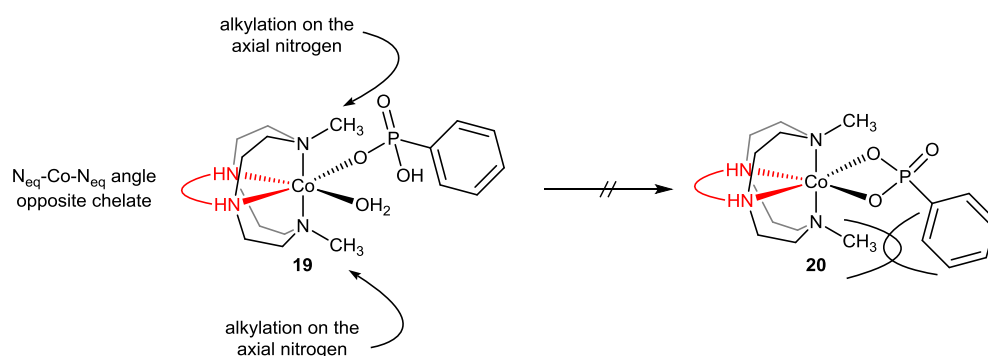


Figure 5.2- Structural features that influence the ease of the four-membered ring formation on Co(III) cyclen-based complexes.

Additionally, given the X-ray crystal structure of $[\text{Co}(\mathbf{78})\text{Cl}_2]\text{Cl}$ (**89**), introduction of the ethylene cross-bridge into the macrocyclic moiety lead to a further reduction in the size of this equatorial angle to 88° . The effect of the axial *N*-alkylation was demonstrated by Kim *et al.*¹⁶ to impose steric hindrance on the metal unit which then inhibited the formation of the four-membered phosphonate ring during the hydrolytic reaction (Scheme 5.3). On the other hand it is also known, that *N*-alkylation also increases Lewis acidity of the central metal cation, which should result in hydrolytic efficiency gain.¹⁷ Thus, it was decided to investigate the steric effect *versus* Lewis acidity on the hydrolytic activity of the target hydrolytically active aqua-hydroxo Co(III) complexes. Electrochemistry studies indeed resulted in *N*-alkylated complexes having slightly more positive reduction potentials indicating some increase in their Lewis acidity. However, only the hydrolytically active $[\text{Co}(\mathbf{75})(\text{OH}_2)\text{OH}]^{2+}$ with the ethylene cross-bridge showed more negative reduction potential as opposed to $[\text{Co}(\mathbf{44})(\text{OH}_2)\text{OH}]^{2+}$ and other *N*-alkylated Co(III) complexes, which is in accord to the work published by Ware *et al.*¹⁸ for similar tetraamine Co(III) complexes.



Scheme 5.3- Binding of the phenyl phosphonate to 18: Inhibition of the formation of the four-membered chelate ring due to steric interactions between the methyl group on the cobalt complex and phenyl ring on the phosphonate, proposed by J.Kim *et al.*¹⁶

Hydrolytic experiments with the target tetraamine Co(III) complexes used in excess over the NPP substrate (3:1 stoichiometry), however, showed the strong dependence of the efficiency of the system on the N_{eq} -Co- N_{eq} angle size. It was found that the decrease in N_{eq} -Co- N_{eq} angle size by nearly 8° (in addition to the unexpected slight drop in Lewis acidity in **55**) upon the cross-bridge incorporation was reflected in a remarkable drop in its ability to facilitate the NPP substrate hydrolysis from 75% to 4% chemical yield of *p*NP product being obtained respectively. The axial mono *N*-alkylation resulted only in a small drop in activity from 75% to 68% and 67% in **50** and **17** respectively, whereas di-*N*-alkylation showed a more pronounced effect and the activity in **18** was reduced to 8%. This indicates the importance of the steric hindrance on the hydrolytic activity of the Co(III) complexes, which is in line with study by Kim *et al.* The combination of both- the axial di alkylation and incorporation of the cross-bridge hampered the activity of **54**, which gave <1% of the *p*NP chemical yield.

One of the most important outcomes of this study is that both steric effects and the decrease in N_{eq} -Co- N_{eq} size have more significant effects on the hydrolytic activity of the complexes, than the increase in Lewis acidity of the Co(III) cation resulting from *N*-alkylation. As the efficiency of these Co(III) complexes strongly depends on the N_{eq} -Co- N_{eq} angle size, with larger angles leading to higher phosphatase-like activities, this is one of the key features that should be reproduced in the future tetraamine mimetic systems. Also, it would be of interest to reduce the equivalents of tetraamine Co(III) complexes to determine the minimum number of equivalents (given that in 1:1 stoichiometry complexes showed no hydrolytic activity-determined in this work) required of Co(III) to facilitate the reaction.

Analogous cyclen-based Zn(II) complexes were prepared and isolated in good to excellent yields with the view to investigate the effect of the metal cation on the hydrolytic efficiency of such tetraamine mimetic systems towards phosphate ester hydrolysis. As expected, based on the literature results, Zn(II) did not show any appreciable hydrolysis in 3:1 metal:substrate stoichiometry towards BNPP hydrolysis even at higher temperatures and pH.^{19,20} This could potentially be attributed to the weaker Lewis acidity of Zn(II) compared to Co(III) cation. Testing these complexes with the biologically relevant Zn(II) cation at higher temperatures and at higher concentrations to fully exploit their hydrolytic potential in P-O bond cleavage would potentially be of interest. Further studies might also include expanding the scope of metal cations to other biologically relevant metal ions, such as Ca(II). Moreover, the facile bisaminal procedure can be utilised as a modular and efficient way to prepare multimetallic tetraamine mimetic systems to more fully explore the effect of metal ion cooperation on the hydrolytic efficiency of the system.

Importantly, as seen from the literature studies and this work, the labile *cis*-positions on these metal complexes play an important role in their applications. The recent study by Maple *et al.*²¹ demonstrated the potential of Zn(II) and Cu(II)-based ethylene-bridged macrocycles to bind biological chemokine receptor CXCR4 (and act as receptor antagonists), which plays an essential role in the growth, survival and metastasis of cancer cells.²¹ This was done by extensively studying the metal complex interaction with acetate ligands, which act as models for the aspartate and glutamate amino acid side chain residues in the receptor. Thus, it would be potentially interesting to explore the interaction with acetate ligands of the tetraamine Co(III) and Zn(II) complexes prepared in this work, which would reflect their potential interactions (e.g. the mode of binding) with biological molecules (e.g. DNA binding proteins). As the identity of the metal ion was demonstrated by the authors to be important for such binding, it would be of special interest to test the effect of the Co(III) metal cation in these systems.

5.3. Molecular Imprinted Polymers as an Alternative to Small-Molecule Metal Complexes.

Studies in this work showed that when a tetraamine Co(III) complex is used in a 1:1 stoichiometry, the reaction results in no turnover due to the tight binding of the second hydrolysis product to the metal, thus hampering further hydrolytic activity of the complex. In order to circumvent this issue, the second part of this work was focussed on studying the

effect of incorporating polymerisable tetraamine Co(III) complexes into nanogels on their hydrolytic efficiency. The imprinted polymers were already available in the research group as a result of previous work carried out by Dr. Jorge.¹⁴ Two nanogelic polymers were imprinted with two different Co(III) monomer bound to two different templates- carbonate (bidentate) **52** and phosphonate (monodentate) **51** (Figure 5.3). The latter resulted in six-coordinate octahedral geometry of the metal complex and the former in predominantly trigonal bipyramidal geometry, which was confirmed by UV-Vis and EPR spectroscopies. The use of a phosphonate template was believed to be advantageous due to its geometrical resemblance to the NPP substrate. The carbonate template on the other hand was used as an analogue of the non-imprinted polymer required for the reference in the study of NPP hydrolysis.

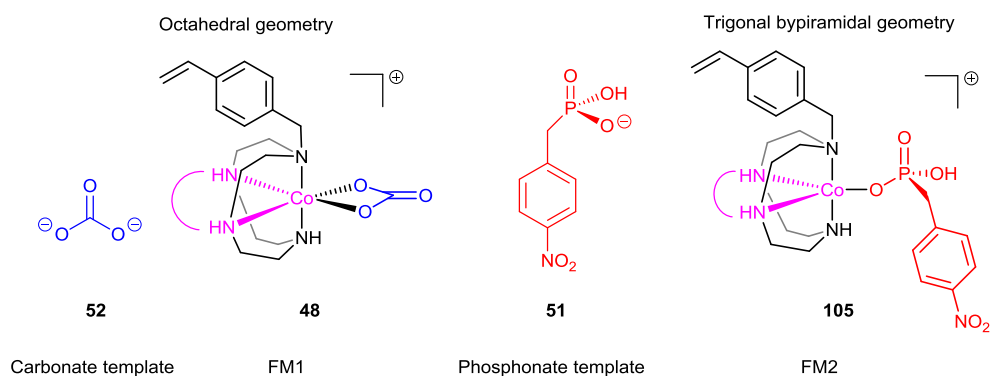


Figure 5.3- Structures of the target templates: *p*-nitrophenyl phosphonate (NPPA) **51** and carbonate **52**; structures of the target functional monomers FM1 **48** and FM2 **105**.¹⁴

One of the most significant outcomes of this study was that the small-molecule cyclen-based Co(III) complexes, normally required in large excess to promote P-O cleavage, can be used in 15% catalytic loads with turnover once incorporated into the larger nanogelic polymer using molecular imprinting technique. While the lower polarity in the nanogels compared to that in the bulk aqueous solution could well have contributed to the catalytic efficiency gain, it was demonstrated that the structure of the template in metallomonomers **FM1 48** and **FM2 105** used to imprint the polymers is key in determining the MIPs activity. This is because it was observed that despite the identical concentration of Co(III) inside the polymers, **P1** MIP imprinted with structurally smaller carbonate template showed enhanced hydrolytic efficiency compared to **P2** MIP imprinted with the larger cognate phosphonate template. It then seems reasonable to suggest that the coordination geometry that is determined by the template structure is ‘frozen’ inside the polymer and the difference in the activity observed is mainly due to the different

HRMS. This characterisation was done with an aim to explore the effect of structural modifications in the ligands on the complexes as well as to investigate the effects, if any, of the anion. d-Block metal complexes with a range of coordination modes, including capped tetrahedral, pseudo-octahedral and trigonal bipyramidal were obtained. The X-ray crystallographic data for complexes **130**, **138**, **141** and **144** (together with a comparison with reported structures) showed that changes in the ligand structure does influence the binding mode around the metal ion. Also some electrochemistry results (in the case of the Cu(II) complexes) seem to indicate the anion also can affect the redox chemistry of such complexes.

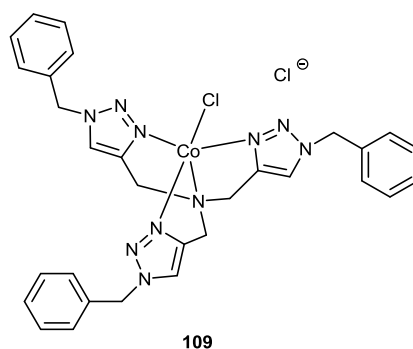


Figure 5.4- Structure of the reported TBTA-based Co(II) complex **109**, where Co(II) is coordinated to TBTA ligand in a capped tetrahedral coordination geometry (one of the most commonly reported geometries in 1:1 metal-ligand complexes of this type).²⁵

Ideally of course in order to determine the exact structure of all of the species it would be advantageous to obtain X-ray quality crystals of all the target metal complexes and compare their characteristics to the bulk solutions.

Unfortunately, the potential phosphatase-like hydrolytic activity of these ‘click’-based metal complexes has not been tested due to a lack of aqueous solubility. Thus, the ability to dissolve in aqueous media is one of the essential requirements for the potential applications of such complexes as phosphatase mimics. One of the approaches to increase the hydrophilicity of these ‘click’ metal complexes is the incorporation of a number of functional hydrophilic groups to the carboxylic moieties of the TCTA ligand **112**. Based on the work published by Parker *et al.*,²⁶ such auxiliary groups include a PEG moiety and larger sugar-based molecules such as **13** and **146** (Figure 5.5). Additionally, the inclusion of such functional groups would potentially allow interactions of these ‘click’ complexes with biologically relevant peptide targeting groups, such as **148** shown in Figure 5.5, which could pave the way for novel applications of these complexes of biological relevance.

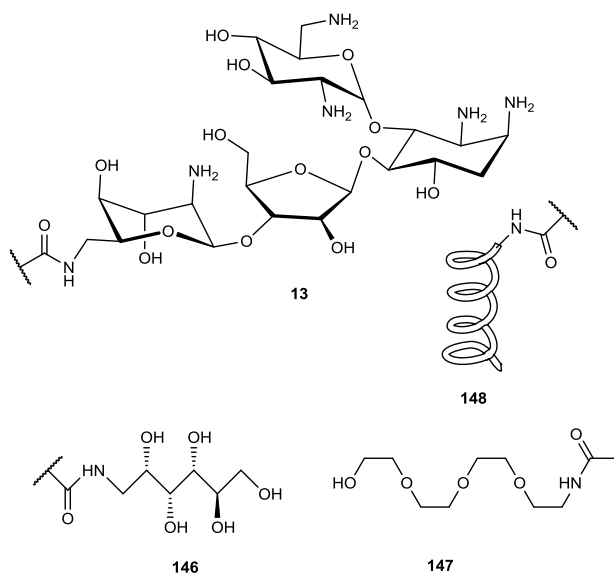
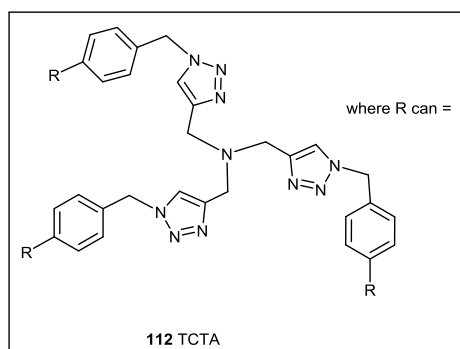


Figure 5.5- TCTA ligand and its potential water soluble functional groups.²⁶

5.5. Bibliography

1. J. Emsley and D. Hall, *The Chemistry of Phosphorus*, Harper & Row, London, 1976.
2. S. Moon, Y. Liu, J. T. Hupp and O. K. Farha, *Angew. Chem. Int. Ed.*, 2015, **54**, 6795-6799.
3. F. Mancin, P. Scrimin and P. Tecilla, *Chem. Commun.*, 2012, **48**, 5545-5559.
4. D. E. Wilcox, *Chem. Rev.* 1996, **96**, 2435-2458.
5. a) M. Diez-Castellnou, F. Mancin and P. Scrimin, *J. Am. Chem. Soc.*, 2014, **136**, 1158-1161; b) O. Iranzo, A. Y. Kovalevsky, J. R. Morrow and J. P. Richard, *J. Am. Chem. Soc.*, 2003, **125**, 1988-1993; c) A. Tamilselvi and G. Mugesh, *Chem. Eur. J.*, 2010, **16**, 8878-8890.
6. L. Marchetti and M. Levine, *ACS Catal.*, 2011, **1**, 1090-1118.
7. M. Resmini, *Anal. Bioanal. Chem.*, 2012, **402**, 3021-3026.
8. J. Rohovec, R. Gyepes, I. Císařová, J. Rudovský and I. Lukeš, *Tetrahedron Lett.*, 2000, **41**, 1249-1253.
9. E. H. Wong, G. R. Weisman, D. C. Hill, David P. Reed, M. E. Rogers, J. S. Condon, M. A. Fagan, J. C. Calabrese, K. Lam, I. A. Guzei, and A. L. Rheingold, *J. Am. Chem. Soc.*, 2000, **122**, 10561-1572.
10. J. Chin and X. Zou, *J. Am. Chem. Soc.*, 1988, **110**, 223-225.
11. D. A. Knight, J. B. Delehanty, E. R. Goldman, J. Bongard, F. Streich, L. W. Edwards and E. L. Chang, *Dalton Trans.*, 2004, **13**, 2006-2011.
12. J. Chin, M. Banaszczyk, V. Jubian and X. Zou, *J. Am. Chem. Soc.*, 1989, **111**, 186-190.
13. J. Chin, *Acc. Chem. Res.*, 1991, **24**, 145-152.
14. R. Jorge, PhD Thesis, Queen Mary University of London, 2011.
15. J. H. Loehlin, *Acta Cryst.*, 1976, **B32**, 3063.
16. J. Kim, *J. Korean Chem. Soc.*, 1998, **42**, 240-244.
17. D. Meyerstein, *Coord. Chem. Rev.*, 1999, **185-186**, 141-147.
18. J. Y. Chang, G. Lu, R. J. Stevenson, P. J. Brothers, G. R. Clark, K. J. Botting, D. M. Ferry, M. Tercel, W. R. Wilson, W. A. Denny and D. C. Ware, *Inorg. Chem.*, 2013, **52**, 7688-7698.
19. T. Koike and E. Kimura, *J. Am. Chem. Soc.*, 1991, **113**, 8935-8941.
20. A. Yatsimirsky, *Coord. Chem. Rev.*, 2005, **249**, 1997-2011.
21. R. D. Maples, A. N. Cain, B. P. Burke, J. D. Silversides, R. E. Mewis, T. D'huys, A. D. Schols, D. P. Linder, S. J. Archibald and T. J. Hubin, *Chem. Eur. J.*, 2016, **22**, 12916-12930.

22. J. E. Hein, L. B. Kransova, M. Iwasaki and V. V. Fokin, *Org. Synth.*, 2011, **88**, 238-247.
23. A. Baschieri, A. Mazzanti, S. Stagni and L. Sambri, *Eur. J. Inorg. Chem.*, 2013, 2432-2439.
24. V. Hong, A. K. Udit, R. A. Evans and M.G. Finn, *Chem. Biochem.*, 2008, **9**, 1481-1486.
25. D. Sweinfurth, S. Demeshko, M. M. Khusniyarov, S. Dechert, V. Gurram, M. R. Buchmeister, F. Meyer and B. Sarkar, *Inorg. Chem.*, 2012, **51**, 7592-7597.
26. M. Delbianco, V. Sadovnikova, E. Bourrier, G. Mathis, L. Lamarque, J. M. Zwier and D. Parker, *Angew. Int. Chem. Ed.*, 2014, **53**, 10718-10722.

Chapter 6: Experimental Section

6.1. General Information

All commercially available reagents and solvents were used without further purification, unless otherwise stated. Anhydrous solvents were obtained using an MBraun MB SPS-800 solvent purification system. To remove traces of water from EtOH, the solvent was dried over freshly activated 3 Å molecular sieves under N₂. Distilled water was obtained from an Elga Purelab Option system. Reagents were purchased commercially from Sigma-Aldrich and CheMatech. Nitrogen used for inert atmospheres was oxygen-free grade. All glassware, glass syringes and metal needles were oven dried and cooled under a stream of nitrogen prior to experimental use. Infrared spectra were recorded in the range 4000-600 cm⁻¹, obtained directly from the compound as a solid or a neat oil on a Bruker Tensor 37 FTIR spectrometer. ¹H NMR and ¹³C NMR spectra were recorded on either Bruker AV400 or AVIII400 NMR spectrometers (¹H NMR: 400 MHz; ¹³C NMR: 100 MHz). The deuterated solvents used to record the spectra are stated before each set of data. Chemical shifts are reported in ppm and referenced to residual protonated solvent. Multiplicity is given as follows: s = singlet, d = doublet, t = triplet, q = quartet, dd = doublet of doublets, m = multiplet, bs = broad signal, and coupling constants are reported to 1 d.p. Effective magnetic moments (μ_{eff}) were determined by the Evan's NMR spectroscopy method¹ in CD₃CN/MeCN/TMS solution at room temperature on a Bruker AVIII400 NMR spectrometer.

UV-Vis spectra were obtained on an HP 8453 and Varian Cary 300 Bio UV-Visible spectrophotometers and absorption maxima (λ_{max}) together with the molar extinction coefficients (ϵ) are reported. High resolution electrospray ionisation mass spectrometry was carried out by the EPSRC National Mass Spectrometry Service, University of Wales, Swansea on a Thermofisher LTQ Orbitrap XL. Melting points were measured on a Stuart SMP3 melting point apparatus and are uncorrected.

Thin layer chromatography (TLC) was carried out using pre-coated silica gel aluminium backed plates with Merck Kieselgel 60 F254. The plates were visualised under a UV lamp (254 nm), or by staining with basified aqueous KMnO₄ solution followed by gentle heating.

Continuous wave (CW) X-band EPR spectra for Dr. Jorge's data were obtained at 18 ± 0.2 K using a Bruker ELEXSYS E500 EPR spectrometer equipped with an Oxford Instruments ESR900 helium flow cryostat. Additional experimental parameters were: 0.5 mW microwave power; 100 KHz field modulation; 0.5 mT field modulation. The spectra were recorded by Dr. Steven Rigby at the Manchester Interdisciplinary Biocentre, University of Manchester (U.K.).

Kinetic studies were carried out by UV-vis spectroscopy using a HP 8453 and Varian Cary 300 Bio UV-Visible spectrophotometers.

The following compounds were all prepared following previously reported literature procedures. All spectroscopic data obtained matched those previously reported; **73** and **74**², **124**³ and **128**⁴.

Perchlorate salts were handled with special care due to their potential explosive properties when combined with organic ligands. Alkyne and azide reagents were mixed only in the presence of the solvents and neat mixing was avoided due to azide's explosive properties.

EPR measurements for the 'click'-based Mn(II) and Cu(II) complexes **129**, **133**, **138**, **142**, **131**, **135**, **140** and **144** were performed in MeOH at 4.5 mM concentration by Dr. Enrico Salvadori. The experiments were carried out using an X-band Bruker Elexsys E580 Spectrometer (Bruker BioSpin GmbH, Germany) equipped with a closed-cycle cryostat (Cryogenic Ltd, UK). The magnetic field was calibrated at room temperature with a Bruker strong pitch sample ($g = 2.0028$). Measurements were carried out in an X-band split-ring resonator module with 2 mm sample access (ER 4118X-MS2). All measurements were recorded at 50 K with a 5 G modulation amplitude and 0.2 mW microwave power. Complexes were dissolved in methanol and flash-frozen in liquid nitrogen prior to use.

All electrochemical measurements were carried out using an EmStat3+ potentiostat (Palmsens) with a PS-Trace software. Glassy carbon, platinum wire and saturated calomel (SCE) were used as working (BASi), counter and reference (Scientific Glassblowing Service, University of Southampton) electrodes respectively. The working electrode surface (area 3 mm²) was regenerated every time using sheets of abrasive papers (Buehler Carbimet 320/P400, 400/P800 and 600/P1200) and subsequently treated with 1 and 0.3 μ m alumina

on polishing cloth (Buehler Micropolish II). The reference electrode potential was determined to be +250 mV vs SHE using quinhydrone (Sigma Aldrich) as an external standard. MeOH, MeCN and HEPES buffer (10 mM, pH 7.2) were used as solvents and 0.1 M of tetrabutylammonium tetrafluoroborate ($n\text{-Bu}_4\text{NBF}_4$) and tetrabutylammonium perchlorate ($n\text{-Bu}_4\text{NClO}_4$) were used as supporting electrolytes for di-chloride and perchlorate complexes respectively. A scan of the blank (i.e. solvent and electrolyte) was recorded prior to every measurement. A scan rate of 50 mV/s and E step of 0.01 V were used as parameters for cyclic voltammetry measurements. Scan ranges between -1.5; 1.0 V and -2.0; 2.0 V were used for the measurements using tetraamine Co(III) complexes and 'click'-based complexes respectively. It is important to note, that there was an oxidation peak observed in the cyclic voltammogram of the blank solution in the region just above 1.00 V followed by a weak reduction peak in some cases. This could not be removed even after the extensive polishing of the glassy carbon electrode. Therefore, analysis of the cyclic voltammograms obtained in this work for the 'click'-based metal complexes required overlaying the appropriate blank voltammogram with that of the metal complex. This allowed identification of processes which were most likely to be due to the electrode-based impurity and to distinguish them from the redox peaks generated by the metal complexes.

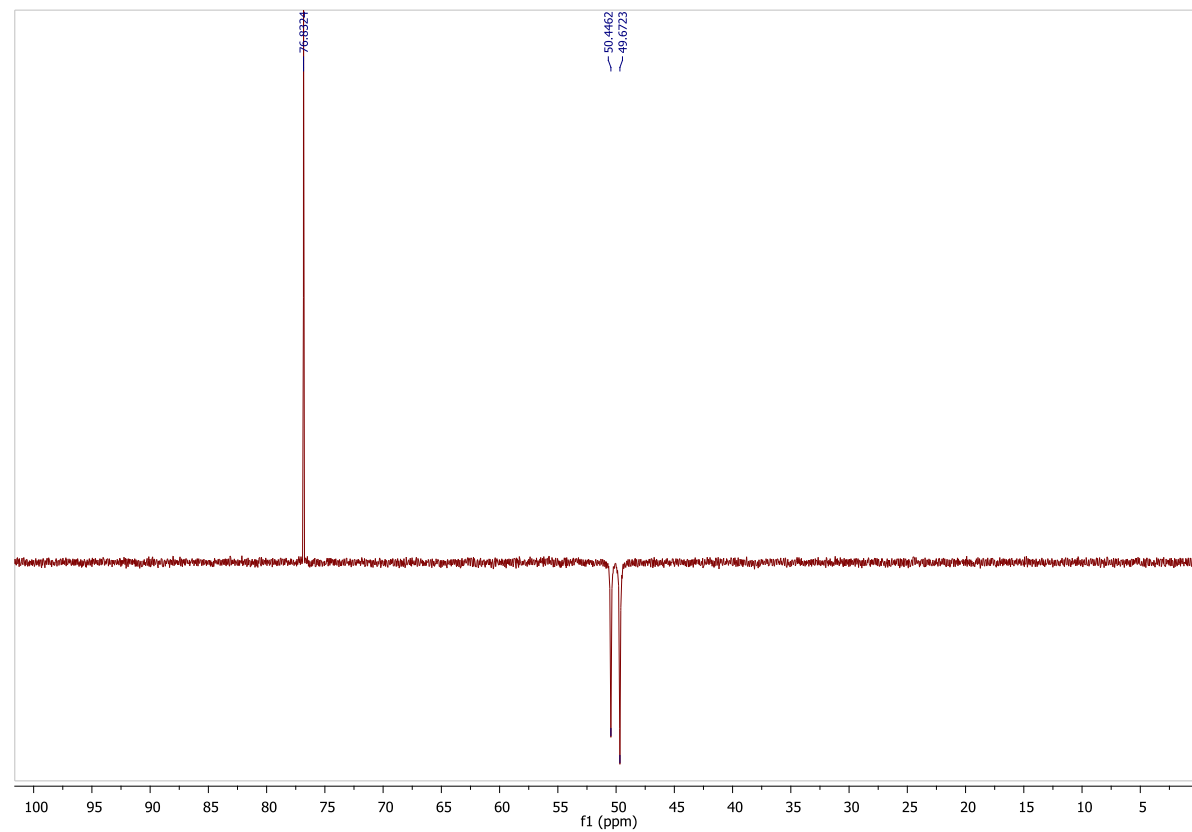
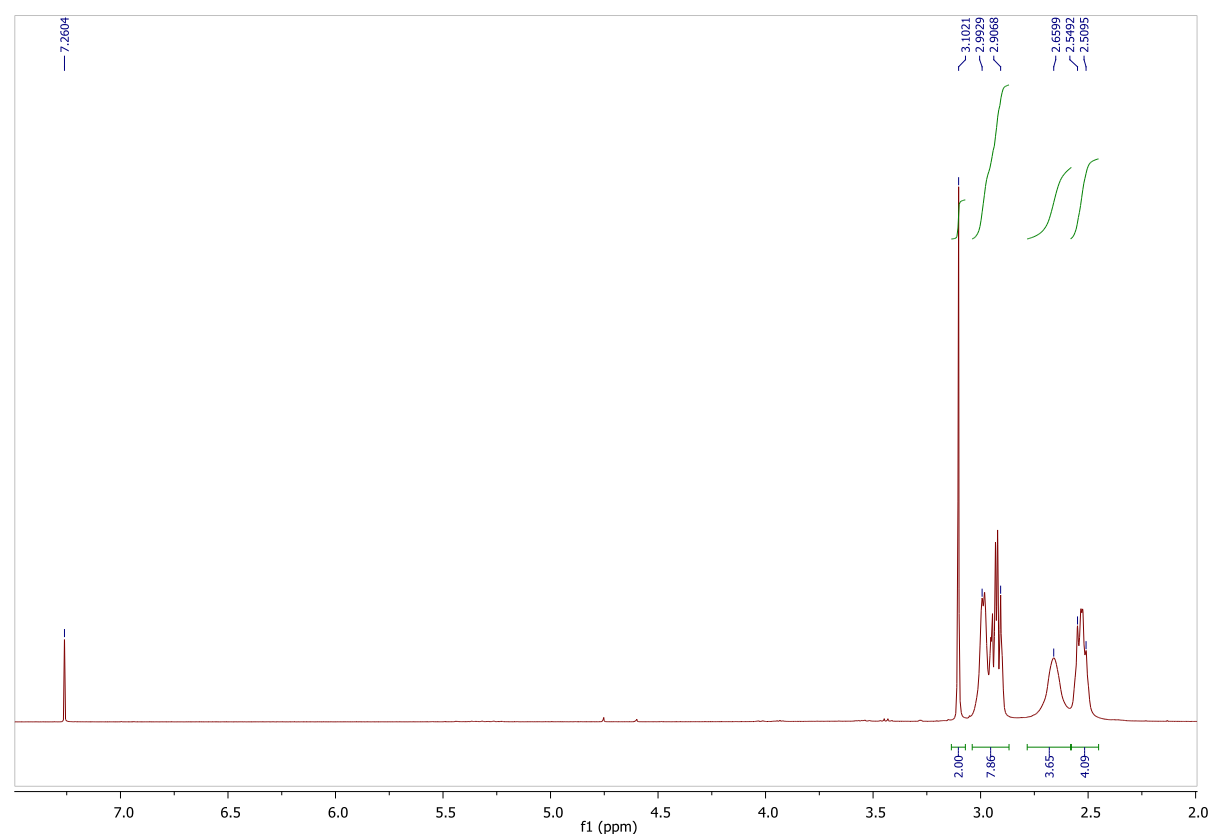
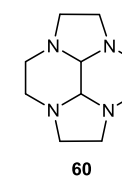


Figure 6.1- ^1H and ^{13}C NMR spectra of **60**.

6.2. Synthesis of the Cyclen-based Compounds

Perhydro-2a,4a,6a,8a-tetraazacyclopenta acenaphtylene (bisaminal) 60^{5,6}



Cyclen **44** was protected as its bisaminal by a slight modification of the reported procedure.^{5,6} A solution of glyoxal (as a 40% aqueous solution, 6.00 mL, 52.0 mmol) in MeOH (15 mL) was added dropwise at 0 °C to a solution of cyclen (8.00 g, 46.4 mmol) in MeOH (80 mL). The mixture was stirred at this temperature for 1 h, heated at 55 °C for a further 2 h, and finally stirred at RT for 16 h. The solution was concentrated *in vacuo* to afford a dark orange oil, which was then triturated with Et₂O (5 x 50.0 mL). The organic fractions were combined and the solvent was removed *in vacuo* to give the bisaminal **60** as a white powder (7.43 g, 83%). The data were consistent with those previously reported.^{5,6} ^1H NMR (400 MHz, CDCl₃): δ = 2.51 - 2.55 (m, 4H, CH₂), 2.66 (bs, 4H, CH₂), 2.91 – 2.99 (m, 8H, CH₂), 3.10 (bs, 2H, CH_{aminal}) ppm; ^{13}C NMR (DEPT 135, 100 MHz, CDCl₃): δ = 49.7, 50.4, 76.8 ppm.

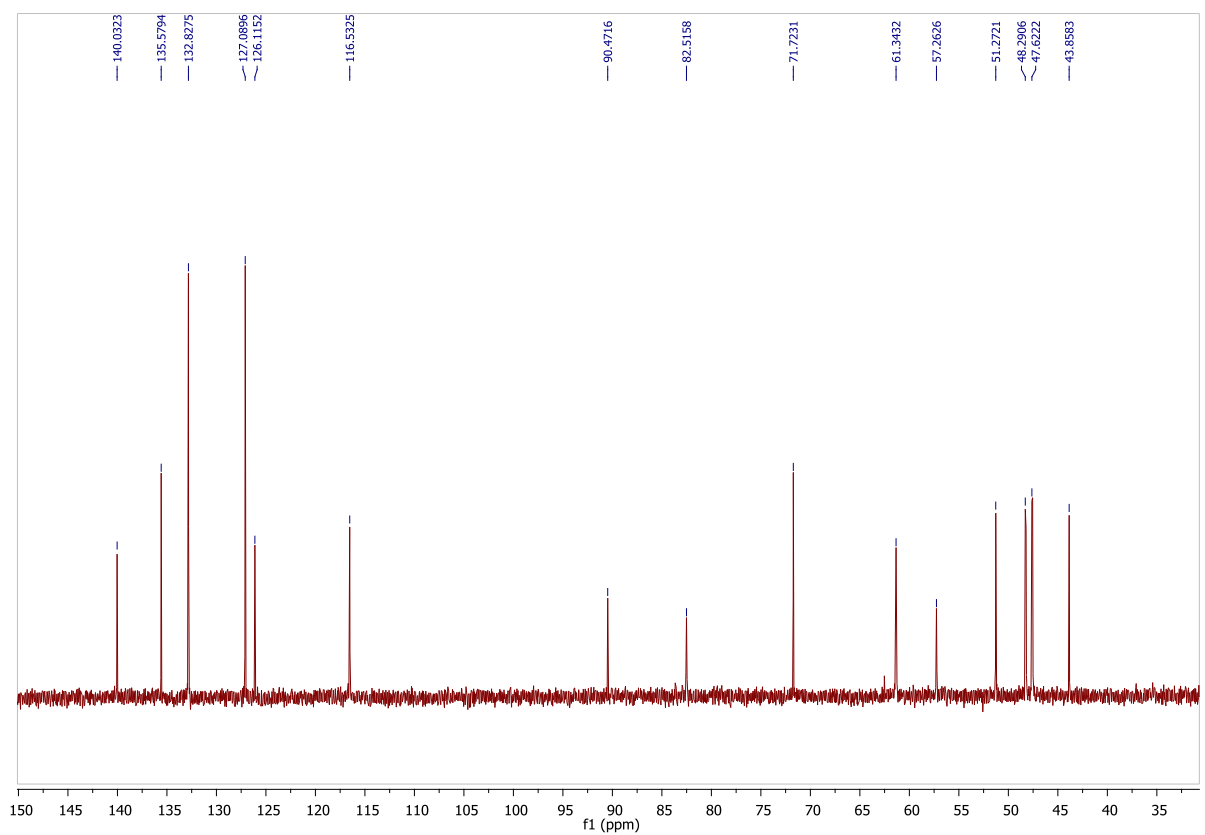
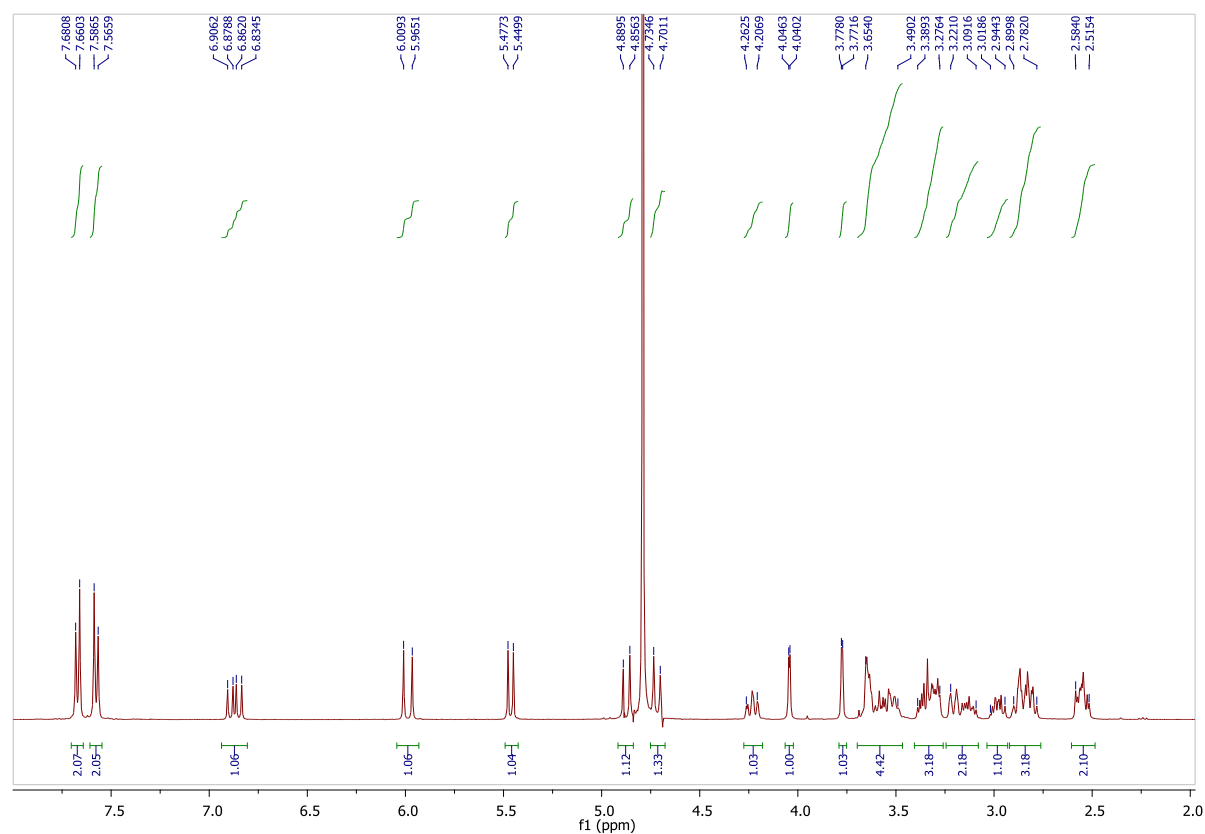
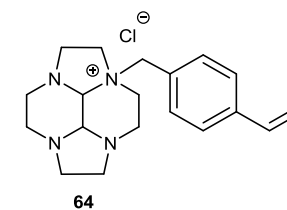


Figure 6.2 - ¹H and ¹³C NMR spectra of **64**.

6.2.1. Synthesis of the Amino Salts

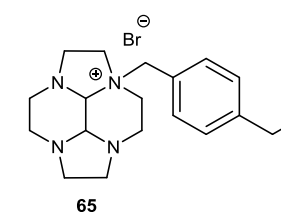
6.2.1.1. Mono-alkylation: General Procedure⁶ as Demonstrated by the Synthesis of **64**

(4-Vinylbenzyl)-4,7,10-triaza-1-azoniatetracyclo tetradecane chloride **64**⁷



1-(Chloromethyl)-4-vinylbenzene (R-X halide) (3.00 mL, 21.2 mmol) was added under an inert atmosphere to a solution of the bisaminal **60** (2.06 g, 10.6 mmol) dissolved in the minimum volume of dry toluene (10.0 mL). The mixture was maintained at RT for 16 h. The resulting white solid was collected by filtration and was washed using freshly distilled toluene (2 x 5.0 mL). The collected solids were dried *in vacuo* to afford the desired product as white solid (hygroscopic) (3.12 g, 95%). The salt exhibits complex ¹H NMR, and the data is consistent with those previously reported.⁷ ¹H NMR (400 MHz, D₂O): δ = 2.51 – 2.58 (m, 2H, CH₂), 2.78-2.90 (m, 3H, CH₂), 2.94-3.02 (m, 1H, CH₂), 3.10-3.22 (m, 2H, CH₂), 3.28-3.39 (m, 3H, CH₂), 3.49-3.65 (m, 4H, CH₂), 3.77 (d, J = 2.4 Hz, 1H, CH_{aminal}), 4.04 (d, J = 2.4 Hz, 1H, CH_{aminal}), 4.21 – 4.26 (m, 1H, CH₂), 4.70 – 4.89 (m, 2H, residual HOD solvent peak overlaps signal, NCH₂-Ar), 5.46 (d, J = 11.0 Hz, 1H, CH=CHH_{cis}), 5.98 (d, J = 17.7 Hz, 1H, CH=CHH_{trans}), 6.87 (dd, J = 11.0, 17.7 Hz, 1H, CH=CH₂), 7.57 (d, J = 8.2 Hz, 2H, Ar-H), 7.67 (d, J = 8.2 Hz, 2H, Ar-H) ppm; ¹³C NMR (100 MHz, D₂O): δ = 43.8, 47.6, 48.3, 51.3, 57.3, 61.3, 71.7, 82.5, 90.5, 116.5, 126.1, 127.1, 132.8, 135.6, 140.0 ppm.

(4-Ethylbenzyl)-4,7,10-triaza-1-azoniatetracyclo tetradecane bromide **65**



Following the general procedure, bisaminal **60** (2.00 g, 10.3 mmol) and *p*-ethyl benzyl bromide **74** (2.05 g, 10.3 mmol) yielded **65** as a white solid (3.70 g, 91%). m.p. 165-168 °C. ^1H NMR (400 MHz, D_2O): δ = 1.26 (t, J = 7.6 Hz, 3H, CH_3), 2.52-2.60 (m, 2H, CH_2), 2.74 (q, J = 7.6 Hz, 2H, CH_3CH_2), 2.80-2.91 (m, 3H, CH_2), 2.95-3.02 (m, 1H, CH_2), 3.11-3.22 (m, 2H, CH_2), 3.29-3.39 (m, 3H, CH_2), 3.49-3.65 (m, 4H, CH_2), 3.80 (d, J = 2.5 Hz, 1H, $\text{CH}_{\text{aminal}}$), 4.05 (d, J = 2.5 Hz, 1H, $\text{CH}_{\text{aminal}}$), 4.21-4.27 (m, 1H, CH_2), 4.71-4.89 (m, 2H, residual HOD solvent peak overlaps signal, $\text{NCH}_2\text{-Ar}$), 7.47 (d, J = 8.0 Hz, 2H, Ar-H), 7.54 (d, J = 8.0 Hz, 2H, Ar-H) ppm; ^{13}C NMR (100 MHz, D_2O): δ = 14.7, 28.2, 43.7, 47.7, 48.3, 51.3, 57.3, 61.2, 71.8, 76.1, 82.3, 124.1, 129.1, 132.6, 148.3 ppm; IR: ν_{max} = 2961, 2883, 2848, 1612, 1514, 1433, 1266, 1219, 1184, 1134, 1053, 1027, 982, 929, 846 cm^{-1} ; HRMS (EI) calcd for $\text{C}_{19}\text{H}_{29}\text{N}_4$ $[\text{M}+\text{H}]^+$ 313.2387, found: 313.2383.

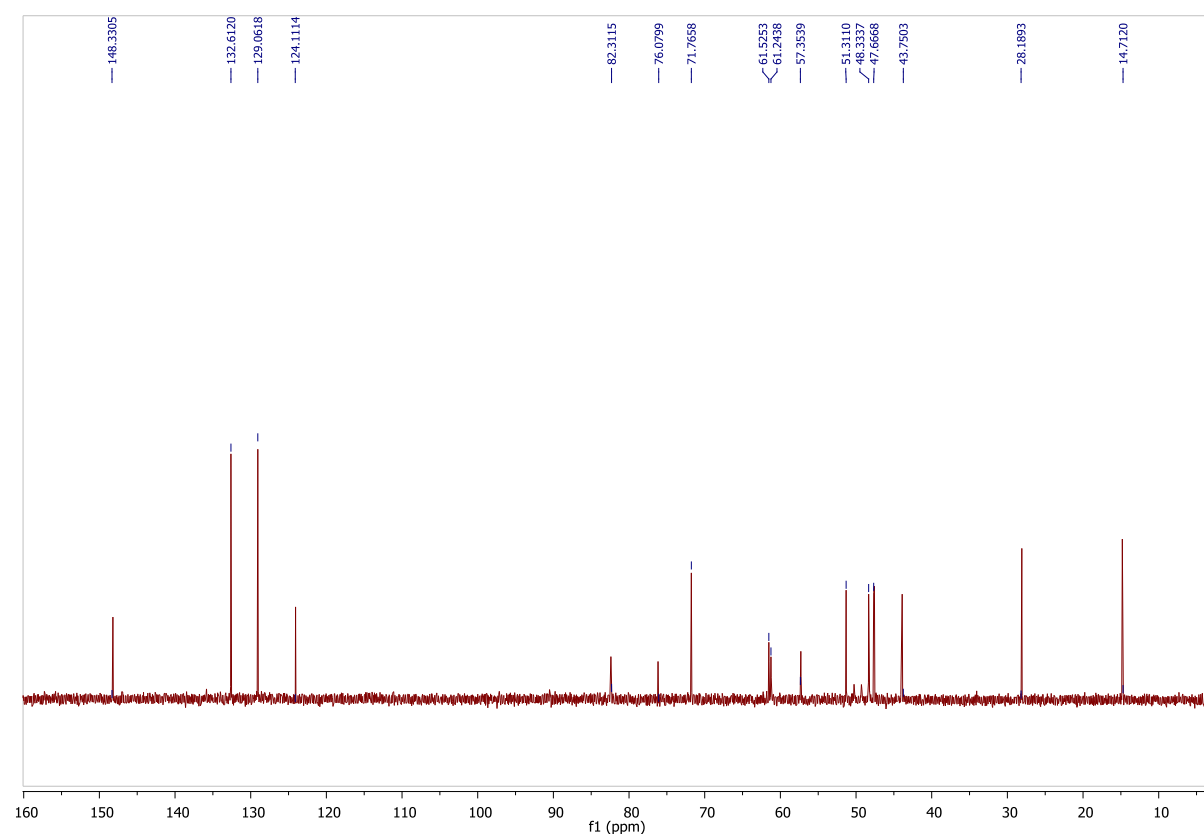
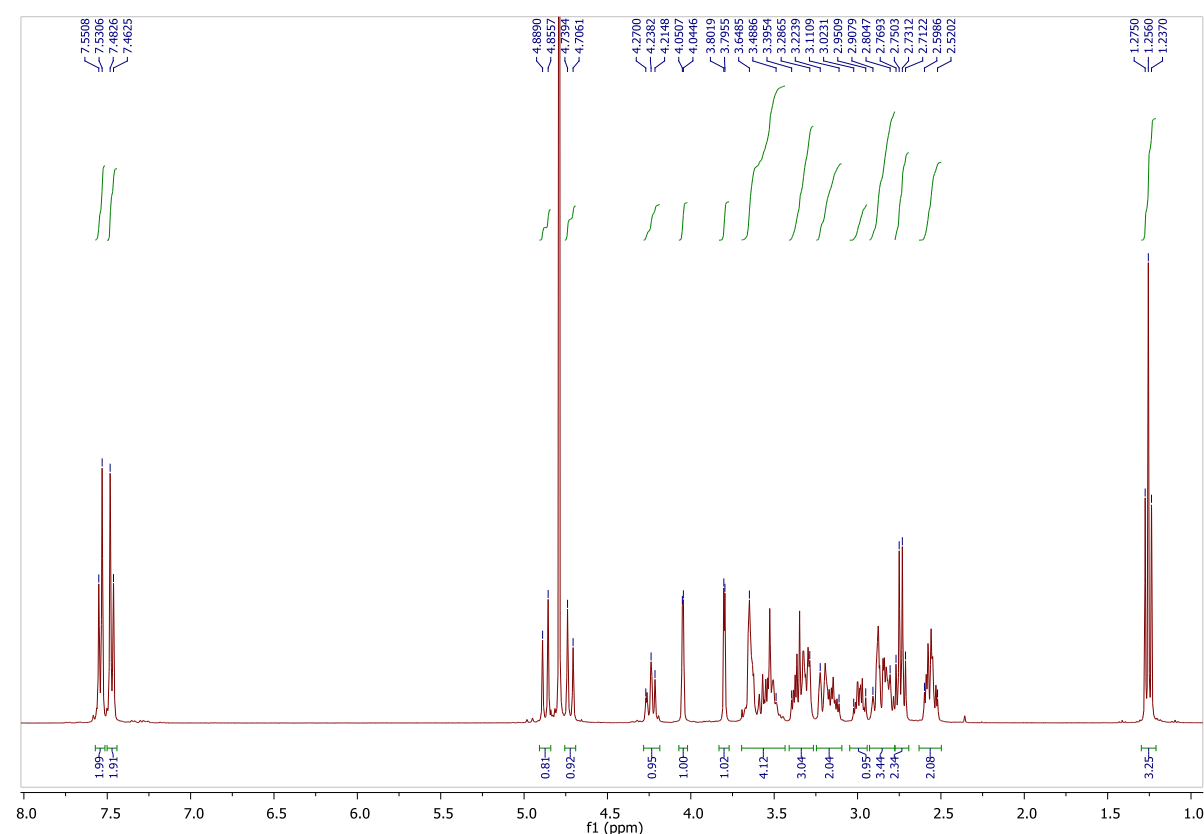


Figure 6.3 - ^1H and ^{13}C NMR spectra of **65**.

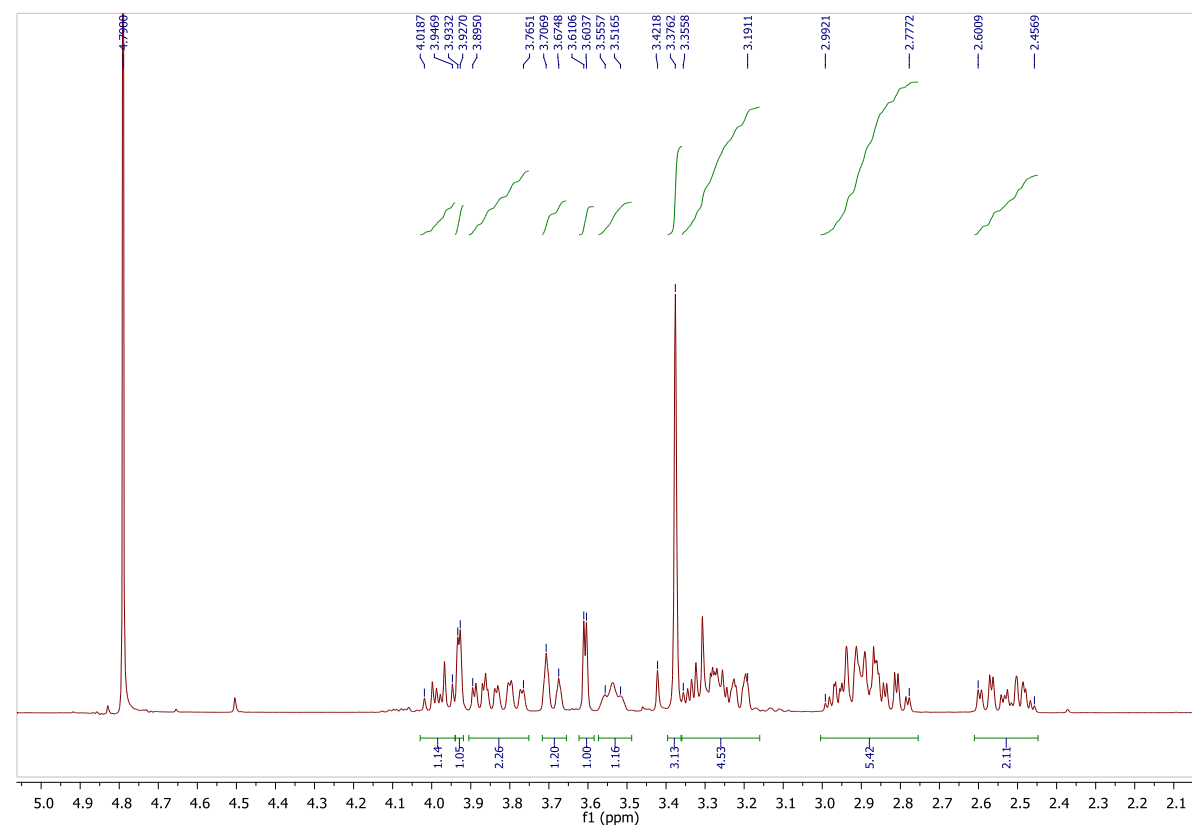
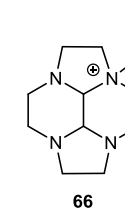


Figure 6.4 - ^1H NMR spectrum of **66**.

*4a-Methyldecahydro-3H-2a, 4a, 6a, 8a-tetraazacyclopenta[fg]acenaphthylen-4a-ium iodide
66⁶*



Following the general procedure, bisaminal **60** (1.5 g, 7.7 mmol) and MeI (0.48 mL, 7.7 mmol) yielded **66** as a white solid (2.45 g, 94%). The data were consistent with those previously reported.⁶ ^1H NMR (400 MHz, D_2O): δ = 2.46-2.60 (m, 2H, CH_2), 2.78-2.99 (m, 5H, CH_2), 3.19-3.35 (m, 4H, CH_2), 3.38 (s, 3H CH_3), 3.52-3.55 (m, 1H, CH_2), 3.60 (d, J = 2.6 Hz, 1H, $\text{CH}_{\text{aminal}}$), 3.67-3.71 (m, 1H, CH_2), 3.76-3.89 (m, 2H, CH_2), 3.93 (d, J = 2.6 Hz, 1H, $\text{CH}_{\text{aminal}}$), 3.95-4.02 (m, 1H, CH_2) ppm.

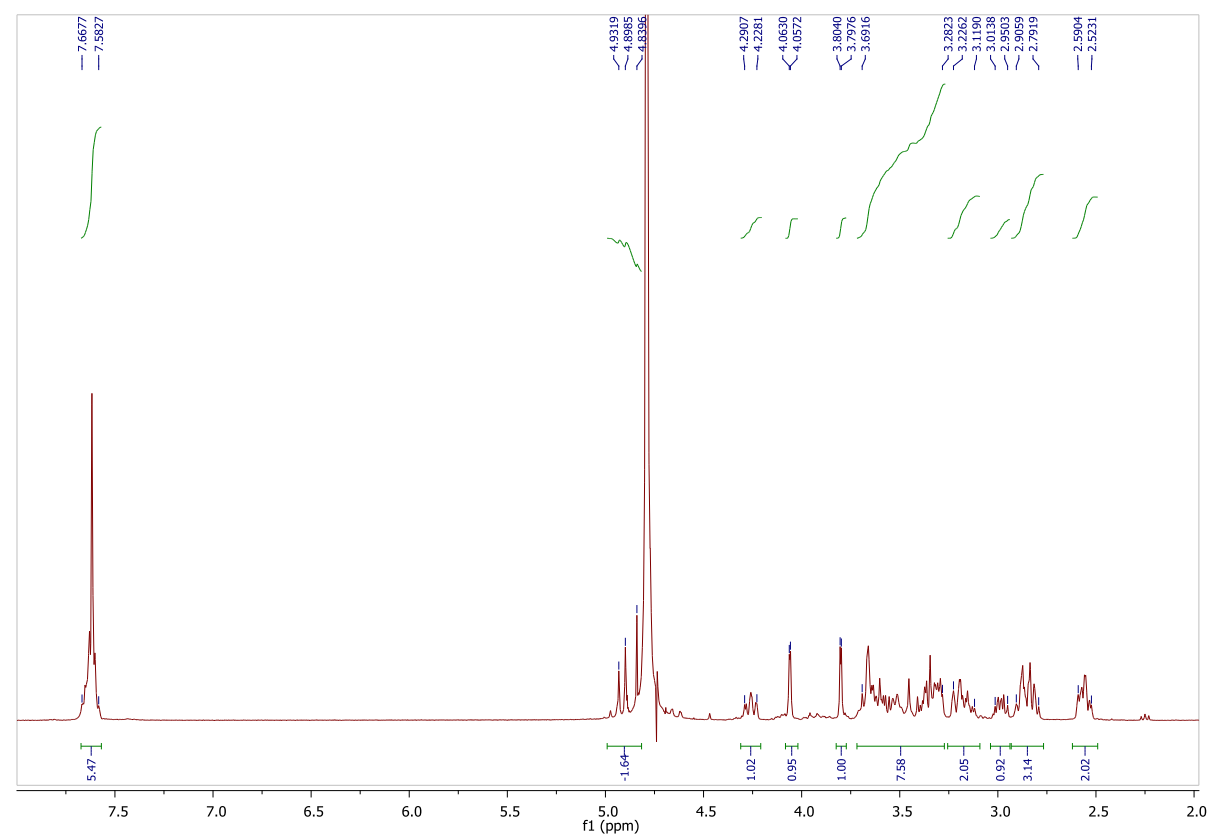
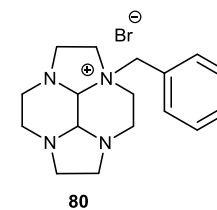


Figure 6.5 - ^1H NMR spectrum of **80**.

*4a-Benzyldecahydro-3H-2a, 4a, 6a, 8a-tetraazacyclopenta[fg]acenaphthylen-4a-ium bromide **80**⁶*



Following the general procedure, bisaminal **60** (0.755 g, 3.89 mmol) and benzyl bromide **123** (0.46 mL, 3.89 mmol) yielded **80** as a white solid (1.36 g, 96%). The data were consistent with those previously reported.⁶ ^1H NMR (400 MHz, D_2O): δ = 2.52-2.59 (m, 2H, CH_2), 2.79-2.90 (m, 3H, CH_2), 2.95-3.01 (m, 1H, CH_2), 3.12-3.23 (m, 2H, CH_2), 3.28-3.69 (m, 7H, CH_2), 3.80 (d, J = 2.4 Hz, 1H, $\text{CH}_{\text{aminal}}$), 4.06 (d, J = 2.4 Hz, 1H, $\text{CH}_{\text{aminal}}$), 4.23-4.29 (m, 1H, CH_2), 4.90 (d, 2H, residual HOD solvent peak overlaps signal, $\text{NCH}_2\text{-Ar}$), 7.58-7.67 (m, 5H, Ar-H) ppm.

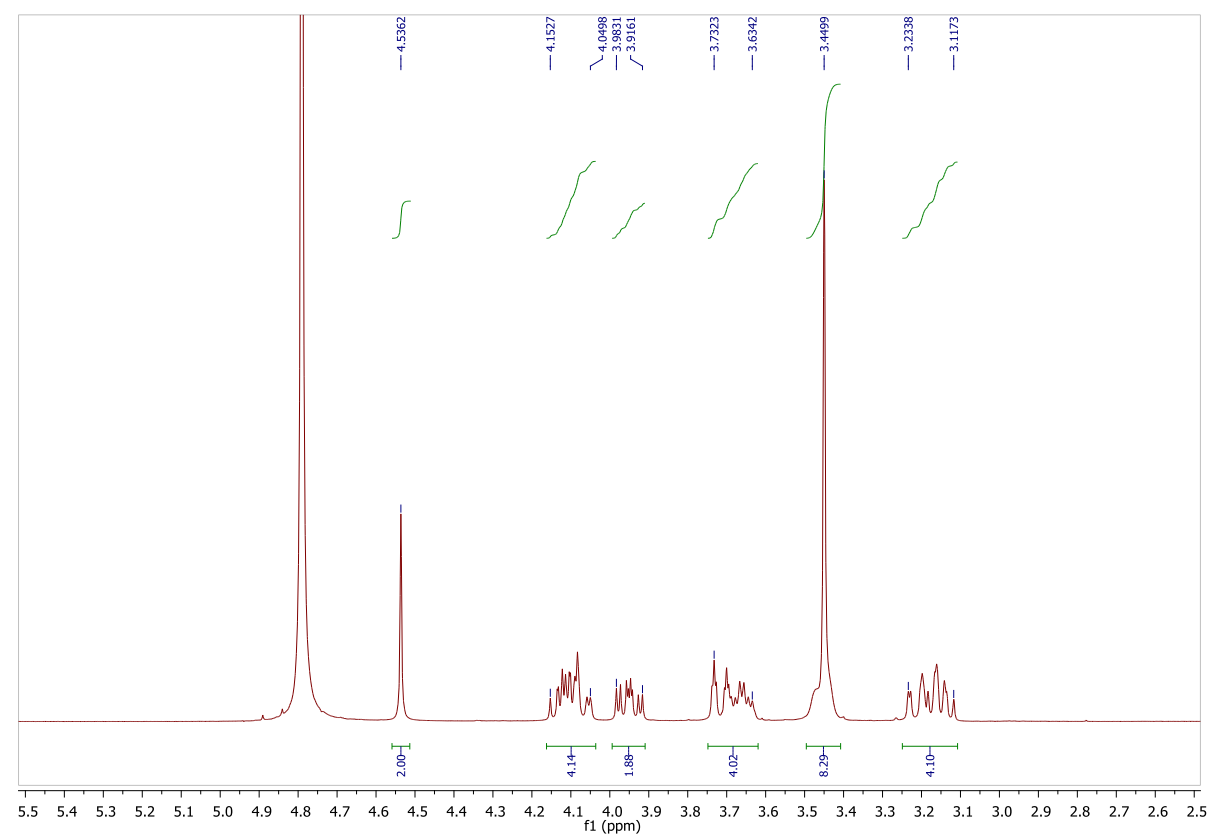
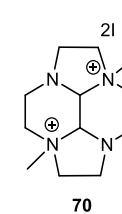


Figure 6.6 - ^1H NMR spectrum of **70**.

6.2.1.2. Di-alkylation: General Procedure⁶ as Demonstrated by the Synthesis of **70**

(8*bR*,8*cR*)-*rel*-Decahydro-2*a*,6*a*-bis(methyl)-2*a*,4*a*,6*a*,
tetraazacyclopent[*fg*]acenaphthylenium diiodide **70**^{6,8,9}

8*a*-



An excess of MeI (R-X halide) (5.00 mL, 78.8 mmol) was added in one portion to a stirred solution of **60** (1.00 g, 5.15 mmol) in anhydrous MeCN (5.00 mL) under an N_2 atmosphere. The reaction was stirred at RT for 16 h. The resulting white precipitate was collected by suction filtration and washed with MeCN (3 x 5.00 mL). The precipitate was collected and further dried under vacuum to obtain pure product **70** as a white powder (2.32 g, 98%). The data were consistent with those previously reported.⁹ ^1H NMR (400 MHz, D_2O): δ = 3.11-3.23 (m, 4H, CH_2), 3.44 (s, 8H, CH_3 , CH_2), 3.63-3.73 (m, 4H, CH_2), 3.92-3.98 (m, 2H, CH_2), 4.05-4.15 (m, 4H, CH_2), 4.54 (s, 2H, $\text{CH}_{\text{aminal}}$) ppm.

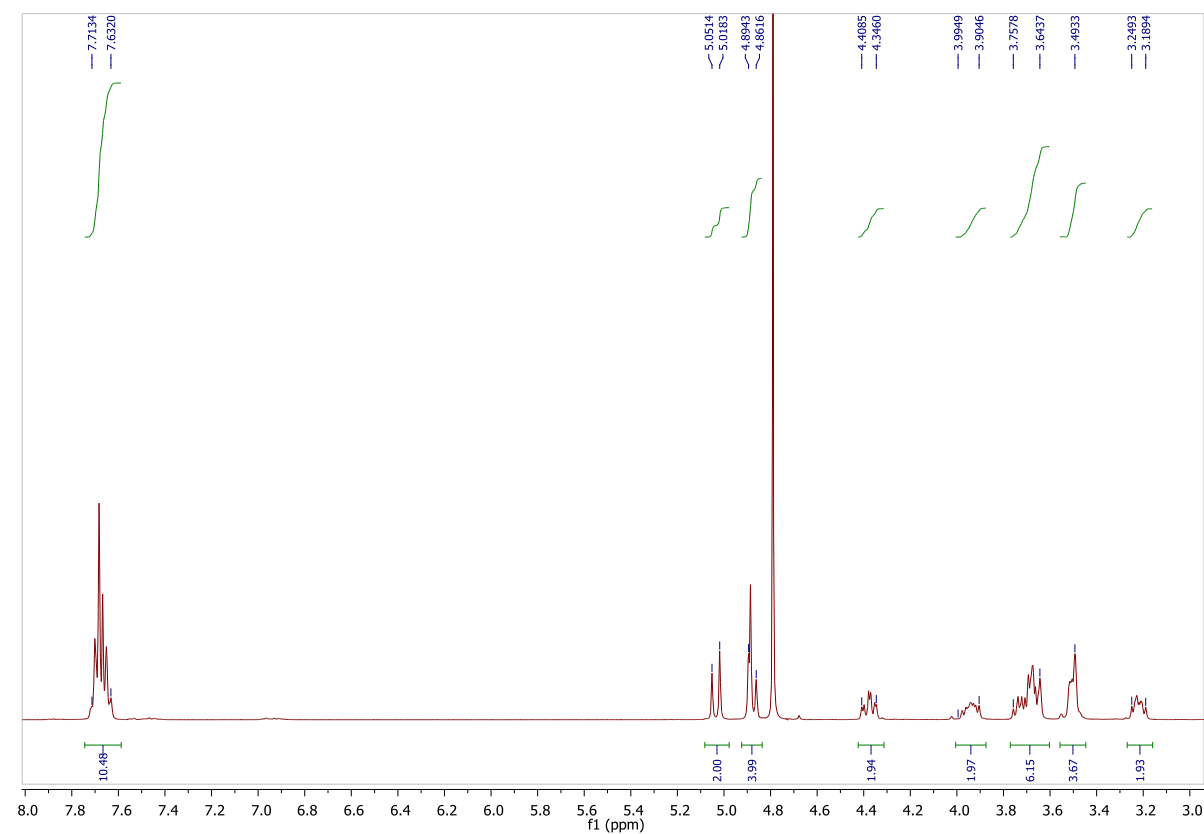
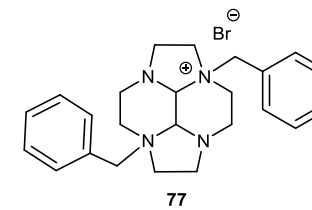


Figure 6.7 - ^1H NMR spectrum of **77**.

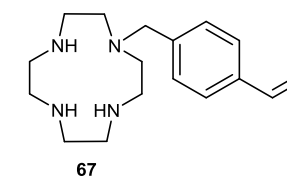
(8*bR*,8*cR*)-*rel*-Decahydro2*a*,6*bis*(phenylmethyl)2*a*,4*a*,6*a*,8*a* tetraazacyclopent[*fg*]acenphenylenuim dibromide **77**¹⁰



Following the general procedure bisaminal **60** (0.500 g, 2.57 mmol) and benzyl bromide **123** (4.40 mL, 38.5 mmol) yielded **77** as a beige solid (1.06 g, 90%). The data were consistent with those previously reported.¹⁰ ^1H NMR (400 MHz, D_2O): δ = 3.19-3.25 (m, 2H, CH_2), 3.49-3.53 (m, 4H CH_2), 3.64-3.76 (m, 6H, CH_2), 3.90-3.99 (m, 2H, CH_2), 4.35-4.41 (m, 2H, CH_2), 4.86-4.89 (m, 4H, $\text{NCH}_2\text{-Ar}$), 5.02-5.05 (m, 2H, $\text{CH}_{\text{aminal}}$), 7.63-7.71 (m, 10H, Ar-H) ppm.

6.2.2. Synthesis of the Cyclen-based Ligands *via* Aminoal Precursors

1-(4-Vinylbenzyl)-1,4,7,10-tetraazacyclododecane **67**^{7,11}



Bisaminal salt **64** (0.500 g, 1.44 mmol) was dissolved in dry EtOH (6 mL). NH_2OH in a 50% aqueous solution (0.420 mL, 14.4 mmol) was added dropwise to this solution and the resulting mixture was stirred for 20 minutes at RT and then for 16 h at *ca.* 60 °C, making the solution turn from a cloudy white to a clear pale yellow. After cooling, the reaction mixture was stirred for a further hour at RT before an equal volume of 10% w/w KOH was added. The mixture was extracted with CHCl_3 (5 x 10 mL) and the organic fractions were combined, dried over MgSO_4 and the solvent removed *in vacuo* to afford the crude product as a yellow oil (0.400 g, 96%). This crude product contained some minor impurities and required further purification. The crude oil was suspended in EtOH (1 mL) and HCl (35%, 2 mL) was added dropwise to obtain the hydrochloride salt of **67** as a white precipitate. This precipitate was collected by filtration, dissolved in a solution of KOH (40% aqueous solution, w/v, 10 mL), and extracted with CHCl_3 (5 x 30 mL). The organic layers were combined, dried over MgSO_4 and removed *in vacuo* to afford **67** as a yellow oil (60.0 mg, 20%). The data were consistent with those previously reported.^{7,11} ^1H NMR (400 MHz, CDCl_3): δ = 2.57- 2.83 (m, 18H, CH_2), 3.60 (s, 2H, $\text{NCH}_2\text{-Ar}$), 5.19 (d, J = 10.9 Hz, 1H, $\text{CH=CHH}_{\text{cis}}$), 5.70 (m, 1H, $\text{CH=CHH}_{\text{trans}}$), 6.68 (dd, J = 10.9, 17.6 Hz, 1H, CH=CH_2), 7.25 (d, residual solvent peak overlaps signal, J = 8.0 Hz, 2H, Ar-H), 7.35 (d, J = 8.0 Hz, 2H, Ar-H) ppm; ^{13}C NMR (100 MHz, CDCl_3): δ = 45.7, 46.6, 47.7, 51.6, 59.5, 113.7, 126.6, 129.5, 136.8, 136.9, 138.9, ppm.

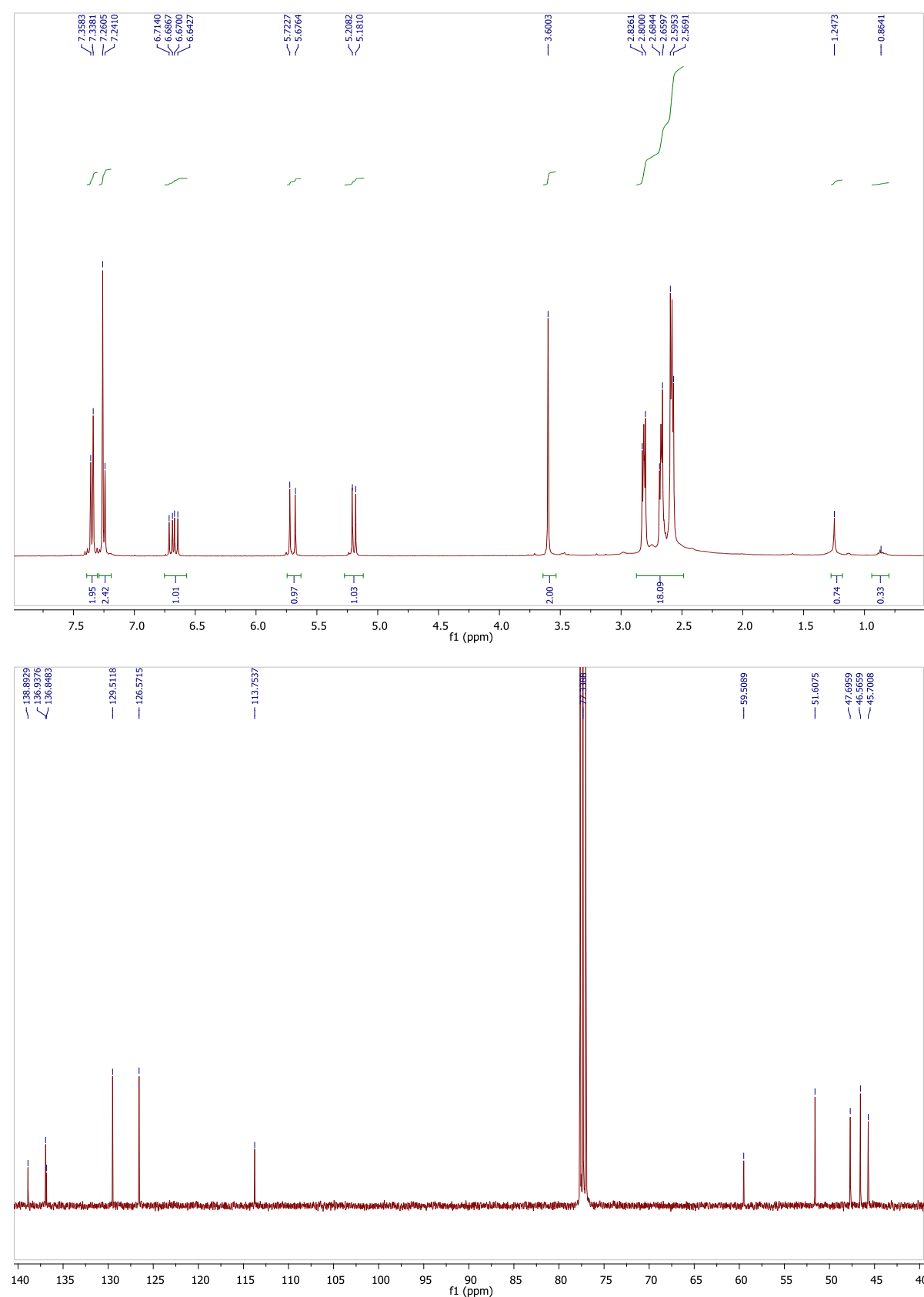


Figure 6.8 - ^1H and ^{13}C NMR spectra of **67**.

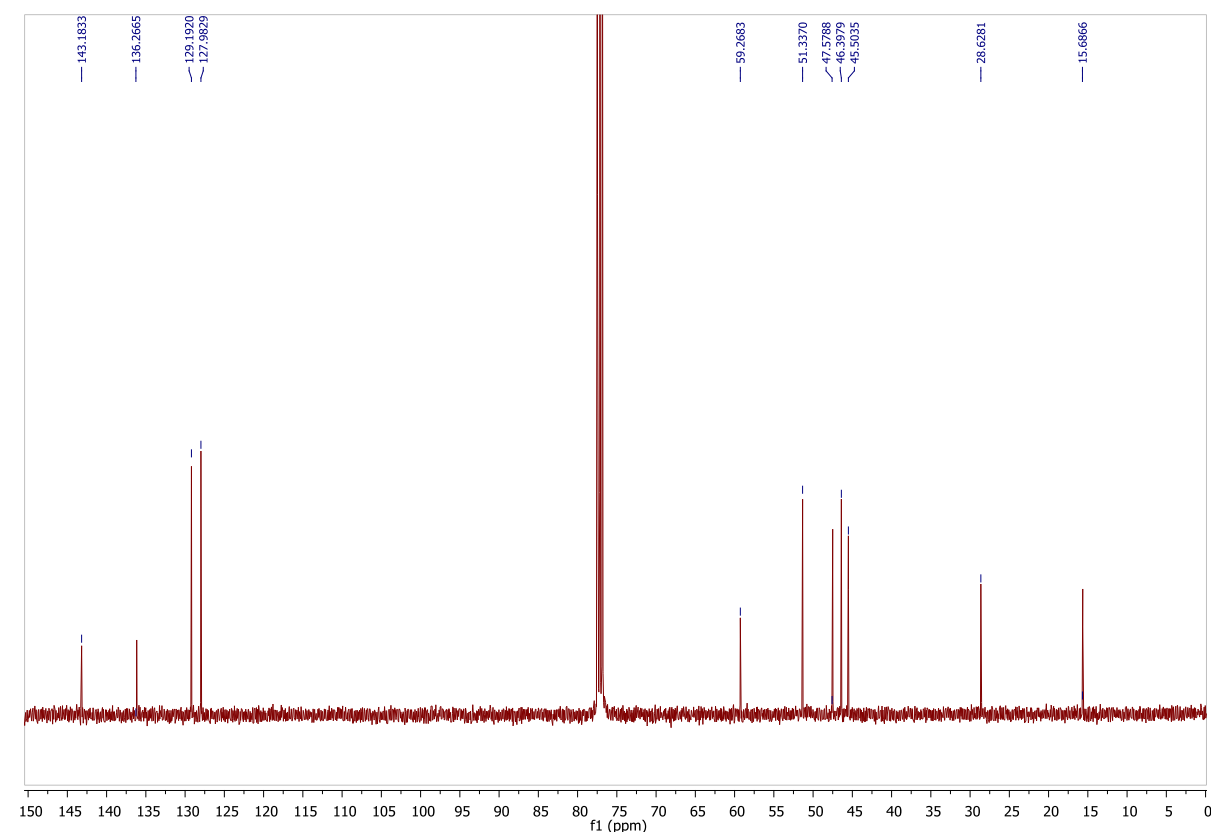
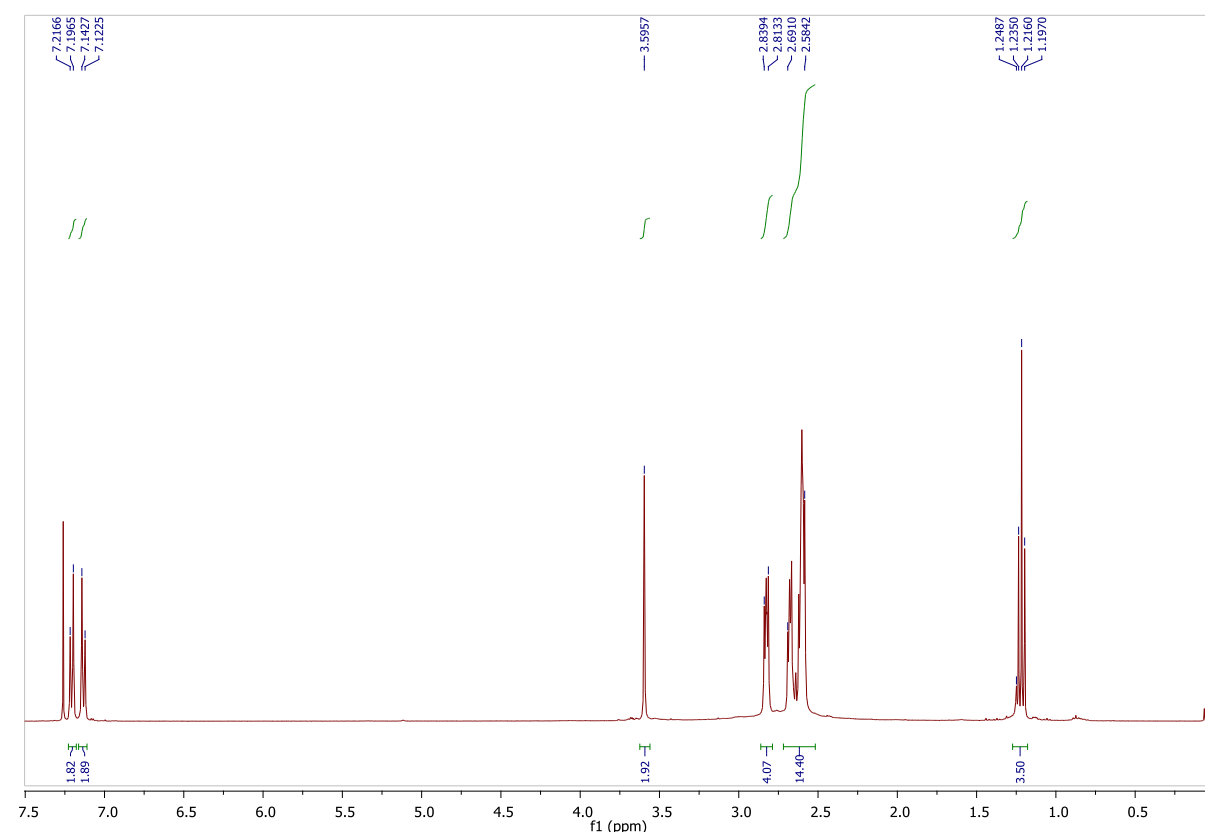
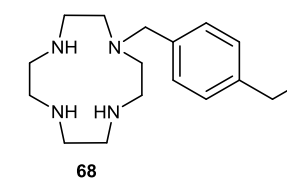


Figure 6.9 - ^1H and ^{13}C NMR spectra of **68**.

1-(4-Ethylbenzyl)-1,4,7,10-tetraazacyclododecane **68**



Bisaminal **65** (0.800 g, 2.03 mmol) was dissolved in dry EtOH (10 mL). NH_2OH in a 50% aqueous solution (0.550 mL, 20.3 mmol) was added dropwise to this solution and the resulting mixture was stirred for 20 minutes at RT and then for 16 h at *ca.* 60 °C, making the solution turn from a cloudy white to a clear pale yellow. After cooling, the reaction mixture was stirred for a further hour at RT. The reaction mixture was then reduced in volume to afford a yellow oil, which was dissolved in HCl (5 M, 2 mL). The aqueous layer was washed with EtOAc (20 mL x 2) and Et_2O (20 mL x 2). The resulting aqueous layer was then adjusted to pH 14 with KOH (40% aqueous solution, w/v, 2 mL) and extracted with CHCl_3 (5 x 30 mL). The organic fractions were then combined, dried over MgSO_4 and concentrated *in vacuo* to afford the crude product as a yellow oil. After suspending the oil in EtOH (1 mL), HCl (35%, 2 mL) was added dropwise to obtain the hydrochloride salt of **68** as a white precipitate. This precipitate was collected by filtration, dissolved in a solution of KOH (40% aqueous solution, w/v, 10 mL), and extracted with CHCl_3 (5 x 30 mL). The organic layers were combined, dried over MgSO_4 and concentrated *in vacuo* to afford **68** as a yellow oil (0.106 g, 18%). ^1H NMR (400 MHz, CDCl_3): δ = 1.22 (t, J = 8.0 Hz, 3H, CH_3), 2.58-2.69 (m, 14H, CH_2), 2.81-2.84 (m, 4H, CH_2), 3.59 (s, 2H, $\text{NCH}_2\text{-Ar}$), 7.13 (d, J = 8.0 Hz, 2H, Ar-H), 7.21 (d, J = 8.0 Hz, 2H, Ar-H) ppm; ^{13}C NMR (100 MHz, CDCl_3): δ = 15.7, 28.6, 45.5, 46.4, 47.6, 51.3, 59.3, 128.0, 129.2, 136.3, 143.2 ppm; IR: ν_{max} 3280, 2928, 1671, 1511, 1455, 1349, 1263, 1113, 1041, 931, 818 cm^{-1} ; HRMS (EI) calcd for $\text{C}_{17}\text{H}_{31}\text{N}_4$ $[\text{M}+\text{H}]^+$ 291.2543, found 291.2542.

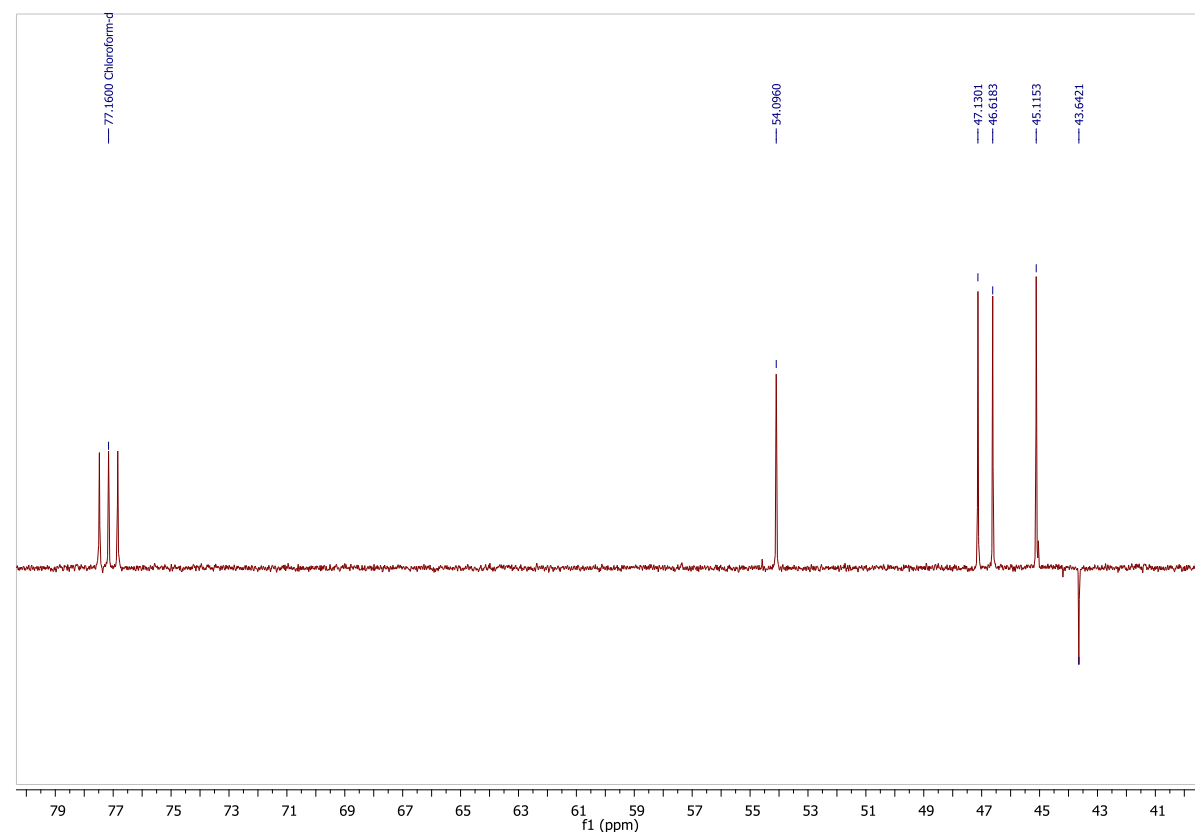
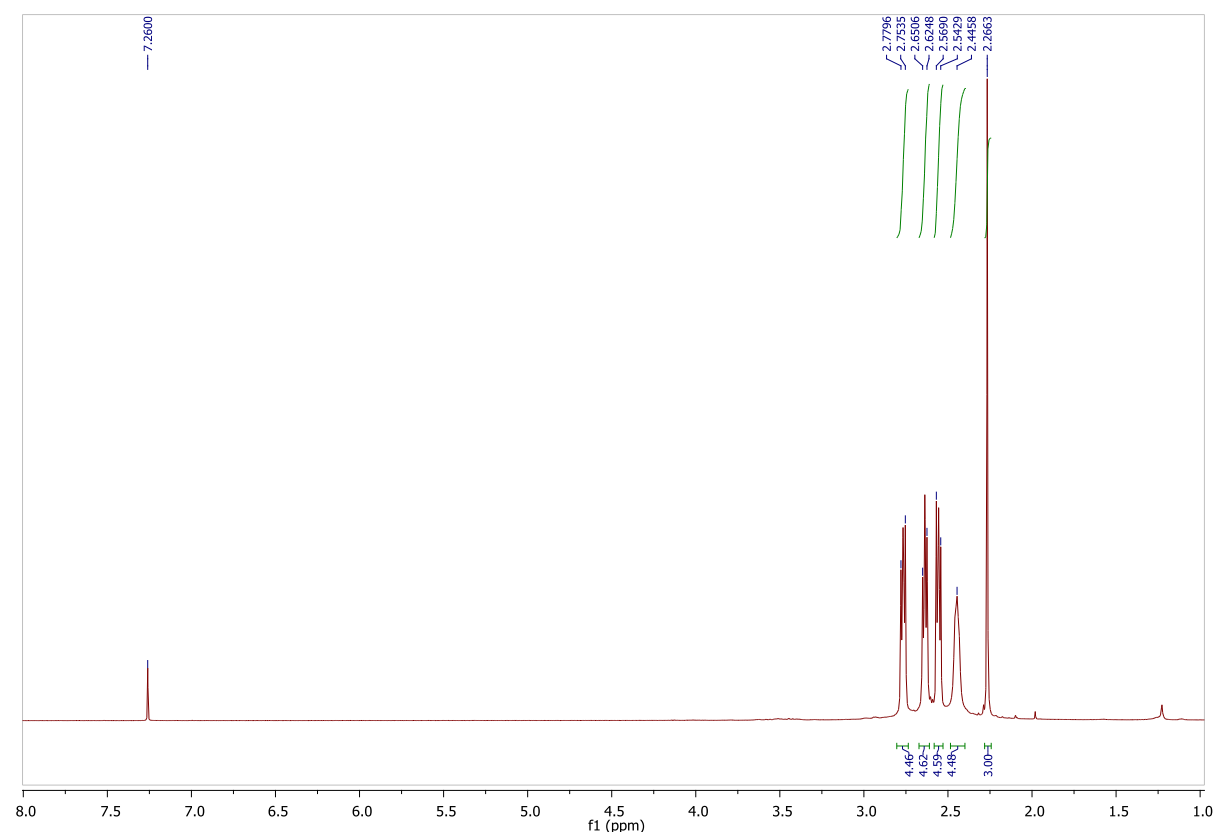
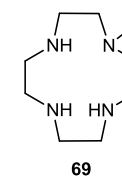


Figure 6.10 - ^1H and ^{13}C NMR spectra of **69**.

1-Methyl-1,4,7,10-tetraazacyclododecane **69**^{6,7}



Bisaminal **66** (2.0 g, 5.96 mmol) was dissolved in dry EtOH (40 mL). NH_2OH in a 50% aqueous solution (1.62 mL, 59.6 mmol) was added dropwise to this solution and the resulting mixture was stirred for 20 minutes at RT and then for 16 h at *ca.* 60 °C, making the solution turn from a cloudy white to a clear pale yellow. After cooling, the reaction mixture was stirred for a further hour at RT. The reaction mixture was then reduced in volume to afford a yellow oil, which was dissolved in HCl (5 M, 4 mL). The aqueous layer was washed with EtOAc (20 mL x 2) and Et_2O (20 mL x 2). The resulting aqueous layer was then adjusted to pH 14 with KOH (40% aqueous solution, w/v, 2 mL) and extracted with CHCl_3 (5 x 30 mL). The organic fractions were then combined, dried over MgSO_4 and the solvent removed *in vacuo* to afford the crude product as a yellow oil. After suspending the oil in EtOH (1 mL), HCl (35%, 2 mL) was added dropwise to obtain the hydrochloride salt of **69** as a fine white precipitate. This heterogeneous solution was reduced to dryness *in vacuo* and the resulting beige solid was dissolved in water (1 mL). Addition of an excess of EtOH (30 mL) to this solution resulted in the precipitation of a white powder and the resulting mixture was kept at -20 °C for two hours. The white solid was then collected by filtration, adjusted to pH 14 with KOH (40% aqueous solution, w/v, 2 mL) and extracted with CHCl_3 (5 x 30 mL). The organic fractions were then combined, dried over MgSO_4 and concentrated *in vacuo* to afford the target product as a white solid (67 mg, 37%). The data were consistent with those previously reported.⁶ ^1H NMR (400 MHz, CDCl_3): δ = 2.27 (s, 3H, CH_3), 2.44 (bs, 4H, CH_2), 2.54-2.57 (m, 4H, CH_2), 2.62-2.66 (m, 4H, CH_2), 2.75-2.78 (m, 4H, CH_2) ppm; ^{13}C NMR (DEPT 135, 100 MHz, CDCl_3): δ = 43.6, 45.1, 46.6, 47.3, 54.1 ppm.

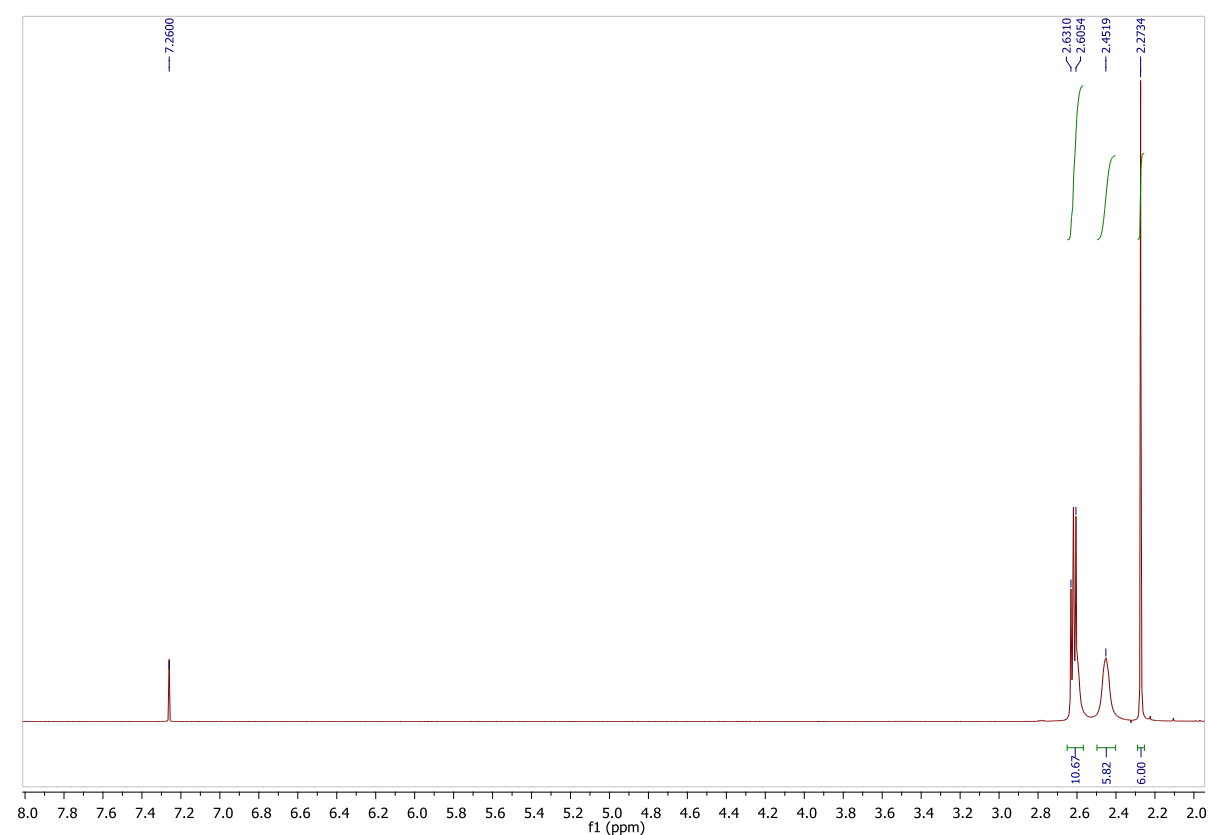
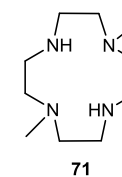


Figure 6.11 - ^1H NMR spectrum of **71**.

1,7-Dimethyl-1,4,7,10-tetraazacyclododecane **71**^{6,7}



Bisaminal **70** (1.00 g, 2.09 mmol) was dissolved in dry EtOH (20 mL). NH_2OH in a 50% aqueous solution (0.570 mL, 20.9 mmol) was added dropwise to this solution and the resulting mixture was stirred for 20 minutes at RT and then for 16 h at *ca.* 60 °C, making the solution turn from a cloudy white to a clear pale yellow. After cooling, the reaction mixture was stirred for a further hour at RT. The reaction mixture was then reduced in volume to afford a yellow oil, which was dissolved in HCl (5 M, 4 mL). The aqueous layer was washed with EtOAc (20 mL x 2) and Et_2O (20 mL x 2). The resulting aqueous layer was then adjusted to pH 14 with KOH (40% aqueous solution, w/v, 2 mL) and extracted with CHCl_3 (5 x 30 mL). The organic fractions were then combined, dried over MgSO_4 and the solvent removed *in vacuo* to afford the pure product as a clear oil (0.350 g, 87%). The data were consistent with those previously reported.⁶ ^1H NMR (400 MHz, CDCl_3): δ = 2.27 (s, 6H, CH_3), 2.45 (bs, 6H, CH_2), 2.60-2.63 (m, 10H, CH_2) ppm.

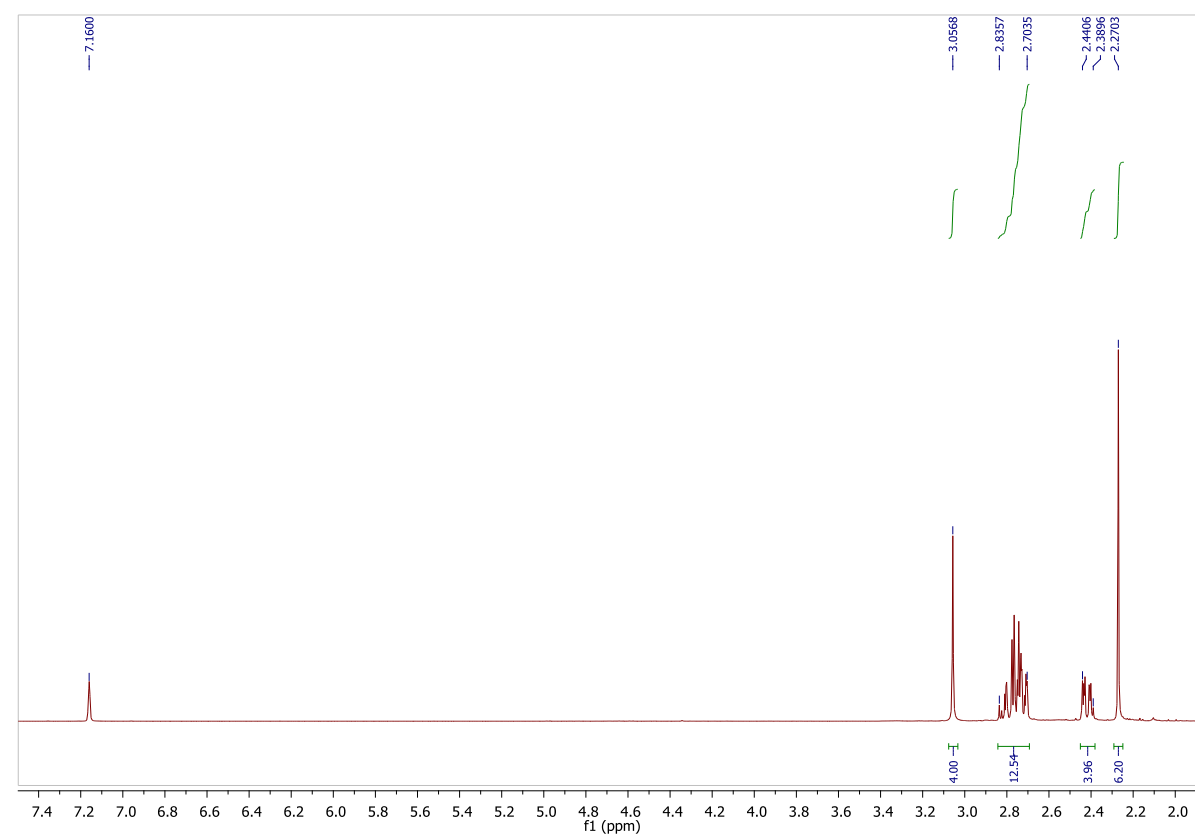
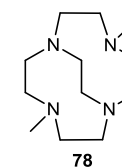


Figure 6.12 - ^1H NMR spectrum of **78**.

4,10-Dimethyl-1,4,7,10-tetraazabicyclo[5.5.2]tetradecane **78**^{8,9}



An excess of NaBH_4 (1.20 g, 31.3 mmol) was added in small portions to a stirred solution of **70** (1.50 g, 3.13 mmol) in EtOH (50 mL) under an N_2 atmosphere. The reaction mixture was stirred at RT for 5 days. Any excess NaBH_4 was then decomposed by the dropwise addition of HCl (5 M, 20.0 mL). This mixture was reduced to dryness *in vacuo* to afford a white solid. The solid was dissolved in water (50 mL) and adjusted to pH 14 using a solution of KOH (40% aqueous solution, w/v). This aqueous solution was extracted with CHCl_3 (5 x 30 mL), the organic extracts were combined, dried over MgSO_4 and concentrated *in vacuo* to obtain the pure product as a viscous oil (0.587 g, 83%). The data were consistent with those previously reported.⁹ ^1H NMR (400 MHz, C_6D_6): δ = 2.27 (s, 6H, CH_3), 2.39-2.44 (m, 4H, CH_2), 2.70-2.83 (m, 12H, CH_2), 3.06 (s, 4H, cross-bridge CH_2CH_2) ppm.

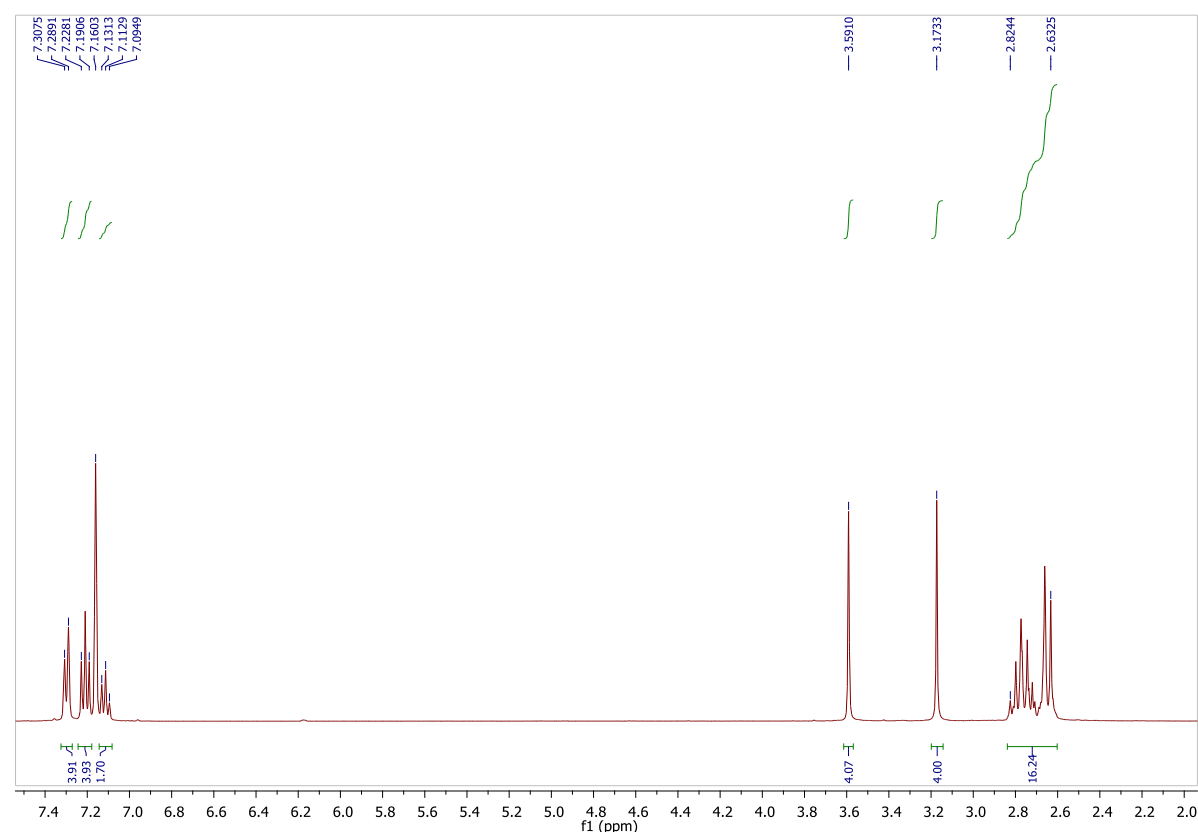
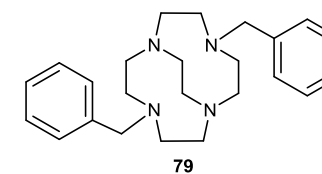


Figure 6.13 - ^1H NMR spectrum of **79**.

4,10-Bis(phenylmethyl)-1,4,7,10-tetraazabicyclo [5.5.2]tetradecane **79**¹⁰



An excess of NaBH_4 (2.80 g, 74.4 mmol) was added in small portions to a stirred solution of **77** (1.00 g, 1.86 mmol) in EtOH (100 mL) under an N_2 atmosphere. Reaction mixture was stirred at RT for 5 days. Any excess of NaBH_4 was then decomposed by the dropwise addition of HCl (5 M, 20 mL). This mixture was reduced to dryness *in vacuo* to afford a white solid. The solid was dissolved in water (50 mL) and adjusted to pH 14 using a solution of KOH (40% aqueous solution, w/v). This aqueous solution was extracted with CHCl_3 (5 x 30 mL), the organic extracts were combined, dried over MgSO_4 and concentrated *in vacuo* to obtain the pure product as a viscous oil (0.504 g, 72%). The data were consistent with those previously reported.¹⁰ ^1H NMR (400 MHz, C_6D_6): δ = 2.63-2.82 (m, 16H, CH_2), 3.17 (s, 4H, cross-bridge CH_2CH_2), 3.59 (s, 4H, $\text{NCH}_2\text{-Ar}$), 7.09-7.13 (m, 2H, Ar-H), 7.19-7.23 (m, 4H, Ar-H), 7.29-7.31 (m, 4H, Ar-H) ppm.

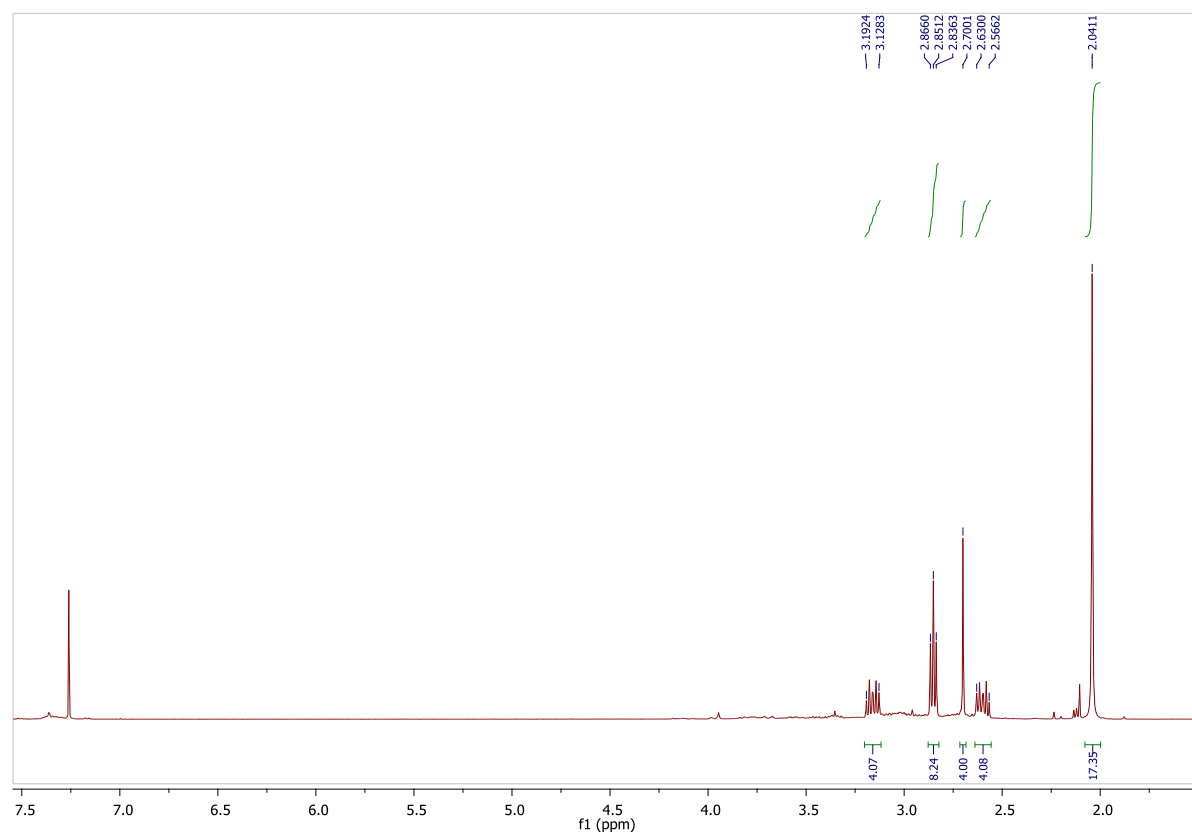
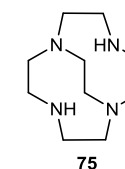


Figure 6.14 - ^1H NMR spectrum of **75**.

1,4,7,10-Tetraazabicyclo[5.5.2]tetradecane **75**¹⁰



Glacial HOAc (50 mL) and 10% Pd/C catalyst (200 mg) were measured into a 2-neck flask. The system was evacuated and flushed with N_2 three times, then with H_2 three times. The catalyst was equilibrated with H_2 over 15 min with stirring. A degassed solution of **79** (0.48 g, 1.26 mmol) in HOAc (30 mL) was then added *via* the sidearm. The reaction mixture was stirred under H_2 at RT for 2 hours. The disappearance of the starting material was followed by ^1H NMR spectroscopy. The presence of the target product without any remaining starting material was realised after 2 hours and the reaction mixture was then evacuated and flushed with N_2 three times. The reaction mixture was filtered through Celite and the resulting yellow solution was concentrated to yield a crude yellow oil (400 mg) containing of the mono-*N*-acetyl impurity **83** (73%) and the target ligand **75** (27%). This crude material was taken forward to the metal complex synthesis. The data of the crude were consistent with those previously reported.¹⁰ ^1H NMR (400 MHz, CDCl_3): δ = 2.57-2.63 (m, 4H, CH_2), 2.70 (s, 4H, cross-bridge CH_2CH_2), 2.84-2.87 (m, 8H, CH_2), 3.12-3.19 (m, 4H, CH_2) ppm.

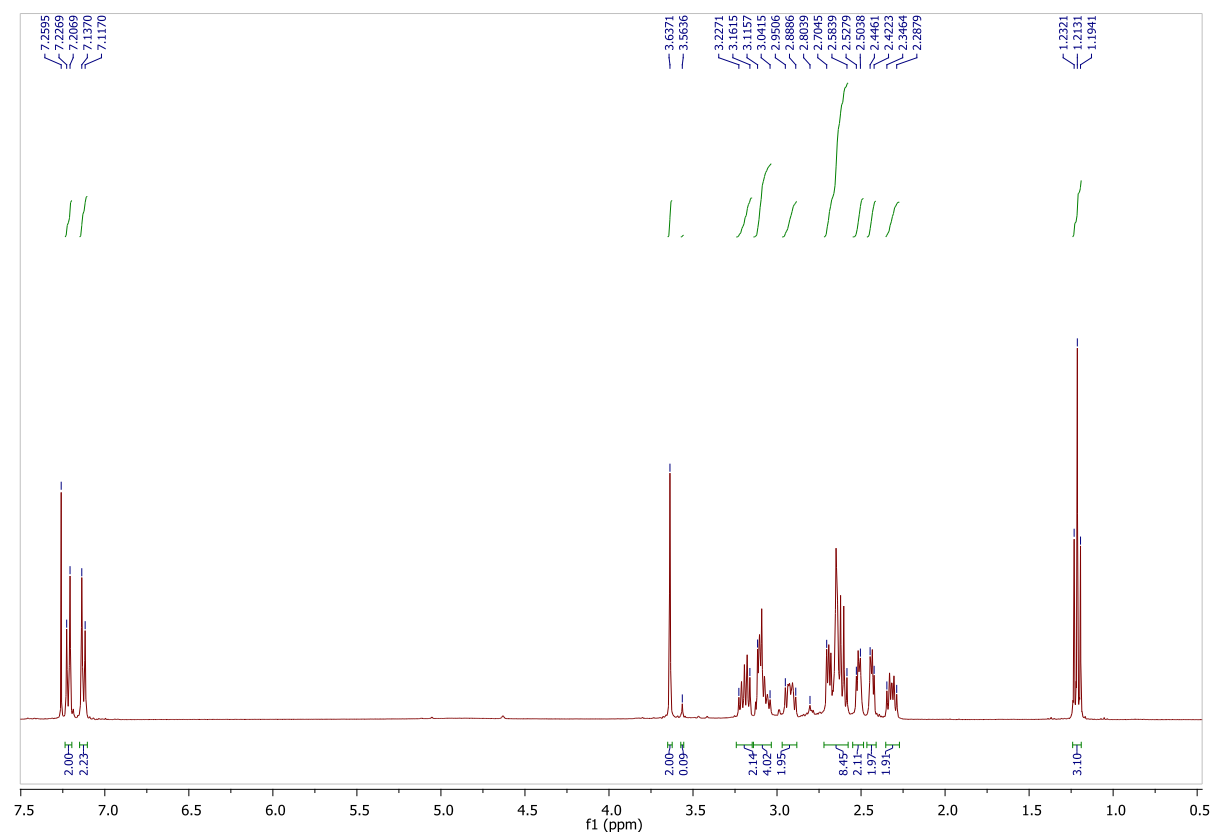
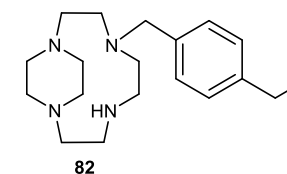


Figure 6.15 - ^1H NMR spectrum of **82**.

4-(4-Ethylbenzyl)-1,4,7,10-tetraazabicyclo[8.2.2]tetradecane **82**



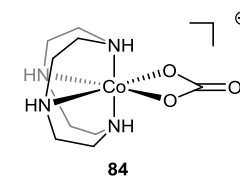
A modified literature procedure was used.¹² An excess of NaBH_4 (0.480 g, 12.7 mmol) was added in small portions to a stirred solution of **65** (0.200 g, 0.50 mmol) in EtOH (30.0 mL) under an N_2 atmosphere. The reaction mixture was stirred at RT for 18 hours followed by 16 hour at reflux. Then the reaction mixture was stirred at RT for 5 days. Any excess NaBH_4 was then decomposed by the dropwise addition of HCl (5 M, 20 mL). This mixture was reduced to dryness *in vacuo* to afford a white solid. The solid was dissolved in water (50 mL) and adjusted to pH 14 using a solution of KOH (40% aqueous solution, w/v). This aqueous solution was extracted with CHCl_3 (5 x 30.0 mL), the organic extracts were combined, dried over MgSO_4 and the solvent removed *in vacuo* to obtain the pure product as a yellow oil (0.103 g, 64%). ^1H NMR (400 MHz, C_6D_6): δ = 1.21 (t, J = 7.6 Hz, 3H, CH_3), 2.29-2.35 (m, 2H, CH_2), 2.42-2.45 (m, 2H, CH_2), 2.50-2.53 (m, 2H, CH_2), 2.58-2.70 (m, 8H, CH_2), 2.88-2.95 (m, 2H, CH_2), 3.04-3.11 (m, 4H, CH_2), 3.16-3.23 (m, 2H, CH_2), 3.64 (s, 2H, $\text{NCH}_2\text{-Ar}$), 7.13 (d, J = 8.0 Hz, 2H, Ar-H), 7.22 (d, J = 8.0 Hz, 2H, Ar-H) ppm.

6.2.3. Synthesis of Inorganic Salts and Coordination Compounds

Sodium tris-carbonatocobaltate (III) trihydrate^{11,13}

A solution of commercial H₂O₂ (30% aqueous solution (v/v), 0.58 mL) was added to an aqueous solution (2.50 mL) of Co(NO₃)₂·6H₂O (1.45 g, 5.00 mmol). The mixture was added dropwise to a stirred slurry of NaHCO₃ (2.10 g, 25.0 mmol) in distilled water (5.00 mL) at 0 °C, and precipitation of a green solid occurred almost immediately. The mixture was stirred for 1 h at 0 °C, after which time the green solid product was collected by filtration and washed with cold water (10 mL), absolute EtOH (10 mL) and Et₂O (10 mL). The resulting olive green solid was dried in air for 4 days to yield target salt Na₃[Co(CO₃)₃]·3H₂O (1.35 g, 75%). The data were consistent with those previously reported.^{11,13} IR: ν_{max} 3218, 1640, 1454, 1354, 832 cm⁻¹.

6.2.3.1. Synthesis of the Co(III) Carbonate Complexes: General Procedure^{11,14} as Demonstrated by the Synthesis of *cis*-[Co(**44**)CO₃]HCO₃ **84**¹⁵



Cyclen **44** (0.193 g, 0.550 mmol) was dissolved in a MeOH:H₂O mixture (1:1) (6 mL) and Na₃[Co(CO₃)₃]·3H₂O (0.200 g, 0.550 mmol) was added. The dark green solution gradually turned burgundy red and was left to react for 16 h at 65°C. The solution was filtered whilst hot under suction to separate the supernatant from a black solid. The filtrate was concentrated *in vacuo*, redissolved in MeOH (6 mL) and the resulting solution was filtered to remove the white precipitate. The resulting filtrate was reduced in volume *in vacuo* and excess of Et₂O (30 mL) was added. The resulting solids were collected by filtration and washed with Et₂O (10 mL) to afford **84** as a pink powder (0.170 g, 87%). The data were consistent with those previously reported.¹⁵ ¹H NMR (400 MHz, D₂O): δ = 2.75-3.20 (m, 14H, CH₂), 3.55-3.62 (m, 2H, CH₂) ppm; UV-Vis (MeOH): λ_{max} (ε) = 525 (271), 368 nm (200 dm³mol⁻¹cm⁻¹).

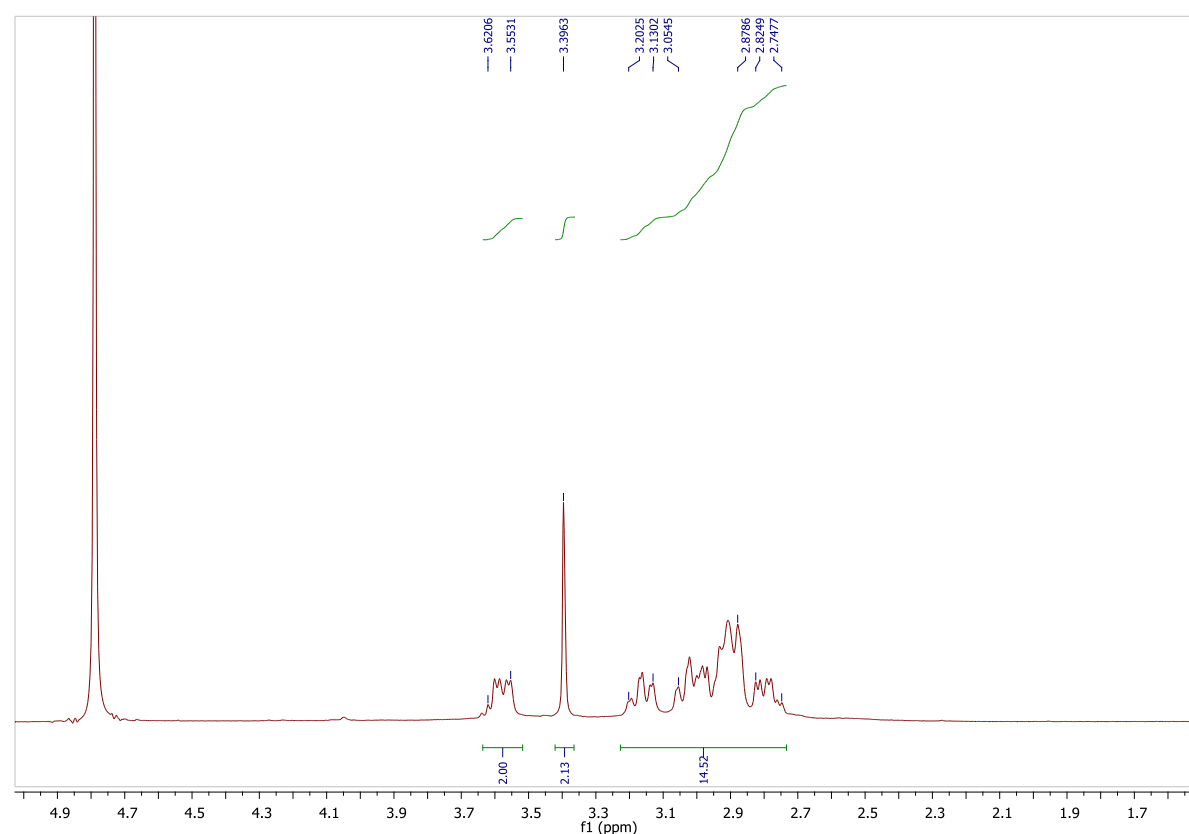


Figure 6.16 - ¹H NMR spectrum of **84**.

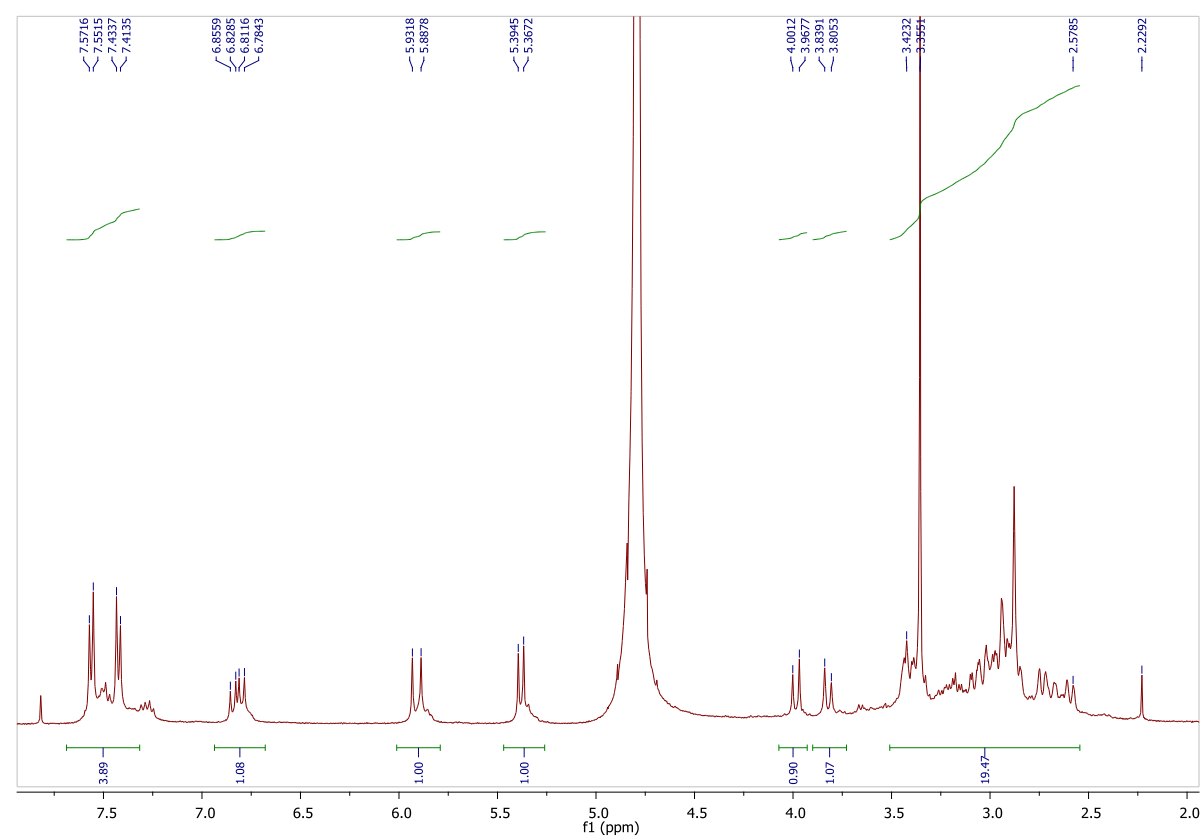
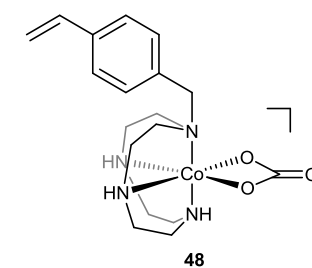


Figure 6.17 - ^1H NMR spectrum of **48**.

cis-[Co(**67**)CO₃]HCO₃ **48**¹¹



Following the general procedure cyclen derivative **67** (0.216 g, 0.750 mmol) and Na₃[Co(CO₃)₃]·3H₂O (0.271 g, 0.750 mmol) yielded complex **48** as a burgundy red powder (0.237 g, 67%). The data were consistent with those previously reported.¹¹ ^1H NMR (400 MHz, D₂O): δ = 2.58 – 3.42 (m, 19H, CH₂), 3.82 (d, J_{AB} = 13.5 Hz, 1H, NCH₂-Ar), 3.98 (d, J_{AB} = 13.5 Hz, 1H, NCH₂-Ar), 5.38 (d, J = 10.9 Hz, 1H, CH=CHH_{cis}), 5.91 (d, J = 17.7 Hz, 1H, CH=CHH_{trans}), 6.80 (dd, J = 10.9, 17.7 Hz, 1H, CH=CH₂), 7.42 (d, J = 8.0 Hz, 2H, Ar-H), 7.56 (d, J = 8.0 Hz, 2H, Ar-H) ppm; UV-Vis (DMSO): λ_{max} (ϵ) = 539 nm (213 dm³mol⁻¹cm⁻¹).

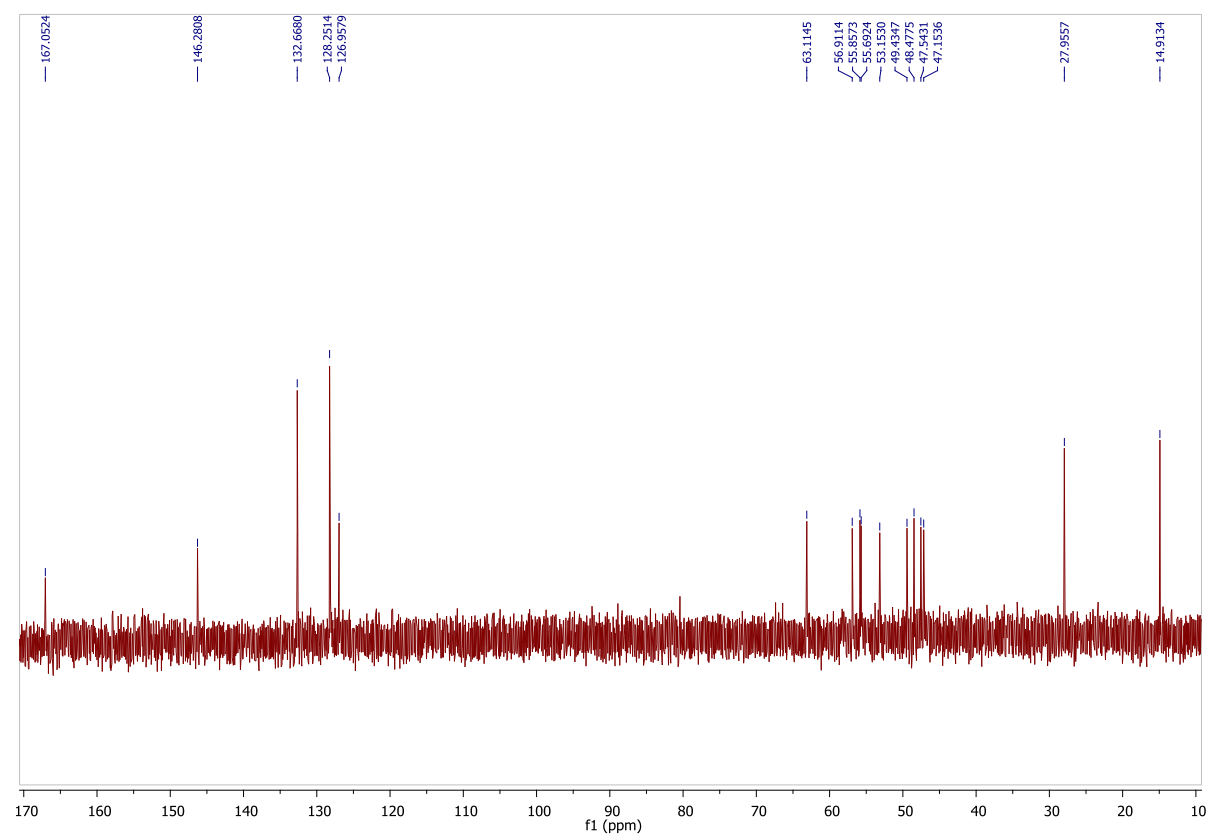
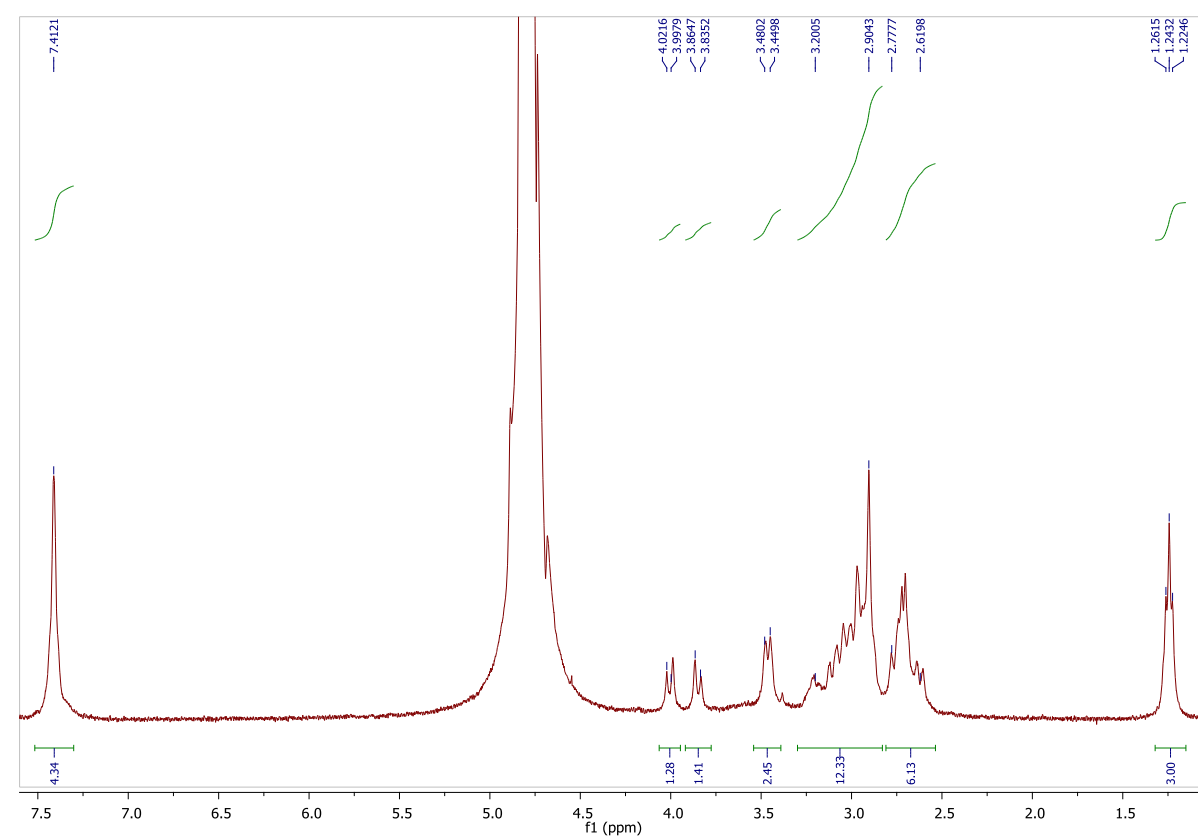
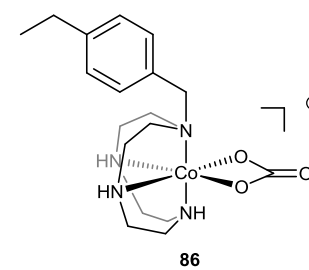


Figure 6.18 - ¹H NMR and ¹³C NMR spectra of **86**.

cis-[Co(**68**)CO₃]HCO₃ **86**



Following the general procedure, cyclen derivative **68** (95.0 mg, 0.330 mmol) and Na₃[Co(CO₃)₃]·3H₂O (0.120 g, 0.330 mmol) yielded complex **86** as a dark pink powder (0.125 g, 81%). Slow diffusion of Et₂O into a MeOH solution of **86** resulted in single crystals of *cis*-[Co(**68**)CO₃]MeCO₃. m.p. 184-186 °C; ¹H NMR (400 MHz, D₂O): δ = 1.24 (t, *J* = 7.4 Hz, 3H, CH₃), 2.62-2.78 (m, 6H, CH₂), 2.90-3.20 (m, 12H, CH₂), 3.45-3.48 (m, 2H, CH₂), 3.84 (d, *J*_{AB} = 11.9 Hz, 1H, N-CH₂), 4.01 (d, *J*_{AB} = 9.48 Hz, 1H, N-CH₂), 7.41 (bs, 4H, Ar-H) ppm; ¹³C NMR (100 MHz, D₂O): δ = 14.9, 27.9, 47.1, 47.5, 48.5, 49.4, 53.1, 55.7, 55.8, 56.9, 63.1, 126.9, 128.2, 132.7, 146.3, 167.0 ppm; IR: ν_{max} 3379, 3112, 2882, 1957, 1450, 1337, 1264, 1058, 1016, 976, 828, 750 cm⁻¹; UV-Vis (HPLC MeOH): λ_{max} (ε) = 540 (542), 366 nm (472 dm³mol⁻¹ cm⁻¹); HRMS (EI) calcd for C₁₈H₃₀CoN₄O₃ [M+H]⁺ 409.1644, found 409.1636.

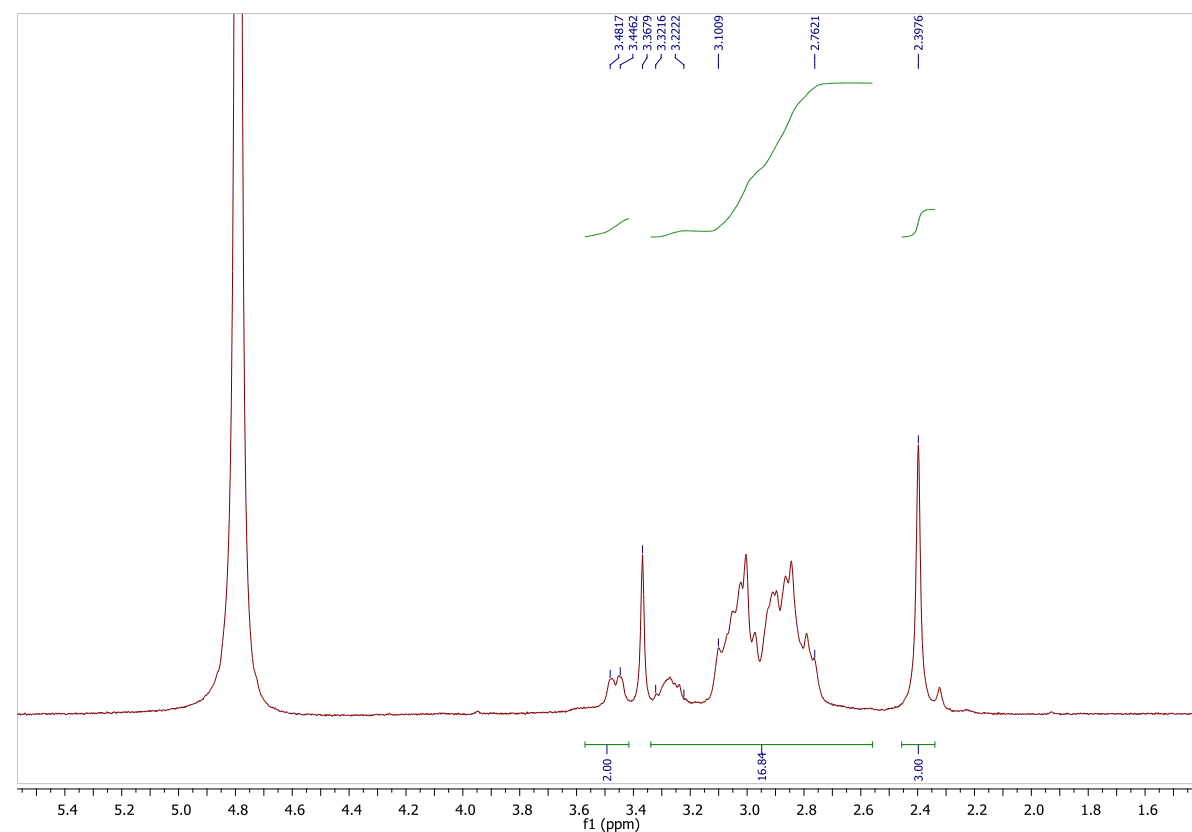
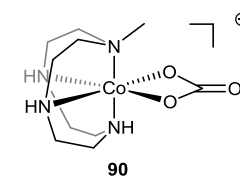


Figure 6.19 - ^1H NMR spectrum of **90**.

cis-[Co(**69**)CO₃]HCO₃ **90**¹⁶



Following the general procedure, cyclen derivative **69** (0.107 g, 0.575 mmol) and Na₃[Co(CO₃)₃]·3H₂O (0.208 g, 0.575 mmol) yielded complex **90** as a dark pink solid (0.186 g, 88%). The data were consistent with those previously reported.¹⁶ ^1H NMR (400 MHz, D₂O): δ = 2.40 (s, 3H, CH₃), 2.76-3.32 (m, 17H, CH₂, NH), 3.45-3.48 (m, 2H, NH) ppm; UV-Vis (HPLC MeOH): λ_{max} (ϵ) = 527 (240), 366 nm (280 dm³mol⁻¹cm⁻¹).

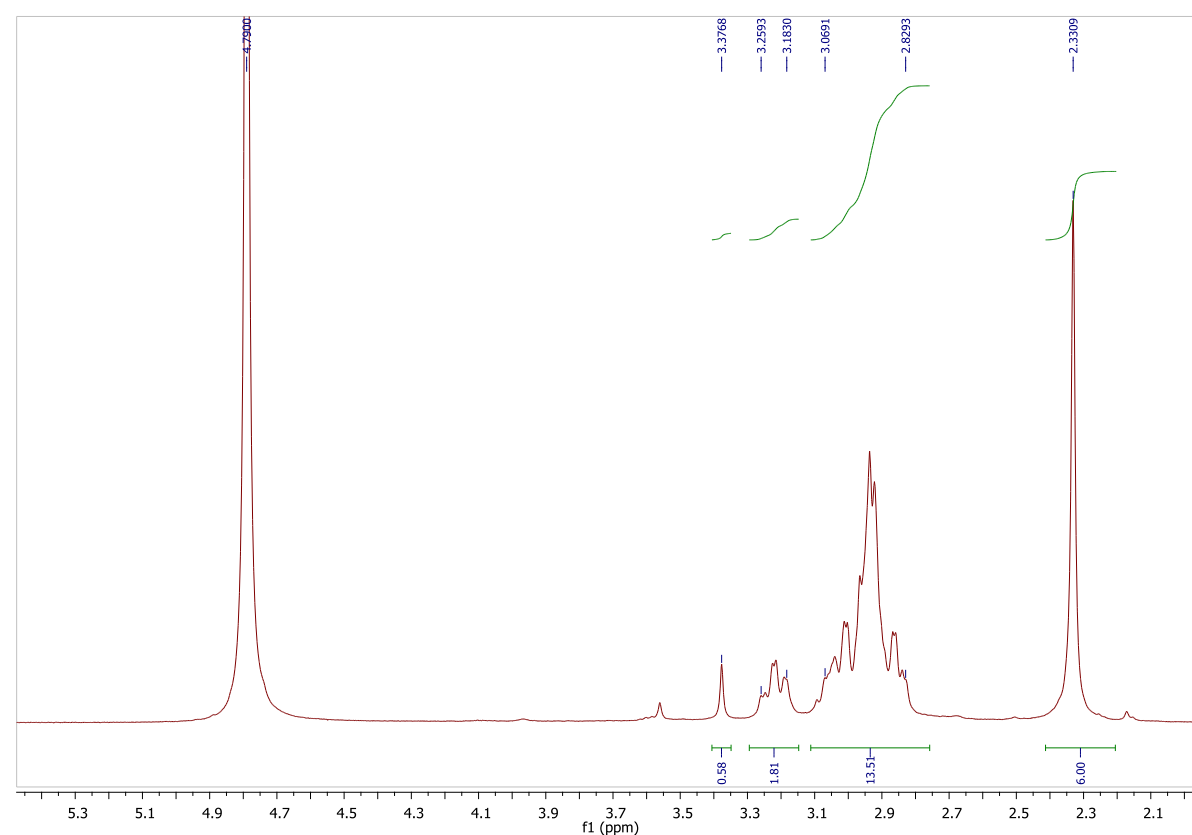
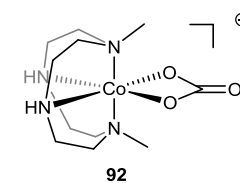


Figure 6.20 - ^1H NMR spectrum of **92**.

cis-[Co(**71**)CO₃]HCO₃ **92**^{16,17}



Following the general procedure, cyclen derivative **71** (0.140 g, 0.698 mmol) and Na₃[Co(CO₃)₃]·3H₂O (0.380 mg, 1.04 mmol) yielded complex **92** as a dark pink solid (220 mg, 83%). The data were consistent with those previously reported.^{16,17} ^1H NMR (400 MHz, D₂O): δ = 2.33 (s, 6H, CH₃), 2.83-3.07 (m, 14H, CH₂), 3.18-3.26 (m, 2H, CH₂) ppm; UV-Vis (HPLC MeOH): λ_{max} (ϵ)= 551 (256), 362 nm (330 dm³mol⁻¹cm⁻¹).

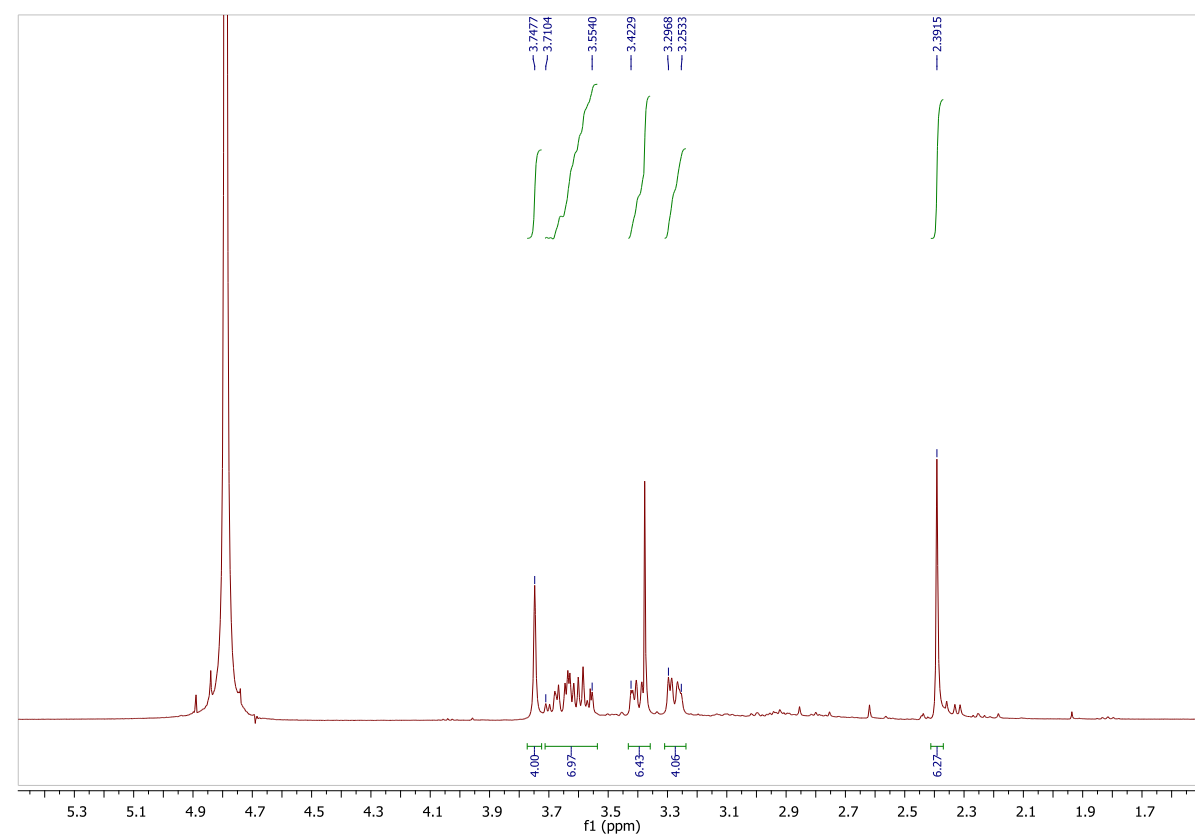
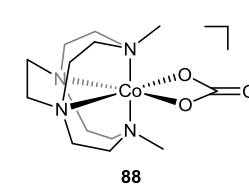


Figure 6.21 - ^1H NMR spectrum of **88**.

cis-[Co(**78**)CO₃]HCO₃ **88**¹⁸



Following the general procedure, cyclen derivative **78** (0.450 g, 1.98 mmol) and Na₃[Co(CO₃)₃]·3H₂O (0.716 g, 1.98 mmol) with a reaction time of 5 days yielded complex **88** as a dark pink solid (0.628 g, 78%). The data were consistent with those previously reported.¹⁸ ^1H NMR (400 MHz, D₂O): δ = 2.39 (s, 6H, CH₃), 3.25-3.30 (m, 4H, CH₂), 3.38-3.42 (m, 6H, CH₂), 3.55-3.71 (m, 6H, CH₂), 3.75 (s, 4H, cross-bridge CH₂CH₂); UV-Vis (HPLC MeOH): λ_{max} (ϵ) = 531 (127), 365 nm (152 dm³mol⁻¹cm⁻¹).

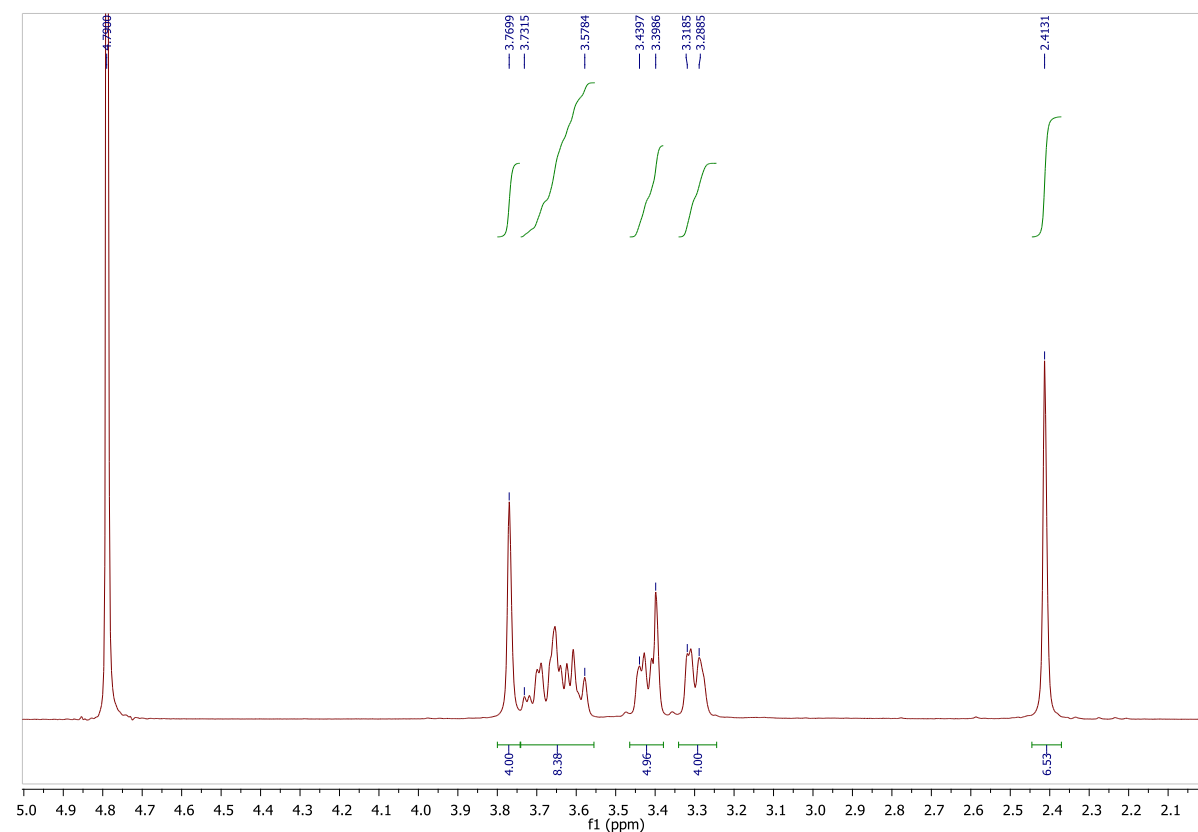
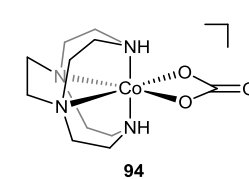


Figure 6.22 - ^1H NMR spectrum of **94**.

cis-[Co(**75**)CO₃]HCO₃ **94**



Following the general procedure, crude cyclen derivative **75** (155 mg that contained 42 mg, 0.21 mmol of the target complex) and Na₃[Co(CO₃)₃]·3H₂O (76 mg, 0.21 mmol) yielded crude complex **94** as a dark pink solid that contained 62% of the *N*-acetyl impurity **83** (overall mass and yield obtained: 167 mg, 57%, which contains 63 mg of the target product). Representative ^1H NMR (400 MHz, D₂O) data for the mixture of **83** and **94** as follows: δ = 3.29-3.32 (m, 4H, CH₂), 3.40-3.44 (m, 4H, CH₂), 3.58-3.73 (m, 8H, CH₂), 3.77 (s, 4H, cross-bridge CH₂CH₂) ppm; UV-Vis (HPLC MeOH): λ_{max} = 494 and 356 nm.

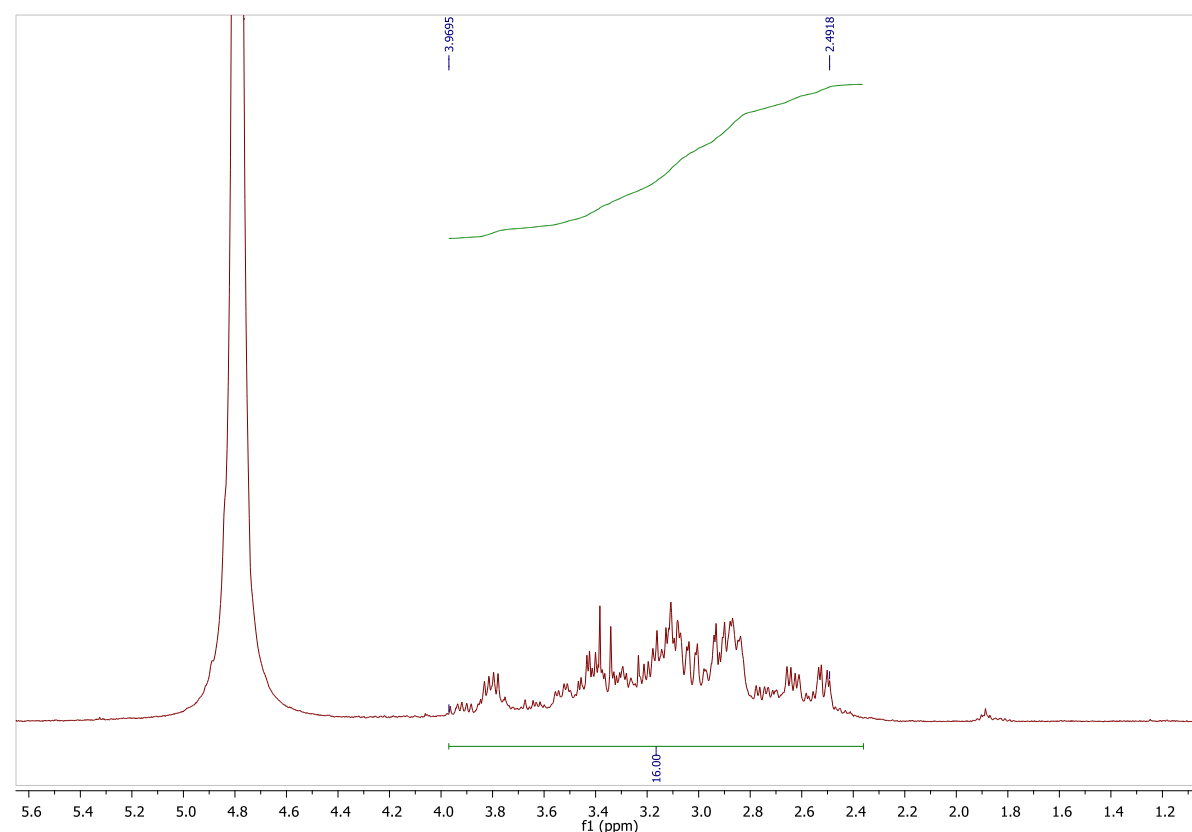
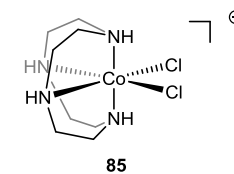


Figure 6.23 - ^1H NMR spectrum of **85**.

6.2.3.2. Synthesis of the Di-chloride Co(III) Complexes: General Procedure^{11,14} as Demonstrated by the Synthesis of *cis*-[Co(**44**)Cl₂]Cl **85**^{11,16,19}



Carbonate complex **84** (0.205 g, 0.580 mmol) was dissolved in MeOH (8 mL) and HCl (35 %, 2 mL) was added dropwise to the solution. The reaction mixture was reduced to dryness and the residue was again dissolved in MeOH (8 mL) and treated with HCl (35%, 2 mL). This procedure was repeated 5 times and a gradual colour change from dark pink to dark violet was observed. The final solution was concentrated *in vacuo* and the resulting violet solid was recrystallised from MeOH/Et₂O to afford **85** as a violet crystalline solid (0.220 g, 75%). The data were consistent with those previously reported.^{11,19} ^1H NMR (400 MHz, D₂O): δ = 2.49–3.97 (m, 16H, CH₂) ppm; UV-Vis (DMSO): λ_{max} (ϵ)= 563 (148), 394 nm (155 dm³mol⁻¹ cm⁻¹).

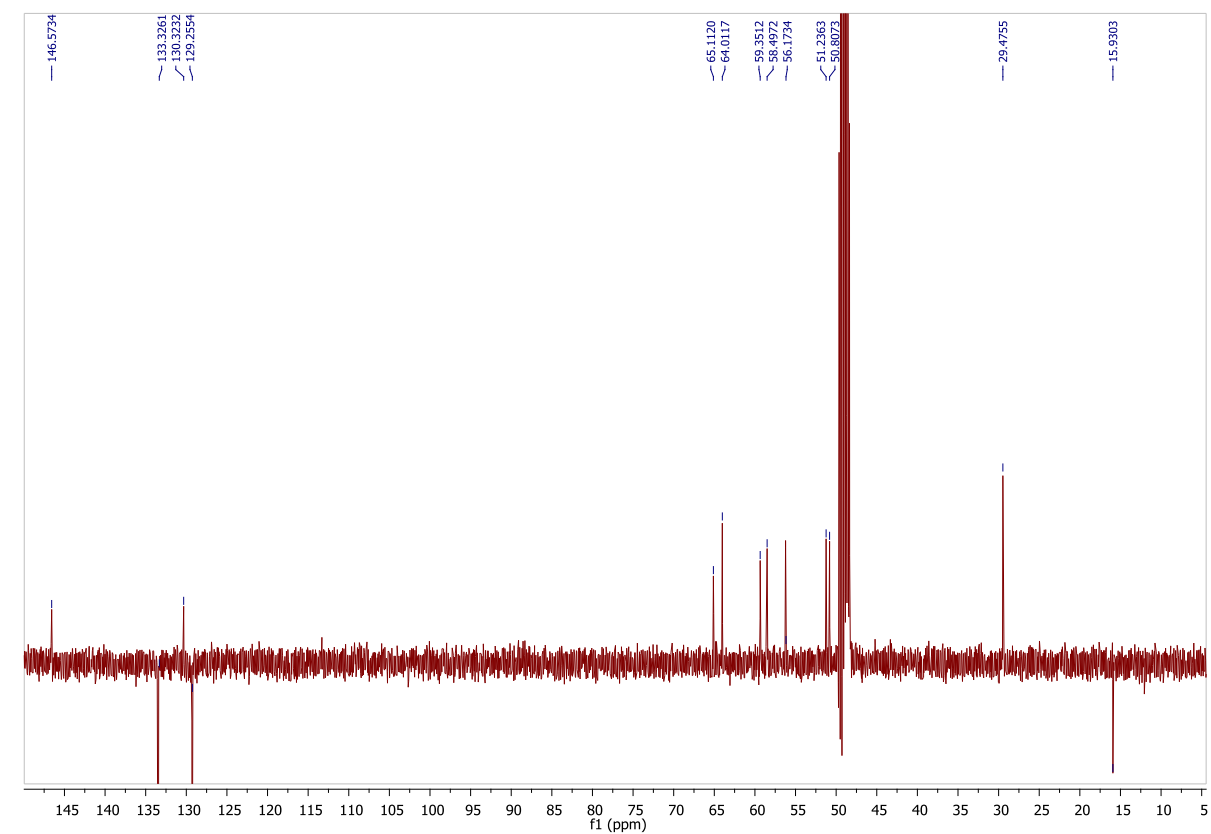
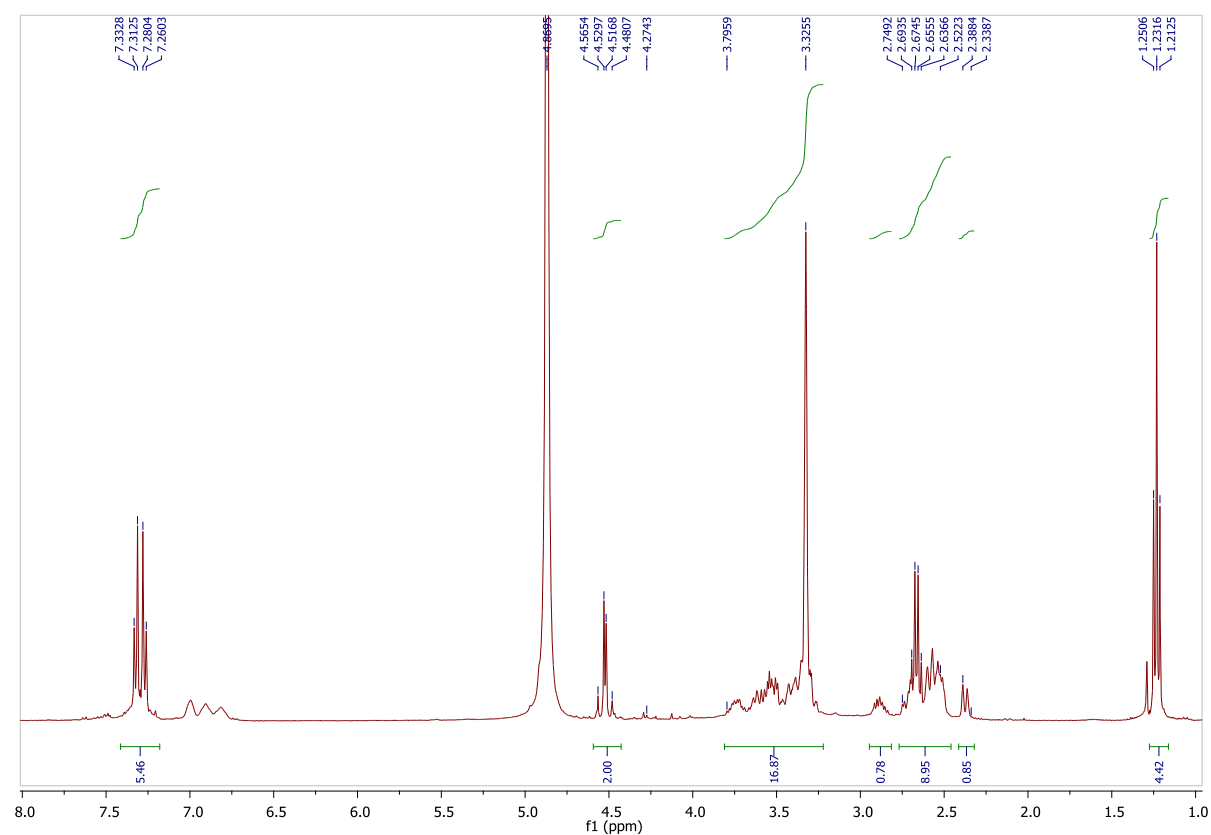
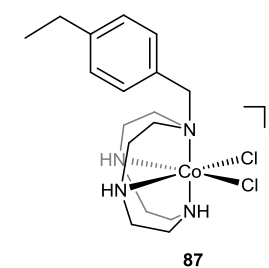


Figure 6.24 - ^1H and ^{13}C NMR spectra of **87**.

cis-[Co(**68**)Cl₂]Cl **87**



Following the general procedure, carbonate complex **86** (0.120 g, 0.255 mmol) yielded complex **87** as a dark violet solid (0.100 g, 86%). m.p. 195-198 °C; ^1H NMR (400 MHz, CD₃OD): δ = 1.23 (t, J = 8.0 Hz, 3H, CH₃), 2.34-2.39 (m, 1H, CH₂), 2.52-2.75 (m, 8H, CH₂), 3.25-3.79 (m, 16H, residual CD₃OD solvent peak overlaps signal, CH₂), 4.52 (dd, J_{AB} = 5.2 Hz, 14.3 Hz, 2H, NCH₂-Ar), 7.27 (d, J = 8.0 Hz, 2H, Ar-H), 7.32 (d, J = 8.0 Hz, 2H, Ar-H) ppm; ^{13}C NMR (100 MHz, D₂O): δ = 15.9, 29.5, 50.8, 51.2, 56.2, 58.5, 59.3, 64.0, 65.1, 129.2, 130.3, 133.3, 146.6 ppm; IR: ν_{max} 3056, 2962, 2870, 1613, 1447, 1098, 1063, 1008, 970, 828 cm⁻¹; UV-Vis (MeOH): λ_{max} (ϵ) = 570 (224), 395 nm (264 dm³mol⁻¹cm⁻¹); HRMS (EI) calcd for C₁₇H₂₈CoN₄ [M+H]⁺ 347.1640, found 347.1639.

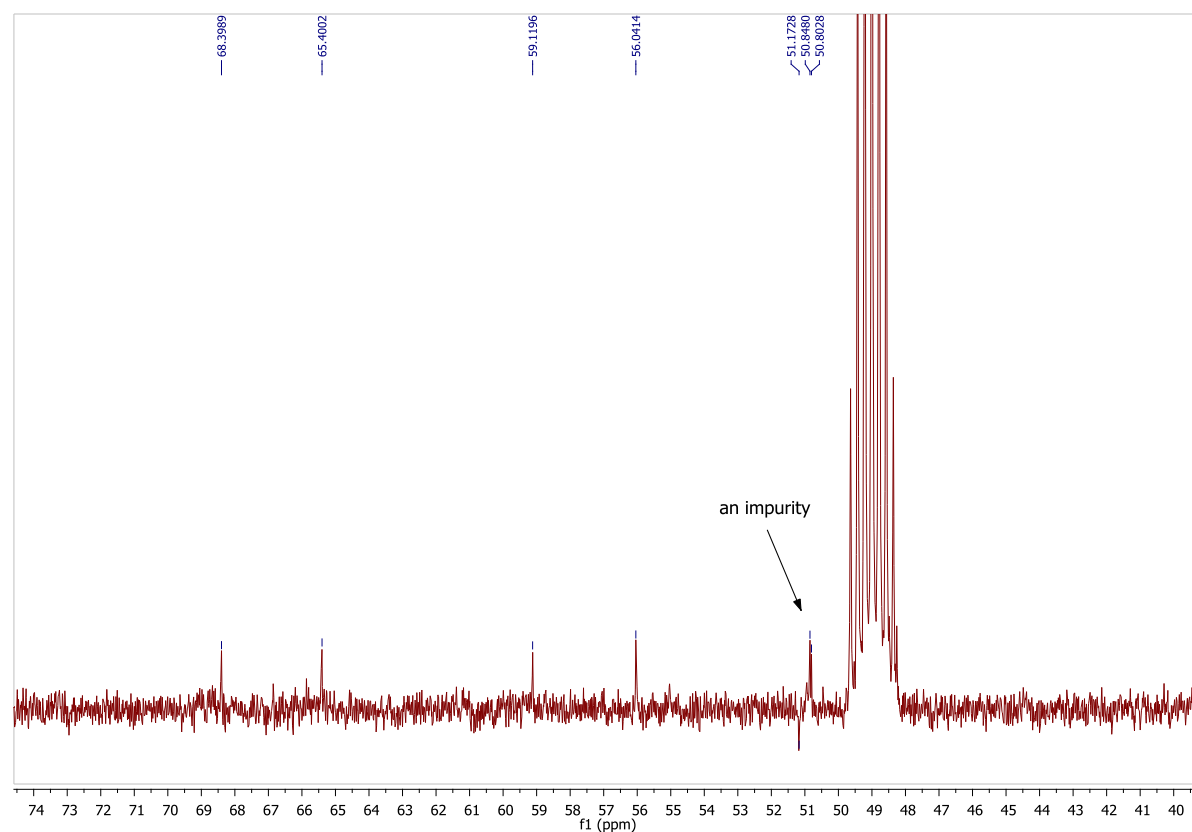
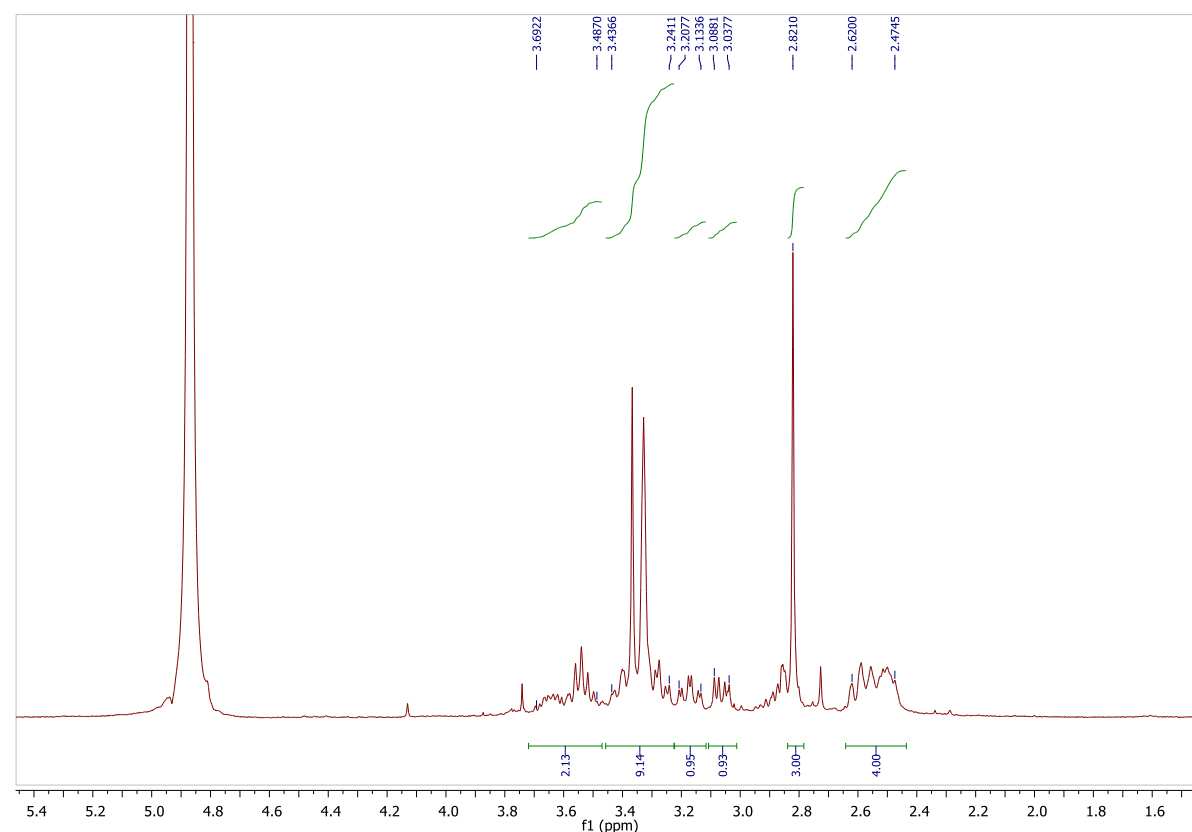
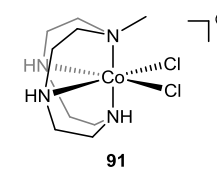


Figure 6.25 - ^1H and ^{13}C NMR spectra of **91**.

cis-[Co(**69**)Cl₂]Cl **91**¹⁶



Following the general procedure, complex **90** (0.107 g, 0.292 mmol) gave complex **91** as a dark crystalline violet solid (79 mg, 78%). The data were consistent with those previously reported.¹⁶ ^1H NMR (400 MHz, CD₃OD): δ = 2.47-2.62 (m, 4H, CH₂), 2.82 (s, 3H, CH₃), 3.04-3.09 (m, 1H, CH₂), 3.13-3.21 (m, 1H, CH₂), 3.24-3.44 (m, 9H, residual CD₃OD solvent peak overlaps signal, CH₂), 3.49-3.69 (m, 2H, CH₂) ppm; ^{13}C NMR (DEPT 135, 100 MHz, CD₃OD): δ = 51.2, 56.0, 59.1, 65.4, 68.4 ppm; UV-Vis (MeOH): λ_{max} (ϵ) = 567 (183), 395 nm (212 dm³mol⁻¹cm⁻¹).

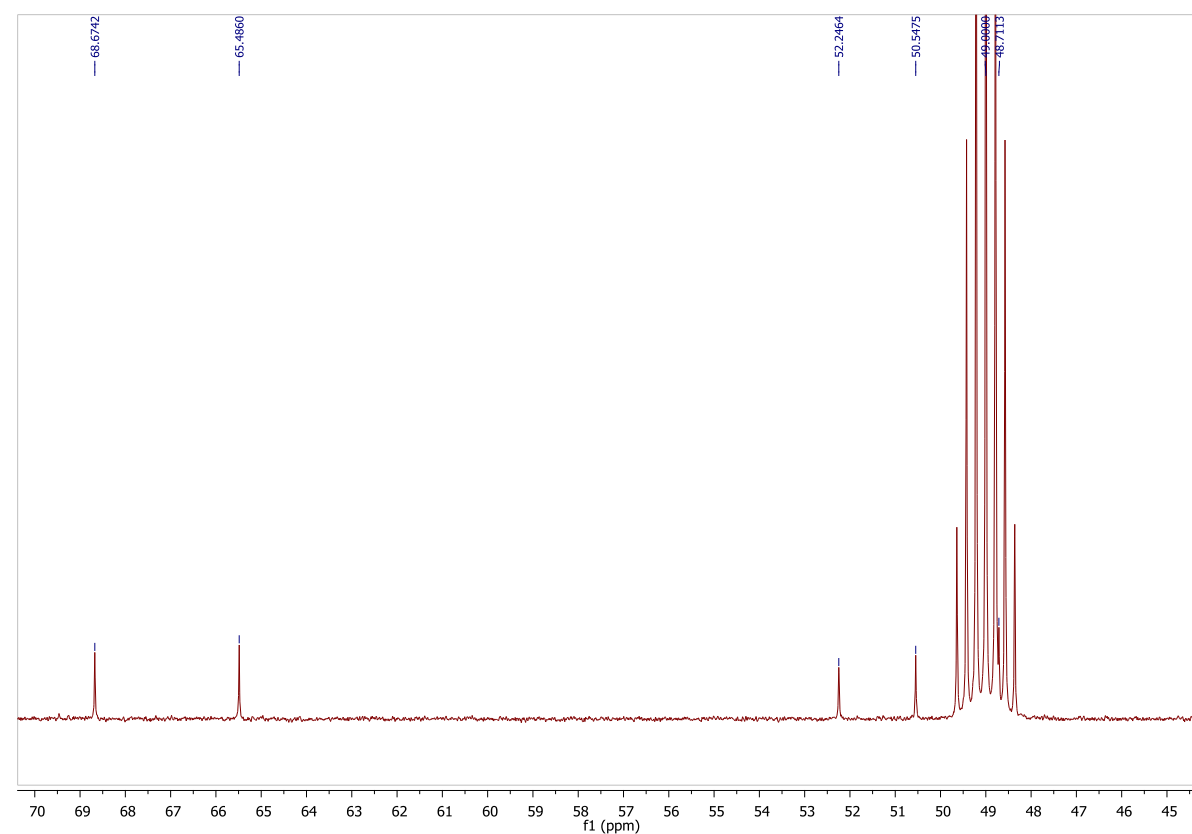
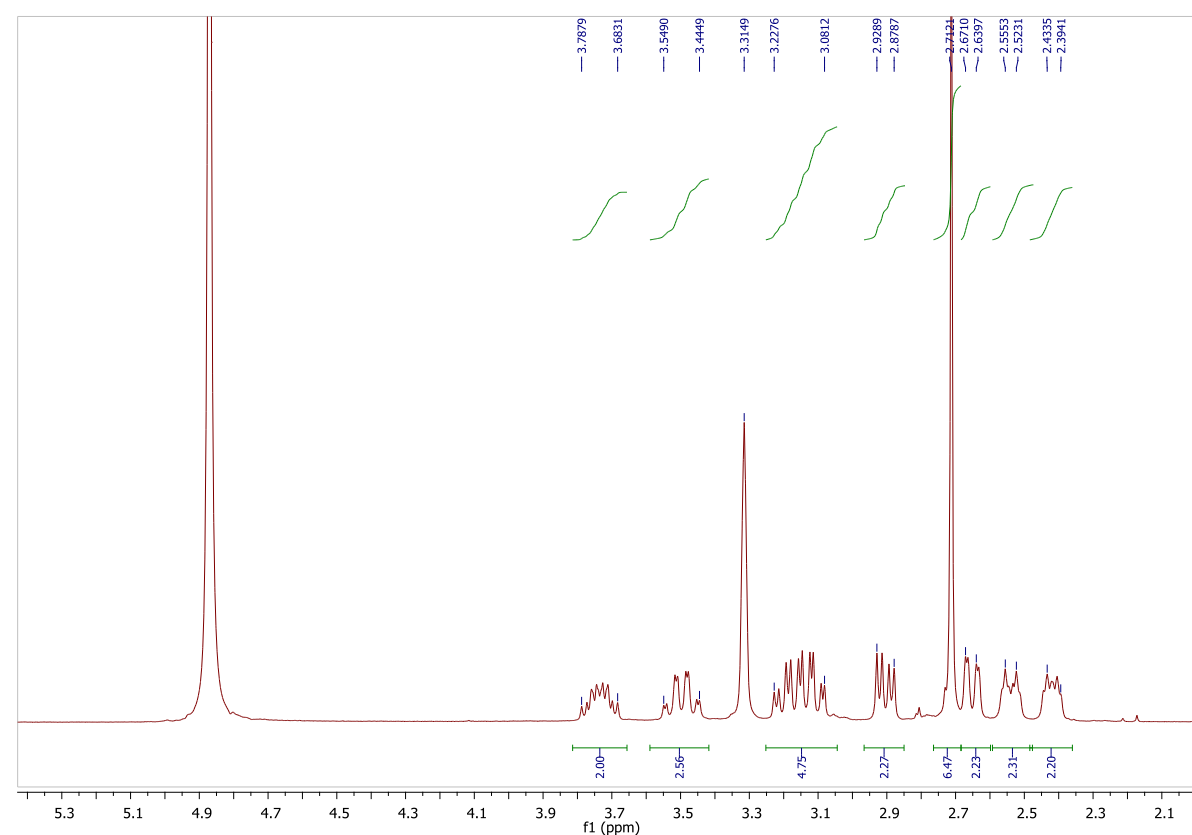
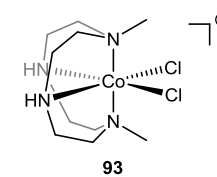


Figure 6.26 - ¹H and ¹³C NMR spectra of **93**.

cis-[Co(**71**)Cl₂]Cl **93**¹⁶



Following the general procedure, complex **92** (0.163 g, 0.428 mmol) gave complex **93** as a dark violet solid (0.140 g, 89%). The data were consistent with those previously reported.¹⁶ ¹H NMR (400 MHz, CD₃OD): δ = 2.39-2.43 (m, 2H, CH₂), 2.52-2.55 (m, 2H, CH₂), 2.64-2.67 (m, 2H, CH₂), 2.71 (s, 6H, CH₃), 2.88-2.93 (m, 2H, CH₂), 3.08-3.23 (m, 4H, CH₂), 3.44-3.55 (m, 2H, CH₂), 3.68-3.79 (m, 2H, CH₂) ppm; ¹³C NMR (100 MHz, CD₃OD): δ = 48.7 (residual CD₃OD solvent peak overlaps signal), 50.5, 52.2, 65.5, 68.7 ppm; UV-Vis (MeOH): λ_{max} (ε) = 589 (192), 400 nm (183 dm³mol⁻¹cm⁻¹).

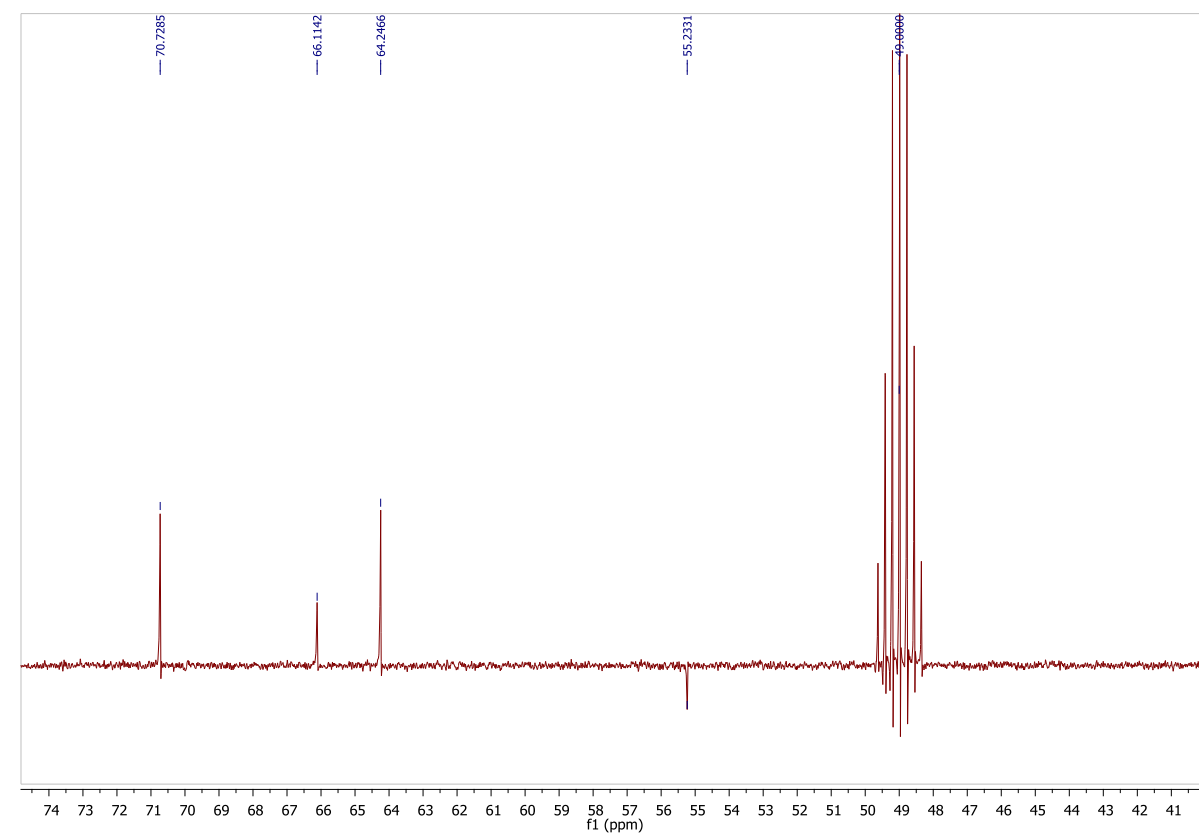
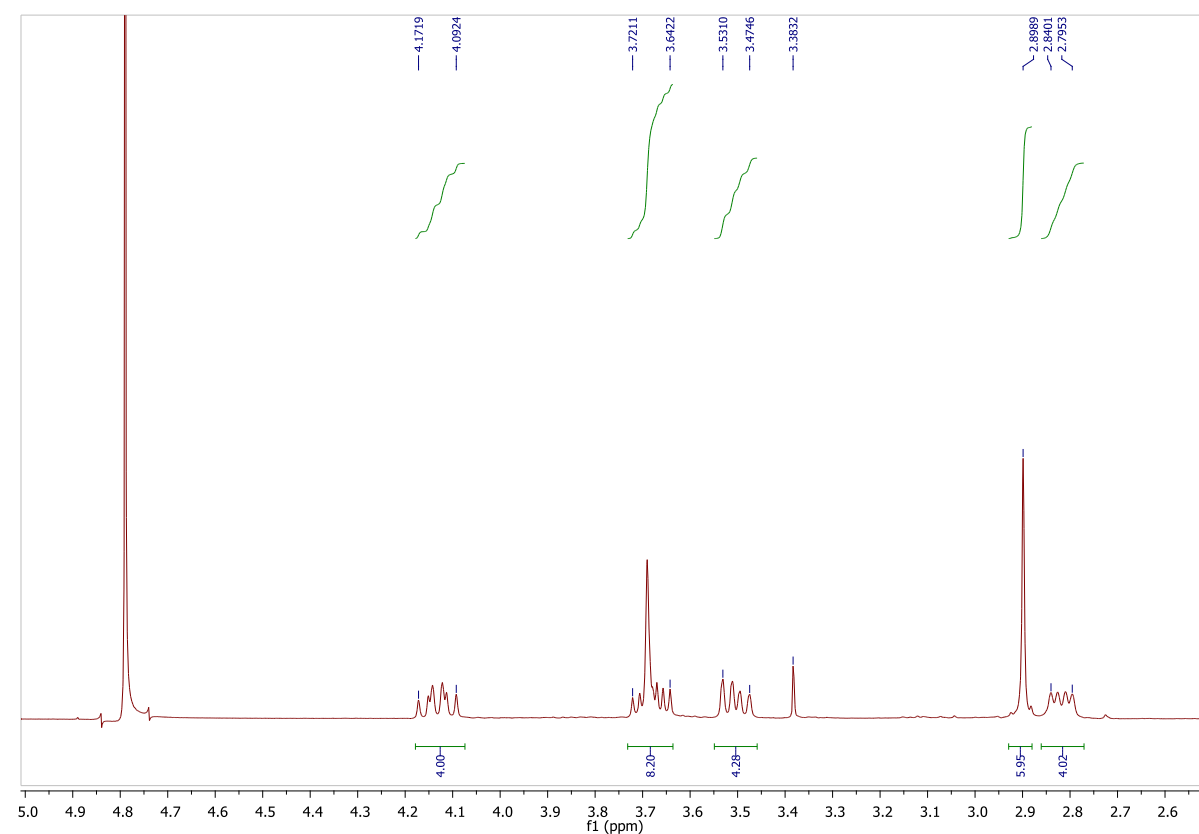
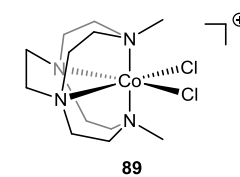


Figure 6.27 - ^1H and ^{13}C NMR spectra of **89**.

cis-[Co(**78**)Cl₂]Cl **89**¹⁸



Following the general procedure, complex **88** (0.506 g, 1.24 mmol) gave complex **89** as a dark crystalline violet solid (0.296 g, 65%). Recrystallisation of **89** from MeOH/Et₂O mixture also afforded violet crystals suitable for single crystal X-ray diffraction. The data were consistent with those previously reported.¹⁸ ^1H NMR (400 MHz, D₂O): δ = 2.79-2.84 (m, 4H, CH₂), 2.90 (s, 6H, CH₃), 3.47-3.53 (m, 4H, CH₂), 3.64-3.72 (m, 8H, CH₂), 4.09-4.17 (m, 4H, CH₂) ppm; ^{13}C NMR (DEPT 135 100 MHz, CD₃OD): δ = 55.2, 64.2, 66.1, 70.7; UV-Vis (MeOH): λ_{max} (ϵ) = 572 (168), 411 (154), 340 nm (671 dm³mol⁻¹cm⁻¹).

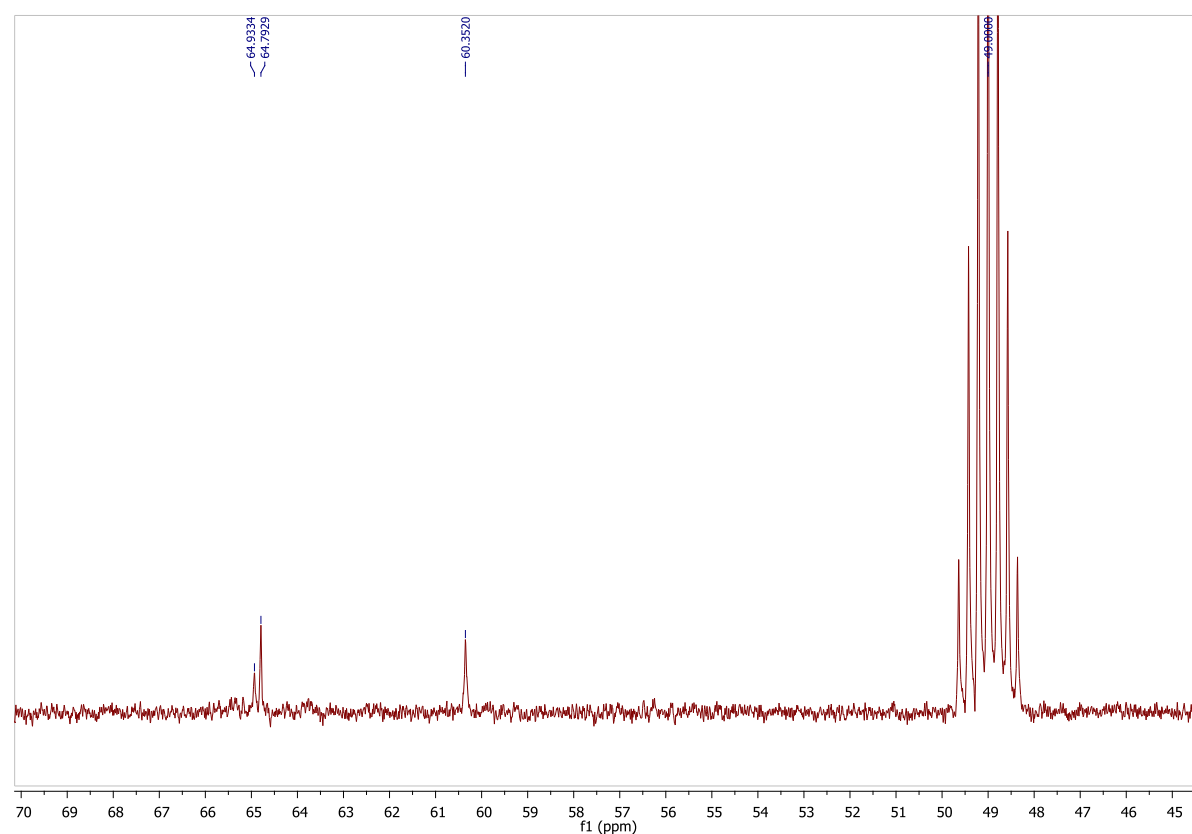
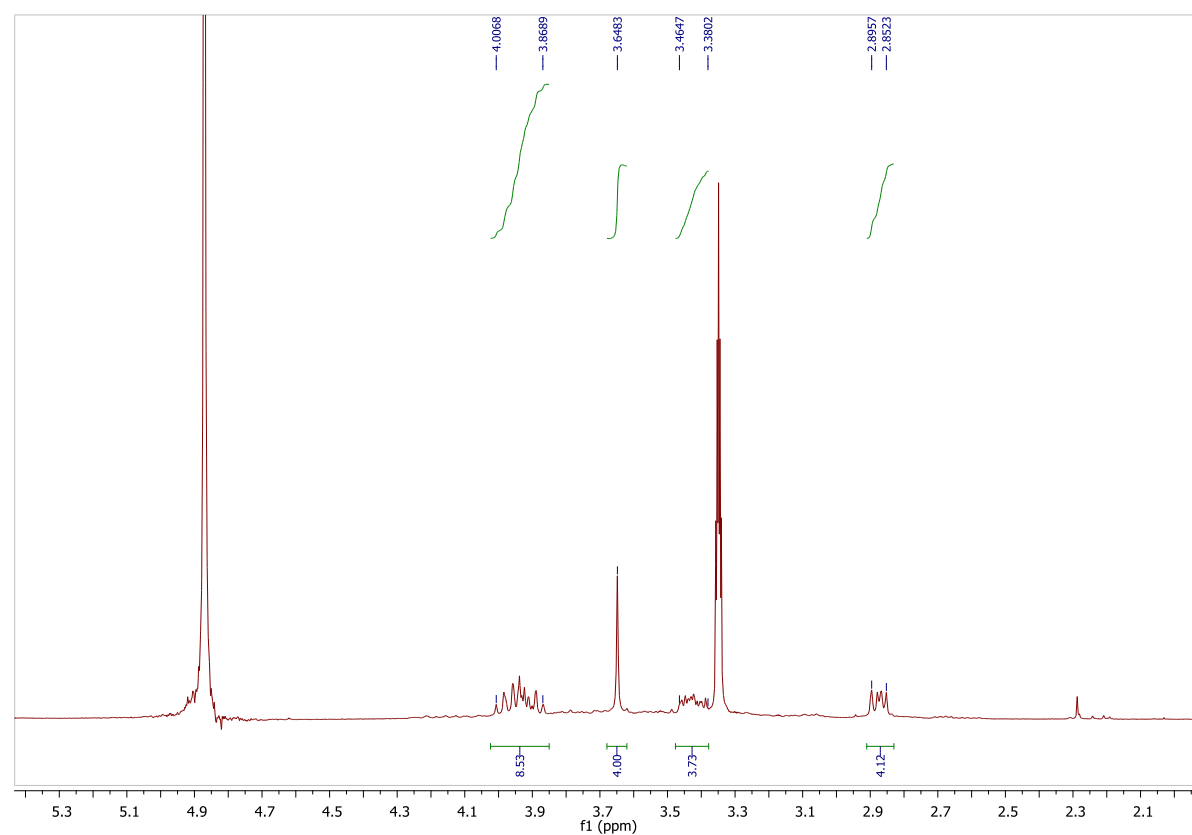
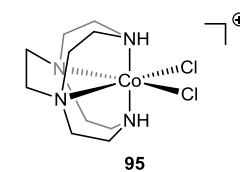


Figure 6.28 - ^1H and ^{13}C NMR spectra of **95**.

cis-[Co(**75**)Cl₂]Cl **95**²⁰



Following the general procedure, complex **94** (27 mg, 0.071 mmol) gave complex **95** as a dark violet solid (20 mg, 77%). The data were consistent with those previously reported.²⁰

^1H NMR (400 MHz, CD₃OD): δ = 2.86-2.89 (m, 4H, CH₂), 3.38-3.46 (m, 4H, CH₂), 3.66 (s, 4H, cross-bridge CH₂CH₂), 3.87-4.01 (m, 8H, CH₂) ppm; ^{13}C NMR (100 MHz, CD₃OD): δ = 60.3, 64.8, 64.9 ppm; UV-Vis (MeOH): λ_{max} (ϵ) = 543 (100), 400 (131), 337 nm (486 dm³mol⁻¹cm⁻¹).

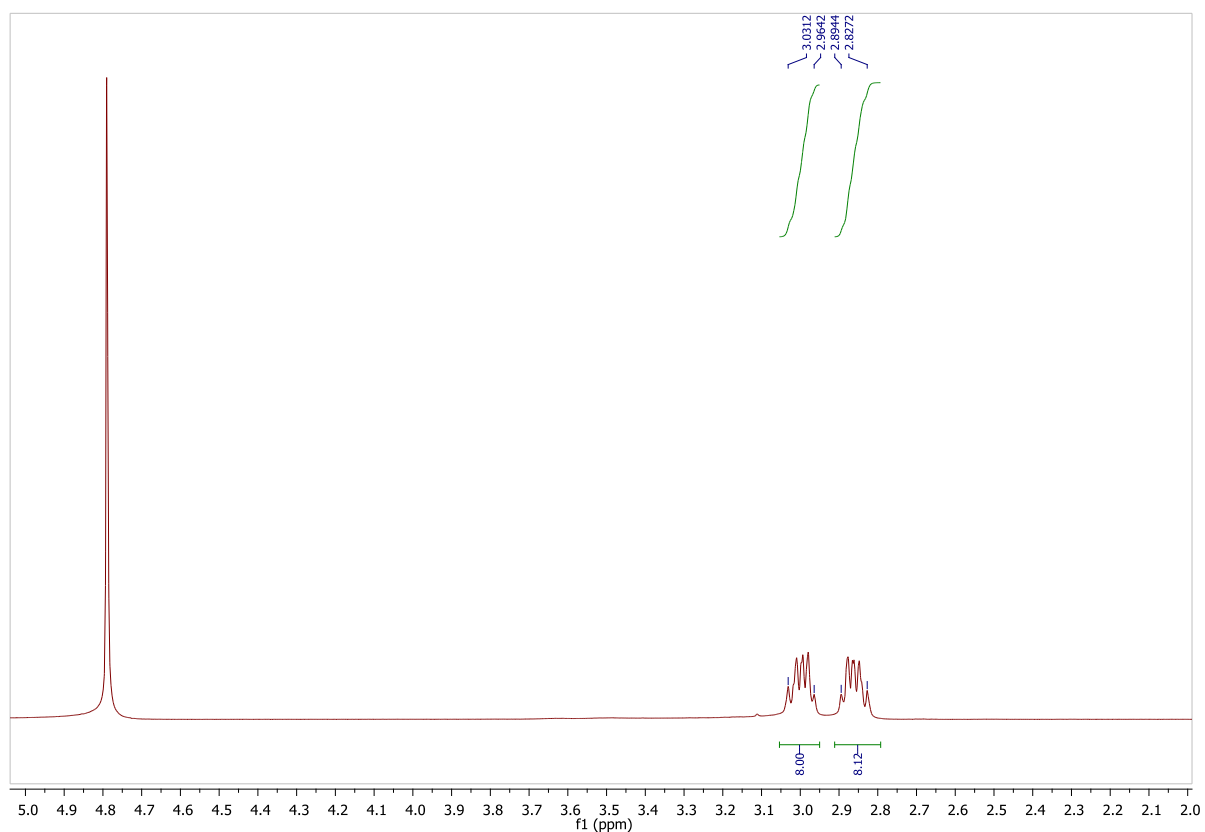
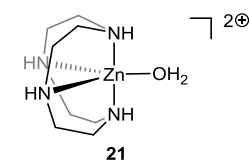


Figure 6.29 - ^1H NMR spectrum of **21**.

6.2.3.3. Synthesis of the Zn(II) Complexes: General Procedure¹⁰ as Demonstrated by the Synthesis of $[\text{Zn}(\mathbf{44})\text{OH}_2](\text{ClO}_4)_2$ **21**²³

Based on the extensive literature precedence, it is assumed, that the coordinating ion in the perchlorate cyclen Zn(II) complexes presented in this work is H_2O .^{10,21,22}



Cyclen **44** (0.100 g, 0.58 mmol) was dissolved in MeOH and an equimolar amount of $\text{Zn}(\text{ClO}_4)_2 \cdot 6\text{H}_2\text{O}$ (0.223 g, 0.598 mmol) was added to this solution. The clear solution was left to react for 16 h at 65°C. The solution was then reduced in volume and a white solid precipitated upon addition of Et_2O (20 mL). The resulting solid was then collected by filtration, dried *in vacuo* and washed with Et_2O (10 mL) to afford **21** as a white powder (0.215 g, 81%). The data were consistent with those previously reported.²³ ^1H NMR (400 MHz, D_2O): δ = 2.83-2.89 (m, 8H, CH_2), 2.96-3.03 (m, 8H, CH_2) ppm.

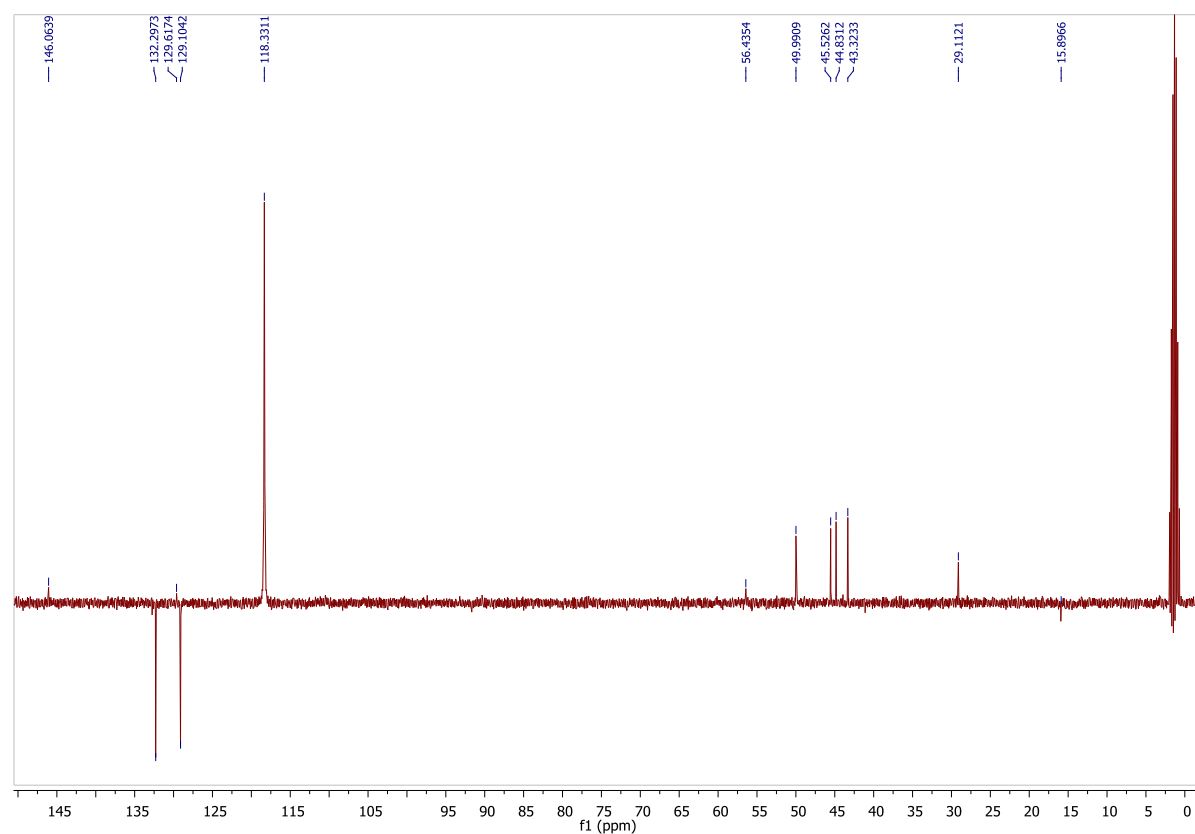
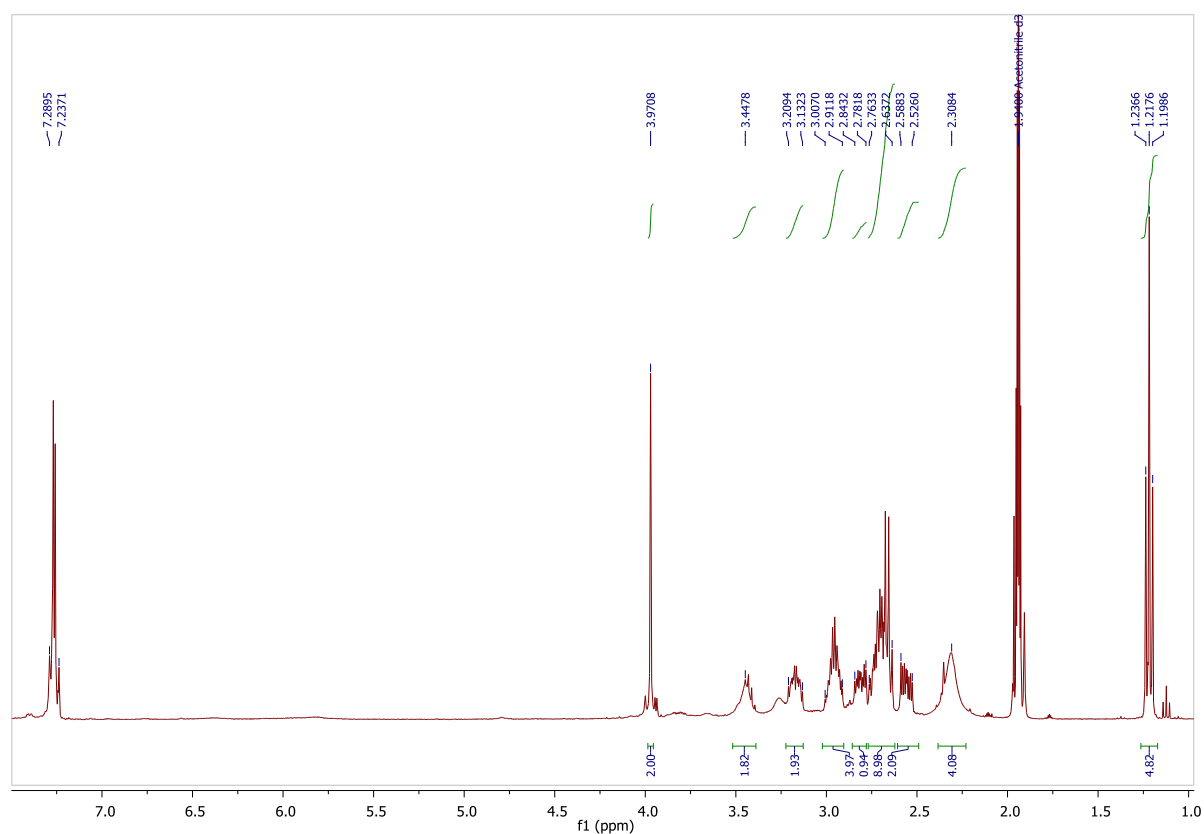
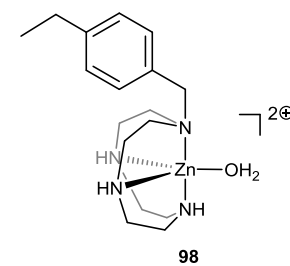
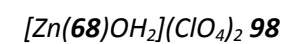


Figure 6.30 - ¹H and ¹³C NMR spectra of **98**.



Following the general procedure, cyclen derivative **68** (0.271 g, 0.929 mmol) and Zn(ClO₄)₂·6H₂O (0.346 g, 0.929 mmol) in MeCN yielded **98** as a beige solid (0.470 g, 88%). ¹H NMR (400 MHz, CD₃CN): δ= 1.22 (t, *J*= 7.6, 3H, CH₃)*, 2.31 (bs, 4H, CH₂), 2.53-2.59 (m, 2H, CH₂), 2.64-2.76 (m, 9H, CH₂), 2.78-2.84 (m, 1H, CH₂), 2.91-3.01 (m, 4H, CH₂), 3.13-3.21 (m, 2H, CH₂), 3.44 (bs, 2H, CH₂), 3.97 (s, 2H, N-CH₂), 7.23-7.29 (m, 6H, Ar-H) ppm; ¹³C NMR (DEPT 135, 100 MHz, CD₃CN): δ= 15.9, 29.1, 43.3, 44.8, 45.5, 50.0, 56.4, 118.3, 129.1, 132.3, 146.1 ppm; HRMS (EI) calcd for C₁₇H₃₀N₄Zn [M+H]²⁺ 177.0875, found 177.0878.

*Footnote: an impurity is present

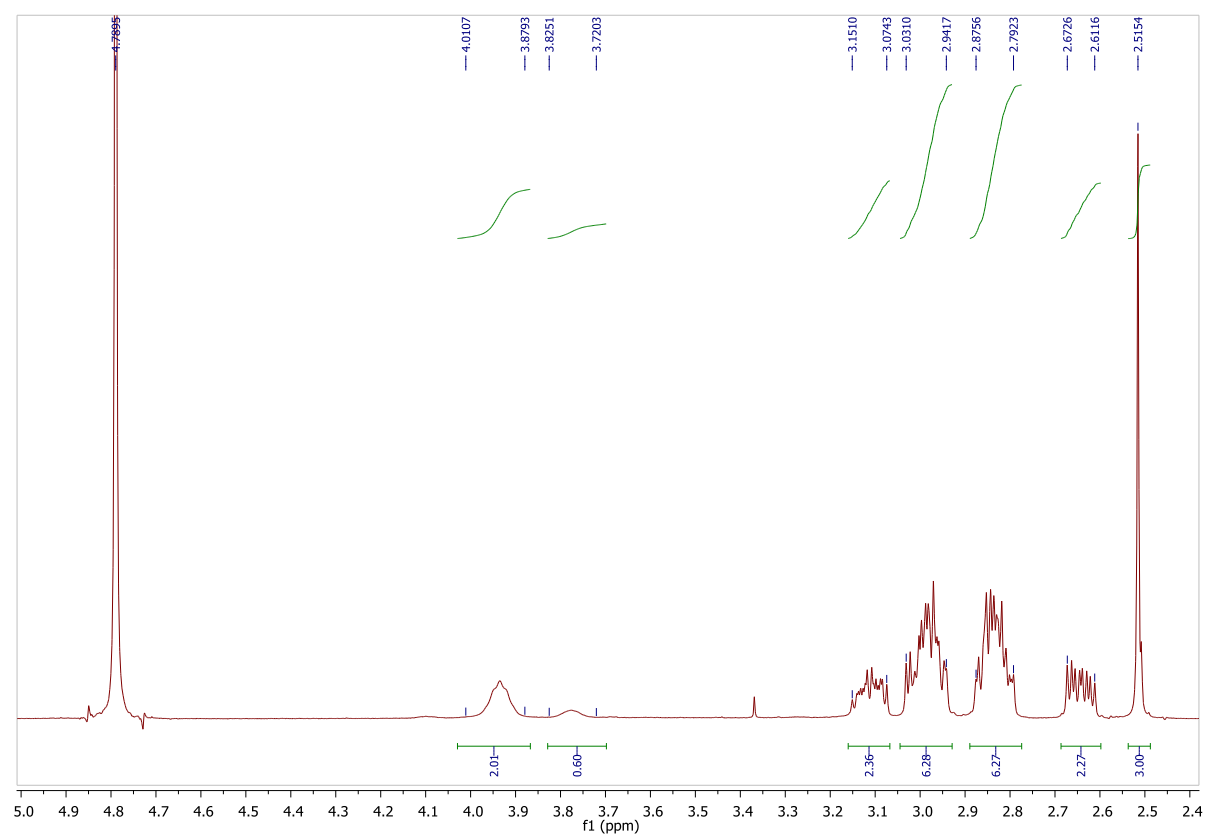
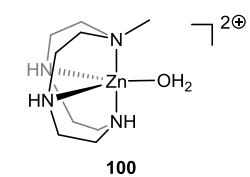
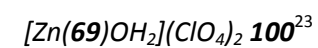


Figure 6.31 - ^1H NMR spectrum of **100**.



Following the general procedure, cyclen derivative **69** (85 mg, 0.457 mmol) and $\text{Zn}(\text{ClO}_4)_2 \cdot 6\text{H}_2\text{O}$ (0.170 g, 0.457 mmol) in MeOH yielded **100** as a beige solid (0.100 g, 81%). The data were consistent with those previously reported.²⁴ ^1H NMR (400 MHz, D_2O): δ = 2.51 (s, 3H, CH_3), 2.61-2.67 (m, 2H, CH_2), 2.79-2.87 (m, 6H, CH_2), 2.94-3.03 (m, 6H, CH_2), 3.07-3.15 (m, 2H, CH_2), 3.72-3.82 (m, 1H, NH), 3.88-4.01 (m, 2H, NH) ppm.

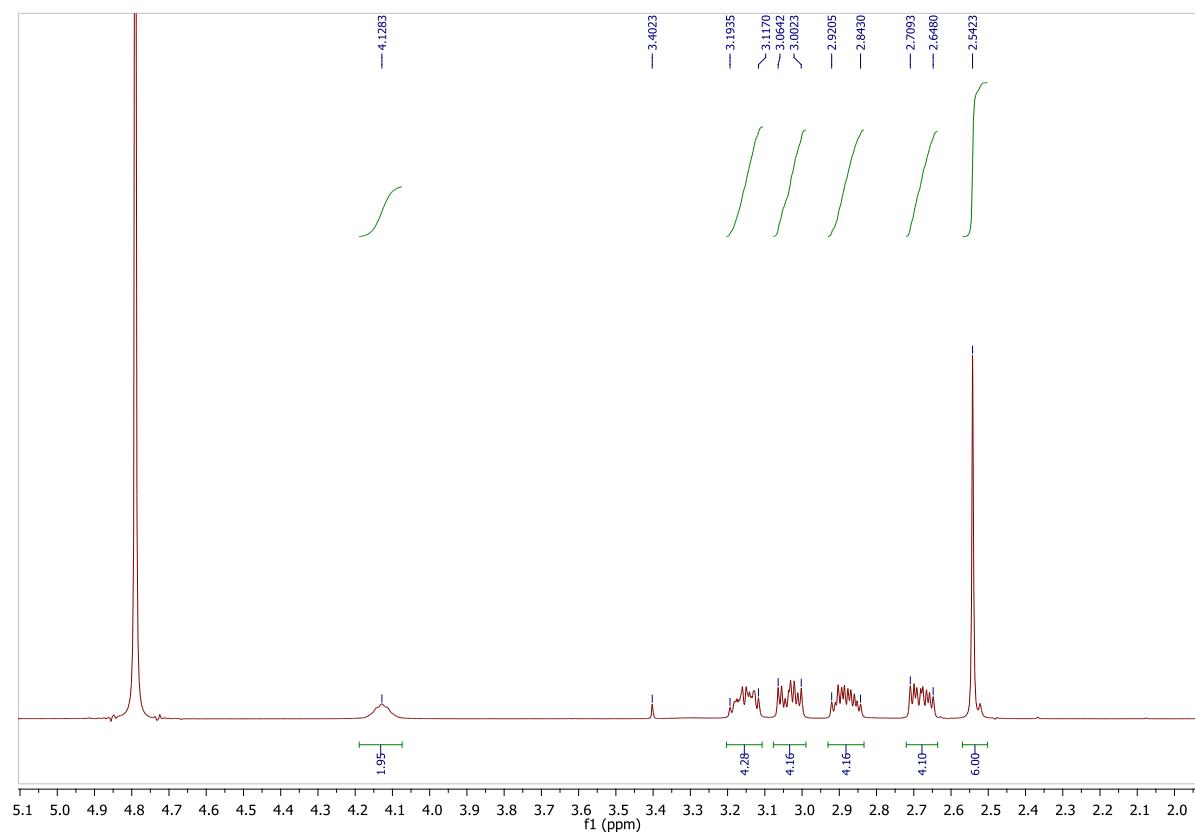
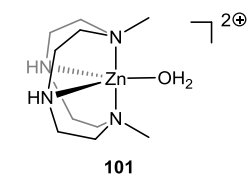
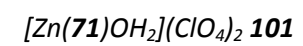


Figure 6.32 - ^1H NMR spectrum of **101**.



Following the general procedure, cyclen derivative **71** (0.100 g, 0.499 mmol) and $\text{Zn}(\text{ClO}_4)_2 \cdot 6\text{H}_2\text{O}$ (0.186 g, 0.499 mmol) in MeOH yielded **101** as a beige solid (0.212 g, 85%). ^1H NMR (400 MHz, D_2O): δ = 2.54 (s, 6H, CH_3), 2.65-2.71 (m, 4H, CH_2), 2.84-2.92 (m, 4H, CH_2), 3.00-3.06 (m, 4H, CH_2), 3.12-3.19 (m, 4H, CH_2), 4.13 (bs, 2H, NH) ppm.

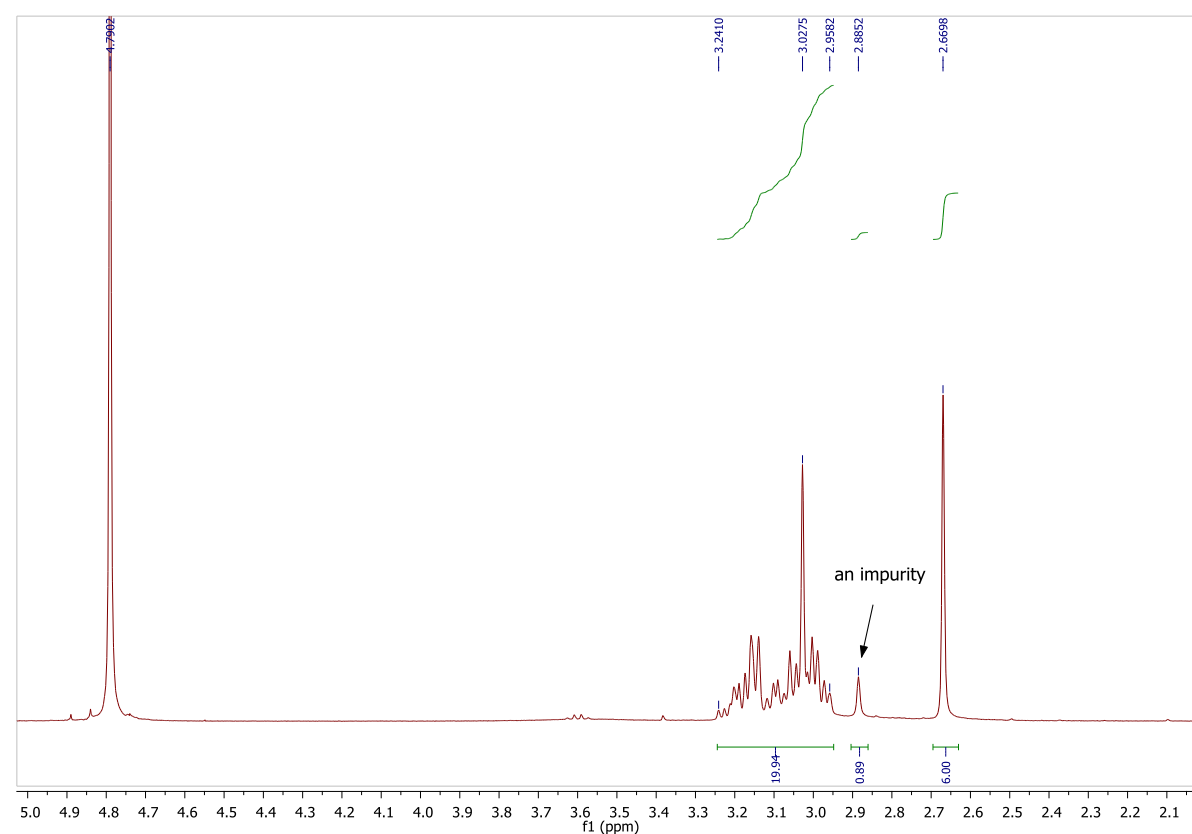
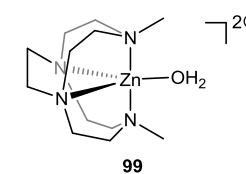
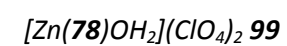


Figure 6.33 - ^1H NMR spectrum of **99**.



Following the general procedure, cyclen derivative **78** (0.109 g, 0.48 mmol) and $\text{Zn}(\text{ClO}_4)_2 \cdot 6\text{H}_2\text{O}$ (0.186 g, 0.50 mmol) in MeOH yielded **99** as a beige solid (0.170 g, 70%). ^1H NMR (400 MHz, D_2O): δ = 2.67 (s, 6H, CH_3), 2.96-3.24 (m, 20H, CH_2) ppm.

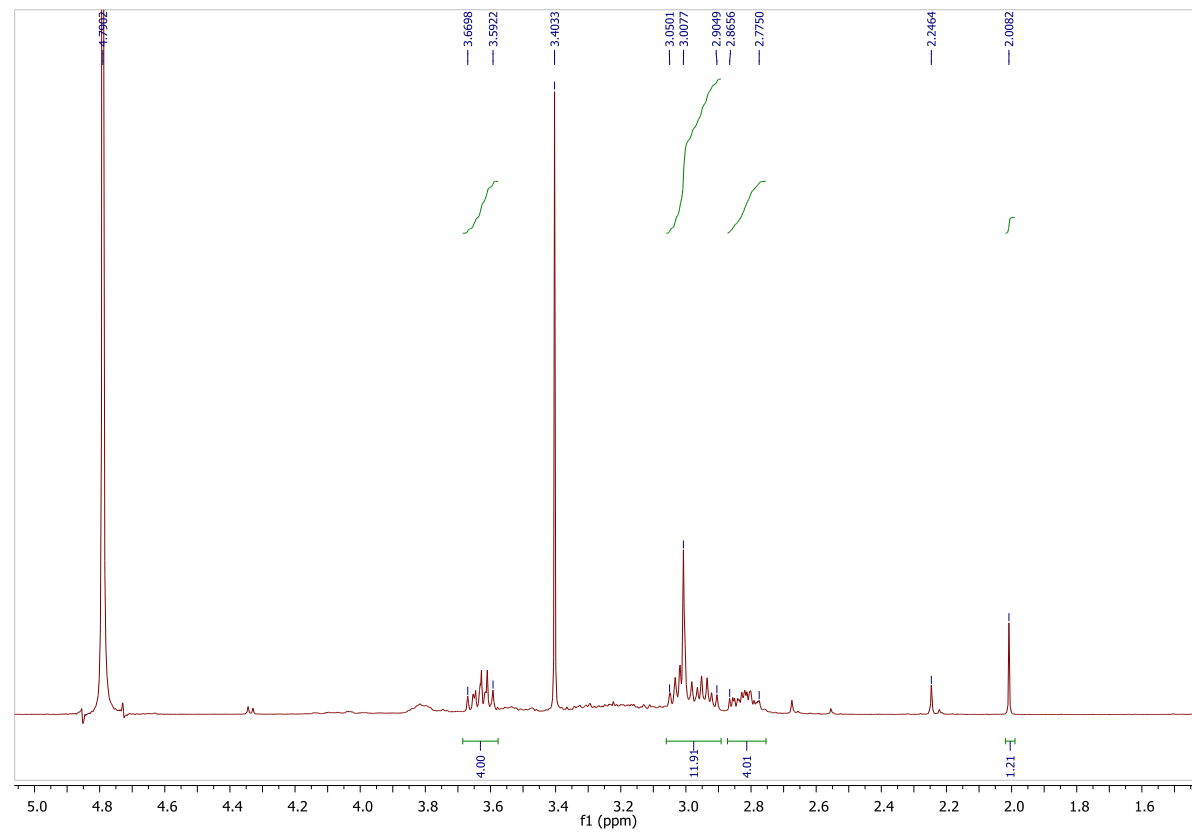
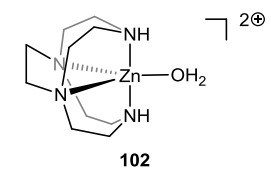
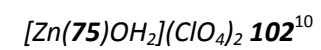


Figure 6.34 - ^1H NMR spectrum of **102**.



Following the general procedure, cyclen derivative **75** (0.428 g crude (contained 0.115 g ligand, 0.58 mmol) and $\text{Zn}(\text{ClO}_4)_2 \cdot 6\text{H}_2\text{O}$ (0.216 g, 0.58 mmol) in MeOH yielded **102** as a beige solid that contained 30% of the *N*-acetyl impurity **83** (0.117 g, 47%- yield of the target complex in the crude mixture). Representative ^1H NMR (400 MHz, D_2O) data for the mixture of **102** as follows: δ = 2.77 (m, 4H, CH_2), 2.90-3.05 (m, 12H, CH_2), 3.59-3.67 (m, 4H, CH_2) ppm.

6.3. Kinetics

The hydrolysis of *p*-nitrophenyl phosphate **7** (NPP) was monitored using UV-Vis spectroscopy: (λ_{max} = 405 nm, ϵ_{max} = 16963 M⁻¹cm⁻¹, in HEPES buffer (10 mM, pH 7.2). The chemical yield of the reaction was determined after a fixed time by converting the resulting absorbance into the true concentration values according to Lambert-Beer Law. The pH of each hydrolysis reaction was measured after 48 hours and 9 days.

6.3.1. Determination of the Amount of Product Formed in the Uncatalysed Reaction

A known amount of substrate was taken from the substrate stock solution and introduced into a glass test tube containing the reaction medium HEPES (10.0 mM, pH 7.2). The time at which the injection was made was taken as $t = 0$ min, and the absorbance of the sample recorded at 405 nm. The test tube was sealed with a rubber septum and placed in a water bath at 25 °C. The solutions were monitored at known time intervals and the absorbance values converted into concentration of product **6** produced according to the Lambert-Beer Law. The yield was taken as a percentage, from the known amount of substrate in solution.

6.3.2. Determination of the Amount of Product Formed in the Presence of the Small-Molecule Metal Complexes Used in Excess.

6.3.2.1. Small-Molecule Aqua-Hydroxo Co(III) Complexes

Stock solutions (5 mM) of di-chloride complexes **85**, **87**, **91**, **92**, **89**, and **95** were prepared in HEPES (10 mM, pH 7.2) in vials equipped with a magnetic stirring bar. The cobalt complexes were activated to the hydrolytically active aqua-hydroxo species **16**, **50**, **17**, **18**, **54** and **55** respectively by addition of 2 equivalents of NaOH (0.1 M).¹⁴ Activation of **85** and **95** occurred rapidly as shown by the almost immediate change in the λ_{max} (ϵ) visible absorption band in **85** from 563 nm (148 dm³mol⁻¹cm⁻¹) to 520 nm (148 dm³mol⁻¹cm⁻¹) and in **95** from 543 nm (100 dm³mol⁻¹cm⁻¹) to 530 nm (100 dm³mol⁻¹cm⁻¹), which was accompanied by colour change from violet to light red and pink respectively. Activation of complexes **87**, **91**, **92** and **89** required stirring at 50°C for 1 hour followed by 1 hour at RT. This conversion from di-chloride (589-570 nm region) to aqua-hydroxo species (554-540 nm region) was also accompanied by a significant colour change from violet to pink (Chapter 2, section 2.3.3.3). The hydrolysis reaction was carried out with the cobalt complex used in 3 fold excess (1200 μ M) over the NPP substrate **7** (400 μ M). Each reaction sample was prepared by adding an aliquot from the Co(III) aqua-hydroxo complex stock solution into a glass test

tube containing HEPES buffer and completing the total volume (2.5 mL) with the addition of substrate at $t = 0$ min. The test tubes were sealed and the samples were checked for absorbance at known time intervals and the obtained values were converted into yield of product **6** formed (%). The pH of the reaction solutions did not change significantly during the course of the hydrolysis reaction ($\text{pH } 7.2 \pm 0.2$). The final product % obtained was corrected for the background hydrolysis reaction. Small molecule Co(III) complexes showed the following % of substrate **7** being hydrolysed after 48 hours: **16**- 75%, **50**- 68%, **17**- 66%, **18**- 8%, **55**-4% and **54**- <1%.

6.3.2.2. Small-Molecule Zn(II) Complexes

Stock solutions (5 mM) of Zn(II) complexes **21**, **98**, **99**, **100**, **101**, and **102** were prepared in HEPES (10 mM, pH 7.2) in vials. The hydrolysis reaction was carried out where the Zn(II) complex was used in 3 fold excess (1200 μM) over the NPP and BNPP substrates (400 μM). Each reaction sample was prepared by adding an aliquot from the Zn(II) complex stock solution into a glass test tube containing an appropriate buffer and completing the total volume (2.5 mL) with the addition of substrate at $t = 0$ min. The test tubes were sealed and the samples were checked for absorbance at known time intervals. The hydrolysis of NPP substrate **7** was carried out in HEPES at pH 7.2. The pH of the reaction solutions did not change significantly during the course of the hydrolysis reaction ($\text{pH } 7.2 \pm 0.2$). As expected, all six cyclen-based Zn(II) complexes used in excess showed no activity in promoting hydrolysis of **7**, in HEPES (10 mM, pH 7.2) at 25°C after 48 hours, as no appreciable absorbance at 405 nm was detected. The hydrolytic activity of Zn(II) complex **21** and **100** towards mono-anionic BNPP **8** was tested at pH 9.0 (50 mM CAPS buffer) and pH 10.0 (50 mM CPASO buffer) at 35°C.²⁵ The pH of the reaction solutions did not change significantly during the course of the hydrolysis reaction ($\text{pH } 9.0 \pm 0.2$ and 10.0 ± 0.2). As expected, both complexes showed no appreciable absorbance at 405 nm in the BNPP hydrolysis after 48 hours at pH 9.0 and 10.0 at 35°C.

6.3.3. Kinetic Studies with Nanogels **P1** and **P2** and Small-Molecule Co(III) Complexes **16** and **50**

All the kinetic studies data described in this section were obtained using small-molecule Co(III) complexes and nanogels at 100 μM cobalt concentration.

6.3.3.1. Small-Molecule Co(III) Complexes **16** and **50**

In order to compare the amount of product produced after 9 days in the hydrolysis of substrate **7** promoted by **16** and **50** complexes, stock solutions (5 mM) of **16** and **50** were prepared in HEPES (10 mM, pH 7.2) and activated to form the aqua-hydroxo species using NaOH (0.1 M) as described earlier. The hydrolysis reaction was carried out under first order conditions where the cobalt complex was used in catalytic amounts (100 μ M) over the NPP substrate **7** (442 μ M). Each reaction sample was prepared by adding an aliquot from the Co(III) aqua-hydroxo complex stock solution into a test tube containing HEPES buffer and completing the total volume (3 mL) with the addition of substrate at $t = 0$ min. A solution containing only substrate **7** in HEPES was also prepared to determine the amount of product formed in the uncatalysed reaction after 9 days. The test tubes were sealed and the samples were checked for absorbance at known time intervals and the obtained values were converted into the amount of product formed (μ M) using the Lambert-Beer Law. The pH of the reaction solutions did not change significantly during the course of the hydrolysis reaction (pH 7.2 \pm 0.2). The final amount of product (μ M) obtained was corrected for the background reaction.

6.3.3.2. Nanogels **P1** and **P2**

The effect of the nanogels on the absorbance of the product was previously tested by Dr. Jorge^{11,26} measuring the absorbance of a known concentration of *p*-nitrophenol **6** in 1.00 mg/mL solutions of the nanogels. No significant increase or decrease of the absorbance values was detected and therefore no corrections were necessary. For the catalytic tests, 2.00 mg/mL stock solutions of the polymers were used in HEPES (10.0 mM, pH 7.2). The polymers had previously been assessed by Dr. Jorge by FAAS so that the cobalt content in each sample was known.¹¹ Known amounts of **P1** and **P2** were measured into a separate test tubes containing HEPES buffer. The remaining volume was completed with the substrate **7** to make up a 3 mL sample with a 100 μ M concentration of cobalt. Solutions were prepared using substrate concentrations at 442 μ M and at 664 μ M. Upon addition of the substrate, the time was set to zero and the absorbance was measured. As for the uncatalysed reaction, the absorbance values were monitored at given time intervals and solutions were kept in sealed test tubes in a water bath at 25°C between measurements. The pH of the samples was always recorded after the measurement to allow the correction of the ϵ values and, consequently, the product concentration.

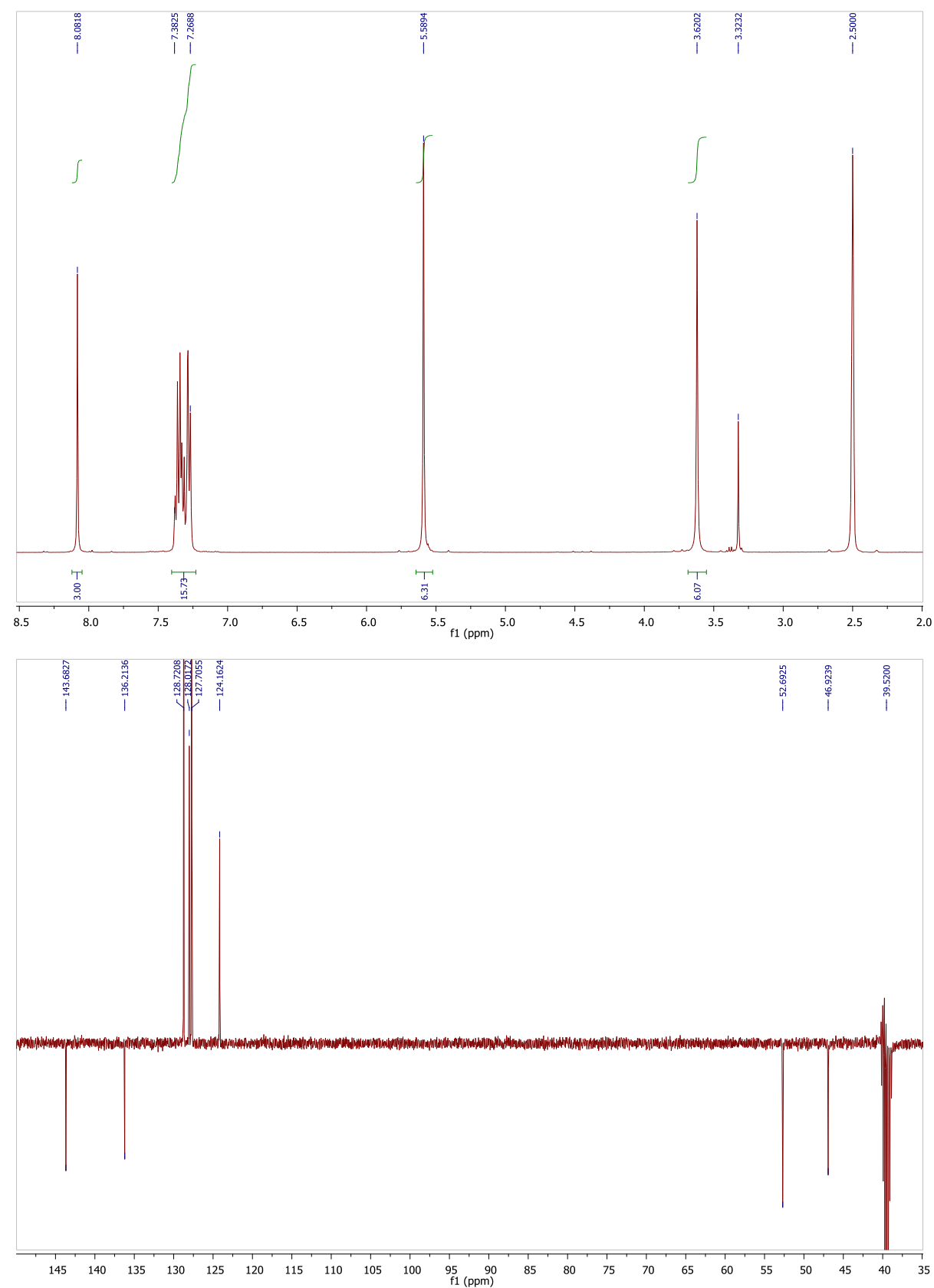
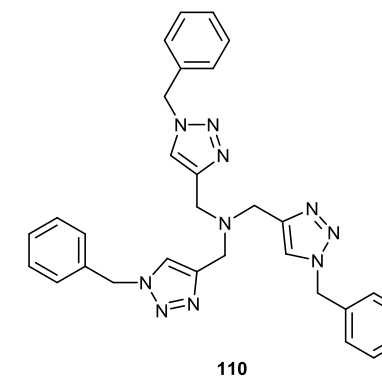


Figure 6.35 - ^1H and ^{13}C NMR spectra of **110**.

6.4. Synthesis of the 'Click'-based Compounds

6.4.1. Synthesis of the 'Click'-based Tripodal Ligands

*Tris((1-benzyl-1H-1,2,3-triazol-4yl)methyl)amine (TBTA) 110*²⁷



$\text{Cu}(\text{OAc})_2 \cdot \text{H}_2\text{O}$ (15 mg, 0.075 mmol) was dissolved in MeCN (10.0 mL) until a bright blue solution was obtained. Tripropargylamine **122** (539 μL , 3.75 mmol) and benzyl azide **123** (796 μL , 6.37 mmol) were dissolved in MeCN (5.0 mL) in a separate flask and this solution was added to the reaction flask. Sodium ascorbate (15 mg, 0.075 mmol) was dissolved in water (2.0 mL) and the resulting solution was added in one portion to the reaction flask. The reaction mixture was then stirred at RT for 30 min and then heated at 45°C for 5 h. A second portion of **123** (140 μL , 1.12 mmol) was added and reaction mixture was heated at 45°C for an additional 20 h. The reaction was followed by TLC (1:4 EtOAc/Pet.Ether), which showed an incomplete consumption of reaction intermediates. Therefore, an additional portion of **123** (140 μL , 1.12 mmol) was added to the reaction mixture and it was allowed to proceed for another 24 h. Upon complete conversion of reaction intermediates to a single product (determined by TLC), the reaction mixture was then concentrated to dryness on a rotary evaporator. The crude residue was then dissolved in a mixture of DCM/ $\text{NH}_3(\text{aq})$ (20 mL 1:1) and stirred for 15 min to remove unreacted copper salts. The aqueous layer was then extracted with DCM (30 mL x 3). The organic fractions were combined, washed with a solution of NH_3 (aq, 35% w/w) and brine (1:1 v/v, 15 mL x 2), dried over MgSO_4 and the solvent removed *in vacuo* to obtain a crude yellow oil. This oil was then dissolved in DCM (5 mL) and gradual addition of Et_2O to this solution resulted in the formation of a beige precipitate, which was isolated by filtration. This process was repeated two more times until no more precipitate was formed. Combined portions of the beige powder were dried *in vacuo* to afford the desired product (1.98 g, quantitative yield). The ^1H and ^{13}C NMR data were consistent with those previously reported; IR data is additionally present.²⁷ m.p.

132-136 °C (lit. m.p.: 140-144 °C²⁷); ¹H NMR (400 MHz, DMSO-d₆): δ= 3.62 (s, 6H, N-CH₂), 5.59 (s, 6H, benzyl-CH₂), 7.27-7.38 (m, 15H, Ar-H), 8.08 (s, 3H, CH_{triazole}) ppm; ¹³C NMR (DEPT 135, 100 MHz, DMSO-d₆): δ= 46.9, 52.7, 124.2, 127.7, 128.0, 128.7, 136.2, 143.7 ppm; IR: ν_{max} 3064, 1410, 1453, 1350, 1217, 1130, 1048, 930, 829 cm⁻¹.

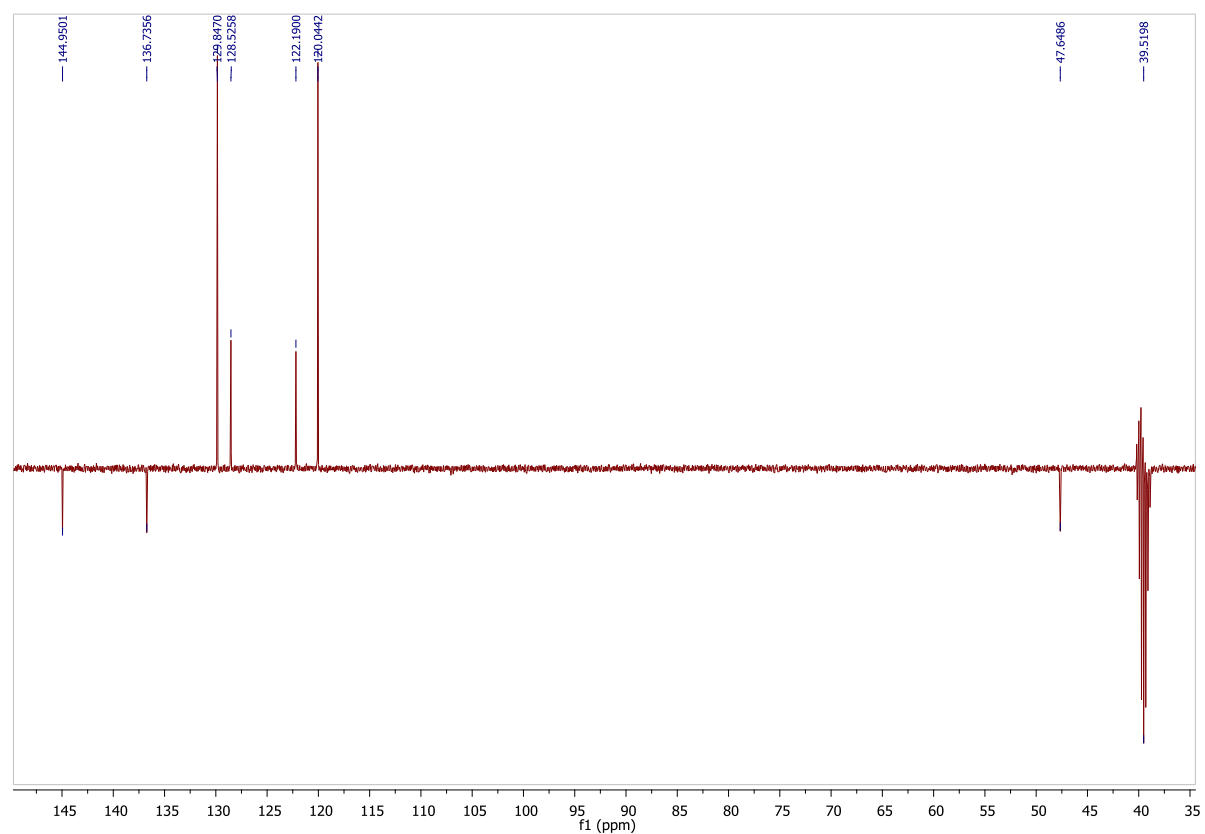
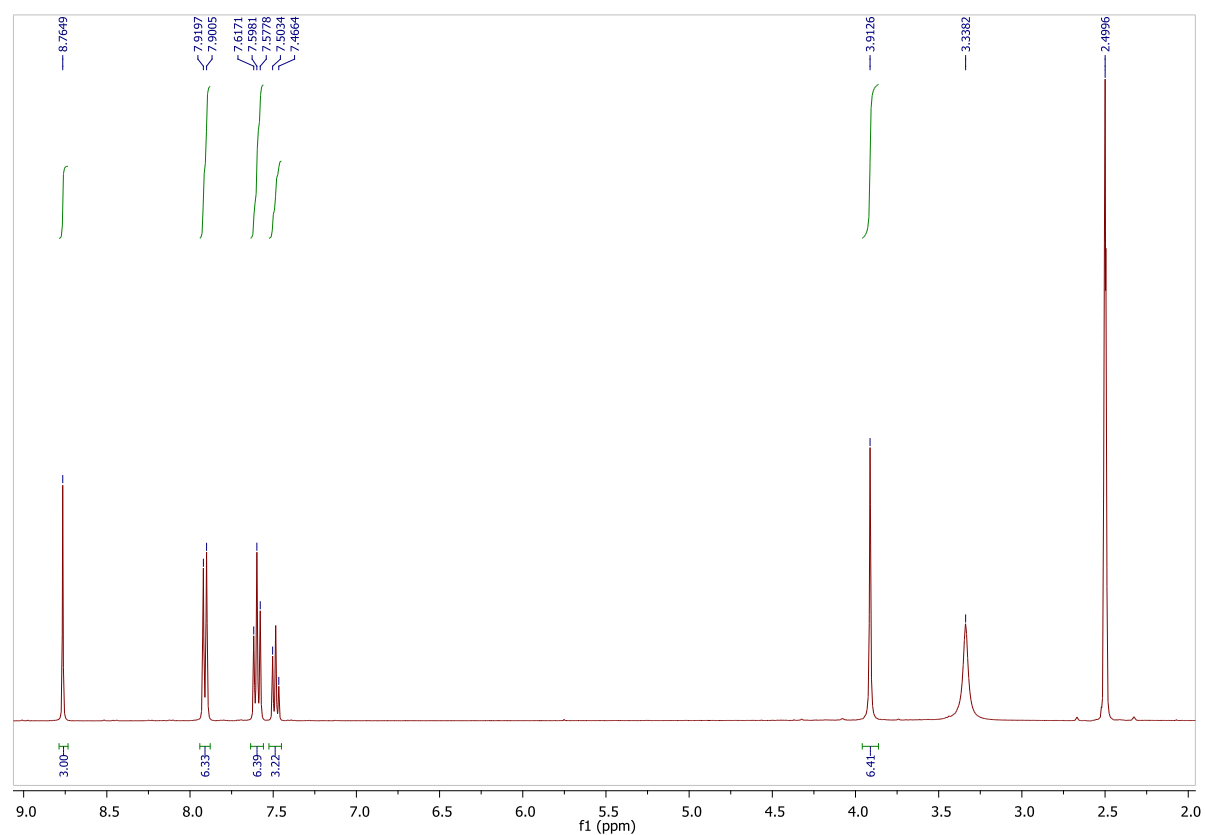
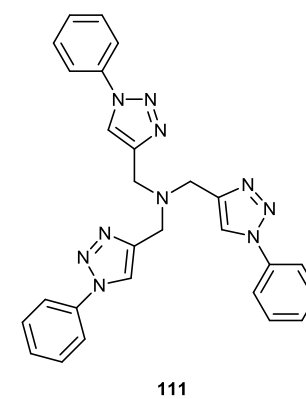


Figure 6.36 - ^1H and ^{13}C NMR spectra of **111**.

Tris((-phenyl-1H-1,2,3-triazol-4-yl)methyl)amine (TPTA) **111**²⁸



Aniline **125** (1.36 mL, 15 mmol) was dissolved in MeCN (25 mL) and cooled to 0°C in an ice bath. To this stirred mixture, *t*-BuONO (2.67 mL, 22.48 mmol) was added dropwise followed by TMSN₃ (2.38 mL, 18.00 mmol). The resulting solution was left to reach RT and was stirred overnight for 20 h. Reaction progress was followed by TLC (1:1 EtOAc/Pet.Ether), which indicated the absence of the aniline and the presence of the corresponding azide **126**. Tripropargylamine **122** (432 μL , 3.00 mmol) was then added to this solution. This was followed by CuSO₄·5H₂O (0.187 g, 0.75 mmol) and sodium ascorbate (0.888 mg, 4.48 mmol) in water (10 mL) and the resulting reaction mixture was left to stir at RT for another 20 h. A portion of beige solid precipitated from the solution and was isolated by filtration. The remaining filtrate was reduced to dryness on a rotary evaporator, dissolved in a mixture of DCM/NH₃(aq, 35% w/w) (1:1, 20 mL) and stirred for 15 minutes. The aqueous layer was then further extracted with DCM (30 mL x 3), organics were combined, washed with NH₃(aq, 35% w/w) and brine mixture (1:1 v/v 20 mL), dried over MgSO₄, and the solvent removed *in vacuo* to yield a further portion of beige solid which was combined with the first portion to afford pure **111** (1.32 g, 90%). The data were consistent with those previously reported.²⁸ m.p. 155-158 °C (lit. m.p.: 149-150 °C²⁸); ^1H NMR (400 MHz, DMSO-*d*₆): δ = 3.91 (s, 6H, N-CH₂), 7.47-7.50 (m, 3H, Ar-H), 7.50-7.62 (m, 6H, Ar-H), 7.90-7.92 (m, 6H, Ar-H), 8.76 (s, 3H, CH_{triazole}) ppm; ^{13}C NMR (DEPT 135, 100 MHz, DMSO-*d*₆): δ = 47.6, 120.0, 122.2, 128.5, 129.8, 136.7, 144.9 ppm; IR: ν_{max} 3056, 2843, 1598, 1502, 1334, 1220, 1074, 1047, 824 cm⁻¹; HRMS (EI) calcd for C₂₇H₂₅N₁₀ [M+H]⁺ 489.2258, found: 489.2244.

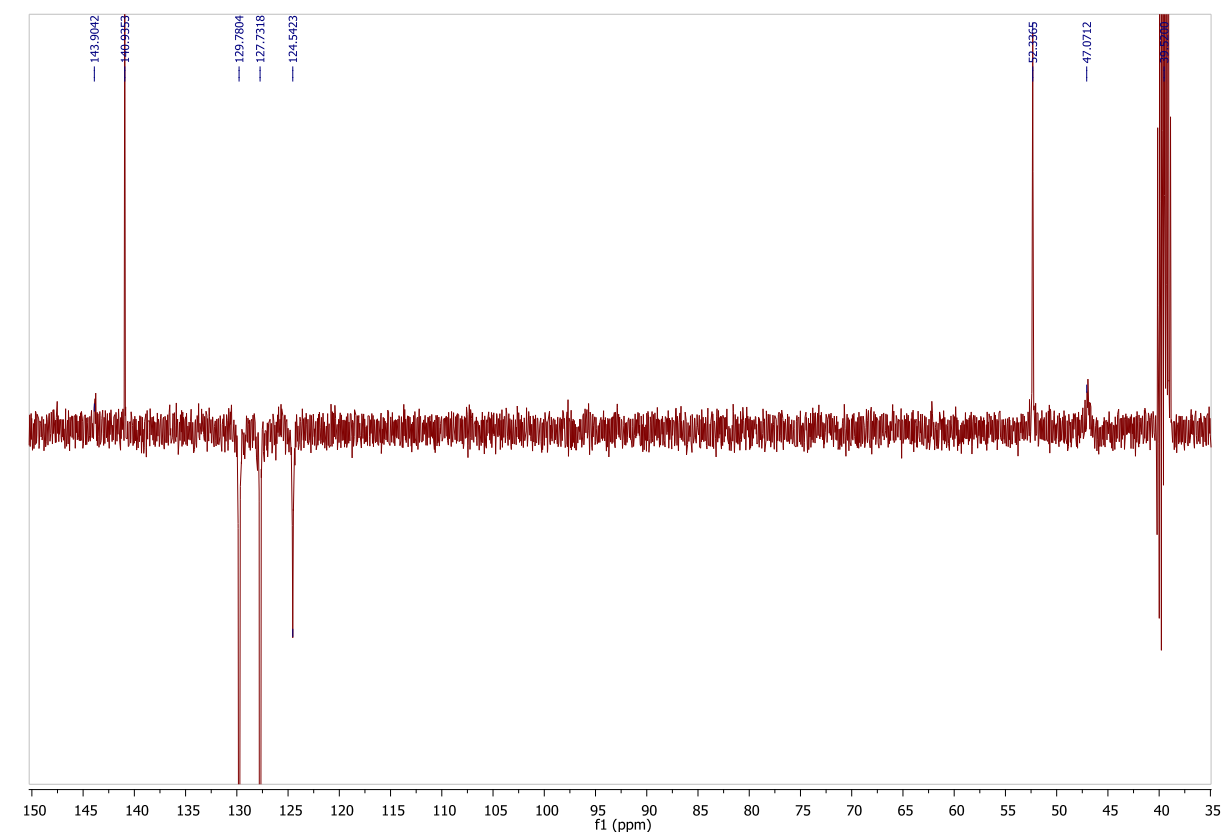
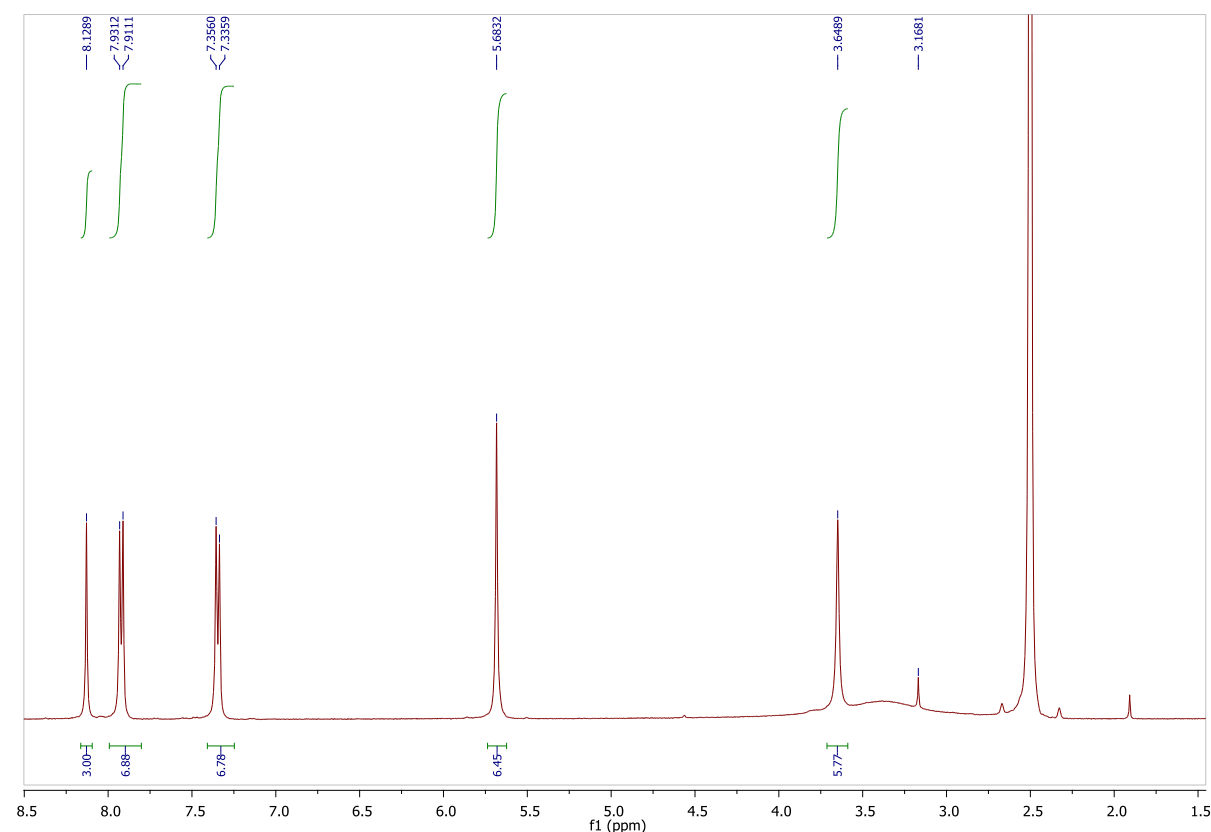
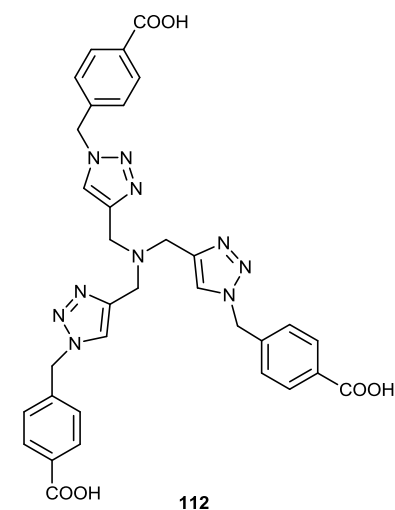


Figure 6.37 - ^1H and ^{13}C NMR spectra of **112**.

4,4',4''-(((Nitrilotris(methylene))))tris(1H-1,2,3-triazole-4,1-diyil)))tris(methylene))tribenzoic acid (TCTA) **112**²⁹



KHCO_3 (0.494 g, 4.95 mmol) was dissolved in H_2O : t -BuOH (1:2, 20 mL). *p*-Azidomethyl benzoic acid **128** (0.800 mg, 4.51 mmol) was added with stirring in order to dissolve the acid, followed by tripropargylamine **122** (216 μL , 1.50 mmol) and sodium ascorbate (14.8 mg, 0.075 mmol, 5 mol%). $\text{CuSO}_4 \cdot 5\text{H}_2\text{O}$ (3.74 mg, 0.015 mmol, 1 mol%) was then added to initiate the reaction, which turned briefly pale green and then a lighter yellow. The reaction mixture was left to stir overnight at 45 $^\circ\text{C}$, and was then reduced in volume and diluted with water (20 mL). A beige solid precipitated with gradual acidification of this aqueous solution with glacial AcOH to *ca.* pH 3-4. The resulting precipitate was isolated by filtration, boiled briefly in MeOH (10 mL), cooled to -10 $^\circ\text{C}$, collected by filtration and dried *in vacuo* to give **112** as a beige powder (0.900 g, 90%). The ^1H NMR data were consistent with those previously reported;²⁹ m.p. and HRMS are additionally reported. m.p. 193-196 $^\circ\text{C}$; ^1H NMR (400 MHz, DMSO-d_6): δ = 3.65 (s, 6H, N- CH_2), 5.68 (s, 6H, benzyl- CH_2), 7.35 (ap.d, 6H, Ar-H), 7.92 (ap.d, 6H, Ar-H), 8.13 (s, 3H, $\text{CH}_{\text{triazole}}$) ppm; ^{13}C NMR (DEPT 135, 100 MHz, DMSO-d_6): δ = 47.1, 52.3, 124.5, 127.7, 129.8, 140.9, 143.9 ppm; HRMS (EI) calcd for $\text{C}_{33}\text{H}_{29}\text{N}_{10}\text{O}_6$ $[\text{M}+\text{H}]^+$ 661.2277, found: 661.2266.

6.4.2. Synthesis of the ‘Click’-based Coordination Complexes

6.4.2.1. Synthesis of the Chloride Complexes of Ligands **110** and **111**: General Procedure⁹ as Demonstrated by the Synthesis of [Co(**110**)Cl]Cl **109**³⁰

For the calculations of yields, magnetic moments by the Evan’s NMR method and ϵ by the Lambert-Beer Law it is assumed that the bulk stoichiometry of the complexes prepared is either [M(L)Cl]Cl or [M(L)](ClO₄)₂, unless otherwise stated.

TBTA **110** (50 mg, 0.094 mmol) and CoCl₂·6H₂O (22 mg, 0.094 mmol) were dissolved in MeCN (5 mL) and the solution was stirred at RT for 16 h. Any precipitate in the reaction mixture was removed by filtration. The resulting reaction solution was reduced in volume and Et₂O (20 mL) was then added causing the precipitation of a violet powder, which was collected by filtration, washed with Et₂O (10 mL) and dried *in vacuo* to afford **109** as a shiny violet powder (62, 84%). m.p. 175-178°C; μ_{eff} = 4.2 μ_{B} ; IR: ν_{max} 3094, 2826, 1542, 1447, 1337, 1230, 1140, 1082, 1041, 997, 964, 920, 879, 802 cm⁻¹; UV-Vis (MeCN): λ_{max} (ϵ) = 510 (210), 589 (188), 610 (280), 631 (274), 663 (188), 691 nm (200 dm³mol⁻¹cm⁻¹); HRMS (EI) calcd for C₃₀H₃₀N₁₀CoCl [M+H]⁺ 624.1670, found: 624.1655.

[Co(**111**)Cl]Cl **137**

Following the general procedure, TPTA **111** (100 mg, 0.204 mmol) and CoCl₂·6H₂O (48.5 mg, 0.204 mmol) in MeOH (10 mL) yielded complex **137** as a violet solid (100 mg, 79%). m.p. 210-212 °C; μ_{eff} = 4.6 μ_{B} ; IR: ν_{max} 3096, 1595, 1498, 1465, 1351, 1249, 1192, 1083, 991, 960 cm⁻¹; UV-Vis (MeCN): λ_{max} (ϵ) = 517 (202), 590 (232), 613 (236), 634 (265), 660 (216), 688 nm (204 dm³mol⁻¹cm⁻¹); HRMS (EI) calcd for C₂₇H₂₄N₁₀CoCl [M+H]⁺ 582.1200, found: 582.1187.

[Cu(**110**)Cl]Cl **129**³¹

Following the general procedure, **110** (100 mg, 0.188 mmol) and CuCl₂·2H₂O (32.0 mg, 0.188 mmol) in MeCN (10 mL) yielded complex **129** as a green solid (67.5 mg, 54 %). m.p. 198-200 °C; μ_{eff} = 2.6 μ_{B} ; IR: ν_{max} 3376, 3096, 1634, 1492, 1455, 1327, 1238, 1138, 1074, 956, 826 cm⁻¹; UV-Vis (MeCN): λ_{max} (ϵ) = 360 (920), 650-700 nm- very broad (168 dm³mol⁻¹cm⁻¹); HRMS (EI) calcd for C₃₀H₃₀N₁₀CuCl [M+H]⁺ 628.1634, found: 628.1620.

[Cu(111)Cl₂] 138

Following the general procedure, **111** (100 mg, 0.204 mmol) and CuCl₂·2H₂O (34.8 mg, 0.204 mmol) in MeOH (10 mL) yielded complex **138** as a green solid (110 mg, 86%). Single crystals of [Cu(**111**)Cl₂] were isolated from the solution of **138** in CD₃CN/MeCN/TMS. m.p. 160-162 °C; μ_{eff} = 1.7 μ_{B} ; IR: ν_{max} 3434, 3068, 1595, 1499, 1456, 1348, 1254, 1192, 1082, 1046, 911, 831 cm⁻¹; UV-Vis (MeCN): λ_{max} (ϵ) = 360 (922), 650-700 nm- very broad (140 dm³mol⁻¹cm⁻¹); HRMS (EI) calcd for C₂₇H₂₄N₁₀CuCl [M+H]⁺ 586.1164, found: 586.1160.

[Ni(110)(OH₂)Cl]Cl 130

Following the general procedure, **110** (100 mg, 0.188 mmol) and NiCl₂·6H₂O (44.7 mg, 0.188 mmol) in MeCN (10 mL) yielded complex **130** as a crystalline green solid (101.5 mg, 82%). Slow diffusion of Et₂O into a MeOH solution of **130** resulted in single crystals of [Ni(**110**)(OH₂)Cl]Cl. m.p. 187-190 °C; μ_{eff} = 2.8 μ_{B} ; IR: ν_{max} 3058, 1618, 1492, 1455, 1331, 1248, 1135, 1074, 960, 804 cm⁻¹; UV-Vis (MeCN): λ_{max} (ϵ) = 367 (69), 580 (17), 790 (7), ~900 nm (11 dm³mol⁻¹cm⁻¹); HRMS (EI) calcd for C₃₀H₃₀N₁₀NiCl [M+H]⁺ 623.1691, found: 623.1689.

[Ni(111)Cl]Cl 139

Following the general procedure, **111** (50.0 mg, 0.102 mmol) and NiCl₂·6H₂O (24.2 mg, 0.102 mmol) in MeOH (5 mL) with a reaction time of 16 h yielded complex **139** as a crystalline green solid (50 mg, 80%). m.p. 278-280 °C; μ_{eff} = 2.9 μ_{B} ; IR: ν_{max} 3368, 3065, 1596, 1499, 1465, 1333, 1255, 1194, 1050, 992, 954, 877 cm⁻¹; UV-Vis (MeCN): λ_{max} (ϵ) = 360 (41), 582 (16), 785 (8), ~900 nm (12 dm³mol⁻¹cm⁻¹); HRMS (EI) calcd for C₂₇H₂₄N₁₀NiCl [M+H]⁺ 581.1222, found: 581.1212.

[Mn(110)Cl]Cl 131

Following the general procedure, **110** (150 mg, 0.282 mmol) and MnCl₂·4H₂O (55.8 mg, 0.282 mmol) in MeOH (15 mL) yielded complex **131** as a beige solid (155 mg, 84%). m.p. 123-125 °C; μ_{eff} = 5.8 μ_{B} ; IR: ν_{max} 3062, 2951, 1496, 1455, 1330, 1230, 1136, 969, 803 cm⁻¹; HRMS (EI) calcd for C₃₀H₃₀N₁₀MnCl [M+H]⁺ 620.1718, found: 620.1731.

[Mn(111)Cl]Cl 140

Following the general procedure, **111** (100 mg, 0.204 mmol) and MnCl₂·4H₂O (40.4 mg, 0.204 mmol) in MeOH (10 mL) yielded complex **140** as a beige solid (78 mg, 62%). m.p. 230-

235 °C; $\mu_{\text{eff}} = 6.7 \mu_{\text{B}}$; IR: ν_{max} 3430, 3090, 1595, 1498, 1456, 1353, 1245, 1192, 1066, 962, 808 cm^{-1} ; HRMS (EI) calcd for $\text{C}_{27}\text{H}_{24}\text{N}_{10}\text{MnCl}$ $[\text{M}+\text{H}]^+$ 578.1249, found: 578.1235.

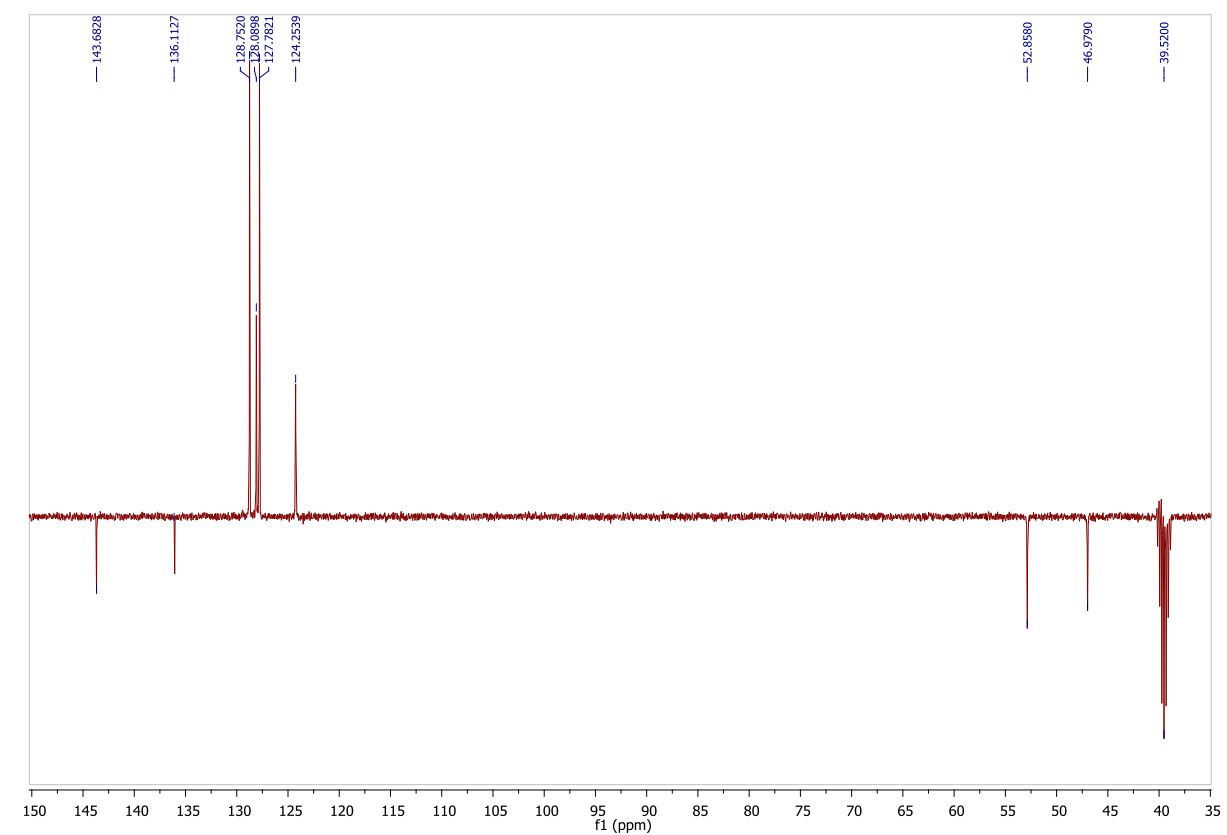
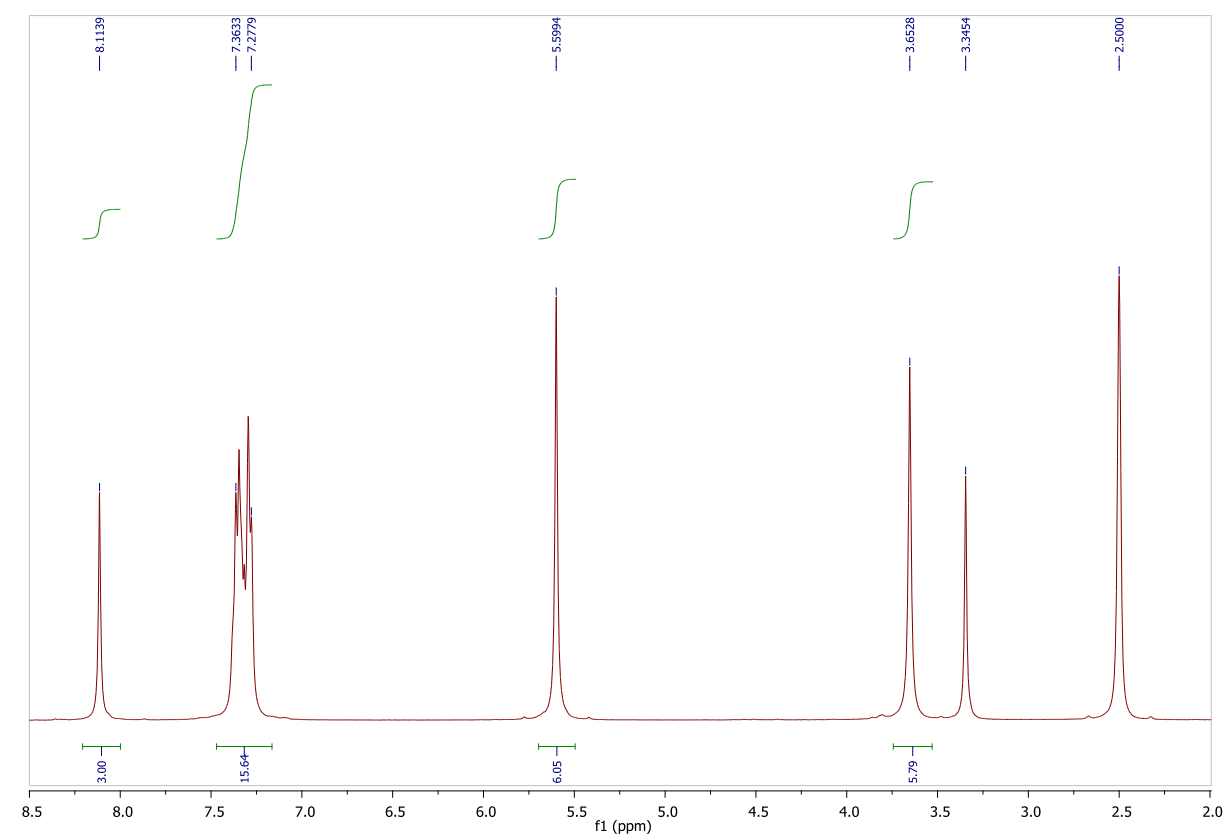


Figure 6.38 - ¹H and ¹³C NMR spectra of **132**.

[Zn(**110**)Cl]Cl **132**

Following the general procedure, **110** (150 mg, 0.282 mmol) and ZnCl₂ (38.4 mg, 0.282 mmol) in MeCN (15 mL) yielded complex **132** as a beige solid (138 mg, 74%). m.p. 178-180 °C; ¹H NMR (400 MHz, DMSO-d₆): δ= 3.66 (s, 6H, N-CH₂), 5.60 (s, 6H, benzyl-CH₂), 7.28-7.36 (m, 15H, Ar-H), 8.11 (s, 3H, H_{triazole}) ppm; ¹³C NMR (DEPT 135, 100 MHz, DMSO-d₆): δ= 47.0, 52.8, 124.2, 127.8, 128.1, 128.7, 136.1, 143.7 ppm; IR: 3130, 1496, 1455, 1331, 1220, 1140, 1081, 1046, 963, 801 v_{max} cm⁻¹; HRMS (EI) calcd for C₃₀H₃₀N₁₀ZnCl [M+H]⁺ 629.1629, found: 629.1615.

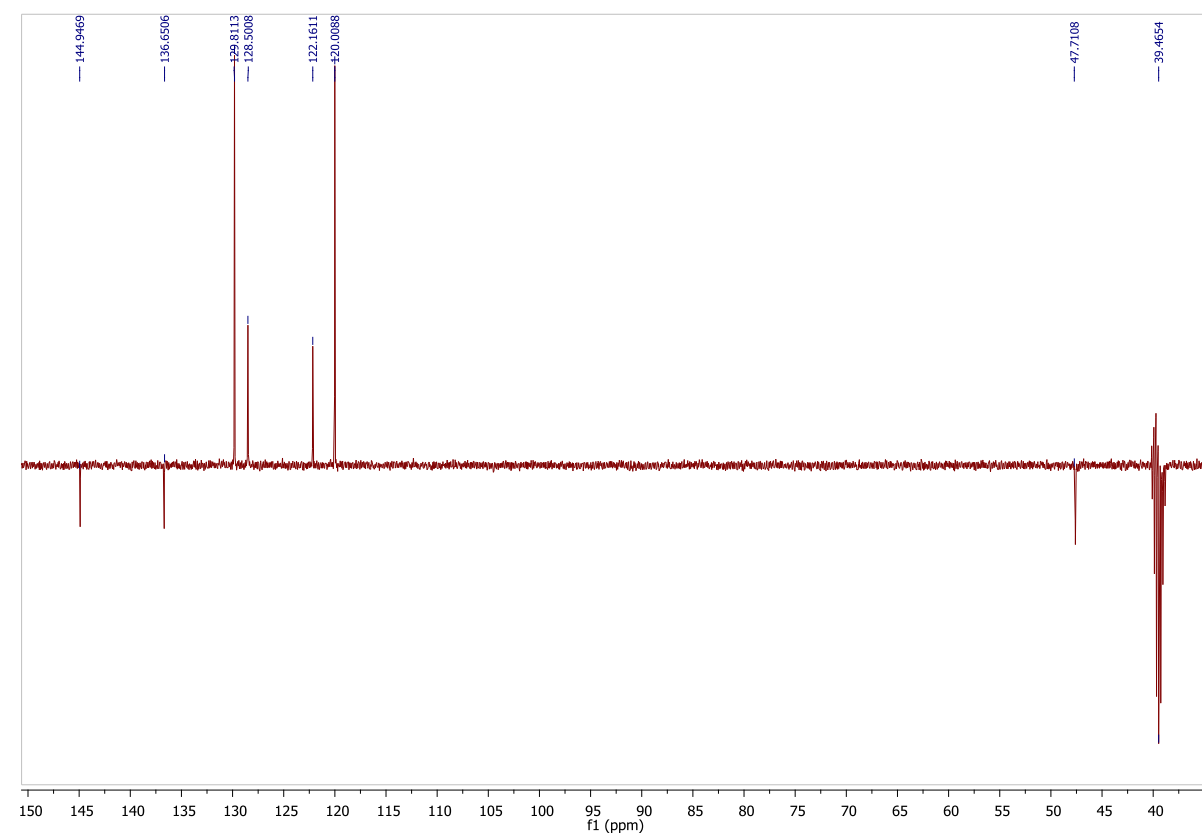
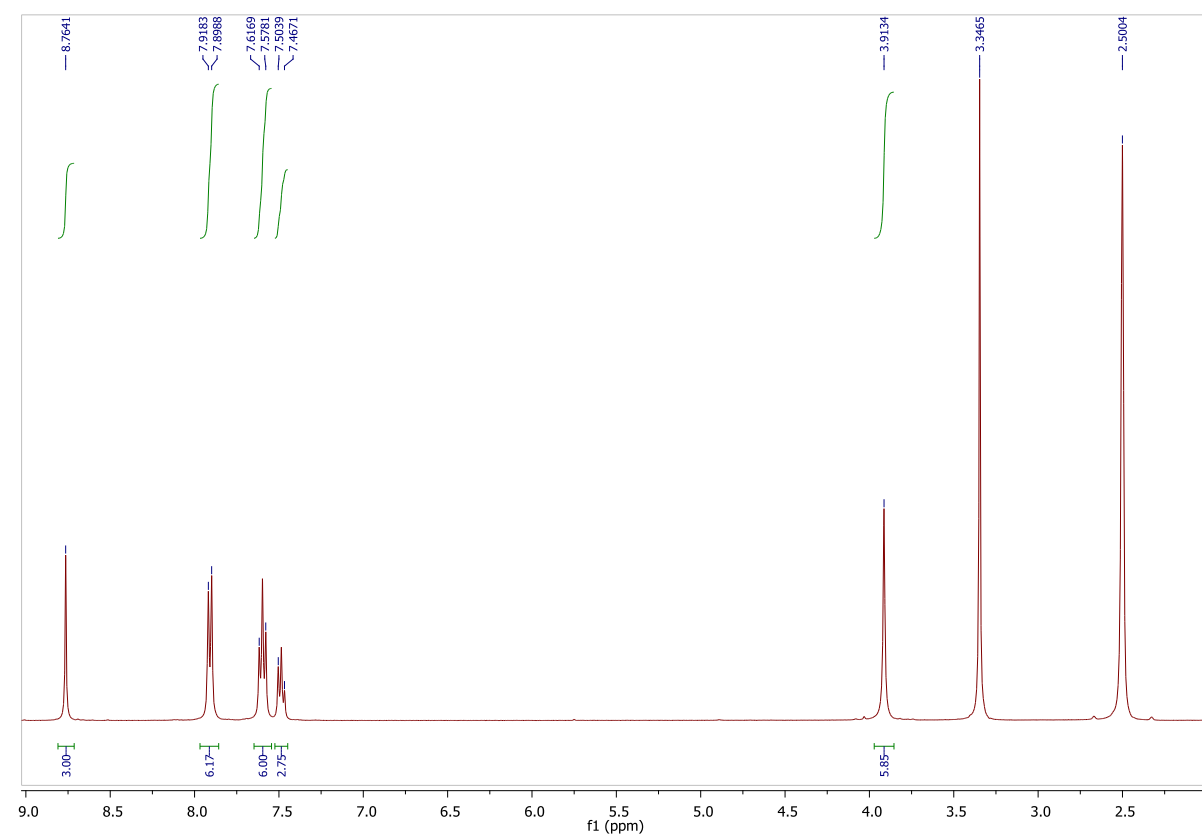


Figure 6.39 - ¹H and ¹³C NMR spectra of **141**.

[Zn(**111**)Cl]₂[ZnCl₄] **141**

Following the general procedure, **111** (100 mg, 0.204 mmol) and ZnCl₂ (55.6 mg, 0.408 mmol) in MeOH (10 mL) yielded complex **141** as a beige solid (100 mg, 86%). Single crystals of [Zn(**111**)Cl]₂[ZnCl₄] were isolated from the solution of **141** in CD₃OD. m.p. 176-178 °C; ¹H NMR (400 MHz, DMSO-d₆): δ= 3.91 (s, 6H, N-CH₂), 7.47-7.50 (m, 3H, Ar-H), 7.58-7.62 (m, 6H, Ar-H), 7.90-7.92 (m, 6H, Ar-H), 8.76 (s, 3H, CH_{triazole}) ppm; ¹³C NMR (DEPT 135, 100 MHz, DMSO-d₆): δ= 47.7, 120.0, 122.2, 128.5, 129.8, 136.6, 144.9 ppm; IR: ν_{max} 3480, 3075, 1596, 1499, 1466, 1354, 1249, 1193, 1085, 1045, 991, 965, 827 cm⁻¹; HRMS (EI) calcd for C₂₇H₂₄N₁₀ZnCl [M+H]⁺ 587.1160, found: 587.1150.

6.4.2.2. Synthesis of the Perchlorate Metal Complexes of Ligands **110** and **111**: General Procedure³² as Demonstrated by the Synthesis of $[\text{Cu}(\mathbf{110})](\text{ClO}_4)_2$ **133**.

110 (100 mg, 0.188 mmol) and $\text{Cu}(\text{ClO}_4)_2 \cdot 6\text{H}_2\text{O}$ (69.7 mg, 0.188 mmol) were dissolved in MeCN (10 mL) and the solution was stirred at RT for 16 h. Any precipitate in the reaction mixture was removed by filtration. The resulting reaction solution was reduced in volume and Et_2O (30 mL) was then added causing the precipitation of a green powder, which was collected by filtration, washed with Et_2O (10 mL) and dried *in vacuo* to afford **133** as a green crystalline powder (153 mg, quantitative yield). $\mu_{\text{eff}} = 1.6 \mu_{\text{B}}$; IR: ν_{max} 3153, 2962, 1629, 1455, 1328, 1071, 953, 930, 806 cm^{-1} ; UV-Vis (MeCN): λ_{max} (ϵ) = 360 (918), 661 (69), 892 nm (156 $\text{dm}^3\text{mol}^{-1}\text{cm}^{-1}$); HRMS (EI) calcd for $\text{C}_{30}\text{H}_{32}\text{N}_{10}\text{OCu} [\text{M}+\text{H}]^{2+}$ 305.6023, found: 305.6023.

$[\text{Cu}(\mathbf{111})](\text{ClO}_4)_2$ **142**

Following the general procedure, **111** (100 mg, 0.204 mmol) and $\text{Cu}(\text{ClO}_4)_2 \cdot 6\text{H}_2\text{O}$ (75.6 mg, 0.204 mmol) in MeCN (10 mL) yielded complex **142** as a green crystalline solid (115 mg, 73%). $\mu_{\text{eff}} = 1.7 \mu_{\text{B}}$; IR: ν_{max} 3489, 3155, 1627, 1596, 1499, 1466, 1358, 1260, 1094, 1058, 955, 819 cm^{-1} ; UV-Vis (MeCN): λ_{max} (ϵ) = 355 (924), 661 (99), 842 nm (150 $\text{dm}^3\text{mol}^{-1}\text{cm}^{-1}$); HRMS (EI) calcd for $\text{C}_{27}\text{H}_{26}\text{N}_{10}\text{OCu} [\text{M}+\text{H}]^{2+}$ 284.5788, found: 284.5790.

$[\text{Ni}(\mathbf{110})](\text{ClO}_4)_2$ **134**

Following the general procedure, **110** (100 mg, 0.188 mmol) and $\text{Ni}(\text{ClO}_4)_2 \cdot 6\text{H}_2\text{O}$ (68.5 mg, 0.188 mmol) in MeCN (10 mL) yielded complex **134** as a light violet solid (120 mg, 79%). $\mu_{\text{eff}} = 2.7 \mu_{\text{B}}$; IR: ν_{max} 3406, 3146, 1630, 1456, 1310, 1074, 961, 873 cm^{-1} ; UV-Vis (MeCN): λ_{max} (ϵ) = 350 (60), 545 (20), 774 (10), ~900 nm (12 $\text{dm}^3\text{mol}^{-1}\text{cm}^{-1}$); HRMS (EI) calcd for $\text{C}_{30}\text{H}_{32}\text{N}_{10}\text{ONi} [\text{M}+\text{H}]^+$ 303.1052, found: 303.1054.

$[\text{Ni}(\mathbf{111})](\text{ClO}_4)_2$ **143**

Following the general procedure, **111** (100 mg, 0.204 mmol) and $\text{Ni}(\text{ClO}_4)_2 \cdot 6\text{H}_2\text{O}$ (74.6 mg, 0.204 mmol) in MeCN (10 mL) yielded complex **143** as a light purple solid (109 mg, 70%). $\mu_{\text{eff}} = 2.9 \mu_{\text{B}}$; IR: ν_{max} 3411, 3156, 1625, 1597, 1504, 1466, 1365, 1261, 1197, 1088, 997, 965 cm^{-1} ; UV-Vis (MeCN): λ_{max} (ϵ) = 360 (65), 542 (19), 771 (6), ~900 nm (12 $\text{dm}^3\text{mol}^{-1}\text{cm}^{-1}$); HRMS (EI) calcd for $\text{C}_{27}\text{H}_{26}\text{N}_{10}\text{ONi} [\text{M}+\text{H}]^{2+}$ 282.0817, found: 282.0817

[Mn(110)](ClO₄)₂ 135

Following the general procedure, **110** (150 mg, 0.282 mmol) and Mn(ClO₄)₂·6H₂O (101 mg, 0.282 mmol) in MeCN (15 mL) yielded complex **135** as a beige solid (92 mg, 41%). μ_{eff} = 5.6 μ_{B} ; IR: ν_{max} 3490, 3150, 1632, 1455, 1312, 1069, 965, 816 cm⁻¹; UV-Vis (MeOH): λ_{max} (ϵ) = 360 (925), 660 (69), 889 nm (155 dm³mol⁻¹cm⁻¹); HRMS (EI) calcd for C₃₀H₃₂N₁₀OMn [M+H]²⁺ 301.6065, found: 301.6068.

[Mn(111)₂](ClO₄)₂ 144

Following the general procedure, **111** (100 mg, 0.204 mmol) and Mn(ClO₄)₂·6H₂O (36.9 mg, 0.102 mmol) in MeOH (10 mL) yielded complex **144** as a beige solid (84 mg, 80%). Slow diffusion of Et₂O into a MeOH solution of **144** resulted in single crystals of [Mn(**111**)₂](ClO₄)₂. μ_{eff} = 5.3 μ_{B} ; IR: ν_{max} 3426, 3150, 1634, 1597, 1400, 1356, 1245, 1068, 992, 875 cm⁻¹; HRMS (EI) calcd for C₅₄H₄₉N₂₀ [M+H]⁺ 977.4444, found: 977.4427.

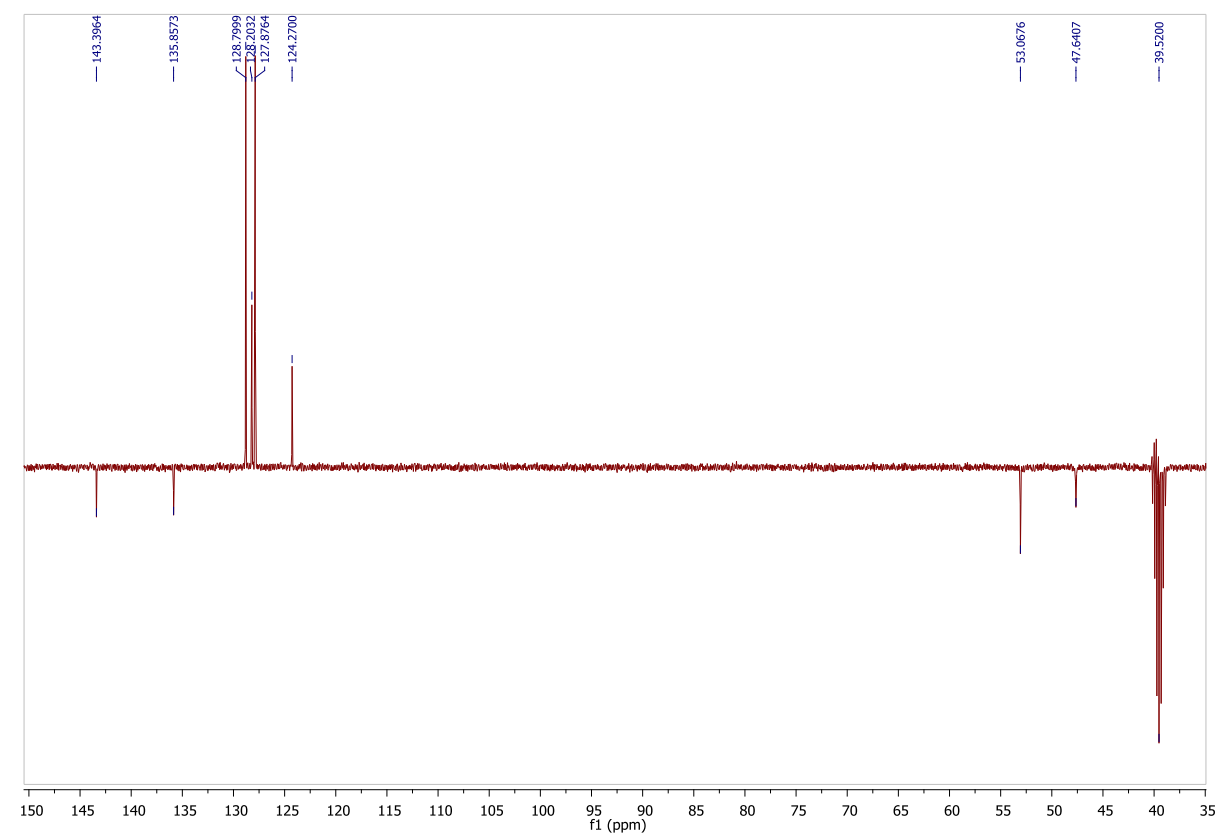
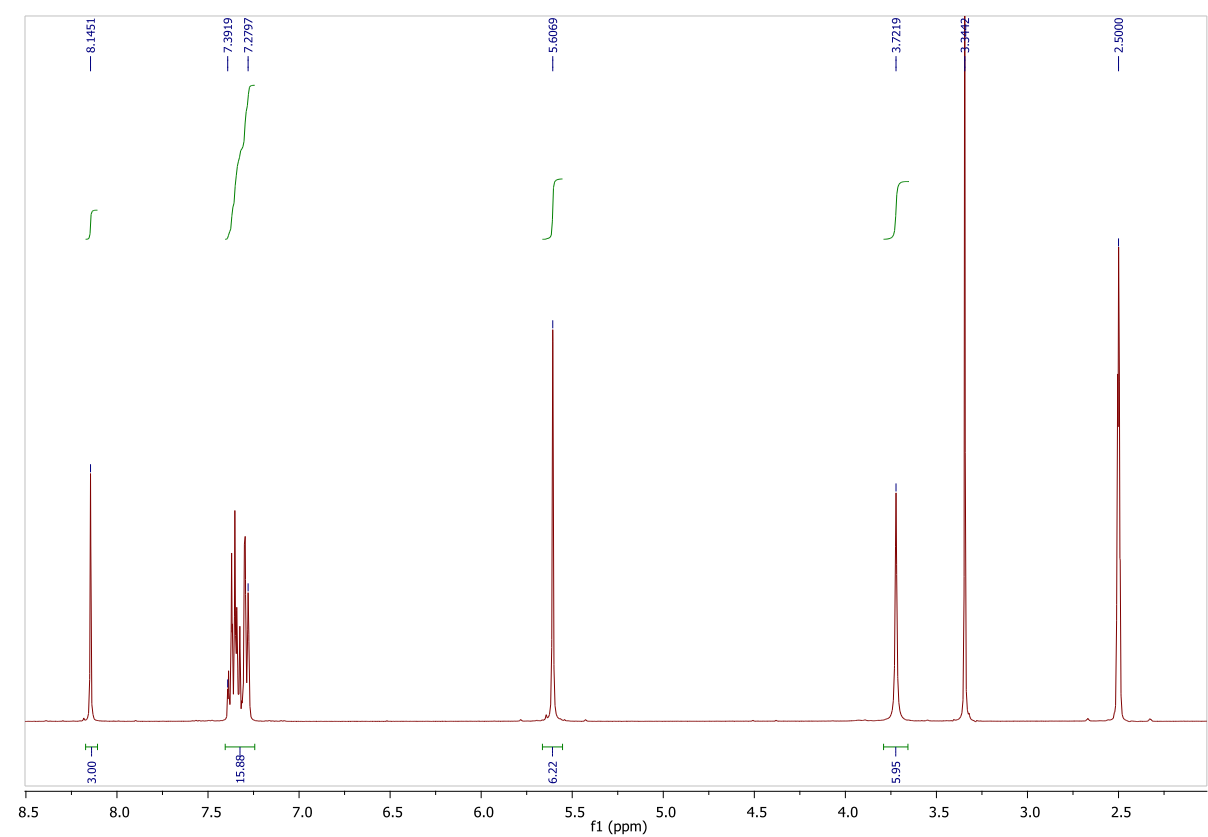


Figure 6.40 - ¹H and ¹³C NMR spectra of **136**.

[Zn(**110**)](ClO₄)₂ **136**

Following the general procedure, **110** (100 mg, 0.188 mmol) and Zn(ClO₄)₂·6H₂O (70.0 mg, 0.188 mmol) in MeCN (10 mL) yielded crude complex **136** as a beige solid (111 mg, 73%). ¹H NMR (400 MHz, DMSO-d₆): δ= 3.72 (s, 6H, N-CH₂), 5.61 (s, 6H, benzyl-CH₂), 7.28-7.32 (m, 15H, Ar-H), 8.14 (s, 3H, H_{triazole}) ppm; ¹³C NMR (DEPT 135, 100 MHz, DMSO-d₆): δ= 47.6, 53.1, 124.3, 127.9, 128.2, 128.8, 135.9, 143.4 ppm; IR: ν_{max} 3150, 3062, 1632, 1455, 1596, 1323, 1076, 962, 802 cm⁻¹; HRMS (EI) calcd for C₃₀H₃₂N₁₀OZn [M+H]²⁺ 306.1021, found: 306.1018.

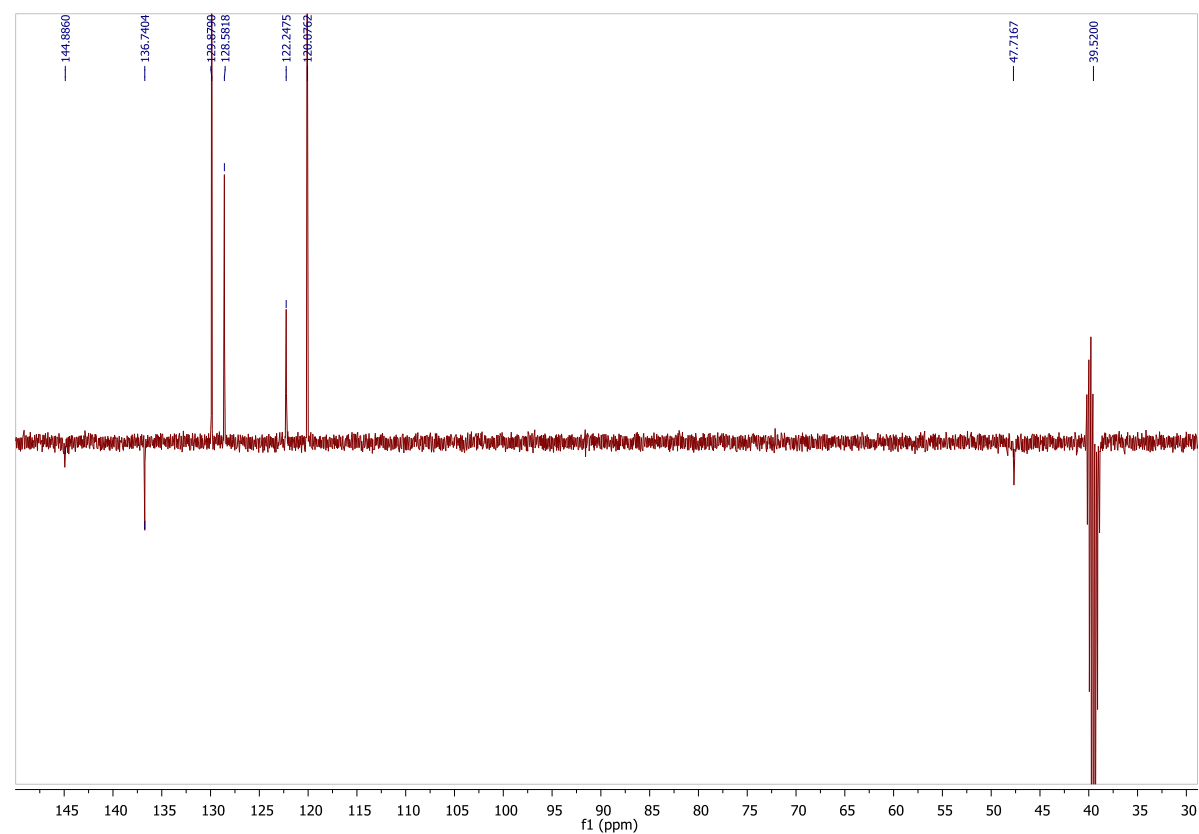
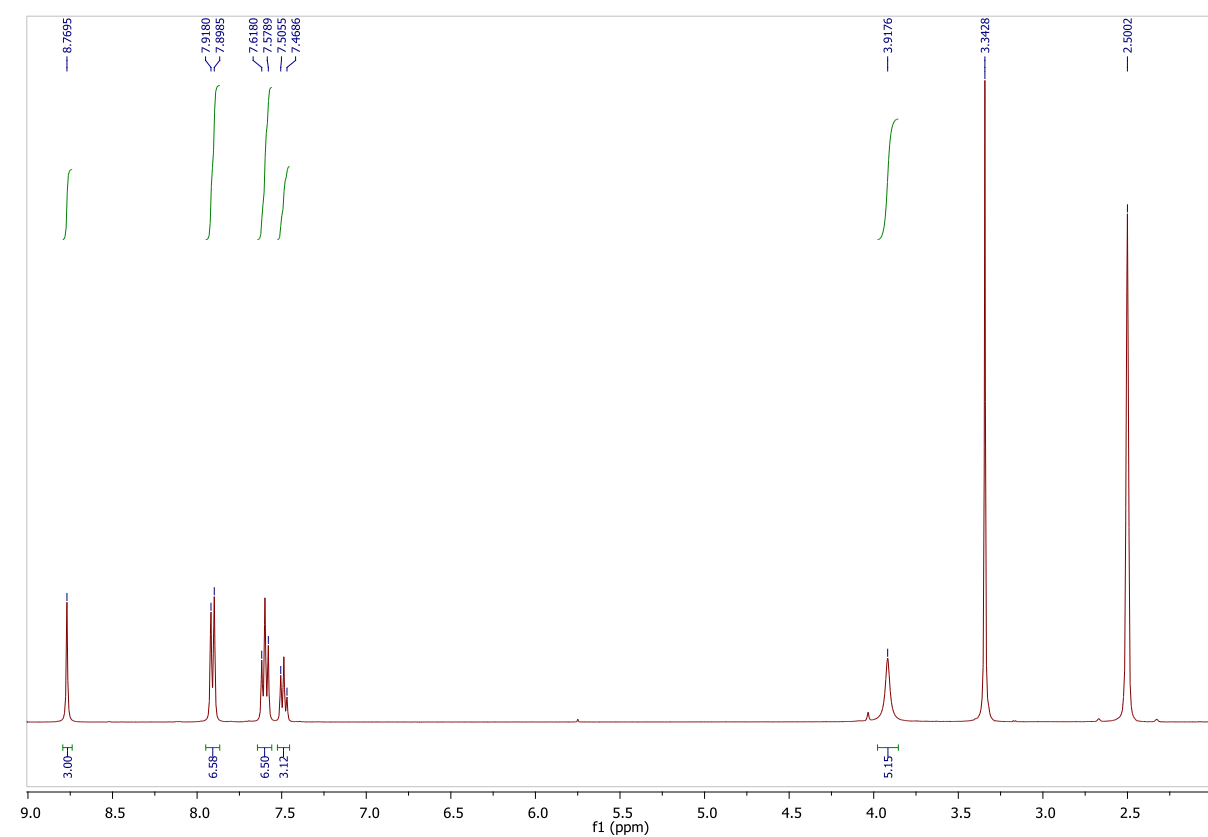


Figure 6.41 - ¹H and ¹³C NMR spectra of **145**.

[Zn(**111**)](ClO₄)₂ **145**

Following the general procedure, **111** (100 mg, 0.204 mmol) and Zn(ClO₄)₂·6H₂O (76.0 mg, 0.204 mmol) in MeOH (10 mL) yielded complex **145** as a beige solid (133 mg, 85%). IR: ν_{max} 3388, 3143, 1646, 1499, 1467, 1347, 1253, 1083, 1067, 960 cm⁻¹; ¹H NMR (400 MHz, DMSO-d₆): δ= 3.92 (s, 6H, N-CH₂), 7.47-7.50 (m, 3H, Ar-H), 7.58-7.62 (m, 6H, Ar-H), 7.90-7.92 (m, 6H, Ar-H), 8.77 (s, 3H, CH_{triazole}) ppm; ¹³C NMR (DEPT 135, 100 MHz, DMSO-d₆): δ= 47.7, 120.0, 122.2, 128.6, 129.9, 136.7, 144.9 ppm; HRMS (EI) calcd for C₂₇H₂₆N₁₀OZn [M+H]²⁺ 285.0786, found: 285.0788.

6.5. Single X-Ray Crystallography

The data were collected on a Bruker Kappa Apex Duo diffractometer with Apex II, area detector and a molybdenum sealed tube X-ray source (50 kV, 30 mA, $\lambda = 0.71073 \text{ \AA}$). The crystal-to-detector distance was 30 mm and φ and Ω scans (2.0° increments, 10 s exposure time) were carried out to fill the Ewald sphere. Data collection and processing were carried out using the SAINT³³ and empirical absorption correction was applied using SADABS.³³ The structures were solved by the direct-method using the program SHELXS-2014/7³⁴ and refined anisotropically (non-hydrogen atoms) by full-matrix least-squares on F² using SHELXL-2014/7.³⁴ The H atom positions were calculated geometrically and refined with a riding model. The program SHELXTL³⁴ was used for drawing the molecules.

6.5.1. Data for [Co(68)CO₃]MeCO₃ 86

Dark pink shard, 0.050 x 0.120 x 0.300 mm; C_{21.5}H₃₈₄CoN₄O_{7.50}; M= 880.23; triclinic; a= 7.8513(9) Å, b= 10.6765(12) Å, c= 16.059(2) Å, $\alpha = 72.921(3)^\circ$, $\beta = 78.999(3)^\circ$, $\gamma = 71.497(2)^\circ$, V= 1213.2(3) Å³ are based upon the refinement of the XYZ-centroids of reflections above 20 $\sigma(I)$; space group *P*₁; Z= 2; T= 100(2) K; $\theta_{\min} = 1.33^\circ$; $\theta_{\max} = 28.52^\circ$; $\mu = 0.794 \text{ mm}^{-1}$; Total reflections measured= 21517; Independent reflections= 6019; Reflections used = 4726 ($>2\sigma(F^2)$); The final anisotropic full-matrix least-squares refinement on F² with 321 variables converged at R₁ = 6.15%, for the observed data and wR₂ = 17.93% for all data. The goodness-of-fit was 1.029. The largest peak in the final difference electron density synthesis was 2.501 e⁻/Å³ and the largest hole was -0.562 e⁻/Å³ with an RMS deviation of 0.130 e⁻/Å³. On the basis of the final model, the calculated density was 2.410 g/cm³ and F(000), 1256 e⁻.

6.5.2. Data for [Co(78)Cl]Cl 89¹⁸

Violet needle, 0.080 mm x 0.240 mm x 0.250 mm; C₁₄H₃₄CoN₄O₂; M= 455.73; orthorhombic; a= 15.7203(6) Å, b= 13.2360(5) Å, c= 18.9413(7) Å, $\alpha = 90^\circ$, $\beta = 90^\circ$, $\gamma = 90^\circ$, V= 3941.2(3) Å³ are based upon the refinement of the XYZ-centroids of reflections above 20 $\sigma(I)$; space group *Pbca*; Z= 8; T= 100(2) K, $\theta_{\min} = 2.15^\circ$; $\theta_{\max} = 28.29^\circ$; $\mu = 1.293 \text{ mm}^{-1}$; Total reflections measured = 21315; Independent reflections= 4890; reflections used= 4189 ($>2\sigma(F^2)$); The final anisotropic full-matrix least-squares refinement on F² with 223 variables converged at R₁ = 4.13%, for the observed data and wR₂ = 10.35% for all data. The goodness-of-fit was 1.032. The largest peak in the final difference electron density synthesis was 1.522 e⁻/Å³

and the largest hole was $-0.893 \text{ e}^-/\text{\AA}^3$ with an RMS deviation of $0.091 \text{ e}^-/\text{\AA}^3$. On the basis of the final model, the calculated density was 1.536 g/cm^3 and $F(000)$, 1920 e^- .

6.5.3. Data for $[\mathbf{78H_3}][\text{CoCl}_4]\text{Cl}$

Translucent light blue shard, 0.060 x 0.100 x 0.450 mm; $\text{C}_{12}\text{H}_{29}\text{Cl}_5\text{CoN}_4$; $M = 465.57$; triclinic; $a = 7.0704(8) \text{ \AA}$, $b = 11.0947(12) \text{ \AA}$, $c = 12.6036(14) \text{ \AA}$, $\alpha = 99.600(2)^\circ$, $\beta = 92.585(2)^\circ$, $\gamma = 92.053(3)^\circ$, $V = 972.90(19) \text{ \AA}^3$ are based upon the refinement of the XYZ-centroids of 9905 reflections above $20 \sigma(I)$ with $5.366^\circ < 2\theta < 56.65^\circ$; space group P_1 ; $Z = 2$; $T = 100(2) \text{ K}$; $\theta_{\min} = 1.64^\circ$; $\theta_{\max} = 28.36^\circ$; $\mu = 1.569 \text{ mm}^{-1}$; Total reflections measured = 17294; Independent reflections = 4855; reflections used = 4604 ($>2\sigma(F^2)$); The final anisotropic full-matrix least-squares refinement on F^2 with 213 variables converged at $R_1 = 1.81\%$, for the observed data and $wR_2 = 4.72\%$ for all data. The goodness-of-fit was 1.045. The largest peak in the final difference electron density synthesis was $0.590 \text{ e}^-/\text{\AA}^3$ and the largest hole was $-0.255 \text{ e}^-/\text{\AA}^3$ with an RMS deviation of $0.049 \text{ e}^-/\text{\AA}^3$. On the basis of the final model, the calculated density was 1.589 g/cm^3 and $F(000)$, 482 e^- .

6.5.4. Data for $[\text{Cu}(\mathbf{111})\text{Cl}_2] \mathbf{138}$

Bright green shard, 0.200 mm x 0.300 mm x 0.400 mm; $\text{C}_{29}\text{H}_{27}\text{Cl}_2\text{CuN}_{11}$; $M = 664.05$; monoclinic; $a = 13.2198(12) \text{ \AA}$, $b = 14.2968(14) \text{ \AA}$, $c = 15.5334(14) \text{ \AA}$, $\beta = 91.108(2)^\circ$, $V = 2935.3(5) \text{ \AA}^3$ are based upon the refinement of the XYZ-centroids of reflections above $20 \sigma(I)$; space group P_{121}/n_1 ; $Z = 4$; $T = 100(2) \text{ K}$; $\theta_{\min} = 1.94^\circ$; $\theta_{\max} = 30.56^\circ$; $\mu = 0.968 \text{ mm}^{-1}$; Total reflections measured = 35132; Independent reflections = 8964; reflections used = 8140 ($>2\sigma(F^2)$); The final anisotropic full-matrix least-squares refinement on F^2 with 389 variables converged at $R_1 = 2.67\%$, for the observed data and $wR_2 = 7.26\%$ for all data. The goodness-of-fit was 1.023. The largest peak in the final difference electron density synthesis was $0.458 \text{ e}^-/\text{\AA}^3$ and the largest hole was $-0.346 \text{ e}^-/\text{\AA}^3$ with an RMS deviation of $0.059 \text{ e}^-/\text{\AA}^3$. On the basis of the final model, the calculated density was 1.503 g/cm^3 and $F(000)$, 1364 e^- .

6.5.5. Data for $[\text{Ni}(\mathbf{110})(\text{OH}_2)\text{Cl}]\text{Cl} \mathbf{130}$

Green shard, 0.100 x 0.150 x 0.450 mm; $\text{C}_{32}\text{H}_{41}\text{Cl}_2\text{N}_{11}\text{NiO}_4$; $M = 773.37$; monoclinic; $a = 22.4131(13) \text{ \AA}$, $b = 9.2438(5) \text{ \AA}$, $c = 17.6763(10) \text{ \AA}$, $\beta = 100.0580(10)^\circ$, $V = 3605.9(4) \text{ \AA}^3$ are based upon the refinement of the XYZ-centroids of reflections above $20 \sigma(I)$; space group P_{121}/c_1 ; $Z = 4$; $T = 100(2) \text{ K}$; $\theta_{\min} = 1.85^\circ$; $\theta_{\max} = 28.30^\circ$; $\mu = 0.739 \text{ mm}^{-1}$; Total reflections measured = 34938; Independent reflections = 8930; reflections used = 7007 ($>2\sigma(F^2)$); The

final anisotropic full-matrix least-squares refinement on F^2 with 484 variables converged at $R_1 = 3.70\%$, for the observed data and $wR_2 = 9.85\%$ for all data. The goodness-of-fit was 1.010. The largest peak in the final difference electron density synthesis was $0.689 \text{ e}^-/\text{\AA}^3$ and the largest hole was $-0.447 \text{ e}^-/\text{\AA}^3$ with an RMS deviation of $0.072 \text{ e}^-/\text{\AA}^3$. On the basis of the final model, the calculated density was 1.425 g/cm^3 and $F(000)$, 1616 e^- .

6.5.6. Data for $[\text{Mn}(\mathbf{111})_2](\text{ClO}_4)_2$ **144**

0.200 mm x 0.300 mm x 0.320 mm; $\text{C}_{54}\text{H}_{50}\text{Cl}_2\text{MnN}_{20}\text{O}_9$; $M = 1248.98$; monoclinic; $a = 22.840(4) \text{ \AA}$, $b = 21.550(4) \text{ \AA}$, $c = 11.752(2) \text{ \AA}$, $\beta = 100.753(4)^\circ$, $V = 5682.8(19) \text{ \AA}^3$ are based upon the refinement of the XYZ-centroids of reflections above $20 \sigma(I)$; space group P_{121}/c_1 ; $Z = 4$; $T = 100(2) \text{ K}$; $\theta_{\min} = 2.05^\circ$; $\theta_{\max} = 27.52^\circ$; $\mu = 0.402 \text{ mm}^{-1}$; Total reflections measured = 75531; Independent reflections = 13012; reflections used = 10667 ($>2\sigma(F^2)$); The final anisotropic full-matrix least-squares refinement on F^2 with 783 variables converged at $R_1 = 5.74\%$, for the observed data and $wR_2 = 17.19\%$ for all data. The goodness-of-fit was 1.053. The largest peak in the final difference electron density synthesis was $1.260 \text{ e}^-/\text{\AA}^3$ and the largest hole was $-0.667 \text{ e}^-/\text{\AA}^3$ with an RMS deviation of $0.087 \text{ e}^-/\text{\AA}^3$. On the basis of the final model, the calculated density was 1.460 g/cm^3 and $F(000)$, 2580 e^- .

6.5.7. Data for $[\text{Zn}(\mathbf{111})\text{Cl}]_2[\text{ZnCl}_4]$ **141**

Beige shard, 0.070 mm x 0.120 mm x 0.300 mm; $\text{C}_{55}\text{H}_{52}\text{Cl}_6\text{N}_{20}\text{OZn}_3$; $M = 1417.97$; monoclinic; $a = 11.8560(14) \text{ \AA}$, $b = 17.548(2) \text{ \AA}$, $c = 14.3322(18) \text{ \AA}$, $\beta = 92.864(3)^\circ$, $V = 2978.1(6) \text{ \AA}^3$, are based upon the refinement of the XYZ-centroids of reflections above $20 \sigma(I)$; space group P_{1211} ; $Z = 2$; $T = 100(2) \text{ K}$; $\theta_{\min} = 1.72^\circ$; $\theta_{\max} = 28.71^\circ$; $\mu = 1.527 \text{ mm}^{-1}$; Total reflections measured = 30858; Independent reflections = 15205; reflections used = 13645 ($>2\sigma(F^2)$); The final anisotropic full-matrix least-squares refinement on F^2 with 768 variables converged at $R_1 = 3.29\%$, for the observed data and $wR_2 = 7.43\%$ for all data. The goodness-of-fit was 1.000. The largest peak in the final difference electron density synthesis was $1.154 \text{ e}^-/\text{\AA}^3$ and the largest hole was $-0.377 \text{ e}^-/\text{\AA}^3$ with an RMS deviation of $0.074 \text{ e}^-/\text{\AA}^3$. On the basis of the final model, the calculated density was 1.581 g/cm^3 and $F(000)$, 1444 e^- .

6.6. Bibliography

1. K. De Buysser, G. G. Herman, E. Bruneel, S. Hoste and I. Van Driessche, *Chem. Phys.*, 2005, **315**, 286-292.
2. D. E. Ward, C. K. Rhee, *Can. J. Chem.*, 1989, **67**, 1206-1211.
3. L. Campbell-Verduyn, P. H. Elsinga, L. Mirfeizi, R. A. Dierckxb and B. L. Feringa, *Org. Biochem. Chem.*, 2008, **6**, 3461, 3463.
4. J. S. Foot, F. E. Luia and R. Kluge, *Chem. Commun.*, 2009, **47**, 7315-7317.
5. S. P. Develay, R. Tripier, F. Chuburu, M. Le Baccon and H. Handel, *Eur. J. Org. Chem.*, 2003, 3047-3050.
6. J. Rohovec, R. Gyepes, I. Císařová, J. Rudovský and I. Lukeš, *Tetrahedron Lett.*, 2000, **41**, 1249-1253.
7. W. C. Baker, M. J. Choi, D. C. Hill, J. L. Thompson and P. A. Petillo, *J. Org. Chem.*, 1999, **64**, 2683-2689.
8. G. R. Weisman, E. H. Wong, D. C. Hill, M. E. Rogers, D. P. Reed and J. C. Calabrese, *Chem. Commun.*, 1996, 947-948.
9. E. H. Wong, G. R. Weisman, D. C. Hill, David P. Reed, M. E. Rogers, J. S. Condon, M. A. Fagan, J. C. Calabrese, K. Lam, I. A. Guzei, and A. L. Rheingold, *J. Am. Chem. Soc.*, 2000, **122**, 10561-1572.
10. W. Niu, E. H. Wong, G. R. Weisman, D. C. Hill, D. J. Tranchemontagne, K.-C. Lam, R. D. Sommer, L. N. Zakharov and A. L. Rheingoldc, *Dalton Trans.*, 2004, 3536-3547.
11. R. Jorge, PhD Thesis, Queen Mary University of London, 2011.
12. R. Smith, D. Huskens, D. Daelemans, R. E. Mewis, C. D. Garcia, A. N. Cain, T. N. C. Freeman, C. Pannecouque, E. Clercq, D. Schols, T. J. Hubin and S. J. Archibald, *Dalton Trans.*, 2012, **41**, 11369-11377.
13. M. Shibata, *Modern Syntheses of Co(III) Complexes*, Springer-Verlag, New York, 1983.
14. D. A. Knight, J. B. Delehanty, E. R. Goldman, J. Bongard, F. Streich, L. W. Edwards and E. L. Chang, *Dalton Trans.*, 2004, **13**, 2006-2011.
15. J. H. Loehlin, *Acta Cryst.*, 1976, **B32**, 3063.
16. J. Kim, *J. Korean Chem. Soc.*, 1998, **42**, 240-244.
17. J. Giusti, S. Chimichi, M. Ciamf'olini, *Inorg. Chim. Acta*, 1984, **88**, 51-54.
18. T. J. Hubin, N. W. Alcock, H. J. Clase, L. L. Seib and D. H. Busch, *Inorg. Chim. Acta*, 2002, **337**, 91-102.
19. J. P. Collman and P. W. Schneider, *Inorg. Chem.*, 1966, **5**, 1380-1384.

20. J. Y. Chang, G. Lu, R. J. Stevenson, P. J. Brothers, G. R. Clark, K. J. Botting, D. M. Ferry, M. Tercel, W. R. Wilson, W. A. Denny and D. C. Ware, *Inorg. Chem.*, 2013, **52**, 7688-7698.
21. T. Koike and E. Kimura, *J. Am. Chem. Soc.*, 1991, **113**, 8935-8941.
22. M. Subat, K. Woinaroschy, C. Gerstl, B. Sarkar, W. Kaim and B. Köing, *Inorg. Chem.*, 2008, **47**, 4661-4668.
23. P. R. Norman, *Inorg. Chim. Acta*, 1987, 130, 1-4.
24. M. Shionoya, T. Ikeda, E. Kimura, M. Shiro, *J. Am. Chem. Soc.*, 1994, **116**, 3848-3859.
25. A. Yatsimirsky, *Coord. Chem. Rev.*, 2005, **249**, 1997-2011.
26. A. Jorge, M. Chernobryva, S. E. J. Rigby, M. Watkinson and M. Resmini, *Chem. Eur. J.*, 2016, **22**, 3764-3774.
27. J. E. Hein, L. B. Kransova, M. Iwasaki and V. V. Fokin, *Org. Synth.*, 2011, **88**, 238-247.
28. A. Baschieri, A. Mazzanti, S. Stagni and L. Sambri, *Eur. J. Inorg. Chem.*, 2013, 2432-2439.
29. V. Hong, A. K. Udit, R. A. Evans and M.G. Finn, *Chem. Biochem.*, 2008, **9**, 1481-1486.
30. D. Schweinfurth, S. Demeshko, M. M. Khusniyarov, S. Dechert, V. Gurram, M. R. Buchmeister, F. Meyer and B. Sarkar, *Inorg. Chem.*, 2012, **51**, 7592-7597.
31. P. S. Donnelly, S. D. Zanatta, S. C. Zammit, J. M. White and S. J. Williams, *Chem. Commun.*, 2008, 2459-2461.
32. D. Schweinfurth, F. Weisser, D. Bubrin, L. Bogani and B. Sarkar, *Inorg. Chem.*, 2011, **50**, 6114–6121.
33. Bruker, APEX2, SAINT and SADABS, *Bruker AXS Inc., Madison*, 2009, W1.
34. G. M. Sheldrick, *A short history of SHELX, Acta Crystallogr Sect A Found Cryst*, 2008, **64**, 112–122.

